LUND UNIVERSITY

R-hadron Searches and Charged Pion Spectra at High Transverse Momentum in Proton-Proton Collisions at the LHC using the ALICE Detector

Dobrin, Alexandru

2010

R-hadron Searches and Charged Pion Spectra at High Transverse Momentum in Proton-Proton Collisions at the LHC using the ALICE Detector

Thesis submitted for the degree of
Doctor of Philosophy
by
Alexandru Florin Dobrin

Thesis Advisor: **Peter Christiansen**
Faculty Opponent: **Brian A. Cole**
To be presented, with the permission of the Faculty of Science of Lund University, for public criticism in lecture hall B of the Department of Physics on Friday, the 15th of October 2010, at 10:15.

LUND
UNIVERSITY

DEPARTMENT OF PHYSICS
LUND, 2010

Organization		Document name	
LUND UNIVERSITY		**DOCTORAL DISSERTATION**	
Department of Physics		**Date of issue**	
Lund University		September, 2010	
Box 118		**CODEN**	
SE-221 00 Lund		LUNFD6/(NFFL-7230)2010	
SWEDEN			
Author(s)		**Sponsoring organization**	
Alexandru Florin Dobrin			
Title and subtitle			
R-hadron Searches and Charged Pion Spectra at High Transverse Momentum in Proton-Proton Collisions at the LHC using the ALICE Detector			

Abstract

With the start-up of the Large Hadron Collider (LHC), a new energy regime has opened up. The Standard Model (SM) can be "rediscovered" and new theories can be tested. ALICE, the dedicated heavy-ion experiment at LHC, will also record proton-proton (pp) collisions. Even though the main goal of the ALICE proton program is to provide the baseline measurements for interpreting the heavy-ion data, the new heavy stable charged particles ($m > 100$ GeV/c^2) predicted by some theoretical models, such as R-hadrons in Supersymmetry, are good candidates of ALICE searches for signals beyond the SM. Gluino R-hadron is chosen as an example of a candidate in this thesis, and cross sections and kinematic properties are obtained from PYTHIA simulations for various gluino masses (100-500 GeV/c^2). Detailed detector response simulations of the most important signatures for R-hadron identification in the ALICE central barrel are performed for 100 GeV/c^2 R-hadron mass. No evidence of particles that pass the R-hadron selection criteria in the Inner Tracking System, Time Projection Chamber (TPC), and the Time-of-Flight detectors can be observed in around 27.5 million pp events at $\sqrt{s} = 7$ TeV (the maximum energy available for the first two years of the LHC operation). First steps towards identified charged particle spectra at intermediate and high transverse momentum (p_T) using the TPC specific ionization energy loss are also taken in this thesis. Two approaches, R_π (STAR method for statistical PID) and Δ_π (the simplest method), are investigated here. The Δ_π method is found to be more suitable in the case of ALICE and is used to extract the charged pion spectra at high p_T in inelastic pp collisions at $\sqrt{s} = 900$ GeV and $\sqrt{s} = 7$ TeV.

Key words:			
Particle spectra, Transverse momentum, SUSY, R-hadrons, LHC, ALICE			
Classification system and/or index terms (if any)			
Supplementary bibliographical information:		**Language**	
		English	
ISSN and key title:		**ISBN**	
		978-91-7473-029-6	
Recipient's notes	**Number of pages**	**Price**	
	199		
	Security classification		

Distribution by (name and address)

Alexandru Florin Dobrin, Department of Physics
Box 118, SE-221 00 Lund, SWEDEN

I, the undersigned, being the copyright owner of the above-mentioned dissertation, hereby grant to all reference sources permission to publish and disseminate the abstract of the above-mentioned dissertation.

Signature _____   Date   7/09, 2010

Contents

List of Figures

List of Tables

Preface

In order to understand Nature one should identify the basic constituents of matter and study the interactions between them. The branch of physics which does all this is called particle physics. Probably it is part of our human nature to believe that there is a smallest building block. Historically, the idea of the smallest possible division of matter dates back to the 5th century BC when the Greeks (or Indians by other sources) introduced the concept of 'atom', meaning indivisible. While these ideas were more philosophical than empirical, the first experimental observation came in the early 19th century when John Dalton concluded that each element of Nature was composed of a single, unique type of particle. He believed that these particles are indivisible and therefore identified them with the uncuttable 'atoms' of long tradition. However, at the end of the century, J. J. Thompson proved that atoms are not indivisible by discovering the electron in cathode rays. In 1911 Ernest Rutherford postulated that atoms have their positive charge concentrated in a very small nucleus through his scattering experiment, and soon after he discovered the proton, the constituent of the nucleus. He also theorized about the existence of neutrons which was proved in 1932 by James Chadwick. It was not clear at that time whether the protons and neutrons could further be divided or not. In 1930 Wolfgang Pauli postulated the electron neutrino and C. D. Anderson discovered the muon in 1936. Electrons, muons and the (electron) neutrino were classified as leptons later on. Throughout the 1950s and 1960s around 100 new particles were discovered and they were initially regarded as fundamental particles. But in 1968 the proton substructure was revealed through electron-proton collisions at the Stanford Linear Accelerator Centre. The constituents of the proton were called partons and later identified with the quarks introduced by Murray Gell-Mann and George Zweig four years earlier. The quarks and leptons at present show no experimental evidence of size or substructure and they are considered fundamental objects of which all matter is composed. No free quarks were found or have been found by now; the quarks must combine to form particles called hadrons: baryons and mesons.

In parallel with all these experimental discoveries, the theoretical part made a great progress in understanding the physics of elementary particles in the last century. From the creation of the theory of relativity to the foundation of quantum mechanics, the construction of quantum field theories (the Higgs mechanism, the electroweak theory, the theory of strong interactions), the theoretical developments and predictions led to the formulation of the Standard Model (SM), currently the best framework of the particle physics field. The SM describes three fundamental interactions between the elementary particles: the

strong, the weak, and the electromagnetic forces, and the elementary particles that take part in these interactions. The only known interaction not described by the SM is the gravitational. The interactions are mediated by gauge bosons of spin 1: photons (electromagnetic), weak bosons (weak), and gluons (strong). The SM also includes 12 elementary particles of spin 1/2 known as fermions: 6 quarks and 6 leptons. In addition to the quarks, leptons, and guage bosons, it predicts the existence of the scalar Higgs boson. Finally, each particle has an antiparticle with the same mass and spin and opposite values for electric charge, color charge, and flavor.

Despite its great success in describing the elementary particle interactions up to the weak scale, the SM falls short of being a complete theory since it does not include gravity. Also it does not account for neutrino masses and none of its particles can be considered a dark matter candidate. Another still unverified ingredient is the yet undiscovered Higgs boson. In view of these problems, new theories are being constructed and only experimental data could give a clear answer.

All eyes turn towards the Large Hadron Collider (LHC) now since it is in its initial phase providing proton-proton (pp) collisions at the center-of-mass energy of 7 TeV, an energy that has never been reached before in a particle accelerator. The main motivation for building the LHC was to test the SM through the discovery of the Higgs boson, but other physics goals, like supersymmetry, extra dimensions, study of CP-violation, understanding the early evolution of our Universe by studying the Quark-Gluon Plasma (QGP), will also be pursued.

The ALICE detector at the LHC has been optimized for the large track density in heavy-ion collisions with the aim of studying the QGP at extreme values of energy density and temperature. Since the LHC is mainly a proton collider, ALICE experiment will also record proton-proton collisions.

Even though the main goal of the ALICE proton program is to provide the baseline measurements for interpreting the heavy-ion data, the new heavy stable charged particles ($m > 100$ GeV/c^2) predicted by some theoretical models, such as R-hadrons in Supersymmetry (SUSY), are good candidates of ALICE searches for signals Beyond the Standard Model.

The first topic of this thesis is dedicated to the search of heavy stable charged particles associated with a new theory, called Supersymmetry. SUSY relates bosons with fermions and predicts that each elementary particle has a supersymmetric partner with the same mass and the spin differing by 1/2. As no superpartners of the SM particles have been observed so far, supersymmetry must be a broken symmetry, allowing for heavier supersymmetric particles than the corresponding SM ones. Due to the low proton-proton integrated luminosity expected in ALICE, the gluino R-hadrons predicted by Split SUSY with the highest production cross section have the best detection potential. In Split SUSY the light gluino decay to neutralino (stable lightest supersymmetric particle) via virtual squarks (to preserve color and R-parity) is suppressed by the much heavier squarks (the mass states are "split") and instead hadronize into R-hadrons. These R-hadrons are predicted to be pair produced and can have very interesting inelastic interactions with hadronic matter. However, only the non-hadronic interactions were considered here due to the low material

budget; the strategy is more general and applies to all heavy charged particles. Because of the excellent particle identification capabilities of ALICE an event where two gluinos produced approximately back-to-back have hadronized into two charged R-hadrons is enough to discover these particles.

In order to outline the ALICE potential discovery of R-hadrons, I did PYTHIA and ALICE detector response simulations. In PYTHIA simulations I investigated four different gluino masses ($100 - 500$ GeV/c^2). I also performed detailed detector response simulations of the most important signatures for R-hadron identification in the ALICE central barrel for 100 GeV/c^2 R-hadron mass (Chapter 7). The results were presented in an ALICE Internal Note and in the proceedings of the SUSY09 conference.

One of the signatures of the QGP is the suppression of particles with high transverse momentum ($p_T > 2$ GeV/c), primarily produced in hard scatterings early in the collision. The experiments at the Relativistic Heavy Ion Collider (RHIC) have observed that the number of hadrons with $p_T > 5$ GeV/c is suppressed by 80% in central gold nuclei collisions as compared to estimates base on proton-proton collisions at the same energy per nucleon; the suppression pattern is also different for baryons and mesons at intermediate transverse momentum ($2 < p_T < 8$ GeV/c) and can be explained by recombination models where the particle production occurs through coalescence of "constituent quarks" rather than fragmentation of high transverse momentum jets.

Since the Time Projection Chamber (TPC) is the only detector which can provide direct particle identification information at these large transverse momenta, the second subject of this thesis describes a particle identification analysis based on the energy loss signal in the TPC. Because of the low multiplicity environment and the lack of heavy-ion data, the analysis was developed for proton-proton systems; it will be optimized for heavy-ion collisions later on.

For this topic I did a comparison between the approach for statistical particle identification used by the STAR experiment at RHIC and the simplest approach (Chapter 8). I found that the simplest method is more suitable in case of ALICE and I used it to extract the π^+ and π^- spectra from the data collected at 900 GeV and 7 TeV center-of-mass energy (Chapter 9). Note that the results presented in these chapters are not ALICE official ones.

The thesis is divided into two parts. The first part (Chapter 1 to 5) covers general issues as theoretical frameworks, the Large Hadron Collider, the ALICE detector. The second part (Chapter 6 to 9) describes the two analysis discussed above. A summary is presented at the end. In detail, the outline is the following: Chapter 1 summarizes the Standard Model. A general introduction to supersymmetry is given in Chapter 2. Chapter 3 focuses on high transverse momentum particle production in electron-proton, proton-proton, and heavy-ion collisions. The subsequent chapters are devoted to the experimental apparatus: Chapter 4 gives a short description of the Large Hadron Collider and the ALICE experiment, while the Time Projection Chamber subsystem of ALICE is detailed in Chapter 5. The next two chapters are dedicated to heavy stable charged particles emphasizing the R-hadrons: arguments why to perform a search for R-hadrons, the production mechanisms, the most relevant existing searches are reviewed in Chapter 6; a Monte Carlo generation of R-hadrons within the ALICE experiment is detailed in Chapter 7. An early study based on ALICE

simulated data done to understand how and to what precision identified particle yields can be obtained using the energy loss measurements in the Time Projection Chamber is described in Chapter 8. The π^+ and π^- spectra from pp collisions at $\sqrt{s} = 900$ GeV and $\sqrt{s} = 7$ TeV are presented in Chapter 9.

Acknowledgments

This thesis is the result of four years of work in the Division of Experimental High Energy Physics at Lund University. It was partly financed from the European Commission Marie Curie Early Stage Training program "Lund-HEP EST" (contract number MEST-CT-2005-019626). Swedish participation in ALICE was granted by the Swedish Research Council (VR) and Knut and Alice Wallenberg foundation (KAW). I have received help and inspiration from many people along the way, and now is the time to say thank you.

First of all I don't have enough words to thank Peter Christiansen, an excellent supervisor and a great support over the last four years. From the beginning he helped with everything concerning the ALICE software, and come up with great ideas and suggestions. From him I have learned the most and it was a pleasure working together. Then, apart from physics, thanks for all the good time that I had during our journeys around the world.

I enjoyed the nice and social atmosphere in the HEP group and I appreciated the freedom to travel everywhere was needed. Thanks for making this possible.

I appreciated the continuous help of our secretary, Bozena Wlosinska, with all the bureaucracy matters.

I am grateful to all my colleagues, from both theory and experimental divisions, for all the interesting discussions and the nice atmosphere in and outside the working space. A special thanks to my office mate Philippe Gros for finding the time to answer most of my questions.

I would like to thank the people from my previous workplace, the National Institute for Physics and Nuclear Engineering "Horia Hulubei" from Măgurele-Bucharest, especially Mihai Petrovici, for everything that I learned during my stay.

Special thanks to Peter, Anders Oskarsson, and Gösta Gustafson for revising this work.

Finally I would like to thank my family for all the love and support. Even though I was miles away, you were always close to me when I needed it. Thanks for believing in me and encouraging to do the things that I like. I could not have done it without this. Săru mâna mamă, tată.

Chapter 1

The Standard Model

The theories which describe the particles and their interactions are gauge theories, a special class of quantum field theories. A good example of such theories is the formulation of electromagnetic, weak and strong interactions in the Standard Model (SM) of elementary particle physics. It will be briefly described in the following. First some basic aspects of the SM will be presented, after that the Lagrangian of the theory will be reviewed and the experimental and theoretical shortcomings of the SM will be outlined at the end of the chapter.

1.1   Introduction

To understand the physics of elementary particles one should study the symmetries they exhibit. A fundamental result that shows the importance of the symmetries in Nature was provided by the mathematician Emmy Noether - in 1918 she established that symmetries imply conservation laws.

Using this principle the SM was constructed. It is a *gauge field theory* of the microscopic interactions. This means that one requires the Lagrangian density of the theory be invariant under gauge transformations. The SM describes the elementary matter particles observable in our world alongside three basic interactions governing them: electromagnetic, weak, and strong interactions. As of now, there is no canonical way to include gravitational interaction in the SM.

In order to describe the particles and interactions, three internal symmetries each associated with a theory are needed: $U(1)$ for the theory of Quantum Electrodynamics (QED), $SU(2)$ for the theory of weak interactions, and $SU(3)$ for the theory of Quantum Chromodynamics (QCD). QED, the best theory ever constructed to describe Nature, is the theory of the electromagnetic interaction and was formed by covariantly quantizing the theory of classical electrodynamics. There were several attempts to construct a theory for the (electro)weak interaction in the fifties and sixties. Eventually a theory was developed by Glashow, Weinberg, Salam [1, 2, 3], employing the idea of spontaneous symmetry breaking and the Higgs mechanism [4, 5] to give mass to the weak bosons Z^0, W^+, and W^- (discov-

	Quarks			Leptons	
Flavor	Mass	Charge	Flavor	Mass	Charge
u	$1.5 - 3.3$ MeV/c^2	$2/3e$	ν_e	< 2 eV/c^2	0
d	$3.5 - 6.0$ MeV/c^2	$-1/3e$	e^-	0.511 MeV/c^2	$-e$
c	$1.27^{+0.07}_{-0.11}$ GeV/c^2	$2/3e$	ν_μ	< 0.19 MeV/c^2	0
s	105^{+25}_{-35} MeV/c^2	$-1/3e$	μ^-	106 MeV/c^2	$-e$
t	171.3 ± 2.3 GeV/c^2	$2/3e$	ν_τ	< 18.2 MeV/c^2	0
b	$4.20^{+0.17}_{-0.07}$ GeV/c^2	$-1/3e$	τ^-	1.78 GeV/c^2	$-e$

Table 1.1: Matter particles of the Standard Model (three generations each with two members) [9].

ered later by SPS [1] with masses found to be as the SM predicted) and, at the same time, to preserve the gauge invariance. QCD describes the interactions between quarks and gluons, and in particular how they bind together to form hadrons. It emerged as a mathematically consistent theory in the seventies as the particle colliders started to probe the structure of the matter at short distances. It is a non-Abelian gauge field theory obtained by taking the color charge to define a local symmetry.

The above theories taken together form the SM of particle physics. More details and aspects of the model can be found in Refs. [6, 7, 8].

1.2 Contents of the Standard Model

The SM is based on the gauge group $SU(3) \times SU(2) \times U(1)$. The symmetry group $SU(3)$ describes the strong force, while the electroweak force is described by the $SU(2) \times U(1)$ part of the SM gauge group. The particles can be divided into two categories, matter particles (fermions) and gauge bosons.

Matter particles are the quarks and the leptons. They have spin 1/2 and are arranged in three families of doublets which are ordered by increasing mass. In turn, every family has two chiral manifestations: the left-handed and right-handed one. The complete fermionic sector of the SM is listed in Table 1.1. The quarks come in six flavors: up (u), down (d), charm (c), strange (s), top (t), and bottom (b). They fall into two classes according to their electrical charge: u, c, t have charge $2/3e$, while d, s, b have charge $-1/3e$. The leptons include charge $-e$ leptons and neutral neutrinos. The charged leptons are the electron (e^-), muon (μ^-), and tau (τ^-). The corresponding neutrinos are the electron neutrino

---

[1]The Super Proton Synchrotron (SPS) is a 6.9 km long particle accelerator at CERN that has been used to accelerate proton, antiprotons, electrons, positrons, and heavy-ions. During 1981-1984 was operated as proton-antiproton collider with a maximum center-of-mass energy of 540 GeV, so it was called Super proton-antiproton Synchrotron (Sp$\bar{\text{p}}$S), which led to the discovery of the $W^\pm$ and Z bosons by the $UA1$ and $UA2$ experiments.

(ν_e), muon neutrino (ν_μ), and tau neutrino (ν_τ). The quarks also carry the color charge of QCD (red, green, and blue), whereas the leptons are colorless (the sum of the three colors is color charge neutral). Thus the quarks can interact through electromagnetic, weak, and strong interactions, while the charged leptons can interact electromagnetically and weakly and the neutral leptons can only interact weakly. Each particle of the fermionic sector has an antiparticle, featuring the same mass, but opposite internal quantum numbers like charge. The quarks and leptons are idealized as pointlike, because they show no evidence of internal structure at the current limit of our resolution ($r \sim 10^{-18}$ m). As a consequence of QCD, no colored particle appears freely but is instead bound inside colorless hadrons. Hadrons are grouped into quark-antiquark states ($q\bar{q}$), the mesons, and three quark states (qqq), the baryons.

The particles that mediate the forces are called gauge bosons (integer non-zero spin) and are summarized in Table 1.2. They are introduced to restore local gauge invariance. The gauge bosons are: eight gluons for the strong force, $W^\pm$ and Z^0 for weak interaction, and the photon for the electromagnetic interaction. The graviton, the yet undiscovered gauge boson of the gravitational force, interacts too weakly to be detected singly.

In addition to quarks, leptons, and gauge bosons, another spin 0 or scalar gauge boson, the Higgs boson, is needed to make a consistent theory of masses and interactions. Its existence remains to be experimentally proven.

1.3 The Standard Model Lagrangian

The QCD part of the SM is described by a Lagrangian density which is given by:

$$\mathcal{L}_{QCD} = -\frac{1}{4} F^a_{\mu\nu} F^{\mu\nu a} + \sum_{flavors} \bar{q}_\alpha i \not{D}_{\alpha\beta} q_\beta, \tag{1.1}$$

where $\alpha, \beta = 1, 2, 3$ denote color indices, $\not{D} = D_\mu \gamma^\mu$ (D_μ is the gauge covariant derivative and γ^μ are the Dirac matrices), q_α represent the quark fields (in the triplet representation of the color group), and $F^a_{\mu\nu}$ is the field strength tensor from the gluon field A^a_μ,

$$F^a_{\mu\nu} = \partial_\mu A^a_\nu - \partial_\nu A^a_\mu - g_s f^{abc} A^b_\mu A^c_\nu \tag{1.2}$$

and the indices a, b, c run over the eight color degrees of freedom of the gluon field, g_s (or $\alpha_s = g_s^2/4\pi$) is the QCD gauge coupling constant, and the structure constants f^{abc} are defined by introducing a matrix representation of $SU(3)$

$$[T^a, T^b] = i f^{abc} T^c, \qquad T^a = \frac{1}{2} \lambda^a, \tag{1.3}$$

where λ^a are the eight Gell-Mann matrices. The terms of Eq. 1.1 describe the interaction of spin 1/2 quarks and massless spin 1 gluons.

The F^2 term leads to cubic and quartic gluon self-interactions since

$$F^a_{\mu\nu} F^{\mu\nu a} = (\partial_\mu A^a_\nu - \partial_\nu A^a_\mu)(\partial^\mu A^{a\mu} - \partial^\nu A^{a\mu}) - 2g_s f^{abc} A^b_\mu A^c_\nu (\partial^\mu A^{a\nu} - \partial^\nu A^{a\mu})$$
$$+ g_s^2 f^{abc} f^{a'b'c'} A^b_\mu A^c_\nu A^{\mu b'} A^{\nu c'}. \tag{1.4}$$

Force	Gauge Boson(s)	Acts on
Gravitation	Graviton (massless, spin 2)	All particles
Electromagnetic force	Photon (γ) (massless, spin 1)	All charged particles
Weak force	$W^\pm$, Z^0 (heavy, spin 1)	Quarks, leptons
Strong force	8 Gluons (g) (massless, spin 1)	Quarks, gluons

Table 1.2: Forces and gauge bosons of the SM.

The consequence of the gluon self-coupling is very important in the QCD framework. It is responsible for the *confinement* of quarks inside hadrons (quarks will notice the strong force at large distances, which prevent them from escaping the nucleon), as well as for the *asymptotic freedom* (quarks can essentially be treated as "free" particles when they are close to each other).

The explicit sum from the second term of Eq. 1.1 runs over all flavors and the gauge covariant derivative is given by:

$$(D_\mu)_{\alpha\beta} = \partial_\mu \delta_{\alpha\beta} + ig(T^a A_\mu^a)_{\alpha\beta}. \tag{1.5}$$

QCD alone allows mass terms in Eq. 1.1, but they are forbidden by the chiral symmetry of the electroweak part of the theory and for this reason discarded here. The quark masses will be generated later by spontaneous symmetry breaking. There is no gauge invariant way of including a mass for the gluon since a term such as $m^2 A_\mu A^\mu$ is not gauge invariant. A detailed description can be found in [8, 10].

The electroweak Lagrangian is given by:

$$\mathcal{L} = \mathcal{L}_{gauge} + \mathcal{L}_f + \mathcal{L}_\varphi + \mathcal{L}_{Yukawa}, \tag{1.6}$$

with:

- $\mathcal{L}_{gauge}$: the gauge term, describing the gauge fields and their interactions;

- $\mathcal{L}_f$: the fermion part, describing their interactions with the gauge fields;

- $\mathcal{L}_\varphi$: scalar part of the Lagrangian, describing the Higgs potential and the interactions between gauge and scalar fields;

- $\mathcal{L}_{Yukawa}$: describing the Yukawa couplings between the Higgs field and the fermions.

The first term is

$$\mathcal{L}_{gauge} = -\frac{1}{4}F^a_{\mu\nu}F^{\mu\nu a} - \frac{1}{4}F_{\mu\nu}F^{\mu\nu}, \tag{1.7}$$

where the field strength tensors of the $SU(2)$ and $U(1)$ gauge fields can be written as:

$$F^a_{\mu\nu} = \partial_\mu W^a_\nu - \partial_\nu W^a_\mu - g\epsilon^{abc}W^b_\mu W^c_\nu \qquad (a = 1,2,3) \tag{1.8}$$

$$F_{\mu\nu} = \partial_\mu B_\nu - \partial_\nu B_\mu \tag{1.9}$$

Here g is the $SU(2)$ gauge coupling constant (related to electromagnetic coupling constant e by the Weinberg angle θ_W as $g = e/\sin\theta_W$), ϵ^{abc} is the Levi-Civita tensor, $W^a_\mu = (W^1_\mu, W^2_\mu, W^3_\mu)$ is a weak isospin triplet and B_μ is a weak isospin singlet. W_μ fields have three and four self-interactions because of the non-Abelian nature of the $SU(2)$ symmetry group, while B_μ has no self-interactions.

The fermion term, $\mathcal{L}_f$ has the form

$$\mathcal{L}_f = i\sum_m (\bar{q}_{m_L}\,\slashed{D}_L q_{m_L} + \bar{l}_{m_L}\,\slashed{D}_L l_{m_L} + \bar{u}_{m_R}\,\slashed{D}_R u_{m_R} + \bar{d}_{m_R}\,\slashed{D}_R d_{m_R} + \bar{e}_{m_R}\,\slashed{D}_R e_{m_R}), \tag{1.10}$$

where m is the family index (number of families ≥ 3), $L(R)$ refer to the left (right) chiral projections $\psi_{L(R)} = (1 \mp \gamma_5)\psi/2$. The left handed quarks and leptons

$$q_{m_L} = \begin{pmatrix} u_m \\ d_m \end{pmatrix}_L \qquad l_{m_L} = \begin{pmatrix} \nu_m \\ e^-_m \end{pmatrix}_L \tag{1.11}$$

transform as $SU(2)$ doublets, while the right handed ones u_{m_R}, d_{m_R}, and $e^-_{m_R}$ are singlets. The coupling of the gauge to fermionic matter fields is implemented using the covariant derivatives for the left and right handed field respectively, defined as

$$D_{L_\mu} = \partial_\mu + i\frac{g}{2}\tau^a W^a_\mu + i\frac{g'}{2}Y B_\mu \tag{1.12}$$

$$D_{R_\mu} = \partial_\mu + i\frac{g'}{2}Y B_\mu \tag{1.13}$$

where g' is the $U(1)$ coupling constant ($g' = e/\cos\theta_W$), τ^a are the Pauli matrices, and the weak hypercharge Y is not the same in Eq. 1.12 and in Eq. 1.13. The different transformations of the L and R fields (i.e., the symmetry is chiral) is the origin of parity violation in the electroweak sector. It also forbids any bare mass terms for the fermions.

The scalar part of the electroweak Lagrangian is given by

$$\mathcal{L}_\varphi = (D^\mu_L \varphi)^\dagger (D_{L_\mu}\varphi) - V(\varphi) \tag{1.14}$$

where $\varphi = \begin{pmatrix} \varphi^+ \\ \varphi^0 \end{pmatrix}$ is a $SU(2)$ doublet, the complex Higgs scalar, with $Y = 1/2$. The square of the covariant derivative leads to gauge-Higgs interactions. The potential $V(\varphi)$

is restricted by the combination of $SU(2) \times U(1)$ invariance and renormalizability to the form

$$V(\varphi) = \mu^2 \varphi^\dagger \varphi + \lambda(\varphi^\dagger \varphi)^2 \tag{1.15}$$

Since λ should be positive to guarantee vacuum stability, the minimum of the potential depends on the sign of μ^2. For $\mu^2 < 0$, the symmetry is *spontaneously broken* since $\mathcal{L}_\varphi$ is invariant but the vacuum is not. This subject will be treated in more detail in Section 1.4.

The last term in Eq. 1.6 provides a way for the Higgs field to generate fermion masses:

$$\mathcal{L}_{Yukawa} = -\sum_{m,n} \left(\lambda^u_{mn} \bar{q}_{m_L} \tilde{\varphi} u_{n_R} + \lambda^d_{mn} \bar{q}_{m_L} \varphi d_{n_R} + \lambda^e_{mn} \bar{l}_{m_L} \varphi e_{n_R} \right) + h.c. \tag{1.16}$$

Here $\tilde{\varphi} = i\tau_2 \varphi^* = \begin{pmatrix} \varphi^{0*} \\ -\varphi^- \end{pmatrix}$ is the charge conjugate of the Higgs field with $Y = -1/2$ and the matrices λ_{mn} are the Yukawa couplings between the Higgs doublet, φ, and the various flavors m and n of the quarks and leptons. All the masses can therefore be generated with a single Higgs doublet if one makes use of both φ and $\tilde{\varphi}$, but the mass of the up type fermions differs from the mass of the down type fermions since we are using the fundamental and the conjugate of the Higgs doublet. However, for higher unitary groups the two representations are not equivalent. Take for example supersymmetry (will be discussed in Chapter 2) which needs a second Higgs doublet to generate masses. Also note that no term with $\tilde{\varphi}$ appears for leptons in Eq. 1.16 because there are no right handed neutrinos in the minimal version of the SM.

1.4   Spontaneous Symmetry Breaking

As already pointed out in Section 1.3 the gauge invariance does not allow mass terms in the Lagrangian. Also no massless gauge bosons can be accepted since the weak interactions are short-ranged. Hence, the gauge invariance should be spontaneously broken. The main idea is that the masses of the gauge bosons arise dynamically from the interactions of the gauge fields with the Higgs field since the vacuum state (the lowest energy state) does not respect the gauge symmetry. The vacuum state of the theory is the one which minimizes the Higgs potential defined in Eq. 1.15.

Considering

$$\varphi = \begin{pmatrix} \varphi^+ \\ \varphi^0 \end{pmatrix} = \begin{pmatrix} \frac{1}{\sqrt{2}}(\varphi_1 + i\varphi_2) \\ \frac{1}{\sqrt{2}}(\varphi_3 + i\varphi_4) \end{pmatrix} \tag{1.17}$$

where φ is a column, $\varphi^\dagger$ a row with

$$\varphi^\dagger \varphi = \begin{pmatrix} \varphi^{+*} \varphi^{0*} \end{pmatrix} \begin{pmatrix} \varphi^+ \\ \varphi^0 \end{pmatrix} = \varphi^{+*}\varphi^+ + \varphi^{0*}\varphi^0 = \frac{\varphi_1^2 + \varphi_2^2 + \varphi_3^2 + \varphi_4^2}{2} \tag{1.18}$$

the Higgs potential becomes:

$$V(\varphi) = \frac{1}{2}\mu^2 \left(\sum_{i=1}^{4} \varphi_i^2 \right) + \frac{1}{4}\lambda \left(\sum_{i=1}^{4} \varphi_i^2 \right)^2 \tag{1.19}$$

Without loss of generality we can choose the direction in the $SU(2)$ space so that $\varphi_1 = \varphi_2 = \varphi_4 = 0$, $\varphi_3 = v$. Thus,

$$V(\varphi) \rightarrow V(v) = \frac{1}{2}\mu^2 v^2 + \frac{1}{4}\lambda v^4 \tag{1.20}$$

For $\mu^2 > 0$ the vacuum corresponds to $v = 0$, so $SU(2) \times U(1)$ is unbroken at the minimum (μ^2 can be interpreted as $mass^2$). For $\mu^2 < 0$, we find the minimum of the potential by requiring

$$\frac{\partial V}{\partial v} = 0 \Rightarrow v(\mu^2 + \lambda v^2) = 0 \tag{1.21}$$

which leads to $v = \sqrt{-\mu^2/\lambda}$. So the vacuum expectation value (VEV) is

$$\varphi_0 = \frac{1}{\sqrt{2}}\begin{pmatrix} 0 \\ v \end{pmatrix} \tag{1.22}$$

In order to study the spectrum we can expand φ around the vacuum

$$\varphi = \frac{1}{\sqrt{2}}\begin{pmatrix} 0 \\ v + H \end{pmatrix} \tag{1.23}$$

The neutral field H is the famous Higgs boson. The choice that only the neutral component φ^0 gets a VEV is done to conserve the electromagnetic charge. The $SU(2)$ symmetry is broken since only one component of the Higgs field acquires VEV. Also the $U(1)$ symmetry is broken because the hypercharge $Y_H \neq 0$. On the other hand, the vacuum carries no electric charge, so $U(1)_{em}$ is not broken. So the $SU(3) \times SU(2) \times U(1)$ symmetry is spontaneously broken to $SU(3) \times U(1)_{em}$. This mechanism, called the Higgs mechanism, generates mass terms for the gauge fields $W_\mu^\pm$ and Z_μ and leaves the photon field A_μ massless. The gauge fields are given by:

$$W_\mu^\pm = \frac{W_\mu^1 \mp iW_\mu^2}{\sqrt{2}} \tag{1.24}$$

$$Z_\mu = \frac{gW_\mu^3 - g'B_\mu}{\sqrt{g'^2 + g^2}} \tag{1.25}$$

$$A_\mu = \frac{g'W_\mu^3 + gB_\mu}{\sqrt{g'^2 + g^2}} \tag{1.26}$$

and the masses

$$M_W = \frac{gv}{2} \qquad M_Z = \frac{v}{2}\sqrt{g^2 + g'^2} = \frac{M_W}{\cos\theta_W} \tag{1.27}$$

The VEV is

$$v = \left(\sqrt{2}G_F\right)^{-1/2} = 246 \text{ GeV}, \tag{1.28}$$

where $G_F = 1.16637(1) \times 10^{-5} \text{ GeV}^{-2}$ is the Fermi weak-interaction coupling constant. The discovery of the $W^\pm$ [11, 12] and Z^0 [13, 14] marked an important milestone for the theory. Subsequent measurements of their properties and masses have been in perfect agreement with the SM expectations.

1.5   Problems with the Standard Model

Although the SM gives a very good description of the known phenomena in particle physics, the minimal version of the model has 21 free parameters. Even though this is not a strong objection there are more rigorous arguments against the SM. Among the shortcomings of the model are:

- Why are there three generations of matter? Experimental studies have shown that there are only three light neutrinos [15] and this ruled out the existence of other families than: (ν_e, e^-, u, d), (ν_μ, μ^-, c, s), and (ν_τ, τ^-, t, b). The SM gives no explanation for the existence of the families and no prediction for their number. Furthermore, there is no explanation or prediction of the mass hierarchy in the lepton and quark sectors.

- The simplest Lagrangian of the SM does not include terms for neutrino masses even though recent measurements have shown that neutrinos have mass. Different models have been proposed to incorporate neutrino masses, but until now the question of how neutrino masses arise has not been answered conclusively.

- Charge quantization is incorporated into SM, but not explained, i.e., why all particles have discrete charge values.

- Gravity is not fundamentally unified with the other interactions in the SM since general relativity is not a quantum theory. In addition to the fact that gravity is not included in the $SU(3) \times SU(2) \times U(1)$ theory and not quantized, the cosmological constant is another problem. In order to accommodate the energy density induced by the spontaneous symmetry breaking and the observational upper limit a severe fine tuning between the generated and the bare pieces is needed. There is no a priory reason to relate this. String theories unify gravity and yield quantum gravity theories, but they do not provide any obvious solution to the cosmological constant problem.

- Experimental observation like the measurement of the cosmic microwave background with WMAP and movements of the galaxies lead to the estimation of the proportion of dark matter in Universe [16, 17]. None of the SM particles can be regarded as explanation of dark matter.

- SM is a direct product of three groups, $SU(3) \times SU(2) \times U(1)$, with different gauge constants. These coupling constants are not constant at all; instead they vary with the energy scale ("running") and seem to converge at a high scale. This led to the idea that strong and electroweak interactions might be embedded in a "Grand Unified" interaction. But as can be seen from Fig. 1.1 the couplings do *not exactly* meet and new physics is needed to obtain grand unification.
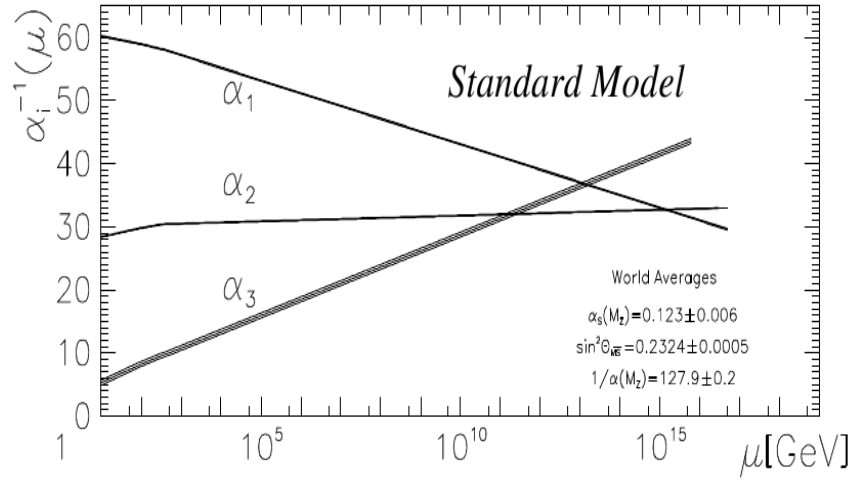
Figure 1.1: Evolution of the inverse of the coupling constants as shown in [18]. The bands reflect the experimental uncertainties. The α_i (i=1,3) denote the three gauge coupling constants of $U(1)$, $SU(2)$ and $SU(3)$, respectively.

The major problem of the SM is the "hierarchy problem", the huge difference between the experimental and theoretical Higgs mass in the absence of new physics below the Planck scale, $\Lambda_P = (\hbar c / G_{Newton})^{-1/2} \approx 1.22 \times 10^{19}$ GeV. As already shown in Section 1.4, the VEV of the Higgs field is approximately 246 GeV which leads to a Higgs mass squared of the order of $(100 \text{ GeV})^2$. However, there is a complication as the bare Higgs mass receives quadratically-divergent quantum corrections from the loop diagrams in Fig. 1.2. One finds [19]:

$$M_H^2(p^2) = M_H^2(\Lambda^2) + Cg^2 \int_{p^2}^{\Lambda^2} dk^2 \tag{1.29}$$

where Λ is a scale at which M_H^2 is known, g is the coupling constant, and C a calculable coefficient. If the SM is valid up to the Planck scale ($\Lambda = \Lambda_P$), the corrections are 34 orders of magnitude larger than the actual value of the Higgs mass squared. Several mechanisms to solve this problem were suggested and some of them will be presented in the following chapter.
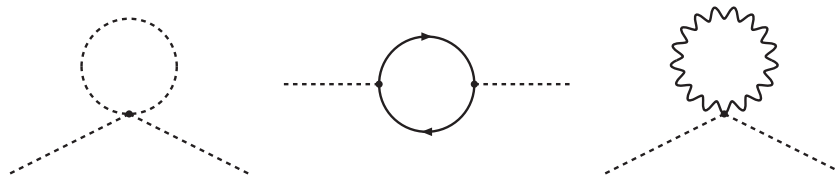
Figure 1.2: Diagrams contributing to the quantum corrections of the Higgs mass from scalars (left), fermions (center), and gauge bosons (right). The figure is taken from [19].

Chapter 2

Extensions of the Standard Model

The previous chapter indicated that the SM can not be the full theory and new physics is needed. There are many models available that can solve one or more of the problems listed above, but only a few are addressed here. This chapter will focus on Supersymmetry (SUSY), a promising candidate of physics Beyond the Standard Model (BSM) and one of the most attractive theories among theoreticians.

2.1 Supersymmetry

Supersymmetry [20] is considered as one of the most appealing BSM theories since it can provide ways to unify the gauge coupling constants and to cancel the quadratic divergences in the Higgs sector, hence solving the hierarchy problem. Furthermore, in SUSY theories the breaking of the electroweak symmetry is naturally induced at the Fermi scale and the lightest supersymmetric particle can be neutral, weakly interacting and absolutely stable, providing therefore a natural solution for the dark matter problem. A very good review on this subject can be found in [21].

SUSY is a hypothetical symmetry of Nature (no experimental evidence yet) that relates fermions and bosons through an anticommuting spinor operator Q,

$$Q \left| Boson \right\rangle = \left| Fermion \right\rangle, \qquad Q \left| Fermion \right\rangle = \left| Boson \right\rangle \tag{2.1}$$

with a conjugate operator $Q^\dagger$. Since Q and $Q^\dagger$ are fermionic operators, they carry spin angular momentum $1/2$. The generators Q and $Q^\dagger$ satisfy the following commuting and anti-commuting relations:

$$\{Q, Q^\dagger\} = P^\mu \tag{2.2}$$

$$\{Q, Q\} = \{Q^\dagger, Q^\dagger\} = 0 \tag{2.3}$$

$$[P^\mu, Q] = [P^\mu, Q^\dagger] = 0 \tag{2.4}$$

where P^μ is the four-momentum operator. The spinor indices have been suppressed here. Since Q and $Q^\dagger$ transform as spin $1/2$ objects the $QQ^\dagger$ and $Q^\dagger Q$ both carry spin 1, and hence

they transform under Lorentz transformations as a spin 1 object. P^μ is also transforming as a spin 1 object under Lorentz boosts and rotations, so Eq. 2.2 is proved. The Eq. 2.4 ensures that the operators of SUSY conserve momentum. Usually, the number of SUSY generators is $N = 1$.

The irreducible representations of the SUSY algebra are called *supermultiplets*. Each supermultiplet contains fermion and boson states, commonly referred to as *superpartners* of each other. From SUSY algebra relations one should note that as the operators Q and $Q^\dagger$ commute with the squared-mass operator $-P^2$ and also with the generators of the gauge transformations, the particles in the same supermultiplet have the same mass, charges, isospin, and color degrees of freedom. But if the SM were part of a supersymmetric theory, with a conserved symmetry, all the quarks, leptons, and gauge bosons would have an almost identical partner (differed only in spin). As such partners are not observed in Nature, SUSY must be spontaneously broken to allow high enough masses for superpartners in order not to be observed. Furthermore, each supermultiplet contains the same number of fermion (n_F) and boson (n_B) degrees of freedom. A *chiral/scalar* supermultiplet consists of a two-component left-handed Weyl fermion, so $n_F = 2$, and a complex scalar field (or two real scalar fields), $n_B = 2$. A *vector/gauge* supermultiplet is a combination between a massless spin 1 boson (has two helicity states, so $n_B = 2$) and a massless spin 1/2 Weyl fermion with two helicity states ($n_F = 2$). If one assumes gravity to be mediated by a spin 2 graviton it will have a spin 3/2 superpartner called gravitino which would be massless if SUSY was unbroken.

2.2 The Minimal Supersymmetric Standard Model

Applying the concept of SUSY to the SM, each of the known particles must have a superpartner with the same quantum numbers and spin differing by 1/2. So they will be therefore in either a chiral or gauge supermultiplet in a supersymmetric extension of the SM. As only chiral supermultiplets can contain fermions whose left-handed parts transform differently under the gauge group than the right-handed parts, all of the SM fermions will be members of chiral supermultiplets. Supersymmetric partners of the quarks and leptons are named by attaching "s" for scalar, so *squarks* and *sleptons*. The chiral supermultiplets of a minimal phenomenologically viable extension of the SM are summarized in Table 2.1. Due to the convention that all chiral supermultiplets are defined in terms of left-handed Weyl spinors, the conjugates of the right-handed fields appear in this table. The supersymmetric fermionic partners of the SM vector bosons are listed in Table 2.2. They reside in gauge supermultiplets named by appending "ino" to the name of the SM bosons (e.g. the superpartner of the W boson is called $Wino$) and generically referred to as *gauginos*. All the supersymmetric partners of the SM states are denoted by a tilde ($\sim$). As no electroweak or SUSY breaking was considered by now, the fields and superpartners show the pure gauge and SUSY structure of the theory. The collection of supermultiplets in Tables 2.1 and 2.2 is generally referred to as the Minimal Supersymmetric Standard Model (MSSM).

The Higgs part of the theory becomes more complicated as two chiral supermultiplets containing a Higgs field are needed. One reason for this is the cancellation of gauge anomalies through condition as $Tr[T_3^2 Y] = Tr[Y^3] = 0$ (T_3 and Y are the third component of weak isospin and the weak hypercharge) which in SM is already satisfied by quarks and leptons. The SM Higgs ($Y = 1/2$) being a scalar does not contribute to these anomalies. But its supersymmetric partner (a weak isodoublet with $Y = 1/2$ or $Y = -1/2$) will spoil the anomaly cancellation. This can be avoided by having a second Higgs with opposite hypercharge. Another reason is related to the superpotential being analytic, so we need two Higgs chiral supermultiplets to give Yukawa couplings, and thus masses.

Name	Supermultiplet	Spin 0	Spin 1/2
Squarks, Quarks	Q	$(\tilde{u}_L \quad \tilde{d}_L)$	$(u_L \quad d_L)$
($\times 3$ families)	$\bar{u}$	$\tilde{u}_R^*$	$u_R^\dagger$
	$\bar{d}$	$\tilde{d}_R^*$	$d_R^\dagger$
Sleptons, Leptons	L	$(\tilde{\nu} \quad \tilde{e}_L)$	$(\nu \quad e_L)$
($\times 3$ families)	$\bar{e}$	$\tilde{e}_R^*$	$e_R^\dagger$
Higgs, Higgsinos	H_u	$(H_u^+ \quad H_u^0)$	$(\widetilde{H}_u^+ \quad \widetilde{H}_u^0)$
	H_d	$(H_d^0 \quad H_d^-)$	$(\widetilde{H}_d^0 \quad \widetilde{H}_d^-)$

Table 2.1: Supersymmetric partners of the fermionic sector of the SM together with the MSSM Higgs sector.

Name	Supermultiplet	Spin 1/2	Spin 1
Gluino, Gluon	G	$\tilde{g}$	g
Winos, W bosons	W	$\widetilde{W}^\pm \quad \widetilde{W}^0$	$W^\pm \quad W^0$
Bino, B boson	B	$\widetilde{B}^0$	B^0

Table 2.2: Gauge supermultiplets present in MSSM.

As already pointed out, SUSY naturally solves the hierarchy problem. The introduction of two complex scalar fields for each of the SM fermions allows the cancellation of the quadratically divergent contributions to the Higgs boson mass (discussed previously in Section 1.5). Considering a fermion f and a sfermion $\tilde{f}$ one obtains [21]:

$$\Delta m_H^2 = \frac{1}{8\pi^2}(\lambda_{\tilde{f}} - |\lambda_f|^2)\Lambda_{UV}^2 + ..., \tag{2.5}$$

where $\lambda_{\tilde{f}}$ and λ_f are the Yukawa couplings of the sfermion, respectively fermion to the Higgs field. The difference between the relative sign for $\lambda_{\tilde{f}}$ and λ_f arises because of the

spin nature. According to the assumption of the same quantum numbers:

$$\lambda_{\tilde{f}} \equiv |\lambda_f|^2, \tag{2.6}$$

thus $\Delta m_H^2 = 0 + \dots$.

Another advantage of SUSY is the unification of the gauge couplings. In the MSSM, the gauge couplings unify precisely around $\mathcal{O}(10^{16})$ GeV with a suitable choice of parameters. This is illustrated in Fig. 2.1; the SUSY particles are assumed to contribute effectively to the running of the coupling constants only for energies above the typical SUSY mass scale, which causes the change in the slope of the lines near one TeV.
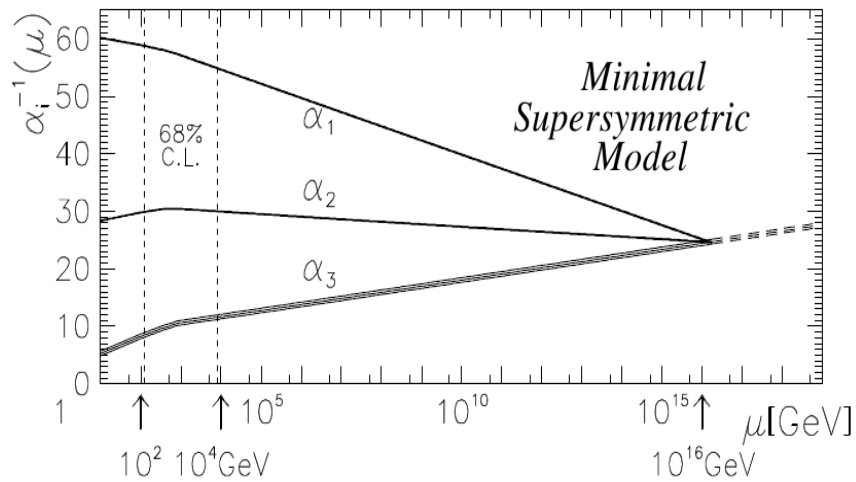
Figure 2.1: Coupling constants unification in MSSM [18]. The dashed lines represent the 68% confidence level in the SUSY scale, while the the uncertainty in the coupling is indicated by the thickness of the lines.

2.3   R-parity

Since the particles in the same supermultiplet have the same quantum numbers (i.e. sparticles have the same charges as their SM counterparts), the most general SUSY Lagrangian (see next section) contains lepton and baryon number violating couplings. This will allow for a very short lifetime of the proton, but current measurements set lower limits on the decay time of the proton of 8.2×10^{33} (6.6×10^{33}) years at 90% confidence level for $p \to e^+ \pi^0$ ($p \to \mu^+ \pi^0$) modes [22]. In order to cure this, a new symmetry which eliminates the possibility of lepton and baryon violating terms is added. It is called R-parity [23] and is a multiplicative quantum number given by:

$$R = (-1)^{3(B-L)+2s}, \tag{2.7}$$

where B is the baryon number, L the lepton number, and s the spin of the particle. The spin difference gives that all the particles of the SM have positive R-parity ($R = 1$), while

their superpartners have negative R-parity ($R = -1$). This symmetry has a great influence of the phenomenology of the MSSM. Its phenomenological consequences are:

- Supersymmetric particles are always produced in pairs;

- The lightest supersymmetric particle (LSP) is absolutely stable. If LSP is neutral and weakly interacting, it could be a good dark matter candidate;

- Each supersymmetric particle except the LSP decays eventually into an odd number of LSPs.

2.4 A Supersymmetric Lagrangian

The SUSY breaking mechanism is a rather complex task that has also to provide a solution to the hierarchy problem, so it should conserve the cancellation of the quadratic divergences. This means that Eq. 2.6 should hold in the concept of SUSY breaking. At the same time, as no SUSY particles were discovered so far, they should have different masses than their SM counterparts. In order to accommodate these observations new mass terms for SUSY particles are introduced explicitly, hereby leaving the Yukawa couplings of the SM unchanged: *soft supersymmetry breaking*. This led to consider an effective Lagrangian of the form:

$$\mathcal{L} = \mathcal{L}_{SUSY} + \mathcal{L}_{soft}, \tag{2.8}$$

where $\mathcal{L}_{SUSY}$ represents all of the gauge and Yukawa interactions with SUSY invariance, and $\mathcal{L}_{soft}$ contains terms with *positive* mass dimension that violate SUSY.

2.4.1 The Simplest SUSY Lagrangian

In this section the simplest SUSY Lagrangian will be derived starting from the general form, Eq. 2.8. The conserving part of the SUSY Lagrangian $\mathcal{L}_{SUSY}$ can be divided into a chiral and gauge part:

$$\mathcal{L}_{SUSY} = \mathcal{L}_{chiral} + \mathcal{L}_{gauge}. \tag{2.9}$$

The Lagrangian density for a chiral supermultiplet is given by:

$$\mathcal{L}_{chiral} = -\partial^\mu \phi^{*i} \partial_\mu \phi_i - i\psi^{\dagger i}\bar{\sigma}^\mu \partial_\mu \psi_i - \frac{1}{2}(W^{ij}\psi_i\psi_j + W^*_{ij}\psi^{\dagger i}\psi^{\dagger j}) - W^i W^*_i. \tag{2.10}$$

Here i runs over all gauge and flavor degrees of freedom, the complex scalar ϕ_i and a left-handed Weyl fermion ψ_i are contained into a supermultiplet, and W^i and W^{ij} are derived from an object called the *superpotential* (W) as

$$W^i = \frac{\partial W}{\partial \phi_i} \qquad W^{ij} = \frac{\partial^2}{\partial \phi_i \partial \phi_j} W. \tag{2.11}$$

The superpotential is an analytic function of the scalar fields ϕ_i treated as complex variables and has the form:

$$W = \frac{1}{2}M^{ij}\phi_i\phi_j + \frac{1}{6}y^{ijk}\phi_i\phi_j\phi_k, \tag{2.12}$$

where M^{ij} is a symmetric mass matrix, and y^{ijk} is a Yukawa coupling of a scalar ϕ_k and two fermions $\psi_i\psi_j$.

Hence the first two terms in the Eq. 2.10 represent the kinetic energy for quarks, squarks, leptons, sleptons, Higgs, and higgsino and are the supersymmetric generalization of Eq. 1.10. The next two terms describe the Yukawa interactions of the fermions, while the last term is a general potential for any scalar field.

The Lagrangian density for a gauge supermultiplet is

$$\mathcal{L}_{gauge} = -\frac{1}{4}F^a_{\mu\nu}F^{\mu\nu a} - i\lambda^{\dagger a}\bar{\sigma}^\mu D_\mu \lambda^a + \frac{1}{2}D^a D^a. \tag{2.13}$$

The interactions involve a massless gauge boson field W^a_μ and a gaugino λ^a, where $a = 1,...,8$ for $SU(3)$ group, $a = 1,2,3$ for $SU(2)$ gauge group, and $a = 1$ for $U(1)$. Here $F^a_{\mu\nu}$ is the Yang-Mills field strength tensor as defined in Eq. 1.8, D_μ is the covariant derivative of the gaugino field and is given by Eq. 1.12, and D^a is a real bosonic auxiliary field with dimensions of [mass]^2 and no kinetic term needed to have a consistent supersymmetry algebra. The first term in Eq. 2.13 is the kinetic energy of the SM gauge bosons, the second one describes the interactions and the kinetic energy of the gauginos, while the last one gives the self interactions of the auxiliary field.

As already argued, the SUSY breaking should be soft in order to keep the hierarchy problem under control. An easy way to do this is achieved by adding extra terms that break SUSY explicitly in the effective SUSY Lagrangian. A general expression for a soft SUSY breaking Lagrangian is

$$\mathcal{L}_{soft} = -(\frac{1}{2}M_a\lambda^a\lambda^a + \frac{1}{6}a^{ijk}\phi_i\phi_j\phi_k + \frac{1}{2}b^{ij}\phi_i\phi_j) + c.c. - (m^2)^i_j\phi^{j*}\phi_i, \tag{2.14}$$

where M_a are the gaugino masses (for each gauge group), $(m^2)^i_j$ and b_{ij} are the squared-mass term of the scalar fields ϕ_i, a^{ijk} is a trilinear coupling totally symmetric under interchange of i,j,k. Since Eq. 2.14 involves only scalars and gauginos, SUSY is broken by $\mathcal{L}_{soft}$. Even more, the soft terms in $\mathcal{L}_{soft}$ can give masses to all of the scalars and gauginos in the theory.

2.4.2   The MSSM Lagrangian

Having written down a general framework for constructing Lagrangians that includes soft SUSY breaking, it can be applied to the MSSM. The $\mathcal{L}_{SUSY}$ is derived from the MSSM superpotential

$$W_{MSSM} = \bar{u}\mathbf{y_u}QH_u - \bar{d}\mathbf{y_d}QH_d - \bar{e}\mathbf{y_e}LH_d + \mu H_u H_d, \tag{2.15}$$

where $H_u, H_d, Q, L, \bar{u}, \bar{d}, \bar{e}$ are the chiral supermultiplets defined in Table 2.1, and $\mathbf{y_u}, \mathbf{y_d}, \mathbf{y_e}$ are dimensionless 3×3 matrices in family space. All the indices have been suppressed in Eq. 2.15 (i.e. the term $\bar{u}\mathbf{y_u}QH_u$ means $\bar{u}^{ia}(\mathbf{y_u})_i^j Q_{j\alpha a}(H_u)_\beta \epsilon^{\alpha\beta}$, where $i = 1, 2, 3$ is a family index, $a = 1, 2, 3$ is a color index, and $\alpha, \beta = 1, 2$ the weak isospin indices). The last term in Eq. 2.15, traditionally called the "μ term", is the supersymmetric version of the Higgs boson mass in the SM. Since the superpotential should be analytic in the chiral superfields, no terms like $H_u^* H_u$ or $H_d^* H_d$ are allowed, so the μ term is unique. Also the $\bar{u}QH_u$, $\bar{d}QH_d$, $\bar{e}LH_d$ Yukawa terms can not be replaced by something like $\bar{u}QH_d^*$, $\bar{d}QH_u^*$, $\bar{e}LH_u^*$ and two Higgs fields are needed in order to get masses: H_u gives masses to the up-type quarks and H_d gives masses to the down-type quarks and to the charged leptons. The soft MSSM breaking Lagrangian can be obtained from Eq. 2.14 by imposing gauge invariance and has the form

$$
\begin{aligned}
\mathcal{L}_{soft}^{MSSM} = &-\frac{1}{2}\left(M_3 \tilde{g}\tilde{g} + M_2 \widetilde{W}\widetilde{W} + M_1 \widetilde{B}\widetilde{B} + c.c.\right) \\
&-\left(\tilde{\bar{u}}\mathbf{a_u}\widetilde{Q}H_u - \tilde{\bar{d}}\mathbf{a_d}\widetilde{Q}H_d - \tilde{\bar{e}}\mathbf{a_e}\widetilde{L}H_d + c.c.\right) \\
&-\widetilde{Q}^\dagger \mathbf{m_Q^2}\widetilde{Q} - \widetilde{L}^\dagger \mathbf{m_L^2}\widetilde{L} - \tilde{\bar{u}}\mathbf{m_{\bar{u}}^2}\tilde{\bar{u}}^\dagger - \tilde{\bar{d}}\mathbf{m_{\bar{d}}^2}\tilde{\bar{d}}^\dagger - \tilde{\bar{e}}\mathbf{m_{\bar{e}}^2}\tilde{\bar{e}}^\dagger \\
&- m_{H_u}^2 H_u^* H_u - m_{H_d}^2 H_d^* H_d - (b H_u H_d + c.c.).
\end{aligned}
\tag{2.16}
$$

The first line generates the gluino mass M_3, the Wino mass M_2 and the Bino mass M_1. The second line contains the (scalar)^3 couplings as the a^{ijk} ones from Eq. 2.14. It generates the mass matrices $\mathbf{a_u}, \mathbf{a_d}, \mathbf{a_e}$ for the three generations of scalar fermions. These 3×3 matrices in family space are in one-to-one correspondence with the Yukawa couplings of the superpotential. The third line gives masses to all squarks and sleptons through the 3×3 matrices in family space $\mathbf{m_Q^2}, \mathbf{m_{\bar{u}}^2}, \mathbf{m_{\bar{d}}^2}, \mathbf{m_L^2}, \mathbf{m_{\bar{e}}^2}$. The last line generates masses for the two Higgs fields. As can be seen from the discussion above soft SUSY breaking introduces many new parameters not present in the SM, but the number can drastically be reduced by constraints imposed to the SUSY breaking scheme and by experimental observations.

2.5 Supersymmetry Models

In the MSSM, the SUSY breaking is done explicitly. However, experimental constraints showed that the soft SUSY breaking Lagrangian can not be arbitrary or random and it is necessary to consider models in which the SUSY is spontaneously broken. Generally, SUSY breaking is believed to occur in a "hidden" sector of particles that have no (or negligible) direct couplings with the "visible" sector of MSSM particles. SUSY breaking is then mediated between the two sectors by flavor-blind interactions. Depending on the nature of the mediating interactions many theoretical scenarios exist. Only a short description of the common models will be presented next.

mSUGRA The most popular scenario arises in the context of supergravity. In these theories the messenger fields are gravitational [24] and the scale associated with the origin

of the SUSY breaking in the hidden sector is the coupling constants unification scale $M_{GUT} \approx 2 \times 10^{16}$ GeV, usually called GUT scale. Since the supergravity parameter space is very large, a simplified model has been introduced, the *Minimal Supergravity* (mSUGRA). It is based on the assumption of gaugino and fermion mass unification at GUT scale:

$$M_3 = M_2 = M_1 = m_{1/2} \qquad (2.17)$$

$$\mathbf{m_Q^2} = \mathbf{m_{\bar{u}}^2} = \mathbf{m_{\bar{d}}^2} = \mathbf{m_L^2} = \mathbf{m_{\bar{e}}^2} = m_0^2 \mathbf{1}, \quad m_{H_u}^2 = m_{H_d}^2 = m_0^2 \qquad (2.18)$$

$$\mathbf{a_u} = A_0 \mathbf{y_u}, \quad \mathbf{a_d} = A_0 \mathbf{y_d}, \quad \mathbf{a_e} = A_0 \mathbf{y_e} \qquad (2.19)$$

$$b = B_0 \mu, \qquad (2.20)$$

where all the above parameters are coming from Eq. 2.16. The theoretical grounds of these assumptions are open for debate, but from the phenomenological perspective they have very nice consequences: it spans different mass hierarchies that can be studied at colliders. So these assumptions allow us to predict the entire mass spectrum of the MSSM in terms of just five parameters: $m_{1/2}$ the universal fermion mass, m_0 the universal boson mass, A_0 the uniform trilinear coupling, $\tan\beta$ the ratio of the VEV values of the two Higgs doublets, and $\arg(\mu)$ the sign of the Higgs mixing parameter μ.

GMSB In Gauge-Mediated Supersymmetry Breaking (GMSB) models, the SM gauge interactions are responsible for SUSY breaking [25]. The gravitational communication between the MSSM and the source of the SUSY breaking is still present, but it is suppressed by the gauge interactions effects. Minimal models are cast in terms of the parameters $N, \Lambda, M, \tan\beta, \arg(\mu)$, and c_{grav}. The basic idea is to introduce N chiral $SU(5)$ supermultiplets, called "messengers", at a scale M. They couple directly to the source of SUSY breaking and indirectly to the (s)quarks, (s)leptons, and Higgs(inos) of the MSSM through the ordinary $SU(3) \times SU(2) \times U(1)$ gauge boson and gaugino interactions. The Λ parameter ($\Lambda \sim 10 - 100$ TeV) represents the effective SUSY breaking scale and is related to the fundamental SUSY breaking scale $\sqrt{F}$ by

$$\Lambda = F/M \qquad (2.21)$$

Since the SUSY breaking terms are induced by gauge interactions the masses of the squarks and sleptons depend only on their gauge quantum number, leading to degeneracy of squark and slepton masses needed for suppression of flavor-changing effects. Also the strongly interacting sparticles should be heavier than the weakly interacting ones because of the gauge coupling hierarchy. The most distinctive phenomenological prediction of these models is that the gravitino is very light ($m_{\widetilde{G}} \leq 1$ keV) and hence becomes the LSP for any relevant choice of parameters. Its mass is related to F and c_{grav} by the relation:

$$m_{\widetilde{G}} = 2.4 \, c_{grav} \left(\frac{\sqrt{F}}{100 \text{ TeV}} \right)^2 \text{ eV}. \qquad (2.22)$$

AMSB In the Anomaly-Mediated Supersymmetry Breaking (AMSB) scenario [26] the SUSY is broken by so-called anomalous interactions. These models are in close relation with the string theory and introduce extra dimensions in order to break SUSY.

Split SUSY Split Supersymmetry (Split SUSY) models [27, 28] do not address the hierarchy problem, but instead focus on solving the dark matter problem and the gauge coupling unification. SUSY breaking is considered to happen at very high scale $m_S \gg$ 1 TeV/c^2 and the fine tuning required to make the Higgs light happens by some kind of new physics. In this case all the scalar particles, except for a single neutral Higgs boson, have very large masses, while all the other new particles have masses around the weak scale since a particle with weak cross section and mass around the Fermi scale is a natural dark matter candidate. Furthermore, the gauge coupling unification requires colored particles with weak charges since adding to the SM only particles without color charges will break the lower limit of the GUT scale imposed by the proton decay lifetime [28]. The new particles should belong to some GUT multiplet and they are identified with the gauginos and higgsinos from the supersymmetric SM with a single Higgs doublet [28] which is the case advocated in Ref. [27]. The framework naturally suppresses both proton decay and CP violation, avoids constraints from flavor physics, predicts a light Higgs ($\sim 120-150\,\mathrm{GeV/c^2}$) and sparticles, provides a dark matter candidate through the lightest neutralino, accounts for the gauge coupling unification.

Name	Spin	Gauge Eigenstates				Mass Eigenstates			
Higgs bosons	0	H_u^0	H_d^0	H_u^+	H_d^-	h^0	H^0	A^0	$H^\pm$
Squarks	0	$\tilde{u}_L$ $\tilde{u}_R$	$\tilde{d}_L$ $\tilde{d}_R$			(same)			
		$\tilde{s}_L$ $\tilde{s}_R$	$\tilde{c}_L$ $\tilde{c}_R$			(same)			
		$\tilde{t}_L$ $\tilde{t}_R$	$\tilde{b}_L$ $\tilde{b}_R$			$\tilde{t}_1$	$\tilde{t}_2$	$\tilde{b}_1$	$\tilde{b}_2$
Sleptons	0	$\tilde{e}_L$ $\tilde{e}_R$	$\tilde{\nu}_e$			(same)			
		$\tilde{\mu}_L$ $\tilde{\mu}_R$	$\tilde{\nu}_\mu$			(same)			
		$\tilde{\tau}_L$ $\tilde{\tau}_R$	$\tilde{\nu}_\tau$			$\tilde{\tau}_1$	$\tilde{\tau}_2$	$\tilde{\nu}_\tau$	
Neutralinos	1/2	$\widetilde{B}^0$	$\widetilde{W}^0$	$\widetilde{H}_u^0$	$\widetilde{H}_d^0$	$\widetilde{\chi}_1^0$	$\widetilde{\chi}_2^0$	$\widetilde{\chi}_3^0$	$\widetilde{\chi}_4^0$
Charginos	1/2	$\widetilde{W}^\pm$	$\widetilde{H}_u^+$	$\widetilde{H}_d^-$		$\widetilde{\chi}_1^\pm$	$\widetilde{\chi}_2^\pm$		
Gluino	1/2	$\tilde{g}$				(same)			
Gravitiono	3/2	$\widetilde{G}$				(same)			

Table 2.3: The particle content of the MSSM assuming no sfermion mixing for the first two families [21].

From the discussion above, the superpartners of the SM fields acquire masses after the spontaneous SUSY breaking. On the other hand the SM particles obtain masses after the

electroweak symmetry breaking, but this is slightly changed in MSSM since two complex Higgs doublets are present. As a consequence the two processes will allow mixing in both gauge and sfermion sectors. The neutral Higgsinos mix with the neutral gauginos to form four mass eigenstates called *neutralinos* (denoted by $\widetilde{\chi}_i^0$, $i = 1, 2, 3, 4$), while the charged Higgsinos mix with charged winos to form two mass eigenstates with charge $\pm 1e$ called *charginos* (denoted by $\widetilde{\chi}_i^{\pm}$, $i = 1, 2$). In most models, the lightest neutralino is assumed to be the LSP. In the sfermion sector the first two families do not mix. So in the slepton sector the two stau states, $\tilde{\tau}_L$ and $\tilde{\tau}_R$, mix to form two mass eigenstates $\tilde{\tau}_1$ and $\tilde{\tau}_2$, while in the squark sector similar mixing will occur for stop and sbottom squarks. The mass eigenstates of the MSSM are listed in Table 2.3.

Chapter 3

Particle Production in ep, pp, and AA Collisions

Particle production in electron-proton (ep), proton-proton (pp), and heavy-ion (AA) collisions within the QCD framework is discussed in this chapter. The perturbative and non-perturbative treatments of the strong interaction are introduced first. Deep Inelastic Scattering together with different approaches to model it are presented next. Finally, a brief description of particle production in hadron-hadron and AA collisions is given.

3.1 Perturbative QCD

As discussed in Chapter 1, QCD is the gauge field theory that describes the strong interactions of colored quarks and gluons. As long as the strong coupling constant α_S is small, perturbative QCD (pQCD) can be used to calculate analytically these interactions in order to predict different experimentally observable quantities (e.g. cross sections). In pQCD, this is done by using a perturbative expansion in α_s with the help of Feynman diagrams. A full set of Feynman rules for QCD is to be found in Ref. [8]. For a given observable, the first non-zero term of this expansion (or the diagram with the smallest number of coupling vertices) is called the leading order (LO), the following term is next-to-leading order (NLO) and so on. More complicated diagrams are needed when considering higher order terms. Second order diagrams where the gluon propagator fluctuates into two gluons or alternatively into a quark-antiquark pair are depicted in Fig. 3.1.
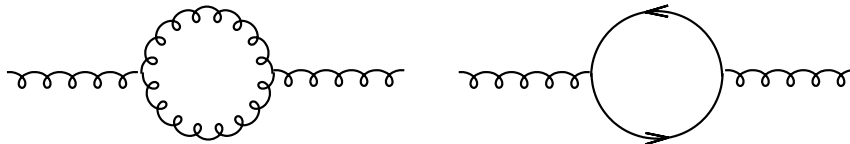
Figure 3.1: QCD diagrams showing gluon and quark loops responsible for ultraviolet divergencies.

When including the loop diagrams of Fig. 3.1, ultraviolet divergencies occur. They arise because the momentum in the loop itself is unrestricted such that it can take any value between zero and infinity, making the loop integral divergent as the momentum goes to infinity (since the integral has the form $\int dp^2/p^2 = \log p^2$). In order to avoid this, the *renormalization* procedure is used. The purpose of renormalization is to replace these divergent integrals by finite expressions by introducing a new scale, on which α_s becomes dependent. This renormalization scale, μ_R, is an arbitrary parameter, and different choices of μ_R correspond to different renormalization schemes. However, a physical quantity R can not depend on the choice made for μ_R, implying that:

$$\mu_R^2 \frac{dR}{d\mu_R^2} \equiv \left[\mu_R^2 \frac{\partial}{\partial \mu_R^2} + \mu_R^2 \frac{\partial \alpha_s}{\partial \mu_R^2} \frac{\partial}{\partial \alpha_s} \right] R = 0. \tag{3.1}$$

But R will depend on μ_R through the dependence of α_s on the scale (running of α_s) and most often μ_R is chosen close to the scale of the momentum transfer Q, e.g. $\mu_R^2 = Q^2$. The running of α_s is determined by the renormalization group equation:

$$Q^2 \frac{\partial \alpha_s}{\partial Q^2} = \beta(\alpha_s) = - \left(b_0 \alpha_s^2 + b_1 \alpha_s^3 + ... \right), \tag{3.2}$$

where

$$b_0 = \frac{33 - 2n_f}{12\pi} \tag{3.3}$$

$$b_1 = \frac{153 - 19n_f}{24\pi^2} \tag{3.4}$$

and n_f is the number of active light flavors ($m_q \ll \mu_R$). Unlike in QED, the b coefficients have negative sign due to the non-Abelian interactions in QCD. Since Eq. 3.2 only describes the α_s scale dependence without given an absolute value of α_s, the strong coupling constant has to be determined experimentally at the energy of the measurement and then can be transformed to any other scale. Conventionally, the α_s is quoted at a given scale (typically the mass of the Z^0 boson). In LO (retaining only the first term of Eq. 3.2), the normalized strong coupling constant is given by:

$$\alpha_s(Q^2) = \frac{\alpha_s(\mu_R^2)}{1 + \alpha_s(\mu_R^2) b_0 \ln \left(\frac{Q^2}{\mu_R^2} \right)}. \tag{3.5}$$

As Q^2 becomes large, the running coupling $\alpha_s(Q^2)$ decreases to zero (rather slow due to the inverse power of $\ln Q^2$), leading to the asymptotic freedom of the partons. On the other hand, as Q^2 becomes smaller, the strong coupling will eventually get so large that pQCD breaks down. This limit is given by the scale $\Lambda_{QCD} \approx 200$ MeV on which the quarks and gluons start forming hadrons. The $\alpha_s(Q^2)$ obtained from different measurements is shown in Fig. 3.2 which also includes the current world average value [29]:

$$\alpha_s(M_Z^2) = 0.1184 \pm 0.0007.$$
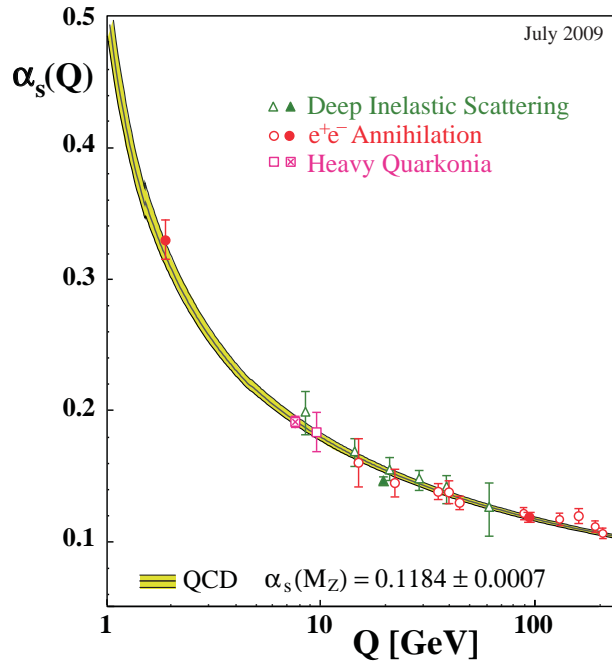
Figure 3.2: The strong coupling constant α_s as a function of the momentum transfer [29].

3.2 Factorization

Another important property of QCD which turns it into a reliable calculational tool with controllable approximations is *factorization*. Factorization deals with the divergencies introduced in the perturbative calculations by gluon emissions at very small angles (collinear divergence) or when the transverse momentum of the radiated gluon approaches zero (soft divergence). In the case of the strong coupling constant, the ultraviolet divergencies could be absorbed into the running of α_s with the introduction of the renormalization scale μ_R. The divergencies from gluon emissions can in a similar way be absorbed into the *parton distribution functions* (PDFs) with the introduction of an arbitrary parameter called *factorization scale*, μ_F. The scale μ_F can be interpreted as the scale which separates the long- and short-distance physics. Thus a parton emitted with a small transverse momentum, less than μ_F, is considered part of the hadron structure and is included in the PDF, while partons emitted at large transverse momentum are taken care of perturbatively. The PDFs describe the probability of finding a specific parton that carries a fraction x of the longitudinal momentum of the hadron in which it is bound. Since PDFs are non-perturbative they must be extracted from data, but the dependence of the quark and gluon distribution functions on the factorization scales can be calculated perturbatively using the so-called evolution equations: Dokshitzer-Gribov-Lipatov-Altarelli-Parisi (DGLAP) equations, Balitsky-Fadin-Kuraev-Lipatov (BFKL) equations, Ciafaloni-Catani-Fiorani-Marchesini (CCFM) equations. These evolution equations describe how a mother parton is split into two daughter partons, one of which is emitted whereas the other con-

tinues as a propagator parton and can be subject of further splittings. They are derived under different approximations and valid in different phase space regions.

3.3   Non-perturbative QCD

As already mentioned in the previous section, pQCD can not be used at small scales (Λ_{QCD}), or large distances (~ 1 fm), since the coupling will no longer converge and non-perturbative effects become important. The most important of these effects is *hadronization*, which converts the partons into colorless hadrons. The connection between the "parton level" and "hadron level" is done using phenomenological models at present. These models introduce the so-called *fragmentation functions* (FFs) that describe the probability for a parton to hadronize into a particular hadron, carrying a certain fraction of the parton's energy. Since the fragmentation process occurs from the different primary partons $i = u, d, ..., g$, the FFs can be represented as a sum of their contributions:

$$F^h(x, s) = \sum_i \int_x^1 \frac{dz}{z} C_i(s; z, \alpha_s) D_i^h(x/z, s), \tag{3.6}$$

where s is the center-of-mass energy squared, z is the fraction of parton momentum carried by the hadron, $D_i^h(x/z, s)$ is the fragmentation function of the hadron h from a parton i, $C_i(s; z, \alpha_s)$ is a coefficient function. The FFs can not be computed from perturbation theory and their parameters are determined from fits to experimental data. However, a similar approach to that used for PDFs, can be applied to the FFs as well. Knowing the z dependence of the fragmentation functions at some energy-squared scale s_0, one can use the evolution equations to predict their form at any other scale s. Different hadronization models are available, but only the Lund string fragmentation model [30] will be briefly described in the following.

   The Lund model assumes a linear confinement potential between two $q/\bar{q}$ endpoints approximated by a string:

$$V_{qq} = \kappa r, \tag{3.7}$$

where $\kappa \approx 1$ GeV/fm ≈ 0.2 GeV^2 is the string tension constant. If the two quarks are moving away from each other, the potential energy becomes large enough for the string to break, creating quark-antiquark or diquark-antidiquark pairs by invoking the idea of quantum mechanical tunneling. In the classic picture, q (qq) and $\bar{q}$ ($\bar{q}\bar{q}$) must be produced at a certain distance when the quarks have mass and/or transverse momentum (so that the field energy between them can be transformed into the sum of the two transverse masses m_T). Quantum mechanically, the pair can be created at one point (in order to assure local flavor conservation) and then tunnel out to the classically allowed region. The tunneling probability is given by [31]:

$$\exp\left(-\frac{\pi m_T^2}{\kappa}\right) = \exp\left(-\frac{\pi m^2}{\kappa}\right) \exp\left(-\frac{\pi p_T^2}{\kappa}\right) . \tag{3.8}$$

where m_T is a common transverse mass of the q (qq) and $\bar{q}$ ($\bar{q}\bar{q}$).

The factorization of the transverse momentum and the mass factors leads to a flavor independent Gaussian spectrum for p_x and p_y components of $q\bar{q}$. The formula also implies a suppression of heavy quark production $u : d : s : c \approx 1 : 1 : 0.3 : 10^{-11}$, with diquarks further suppressed. Charm and heavier quarks are hence not expected to be produced in the soft fragmentation. The fragmentation process continues until there is no energy left to create new $q\bar{q}$ ($qq\bar{q}\bar{q}$) pairs. Due to the kinetic energy of the initial quarks, the string will primarily break at the ends and it is expected that the produced hadrons will move in the same direction as the original parton. This collimated flow of particles is called a *jet*. Mesons are produced by combining the initial quark (antiquark) with the antiquark (quark) from the created pair. Baryons may be produced either by connecting quarks and antiquarks from the created quark-antiquark pairs, or by combining the original quark (antiquark) to the created diquark (antidiquark). Since baryons have higher masses, the probability to form a baryon is lower than of a meson. When gluons are emitted by the initial partons, a kink in the string will be produced which leads to an additional jet due to the kinetic energy gained in the direction of the gluon.

3.4 Deep Inelastic Scattering

To understand the dynamics of the partons, confined inside the hadrons, lepton-hadron scatterings have an obvious advantage as the lepton is a particle without any substructure. Within the SM, these interactions are mediated by γ, Z^0 or $W^\pm$. Due to the high masses of the Z^0 and $W^\pm$ the later two processes are suppressed and the photon exchange dominates at low energies. If the momentum transfer is far above the proton mass (but far below the Z^0 mass), the wavelength of the photon is small enough for it to interact with the partons inside the proton. Such interactions are always inelastic (i.e. the proton breaks up), therefore called Deep Inelastic Scattering (DIS) events.

A schematic diagram of the DIS process $ep \rightarrow eX$ is illustrated in Fig. 3.3, where an electron e with four-momentum k scatters off a proton with four-momentum p via the exchange of a highly off-shell photon with four-momentum q. The final states, the scattered electron and a hadronic final state X, have the four-momentum k' and the invariant mass W, respectively. Then the kinematic variables are defined by:

- $Q^2 = -q^2 = -(k - k')^2$, the virtuality of the exchanged photon. Since k and k' are timelike, the resulting photon four-momentum is spacelike ($q^2 < 0$), and thus $Q^2 > 0$.

- $x = Q^2/(2p \cdot q)$, the Bjorken scaling variable which can be interpreted as the fraction of the longitudinal proton momentum carried by the interacting parton.

- $y = (p \cdot q)/(p \cdot k)$, the inelasticity which, in the rest frame of the proton, is the energy fraction of the incoming electron carried by the photon.

- $s = (p + k)^2$, the center-of-mass energy squared.
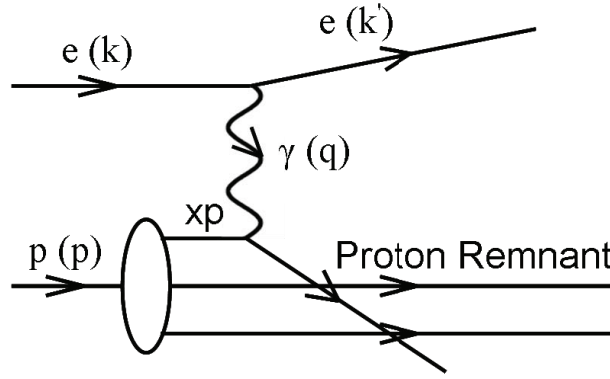
Figure 3.3: Schematic illustration of a deep inelastic charged lepton-proton scattering. The photon interacts with a parton carrying the momentum fraction xp. The four-momentum is given in brackets.

- $W^2 = (p + q)^2$, the invariant mass of the hadronic final state X.

Neglecting the proton and electron masses, the kinematic variables Q^2, x, and y are related by:

$$Q^2 = xys \approx W^2 \frac{x}{1-x} \qquad (3.9)$$

and for fixed s, only two independent variables need to be determined in order to describe the full kinematics of a DIS event.

A differential DIS cross section can be written in terms of the kinematic variables as:

$$\frac{d^2\sigma}{dxdQ^2} = \frac{4\pi\alpha^2}{Q^4}\left[(1 + (1-y)^2)F_1(x, Q^2) + \frac{1-y}{x}\left(F_2(x, Q^2) - 2xF_1(x, Q^2)\right)\right], \qquad (3.10)$$

where α is the electromagnetic coupling constant and $F_1(x, Q^2)$ and $F_2(x, Q^2)$ are proton structure functions. Since the photon is virtual, in addition to being transversely polarized it also has a longitudinal component. The absorption of transversely polarized photons is described by F_1, while longitudinally polarized photon interactions are described by the longitudinal structure function given by $F_L = F_2 - 2xF_1$. Introducing F_L, Eq. 3.10 reads:

$$\frac{d^2\sigma}{dxdQ^2} = \frac{4\pi\alpha^2}{2xQ^4}\left[(1 + (1-y)^2)F_2(x, Q^2) - y^2F_L(x, Q^2)\right]. \qquad (3.11)$$

3.4.1   Quark Parton Model

The Quark Parton Model (QPM) [32, 33] is formulated in the 'infinite momentum frame' $(m_p \ll |\vec{p}|)$ where the quarks are moving parallel with the proton and carry fractions of

its momentum. In this limit the structure functions are observed to obey an approximate scaling law, i.e. they are independent of the scale Q^2:

$$F_i(x, Q^2) \rightarrow F_i(x), \tag{3.12}$$

and reduce to:

$$F_2(x) = 2xF_1(x) = x \sum_q e_q^2 f_q(x), \tag{3.13}$$

which is called the Callan-Gross relation. Here the e_q and $f_q(x)$ are the charge and the PDF for quarks of type q inside the proton. The scaling implies that the virtual photon scatters off pointlike constituents, since otherwise the structure functions would depend on the ratio Q/Q_0, with $1/Q_0$ a length scale which characterizes the size of the constituents.

Figure 3.4 presents measurements of the structure function F_2 as a function of Q^2 for different values of x. As can be seen from the figure F_2 is increasing with increasing Q^2 for low x, whereas F_2 is decreasing with increasing Q^2 for high x. This is a clear evidence of the scaling violation; it could be explained by the existence of the gluon. It should also be noted that the structure function is independent of Q^2 for $x \sim 0.13$ and that QCD describes the data.

3.4.2 QCD in DIS

The LO DIS process is depicted in Fig. 3.3, while higher orders in α_s involve gluon emissions. As already discussed in Section 3.2, these gluons lead to divergencies in pQCD and a factorization scale μ_F is needed to separate the perturbative and non-perturbative parts of the cross section.

There are two main approaches to factorizing DIS cross sections: *collinear factorization* and *k_T-factorization*. In the first case, the partons are approximated to be collinear with the proton (their transverse momenta are neglected) and the cross section can be written as:

$$\sigma(ep \rightarrow e'X) = \sum_{i=q,g} \int_0^1 \frac{dz}{z} f_i(\frac{x}{z}, \mu_F^2) \cdot \hat{\sigma}_i, \tag{3.14}$$

where z is the ratio between the parton momentum when it interacts with the photon and the parton momentum when it was extracted from the proton (the two momenta can be different since the parton may have radiated gluons in between), $f_i(\frac{x}{z}, \mu_F^2)$ is the factorized PDF of parton i, and $\hat{\sigma}_i$ is the factorized partonic cross section (perturbatively calculable). In the kinematic region where the collinear approximation is valid, the DGLAP equation is used to evolve the PDF. However, the collinear approximation does not reproduce the data for small x and the k_T-factorization scheme is used in which the cross section is given by:

$$\sigma(ep \rightarrow e'X) = \sum_{i=q,g} \int_0^1 \frac{dz}{z} dk_T^2 \mathcal{F}_i(\frac{x}{z}, k_T) \cdot \hat{\sigma}_i. \tag{3.15}$$
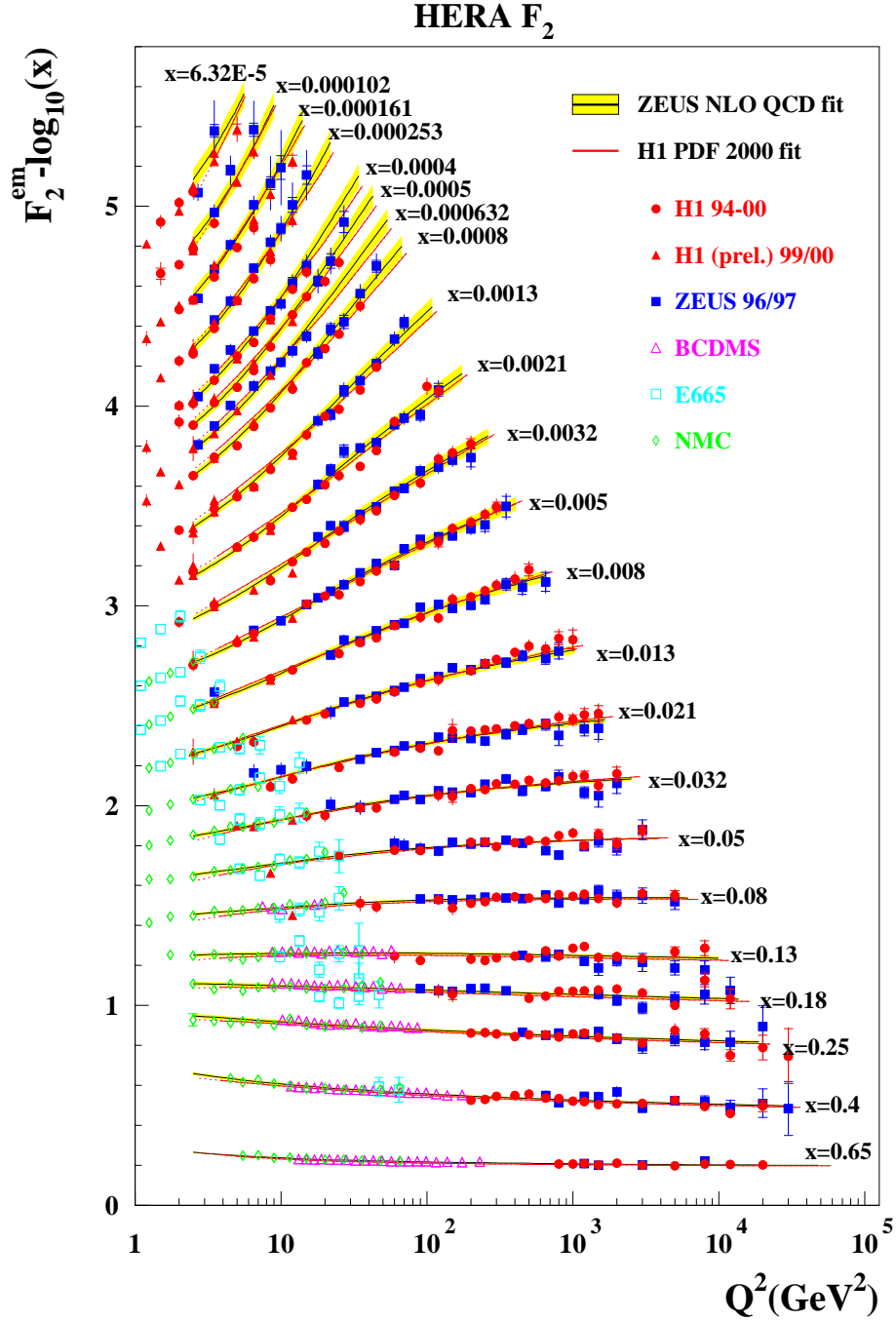
Figure 3.4: The proton structure function F_2 as a function of Q^2 at fixed values of x measured by the $H1$, $ZEUS$, $BCDMS$, $E665$, NMC experiments. Predictions from pQCD calculations/fits to the data are shown as the solid line. The figure is taken from [34].
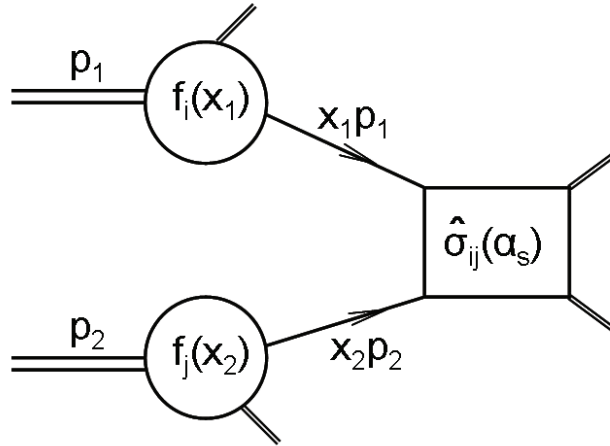
Figure 3.5: Schematic diagram of a hard scattering process in a hadron-hadron collision.

Here the $\hat{\sigma}_i$ is the k_T-dependent partonic cross section and $\mathcal{F}_i(\frac{x}{z}, k_T)$ is the unintegrated PDF (uPDF), where the transverse momenta of the partons are taken into account. The k_T approximation is used in combination with the BFKL equation.

Although factorization provides a prescription for handling the divergencies, there is an arbitrariness in choosing which finite contributions should be absorbed into the PDFs. In the *DIS scheme* all the gluon contributions are included into the PDFs, while in the $\overline{MS}$ *scheme* only the divergent terms are hidden in PDFs.

3.5 Hadron-Hadron Collisions

In order to verify the description of short-distance interactions one should study the production of hadrons with large transverse momentum in hadron-hadron collisions. Therefore, it is necessary to consider processes in which the constituents of one hadron (e.g. quarks and gluons with varying fractions of the momenta of their parent hadron) can undergo hard scatterings with those of another hadron. In such collisions, it has been well established that the primary source of hadrons with high transverse momentum ($p_T \geq 2$) GeV/c is the fragmentation of the hard-scattered partons, and that the p_T spectra can be described using pQCD [35]. A schematic diagram of a hard scattering is illustrated in Fig. 3.5. The cross section for such a process is given by:

$$\sigma(p_1, p_2) = \sum_{i,j} \int dx_1 dx_2 f_i(x_1, \mu_F^2) f_j(x_2, \mu_F^2) \hat{\sigma}_{ij}(k_1, k_2, \mu_R^2, \mu_F^2), \qquad (3.16)$$

where p_1 and p_2 are the four-momenta of the two colliding hadrons, $k_1 = x_1 p_1$ and $k_2 = x_2 p_2$ are the momenta of the partons which participate in the hard interaction, $f_i(x, \mu_F^2)$ is the factorized PDF of parton i, $\hat{\sigma}_{ij}$ is the short-distance cross section for the scattering of partons of types i and j and can be calculated as a perturbation series in the running

coupling α_s:

$$\hat{\sigma} = \alpha_s^k \sum_{m=0}^{n} C^{(m)} \alpha_s^m, \tag{3.17}$$

where $C^{(m)}$ are functions of the kinematic variables and the factorization scale and can be calculated using Feynman graphs. Different hard processes will contribute with different leading powers k. In the leading approximation ($n = 0$) the short-distance cross section is identical to the normal parton scattering cross section (calculable in the same way as for a QED process), while in higher orders it is the factorized partonic cross section.

More generally, Eq. 3.16 becomes:

$$\sigma = \sum_{i,j} \int dx_1 dx_2 f_i(x_1, \mu_F^2) f_j(x_2, \mu_F^2) \times \sum_{m=0}^{n} \left(\alpha_s(\mu_R^2) \right)^{(m+k)} \hat{\sigma}_{ij}^{(m)}(k_1, k_2, \mu_R^2, \mu_F^2). \tag{3.18}$$

The standard choice for the scales is usually $\mu_R = \mu_F = Q$, the hard scattering scale. Moreover, the PDFs extracted in DIS can be directly used in pp or p$\bar{\text{p}}$ predictions as long as the factorization scheme is the same.

For example, the inclusive hadron production cross section in $p + p \rightarrow h + X$ can be written as:

$$\frac{d\sigma^{pp}}{dyd^2p_T} = K \sum_{abcd} \int_0^1 dz_c \int_{x_{a}min}^1 dx_a \int_{x_{b}min}^1 dx_b f_a(x_a, Q^2) f_b(x_b, Q^2) \times \frac{d\sigma^{(ab \rightarrow cd)}}{d\hat{t}} \frac{D_{h/c}^0(z_c, s)}{\pi z_c^2}, \tag{3.19}$$

where x_a and x_b are the initial momentum fractions of the interacting partons a and b, $z_c = p_h/p_c$ is the momentum fraction of the final observable hadron, $d\sigma^{(ab \rightarrow cd)}/d\hat{t}$ is the hard partonic cross section to produce the outgoing partons c and d, with $\hat{t} \equiv (p_a - p_c)^2$ the invariant momentum transfer from parton a to parton c, $f_a(x, \mu_F^2)$ is the factorized PDF of parton a, $D_{h/c}^0(z_c, s)$ is the FF for the parton c into the hadron h. The K is a phenomenological factor used to account for higher order QCD corrections to the jet production cross section; typical values for K are 1-4.

3.6 Heavy-Ion Collisions

The focus of heavy-ion physics is to study and understand how collective phenomena and macroscopic properties, involving many degrees of freedom, emerge from the microscopic laws of elementary particle physics. This is done in the QCD sector by studying nuclear matter under conditions of extreme density and temperature through collisions between large nuclei ($A \gg 1$). The main goal is to characterize the properties of the highly dense and hot states that matter exhibits in such conditions, and to verify the existence of a new phase of matter called Quark-Gluon Plasma (QGP). Experimental physics with relativistic heavy-ions have been carried out at the Alternating Gradient Synchrotron (AGS) at Brookhaven National Laboratory (BNL), Super Proton Synchrotron (SPS) at CERN
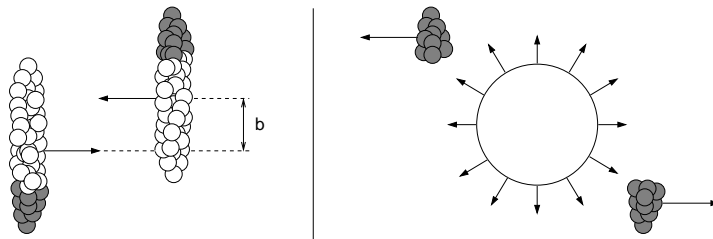
Figure 3.6: Schematic view of a relativistic heavy-ion collision: impact parameter b in heavy-ion collisions (left) and the spectators and participants picture (right).

(European Organization for Nuclear Research), and are currently carried out at Relativistic Heavy Ion Collider (RHIC) at BNL. The LHC should start colliding lead ions at $\sqrt{s_{NN}} = 2.75$ TeV soon (see Section 4.1). In this section some key observable in relativistic heavy-ion collisions will be presented using the variables defined in Appendix A.

A schematic drawing of a relativistic heavy-ion collision is shown in Fig. 3.6. The two Lorentz-contracted nuclei (due to their relativistic speed) approach each other in the center of mass system with *impact parameter b*. The impact parameter is defined as the transverse distance between the center of the two colliding nuclei. In the region of overlap, the participating nucleons interact with each other and give rise to an expanding volume of high energy density called *fireball*. In the non-overlap region, the spectator nucleons keep their initial momentum and simply continue on their original trajectories without interacting.

The degree of overlap is called *centrality* and is defined as

$$c = \frac{\int_0^{b_c} \frac{d\sigma_{in}(b')db'}{db'}}{\sigma_{in}} \cdot 100\% \tag{3.20}$$

where σ_{in} is the total inelastic cross section and b_c the impact parameter cut-off. This implies that c is the probability that a collision occurs at $b \leq b_c$. The most central collision has $c \sim 0\%$ when $b \sim 0$ fm, while for the most peripheral one $c \sim 100\%$. For two identical colliding spherical nuclei the inelastic cross section is $\frac{d\sigma_{in}(b)}{db}db = 2\pi b db$, so $c = \frac{b_c^2}{4R^2}$ since $b_{max} = 2R$, where R is the radius of the nuclei.

Since the impact parameter is not a directly measurable quantity, the quantification of the collision geometry can be done using the Glauber model [36]. The model is used to calculate the number of participants, N_{part}, the number of binary collisions, N_{coll}, and from this to estimate experimentally the centrality of the collision (Fig. 3.7).

A possible space-time evolution of a relativistic heavy-ion collision is illustrated in Fig. 3.8. After a short initial formation time ($\tau \sim 1$ fm/c) the QGP is formed. It then cools off by expanding and eventually hadronizes. During the expansion of the fireball, chemical freeze-out is reached when the hadrons stop interacting inelastically and new particles are only produced by secondary interactions in material out of collision zone or by decays of resonances. Elastic interactions continue until thermal freeze-out when the momentum transfer between particles stops.
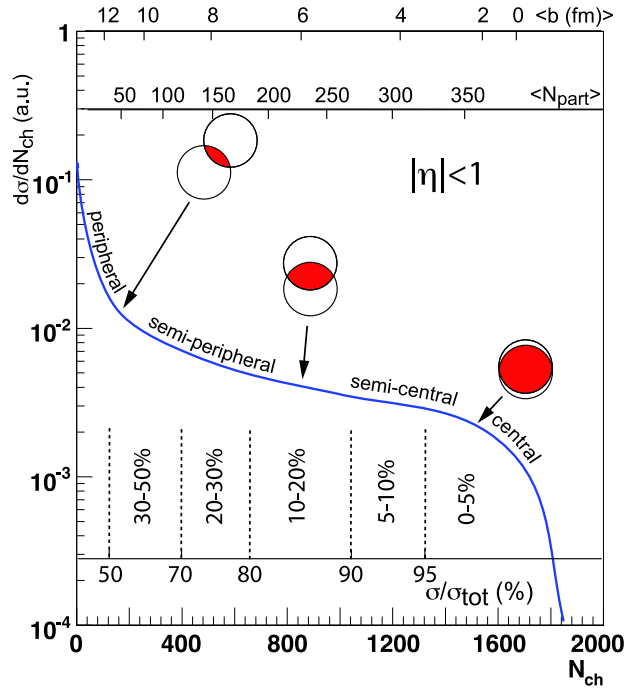
Figure 3.7: Correlation of the final state observables with Glauber calculated quantities: the number of participants and the impact parameter [37].

3.6.1   Quark-Gluon Plasma

Since phase transitions are related to large-distance phenomena in a thermal medium, they can not be treated using perturbative methods. Numerical studies inside the Lattice QCD (LQCD) framework have been used to study from a theoretical point of view the qualitative features of the QGP and to make quantitative predictions about its properties, e.g. the transition temperature T_c and the energy density ϵ_c at this temperature.

A typical expected phase diagram of nuclear matter is presented in the left panel of Fig. 3.9. The expected phase transition and its theoretical uncertainty based on LQCD calculations at zero baryon chemical potential $\mu_B = 0$ is given by the cross-hatched region. The arrows indicate how different colliders probe the deconfinement transition during the expansion phase in heavy-ion collisions; the chemical and thermal freeze-out curves are also presented in the figure. As can be seen from the figure the phase transition can be reach along different paths on the (μ_B, T) plane. According to Big Bang cosmology, the Universe evolved from QGP to hadrons at $\mu_B \approx 0$ due to rapid expansion and cooling (path downward along the vertical axis). Currently QGP may exist in the very dense cores of neutron stars since the gravitational collapse causes an increase in the baryonic density at temperature close to zero (path towards the right along the horizontal axis). The order of the phase transition and the existence and the position of a critical point are disputed, but the common claim is that the phase transition is second order (crossover) for $\mu_B \approx 0$ and first order for $T = 0$.
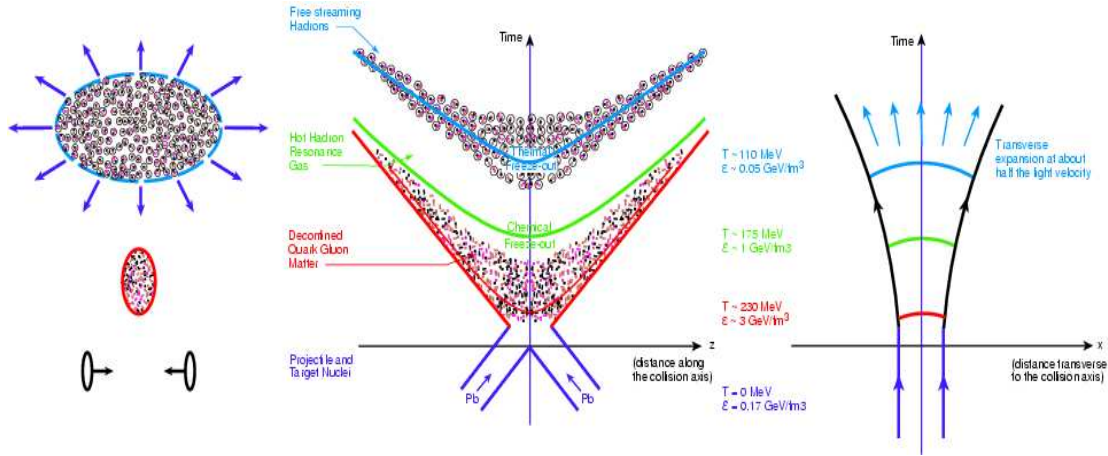
Figure 3.8: Space-time evolution of a relativistic heavy-ion collision.
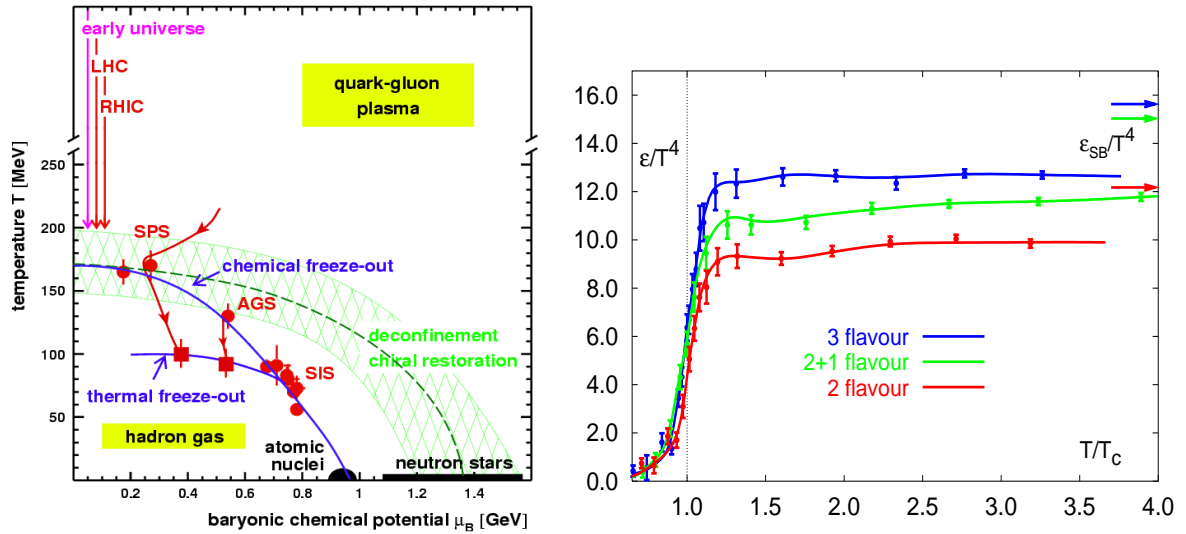
Figure 3.9: Left: QCD phase diagram in temperature T versus baryon chemical potential μ_B plane. The cross-hatched region indicates the expected phase transition and its present theoretical uncertainty based on LQCD calculations at $\mu_B = 0$. The points indicate the region reached by different experiments. Right: Lattice calculation of energy density as a function of active flavours ($\mu_B = 0$); arrows indicate the value for a gas of light quarks and gluons. For all calculations, the sharp energy increase around a critical temperature T_c reveals a phase transition [38].

The right panel of Fig. 3.9 illustrates lattice calculations of the energy density scaled by T^4, ϵ/T^4, as a function of system temperature T scaled by T_c. The values are computed for 2, 3 and 2+1 flavors [38]. At high temperature, it is expected that ϵ/T^4 will asymptotically approach the ideal gas limit (Stefan-Boltzmann limit) indicated by the arrows. The energy density shows a sharp rise when the temperature increases above T_c and eventually at $T > T_c$ flattens without reaching the Stefan-Boltzmann limit, meaning that LQCD predicts a phase transition to QGP. The critical temperature is estimated to be $T_c = 173 \pm 3$ MeV and critical energy density $\epsilon_c \simeq 0.3 - 1.3$ GeV/fm^3 at vanishing μ_B. In this calculation the main uncertainty sources for T_c and ϵ_c are the number of flavors and the quark masses. Recent calculations indicate a transition temperature of $T_c = 192(7)(4)$ MeV, with almost physical light quark masses and a heavier strange quark mass [39]. Also, an energy density $\epsilon_c \sim 1$ GeV/fm^3 was found, though with a large error due to the uncertainty on T_c.

3.6.2   Particle Production

The particle production in AA collisions is different from pp collisions since nuclear PDFs are different from those in free protons and the eventually produced medium can modify the fragmentation process. The medium that changes the parton fragmentation could be the nucleus itself and/or the high particle multiplicity. Thus, for an accurate description of particle production in AA collisions, nuclear PDFs and medium modified FFs are needed. The nuclear effects are usually divided in two classes:

- Initial-state effects: the hard cross section depends on the size and energy of the colliding nuclei, but not on the medium formed in the collision. Such effects are: Cronin enhancement, nuclear shadowing, and gluon saturation. For a detailed description see Ref. [40].

- Final-state effects: the yields and the kinematic distributions of the produced hard partons are influenced by the created medium. Final-state effects are not correlated to initial-state effects and provide information on the properties of the medium (gluon density, temperature, volume). Such effects are: parton radiative and collisional energy loss. For a review see [41].

Including initial and final nuclear effects (nuclear modification of the PDFs, nuclear broadening of the transverse momentum k_T of the colliding partons, parton energy loss), the inclusive hadron production cross section in $AB \rightarrow h + X$ can be written as

$$
\begin{aligned}
\frac{d\sigma^{AB}}{dy d^2 p_T} =& K \sum_{abcd} \int d^2 b d^2 r dx_a dx_b d^2 k_{T_a} d^2 k_{T_b} t_A(\mathbf{r}) t_B(|\mathbf{b} - \mathbf{r}|) g_A(k_{T_a}, \mathbf{r}) \\
& g_B(k_{T_b}, |\mathbf{b} - \mathbf{r}|) f_{a/A}(x_a, Q^2, \mathbf{r}) f_{b/B}(x_b, Q^2, |\mathbf{b} - \mathbf{r}|) \frac{d\sigma^{ab \rightarrow cd}}{d\hat{t}} \frac{D'_{h/c}(z_c, s)}{\pi z_c^2},
\end{aligned}
\tag{3.21}
$$

where $z_c = p_h/p_c$ is the fractional momentum, b is the impact parameter, $T_{AB}(b) = \int d^2 r t_A(\mathbf{r}) t_B(|\mathbf{b} - \mathbf{r}|)$ is the nuclear overlap function, $D'_{h/c}(z_c, s)$ is the medium modified

FF for parton c, $g_A(k_{T_A}, \mathbf{r})$ is the position dependent initial parton transverse momentum distribution (broadened due to the multiple scattering that partons from both projectile and target nuclei suffer before the hard process), $f_{a/A}(x_a, Q^2, \mathbf{r})$ is the position dependent nuclear PDF of parton a, $K \approx 1.5\text{-}4$ is the factor used to account for higher order pQCD corrections.

Disregarding the nuclear effects, QCD factorization implies that inclusive AB cross sections for hard processes scale simply as $A \cdot B$ times the corresponding pp cross section:

$$d\sigma_{AB}^{hard} = A \cdot B \cdot d\sigma_{pp}^{hard}. \tag{3.22}$$

For a given impact parameter b, one writes instead:

$$dN_{AB}^{hard}(b) = \langle T_{AB} \rangle \, d\sigma_{pp}^{hard} = \langle N_{coll} \rangle \, dN_{pp}^{hard} \tag{3.23}$$

since the averaged nuclear overlap function is given by:

$$\langle T_{AB} \rangle = \frac{\int d^2 b \, T_{AB}(b)}{\int d^2 b (1 - e^{-\sigma_{pp}^{inel} T_{AB}(b)})} = \frac{\langle N_{coll} \rangle}{\sigma_{pp}^{inel}}, \tag{3.24}$$

where $\langle N_{coll} \rangle$ is the average number of inelastic nucleon-nucleon collisions, with cross section σ_{pp}^{inel}.

A standard method to quantify the medium effects on particle production at high p_T in a AA collision is thus given by the *nuclear modification factor*:

$$R_{AA} = \frac{d^2 N_{AA}/dy dp_T}{\langle N_{coll} \rangle \, d^2 N_{pp}/dy dp_T} \tag{3.25}$$

In the absence of nuclear effects, the heavy-ion collisions can be seen as a superposition of binary NN collisions and $R_{AA} = 1$. If $R_{AA} > 1$, the nuclear effects enhance the particle production compared to pp collisions (e.g. Cronin enhancement), and if $R_{AA} < 1$, the nuclear effects suppress the particle production (e.g. jet quenching). For $p_T < 2$ GeV/c, where the particle production follows a scaling with the number of participants, $R_{AA} < 1$.

When no pp collision distributions are available, another quantity called the central-to-periphal ratio, R_{cp}, is constructed. This ratio uses the peripheral collisions to construct the reference spectrum and is thus defined as:

$$R_{CP} = \frac{\langle N_{coll}^{per} \rangle \, d^2 N_{cen}/dy dp_T}{\langle N_{coll}^{cen} \rangle \, d^2 N_{per}/dy dp_T}, \tag{3.26}$$

where $\langle N_{coll}^{per} \rangle$ and $\langle N_{coll}^{cen} \rangle$ are the average number of incoherent binary collisions in the peripheral and central centrality bins, respectively.

Recombination Models

Different models are used to describe hadron production at high transverse momentum in AA collisions (see Ref. [40]). The focus here will be on the recombination models since they

provide solutions to some of the puzzling features of high p_T data obtained by the RHIC experiments and distinct predictions for LHC. These features can not be explained using the "standard approach" concerning the treatment of hadron production at high p_T, namely the fragmentation process, and may be regarded as anomalies. If hard partons fragment in vacuum, whether or not they have lost energy traversing the medium, the fragmentation products should be independent of the medium. Thus the ratio of the produced hadrons should depend only on the ratio of the FFs, $D_h(z)$. Given a parton (quark or gluon), its FF for the production of a proton $D_p(z)$ is much smaller than that for a pion $D_\pi(z)$. The observed data reveal several anomalies according to that picture:

- The ratio of proton to pion, $R_{p/\pi}$, in AuAu collisions ($\sqrt{s_{NN}} = 200$ GeV, $y = 0$) is approximately 1 at $p_T \approx 3$ GeV/c [42].

- The R_{CP} in dAu collisions ($\sqrt{s_{NN}} = 200$ GeV) is greater for p than for π at $p_T > 2.5$ GeV/c for $|y| < 1.0$ [43].

- The azimuthal anisotropy parameter v_2 is larger for baryons than for mesons for $p_T > 2$ GeV/c in AuAu collisions ($\sqrt{s_{NN}} = 200$ GeV) [44, 45].

All these anomalies can be understood if hadrons are produced by parton recombination instead of hard parton fragmentation. The basic reason why hard parton fragmentation works so well in describing the high p_T data in leptonic and hadronic collisions, but poorly in heavy-ion collisions, would then be the absence of the large body of soft partons in the former case. When a multi-parton state is to hadronize, it is more easy for a q and $\bar{q}$ to recombine than for a higher momentum quark q to fragment, assuming a rapidly falling parton momentum distribution. That is simply because recombination involves the addition of two lower momenta q and $\bar{q}$, where the densities are higher, while fragmentation involves first the creation of a high momentum parton (at a cost in yield), and then the production of a hadron at some momentum fraction at the cost of another factor of suppression. Baryon production is enhanced because of the extra quark compared with the mesons. Since there are many soft partons moving collinearly with a hard parton in a AA collision, the above comparison is meaningful.

A specific parton recombination model that describes well the RHIC data and makes prediction for LHC is the one of R. C. Hwa and C. B. Yang. They introduce semi-hard shower parton and assume that all hadrons are produce by recombination at any p_T [46]. The fragmentation of a hard parton is accounted for by the recombination of shower partons that it creates. The shower partons can also recombine with the soft partons in the environment; this is considered the dominant mode of hadronization in the intermediate p_T region and stands between the recombination of thermal partons at low p_T and the fragmentation of hard partons at high p_T.

The invariant inclusive distribution for a produced meson with momentum p is [47]:

$$p\frac{dN_M}{dp} = \int \frac{dp_1}{p_1}\frac{dp_2}{p_2}F_{q\bar{q}'}(p_1,p_2)R_M(p_1,p_2,p), \qquad (3.27)$$

where $F_{q\bar{q}'}(p_1, p_2)$ is the joint distribution of a quark q with momentum p_1 and an antiquark $\bar{q}'$ with momentum p_2, $R_M(p_1, p_2, p)$ is the recombination function (RF) which specifies the probability that these two quarks recombine to form a meson with momentum p.

For pions the RF is $R_\pi(p_1, p_2, p) = (p_1 p_2/p)\delta(p_1 + p_2 - p)$, so the pion production can be written as

$$\frac{dN_\pi}{pdp} = \frac{1}{p^3} \int_0^p dp_1 F_{q\bar{q}'}(p_1, p - p_1). \tag{3.28}$$

The $F_{q\bar{q}'}$ can be expressed in terms of the thermal (T) and shower (S) components of the parton sources as:

$$F_{q\bar{q}'} = TT + TS + (SS)_1 + (SS)_2, \tag{3.29}$$

where TT signifies two thermal partons whose recombination yields the soft hadrons, TS denotes thermal-shower pairing, $(SS)_1$ represents two shower partons arising from one hard parton (hence within one jet), and $(SS)_2$ denotes two shower partons that are from two separate, but nearby hard partons (therefore associated with two overlapping jets). The $(SS)_2$ term is expected to be important at LHC where the density of hard parton should be extremely high. Even though each term is important in different p_T regions, they make contributions to all p_T.

Since the observed pion distribution at low p_T is exponential, the invariant thermal parton distribution is

$$T(p_1) = p_1 \frac{dN_q^T}{dp_1} = Cp_1 \exp(-p_1/T) \tag{3.30}$$

and the TT component yields:

$$\begin{aligned} \frac{dN_\pi^{TT}}{pdp} &= \frac{1}{p^3} \int_0^p dp_1 Cp_1 \exp(-p_1/T)C(p - p_1)\exp(-(p - p_1)/T) \\ &= \frac{C^2 \exp(-p/T)}{p^3} \int_0^p p_1(p - p_1)dp_1 = \frac{C^2}{6}\exp(-p/T), \end{aligned} \tag{3.31}$$

where C and T are model parameters obtained from fits to the low p_T data.

The distribution of a shower parton j with transverse momentum p_1 in central heavy-ion collisions is

$$S(p_1) = \xi \sum_i \int_{k_0}^\infty dk k f_i(k) S_i^j(p_1/k), \tag{3.32}$$

where $f_i(k)$ is the probability of producing a hard parton i with transverse momentum k, k_0 represents the lower limit for which pQCD derivation of $f_i(k)$ is still valid (set to 3 GeV/c in the model), $S_i^j(p_1/k)$ denotes the shower parton distributions obtained from FFs and can be found in Ref. [48]. The ξ parameter is the average fraction of hard partons that are to hadronize; it can be regarded as an empirical quantification of the degree of energy loss.

The contribution to the pion spectrum from the TS component is then

$$\frac{dN_\pi^{TS}}{pdp} = \frac{1}{p^3} \int_0^p dp_1 T(p_1) S(p - p_1) \tag{3.33}$$

and from $(SS)_1$ is

$$p\frac{dN_\pi^{(SS)_1}}{dp} = \xi \sum_i \int dk k f_i(k) \frac{p}{k} D_{\pi/i}\left(\frac{p}{k}\right), \qquad (3.34)$$

where $D_{\pi/i}(p/k)$ is the FF of a parton i into a pion. The $(SS)_2$ term in Eq. 3.29 is

$$(SS)_2(p_1, p_2) = \delta_{y\phi}\xi^2 \sum_{i,i'} \int dk dk' k k' f_i(k) f_{i'}(k') S_i^j(p_1/k) S_{i'}^{j'}(p_2/k'), \qquad (3.35)$$

where $\delta_{y\phi}$ reflects the probability for overlap in y and ϕ of the two showers in order for collinear recombination of the partons j and j' to happen. The value of $\delta_{y\phi}$ is expected to be small at RHIC energies, and hence this mode of recombination is ignored in the calculations, but may well become significant at LHC energies. Collecting all the pieces of Eq. 3.29 together and substituting them in Eq. 3.28, the formula for the inclusive pion distribution is obtained.

A similar procedure can be applied for baryon production. They are produced from thermal and shower parton recombinations:

$$p\frac{dN_B}{dp} = \int \frac{dp_1}{p_1}\frac{dp_2}{p_2}\frac{dp_3}{p_3} F(p_1, p_2, p_3) R_B(p_1, p_2, p_3, p), \qquad (3.36)$$

where $F(p_1, p_2, p_3)$ is the joint distribution of three relevant quarks to form the baryon B and $R_B(p_1, p_2, p_3, p)$ is the RF for a baryon with momentum p. The joint quark distribution has more terms in the various possible contributions from the thermal and shower partons than in meson production. Schematically, it takes the form (in increasing order of the number of hard partons involved):

$$F_{qq'q''} = TTT + TTS + T(SS)_1 + (SSS)_1 + T(SS)_2 + (S(SS)_1)_2 + (SSS)_3. \qquad (3.37)$$

Here the first term only consists of thermal partons, the next three terms involve a hard parton, the following two have two hard partons, and the last one has three. Only the first four terms are considered when doing calculations at RHIC energies.

The left panel in Fig. 3.10 shows a comparison between the π^0 spectrum for central AuAu collisions at $\sqrt{s_{NN}} = 200$ GeV calculated in the recombination model and data from PHENIX. Thermal-thermal recombination (dashed line) dominates for $p_T < 3$ GeV/c, while in the region $3 < p_T < 8$ GeV/c the dominant contribution is from thermal-shower recombination (line with crosses). The shower-shower recombination in one jet (line with circles) is the conventional jet fragmentation and becomes important for $p_T > 9$ GeV/c. The shower-shower recombination from 2 jets (line with squares) has no important contribution to particle production. The model calculation fits very well the data up to $p_T \simeq 10$ GeV/c.

The proton spectrum from recombination model calculation is depicted in the right panel of Fig. 3.10. The sum of the various types of contributions considered in the calculation (solid line) agrees well with the data from PHENIX in AuAu collisions at $\sqrt{s_{NN}} = 200$
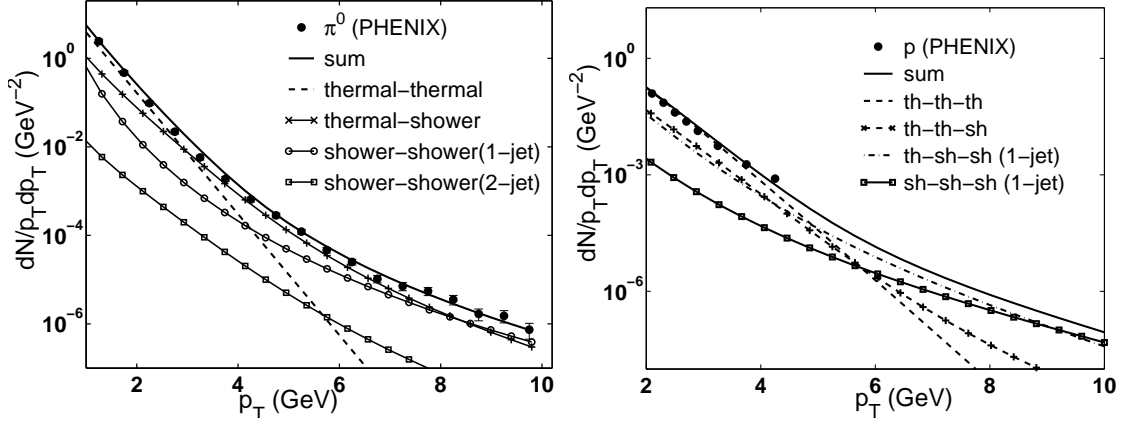
Figure 3.10: Transverse momentum distribution of π^0 (left) and proton (right) in AuAu collisions from PHENIX compared with expectations from the recombination model. The solid line represents the sum of the contributions to the recombination of partons included in the calculations: TT (dashed line), TS (line with crosses), $(SS)_1$ (line with open circles), $(SS)_2$ (line with squares) for π^0; TTT (dashed line), TTS (line with crosses), TSS (dashed-dot line), SSS (line with squares) for proton. Figure is taken from [46].
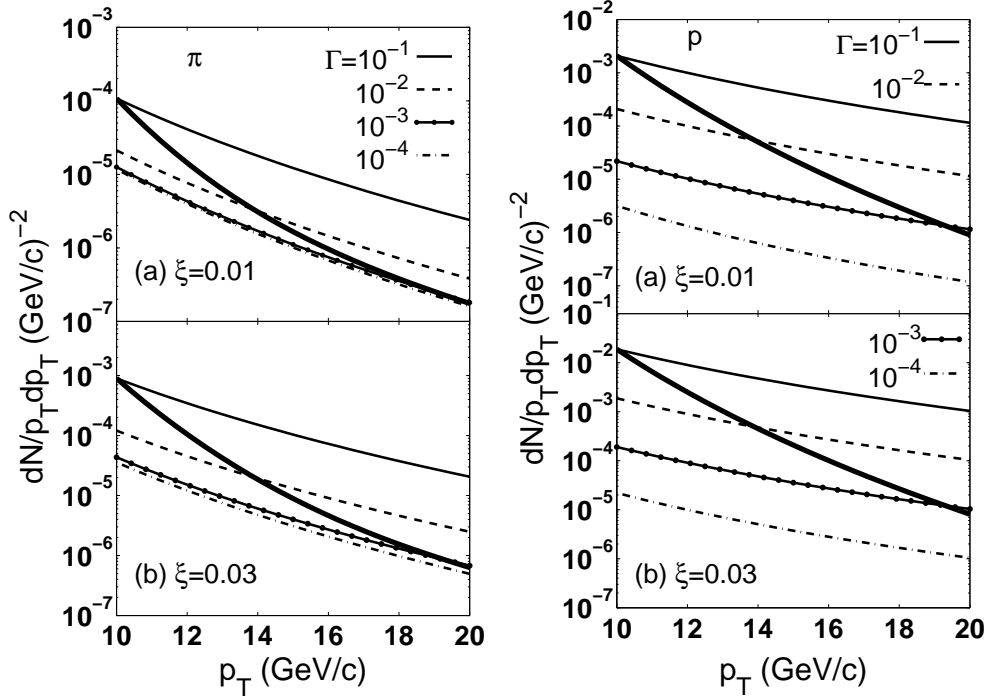
Figure 3.11: The transverse momentum distributions of π (left) and proton (right) predicted by the recombination model at LHC for two values of the nuclear suppression factor ξ and for various fixed values of the probability $\delta_{y\phi} \equiv \Gamma$ of overlap of neighboring jets. The heavy solid line represents the distributions for $\delta_{y\phi}(p_T) \propto p_T^{-7}$. Figure is taken from [49].

GeV. The comparison stopped at $p_T = 2$ GeV/c due to the proton mass effect which becomes important at low p_T. The thermal quarks recombination is expected to dominate for $p_T < 5$ GeV/c. At higher p_T the recombination of one thermal quark with two shower quarks from one jet, TSS component, becomes important for $p_T > 9$ GeV/c where the SSS component takes over.

The pion and proton transverse momentum distributions predicted by the recombination model for heavy-ion collisions at LHC are presented in Fig. 3.11. The calculations are performed for two values of the nuclear suppression factor ξ ($\xi = 0.01$ upper panel and $\xi = 0.03$ lower panel) and four different values of the probability $\delta_{y\phi}$ (denoted by Γ in the legend of Fig. 3.11) of overlap neighboring jets (the values are indicated in the legend). The heavy solid line represents the distribution when $\delta_{y\phi}$ is taken to decrease as p_T^{-7}. The contribution to the particle production is expected to be dominated by the recombination of the shower partons from different jets (two for pions, three for protons) since the momentum fractions of each parton in the two-jet (three-jet) case can be lower than the parton momentum in the one-jet case. One also expects the effect to be more amplified in the three-jet case compared to the two-jet situation, so protons should be more copiously produced than pions. As can be seen from the figure, the $\delta_{y\phi}$ dependence of the proton distribution is very different from the pion one; for $\delta_{y\phi} = 0.1$, the rate of proton production is more than an order of magnitude higher than that of pion. This leads to a proton-to-pion ratio as high as 20 at LHC.

Although the explanations offered by the recombination model are by no means yet the final word, the large p/π ratio observed at RHIC energies shows the need for identified particle spectra at intermediate and high p_T at LHC energies, both as reference data from pp collisions as well as in heavy-ion collisions. In this thesis I take the first steps along this road.

Chapter 4

ALICE@LHC

This chapter will briefly introduce the Large Hadron Collider (LHC) [50, 51] accelerator at CERN by describing the main components. Next, the layout and various subsystems of the A Large Ion Collider Experiment (ALICE) [52, 53] will be reviewed with emphasis on the subdetectors that are used for the analysis described in this thesis. For this discussion the variables defined in Appendix A and the ALICE coordinate system (Appendix B) are used.

4.1 The Large Hadron Collider

The LHC is the most powerful particle accelerator world-wide. The LHC project was approved by the CERN Council in 1994 [54]. At that time, LHC was supposed to start in 2004 with a center-of-mass energy of 10 TeV and to be upgraded to 14 TeV in 2008. However, in 1996 it was decided to go for the full energy at start-up. The LHC is installed in the LEP [1] tunnel located between the Jura mountain, in France, and the Léman lake, in Switzerland. The tunnel has a circumference of 26.7 km and lies between 45 m and 170 m below ground. The LHC is designed to collide proton beams at $\sqrt{s} = 14$ TeV (a factor seven higher than the Tevatron), but collisions between heavy-ions (Pb) at $\sqrt{s_{NN}} = 5.5$ TeV (a factor 30 increase with respect to RHIC) will also be provided. These will be the highest energies ever reached in particle collision experiments.

The design of the Large Hadron Collider was driven by the need to test the various predictions of high energy physics, such as:

- The Higgs boson: Does the theoretical Higgs mechanism responsible for generating particle masses exists in Nature? How many Higgs bosons are there, and what are their masses?

- Supersymmetry: Do particles have supersymmetric partners?

---

[1] The Large Electron Positron (LEP) Collider had a maximum center-of-mass energy of 209 GeV and operated between 1989-2000.

- Dark matter: What is the nature of the dark matter?

- Antimatter: Why are there apparent violations of the symmetry between matter and antimatter in the observed Universe?

- Quark-Gluon Plasma: How did the Quark-Gluon Plasma behave in the early Universe?

In order to help answer many of these fundamental questions, a hadron collider at a high luminosity was chosen as this gives the optimal conditions to cover a large part of the possible parameter space for new physics.

4.1.1   Layout of the LHC
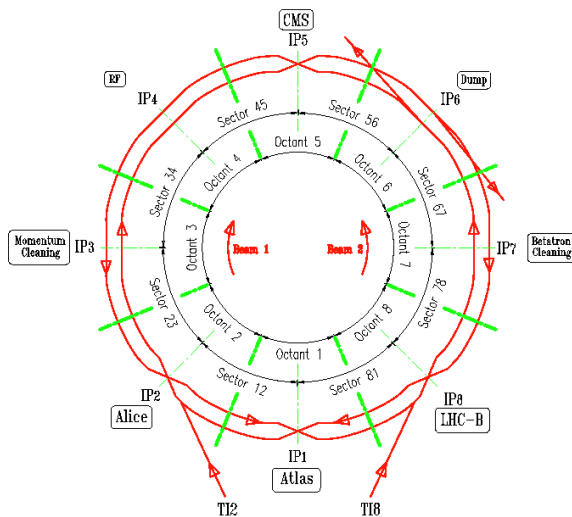
Figure 4.1: Schematic drawing of the LHC.
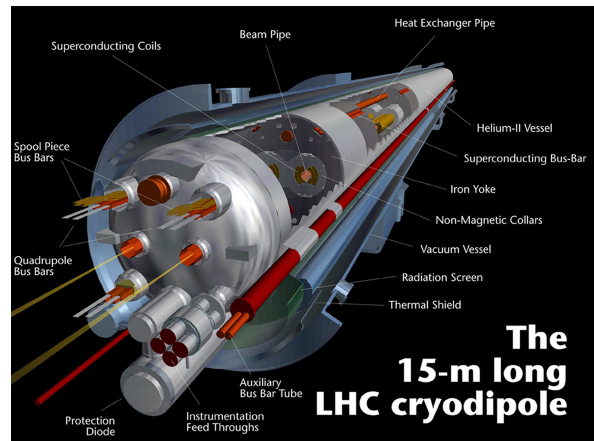
Figure 4.2: LHC dipole magnet.

The LHC is a particle-particle accelerator and collider with two rings containing counter-rotating beams installed in the old LEP tunnel. The layout of the LHC is illustrated in Fig. 4.1. The synchrotron rings are segmented into octants and has eight crossing points with long straight sections (in the center of each octant) and eight arcs called *Sector ab*, where a, b are the number of the corresponding octants in clock-wise order (as its geometry was designed for LEP). For the LHC, four of the crossing points contain experiments (points 1, 2, 5, and 8), while in the others the beam crossings have been suppressed and new systems were installed: eight radio-frequency (RF) cavities that accelerates the particles (point 4), collimation systems that "clean" the beam (points 3 and 7), and the beam dumping system (point 6). Particles are injected upstream of points 2 and 8.

The magnet system is the main component of the machine since the strength of the magnets determines the achievable center-of-mass energy (the energy losses in the form of synchrotron radiation are small and the LHC curvature radius is already defined by that of
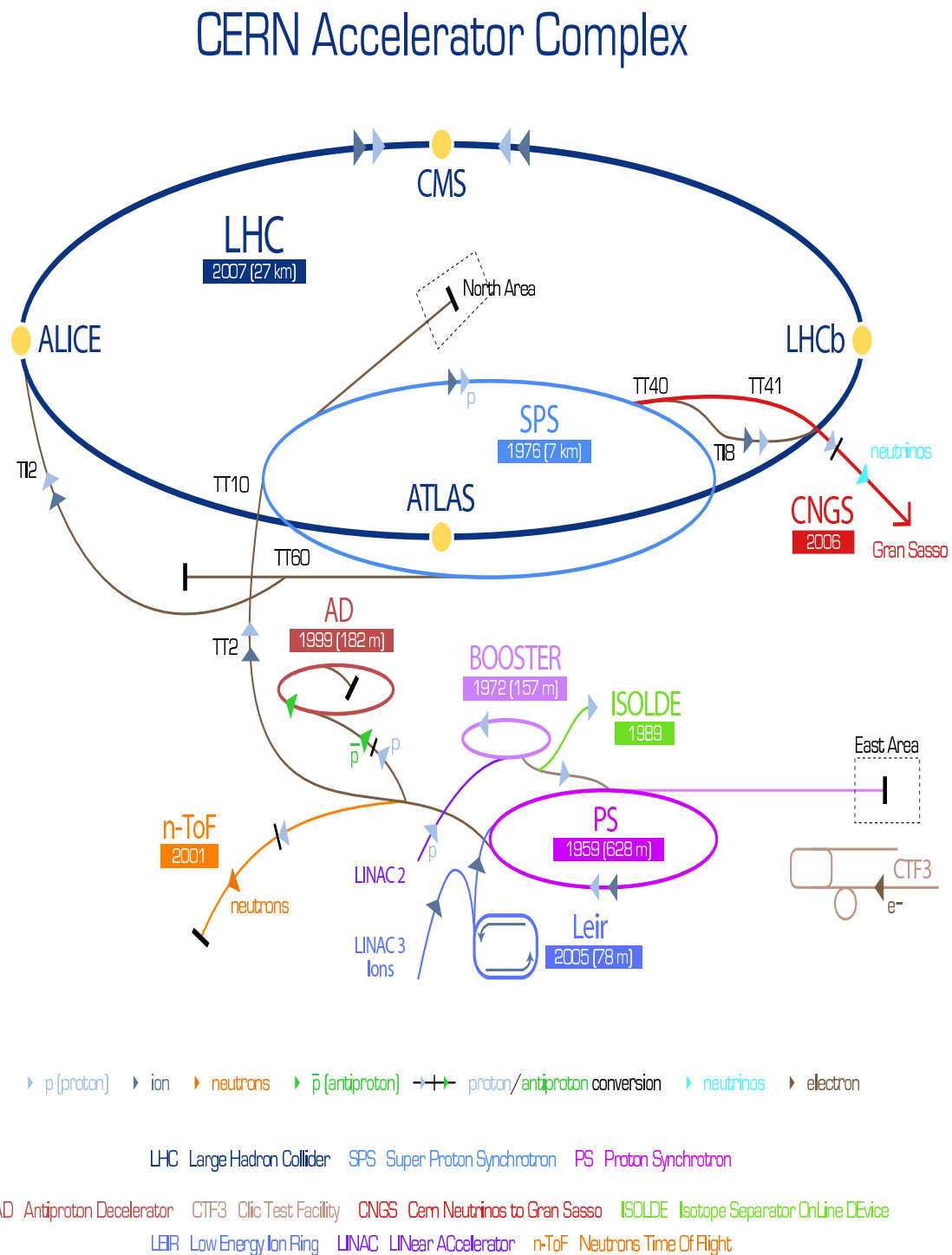
Figure 4.3: The CERN accelerator complex. The figure is not to scale and taken from [55].

Ring circumference	26659 m
Number of magnets	9593
Number of dipoles	1232
Dipole operating temperature	1.9 K
Peak magnetic dipole field	8.33 T
Number of quadrupoles	392
Number of RF cavities	8 per beam
Proton energy	7 TeV
Proton bunch separation	25 ns
Number of bunches per proton beam	2808
Number of protons per bunch	1.15×10^{11}
pp design luminosity	10^{34} cm^{-2} s^{-1}
pp luminosity lifetime	15 hrs
Gamma factor of protons	7461
Pb ions energy	2.76 TeV/u
Pb ions bunch separation	100 ns
Number of bunches per Pb ions beam	592
Number of Pb ions per bunch	7×10^{7}
PbPb luminosity	10^{27} cm^{-2} s^{-1}
PbPb luminosity lifetime	6 hrs
Gamma factor for Pb ions	2964

Table 4.1: LHC parameters for protons and ^{208}Pb ions [51].

the LEP tunnel) [2]. It is also complicated because separate magnet channels for each beam are required, but the internal diameter of the tunnel is 3.7 m in the arcs, which makes it almost impossible to install two completely separate rings. This led to the adoption of twin bore superconducting magnets. Over 1600 superconducting magnets have been installed in the tunnel: 1232 dipoles that bend the beam trajectories and 392 quadrupoles that focus the beams. A LHC dipole and the cryostat is shown in Fig. 4.2. It has a length of 14.3 m and operates at a temperature of 1.9 K. Approximately 96 tonnes of liquid helium is needed to keep the magnets at their operating temperature, making the LHC the largest cryogenic facility in the world. Powered by a maximum current of 11.7 kA, the field of the superconducting dipole magnets is ramped from 0.54 T (injection energy of 450 GeV per beam) to 8.33 T (nominal collision energy of 7 TeV per beam).

The beam is injected into the LHC through a series of older accelerators that successively increase the energy. The beam road from the production to the interaction points is depicted in Fig. 4.3.

---

[2]The momentum p of the beam particles is given by: $p = qB\rho$ since $F = qvB = mv^2/\rho$ (the balance between the Lorentz force and the centripetal acceleration of motion in a circle), where v is the velocity, q the charge, B the magnetic field, ρ radius of the tunnel, and $(B\rho)$ is the magnetic rigidity.

The proton beam starts at Linac2 where the electrons are stripped off from hydrogen atoms and the remaining protons are accelerated to 50 MeV. From here, the proton beam progresses into the Proton Synchrotron Booster (PSB) where it is ramped up to an energy of 1.4 GeV. Then it is injected into the Proton Synchrotron (PS), where the protons are accelerated to 25 GeV. The beam is fed to the Super Proton Synchrotron (SPS) that increases the energy to 450 GeV. From SPS the beam is transferred to LHC and the protons are accelerated to their nominal energy of 7 TeV.

The lead ions are produced by the Electron Cyclotron Resonance (ECR) and afterwards fed to LINAC3 that accelerates them to 4.2 MeV/u. In this process of lead acceleration they loose 27 electrons. The Low-Energy Ion Ring (LEIR) then takes over, accumulating and accelerating the lead ions to 72.2 MeV/u. The lead particles loose additionally 27 electrons at the LEIR, while the rest are removed in the PS and SPS that accelerates them to 5.9 GeV/u and 176.4 GeV/u, respectively. When this energy is reached the beam is moved into the LHC main ring where the energy is ramped up to 2.76 TeV/u.

The key parameters of the LHC are summarized in Table 4.1. As can be seen from the table the proton beams have a bunch-to-bunch distance of 25 ns (or a multiple of 25 ns) which corresponds to a maximum bunch crossing frequency of 40 MHz, while for ion beams the time between bunches will be 100 ns with a maximum crossing frequency of 10 MHz.

The collisions between the two beams of particles will be recorded by the six experiments constructed at the LHC. The ATLAS and CMS experiments are the largest detectors, while the other four experiments, ALICE, LHCb, LHCf, and TOTEM, are smaller and more specialized. All experiments are located in caverns below ground, where the beams intersect. A short description of each experiment is given below:

ALICE (A Large Ion Collider Experiment) [52, 53] is a dedicated heavy-ion experiment designed to address the physics of strongly interacting matter and the Quark-Gluon Plasma at extreme values of energy density and temperature in nucleus-nucleus collisions. Furthermore, ALICE will also take data with proton beams to collect reference data for the heavy-ion program and to address several QCD topics for which ALICE has complementary capabilities to the other LHC detectors. This thesis is based on the ALICE experiment described in detail in Section 4.2.

ATLAS (A Toroidal LHC ApparatuS) [56] and **CMS (Compact Muon Solenoid)** [57] are general-purpose proton-proton detectors designed to elucidate the nature of electroweak symmetry breaking for which the Higgs mechanism is presumed to be responsible and to shed light on new BSM theories, e.g. searching for SUSY particles and evidence of extra dimensions. Both detectors will also take part in the LHC heavy-ion program.

LHCb (Large Hadron Collider beauty experiment) [58] is a b-physics experiment, particularly aimed to precision measurements of CP-symmetry violation and rare decays of B hadrons.

LHCf (Large Hadron Collider forward experiment) [59] is dedicated to the measurement of neutral particles emitted in the very forward region of collisions in order to provide data for calibrating the hadron interaction models that are used in the study of high-energy cosmic rays. The detector is located closed to the ATLAS experiment.

TOTEM (TOTal Elastic and diffractive cross section Measurement) [60] measures the total proton-proton cross section, elastic scattering, and diffractive processes. The detector shares the same interaction point (IP5) with CMS.

4.1.2   Status of the LHC

LHC started on September 10, 2008 when proton beams were successfully circulated in both directions in the main rings for the first time. Unfortunately, on September 19, 2008 a serious fault between two dipoles occurred in Sector 34 during the 10 TeV magnet commissioning without beam [61]. This incident delayed LHC operations little more than a year.
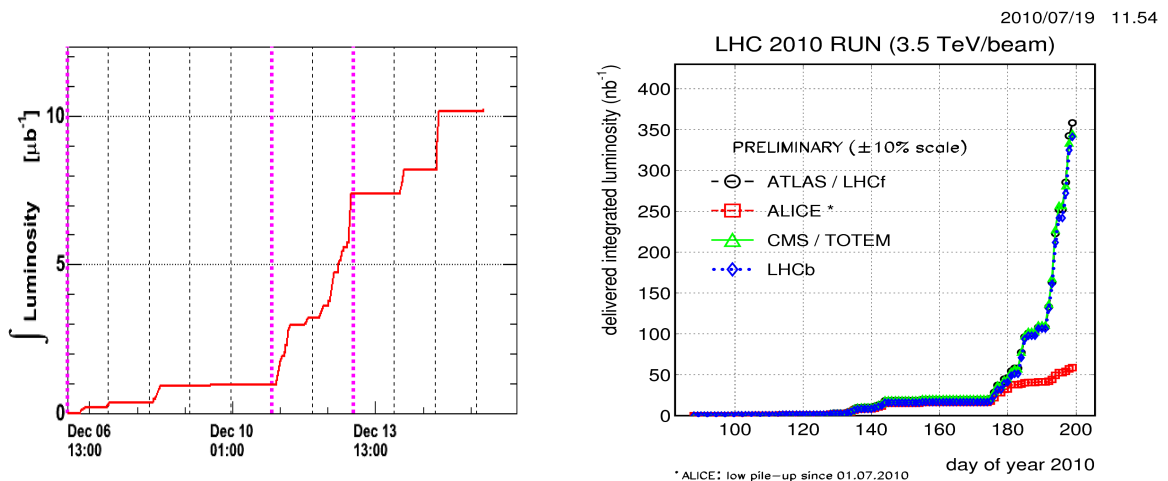
Figure 4.4: Left: Integrated luminosity recorded by ALICE for the $\sqrt{s} = 900$ GeV data collected during 2009. Right: Delivered integrated luminosity to the experiments at $\sqrt{s} = 7$ TeV until July 2010.

On November 20, 2009 bunches of protons circulated once again and the first pp collisions were recorded by the LHC detectors three days later at the injection energy of 450 GeV per beam. These first collisions were all obtained with a single bunch per beam at a bunch intensity of about 3×10^9 protons (the so-called "pilot bunches"). Even though a small data sample was acquired, this was enough for the ALICE collaboration to submit the first paper for publication. The collaboration analyzed the 284 events recorded on November 23, 2009 to measure the charged particle pseudo-rapidity density in the central region at $\sqrt{s} = 900$ GeV. The paper was accepted for publication two days later [62]. The

LHC became the world's highest-energy particle accelerator on November 30, 2009 when both beams were successfully accelerated to 1.18 TeV per beam. Between December 6 and 16, 2009 LHC delivered collisions at $\sqrt{s} = 900$ GeV and $\sqrt{s} = 2.36$ TeV with four bunches per beam at a bunch intensity typically of 5×10^9 protons and sixteen bunches per beam at a bunch intensity of 1.85×10^{11} per beam (only for a short period on December 15, 2009). The integrated luminosity recorded during the 2009 run by the ALICE detector is 11.2 μb^{-1} (see Fig. 4.4 left).

After the winter shutdown, the LHC was restarted and the first pp collisions took place on March 30, 2010 at $\sqrt{s} = 7$ TeV, half the maximum energy. The plan is to run with this energy for the next 18-24 months with the objective of delivering enough data (≈ 1 fb^{-1}) to the experiments to make significant advances across a wide range of physics channels [63]. Also the LHC heavy ion program should start at the end of 2010 when PbPb collisions at $\sqrt{s_{NN}} = 2.75$ TeV (same magnetic field as for proton beams) shall be delivered during four weeks [64]. Following these 18-24 months, the LHC will shutdown for routine maintenance, and to complete the repairs and consolidation work needed to reach its design energy of 14 TeV. The delivered integrated luminosity to the experiments at $\sqrt{s} = 7$ TeV until July 2010 is depicted in the right panel of Fig. 4.4.

4.2 The ALICE Experiment

ALICE (A Large Ion Collider Experiment) [52, 53] is a general-purpose, heavy-ion detector designed to study the strong interaction sector of the SM. The choice and design of ALICE was driven by the physics requirements as well as by the experimental conditions expected in nucleus-nucleus collisions at the LHC. Because of the extreme particle multiplicity expected in central nucleus-nucleus collisions at LHC energies, the design of ALICE was optimized for $dN_{ch}/d\eta = 4000$, but tested up to $dN_{ch}/d\eta = 8000$ [3]. Due to this very high particle density environment, ALICE has an efficient and robust tracking system over a large momentum range, from tens of MeV/c (soft physics) to over 100 GeV/c (jet physics). Also particle identification (PID) over much of this momentum range is achieved by employing essentially all known PID techniques: specific ionization energy loss dE/dx, time-of-flight, transition and Cherenkov radiation, electromagnetic calorimetry, muon filters, and topological decay reconstruction.

The ALICE detector is built and operated by a collaboration including over 1000 members from 111 institutes in 31 countries. It is 26 m long, 16 m high with a total weight of approximately 10000 t. The detector consists of a central barrel which measures hadrons, electrons, and photons, and a forward spectrometer for identification of muons. The central part covers $|\eta| < 0.9$ and is located in the L3-solenoid (inherited from the L3 experiment at LEP) which provides a magnetic field of up to 0.5 T and has an internal length of 12.1 m and a radius of 5.75 m. The barrel contains four detectors that cover the full azimuth (in order of increasing radii): an Inner Tracking System (ITS) made of three pairs of

---

[3]Recent extrapolations from RHIC measurements point to lower values of $dN_{ch}/d\eta = 1000 - 4000$ than previous estimated $dN_{ch}/d\eta = 2000 - 8000$ [53].
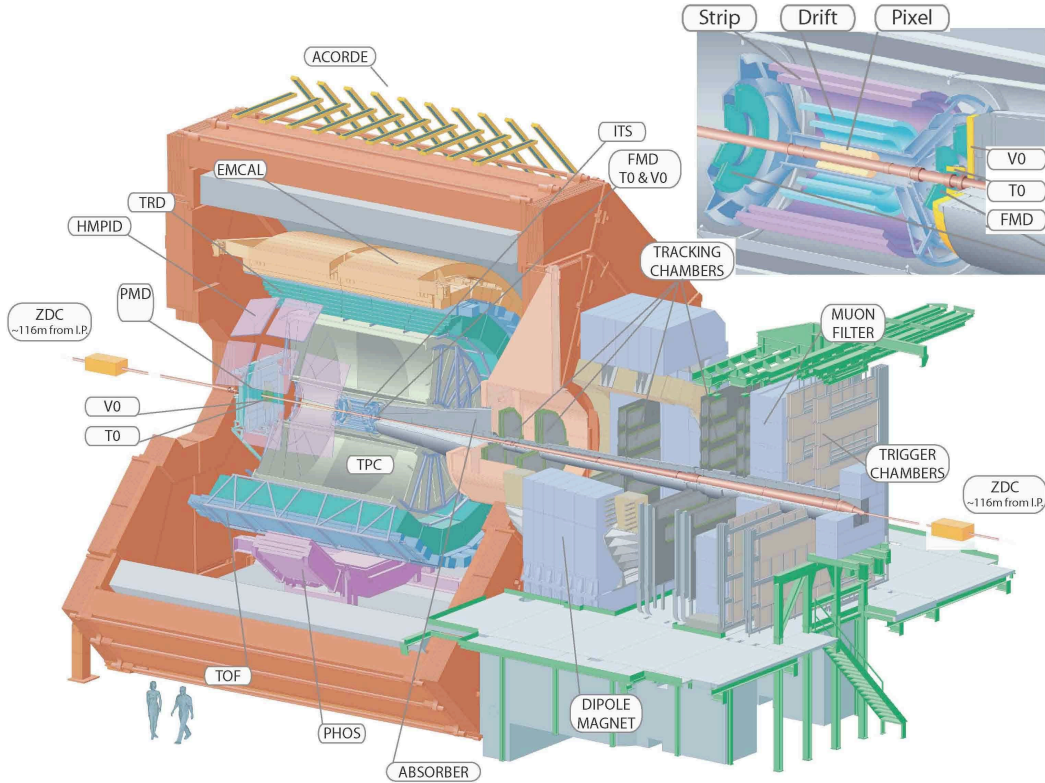
Figure 4.5: ALICE schematic layout.
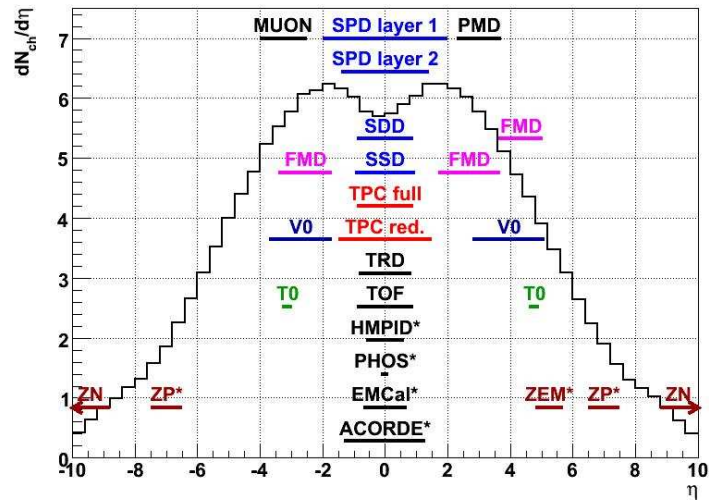
Figure 4.6: Pseudo-rapidity coverage of the ALICE detectors. The overlayed $dN_{ch}/d\eta$ prediction for pp collisions is given by PYTHIA (the pseudo-rapidity density for central PbPb collisions can be up to a factor 1000 larger). The detectors marked with an asterisk do not have full coverage in azimuth, while the two ranges given for the TPC depend on the track length. The detector abbreviations are defined in the next sections.

planes [4], a Time Projection Chamber (TPC), a Transition Radiation Detector (TRD), and a Time-Of-Flight (TOF) detector. It also contains three detectors with limited acceptance: the High-Momentum Particle Identification Detector (HMPID), the Photon Spectrometer (PHOS), and the Electromagnetic Calorimeter (EMCal). The Forward Muon Spectrometer covers $-4.0 < \eta < -2.5$ and consists of absorbers, a large dipole magnet, and fourteen planes of tracking and triggering chambers. Several smaller detectors (ZDC, PMD, FMD, T0, V0) in the forward regions are used for triggering and global event characterization. An array of scintillators (ACORDE) on top of the L3 magnet is used to trigger on cosmic rays. The apparatus is illustrated in Fig. 4.5, while Fig. 4.6 shows an overview of the η coverage of the ALICE systems.

4.2.1 Central detectors

Inner Tracking System (ITS)
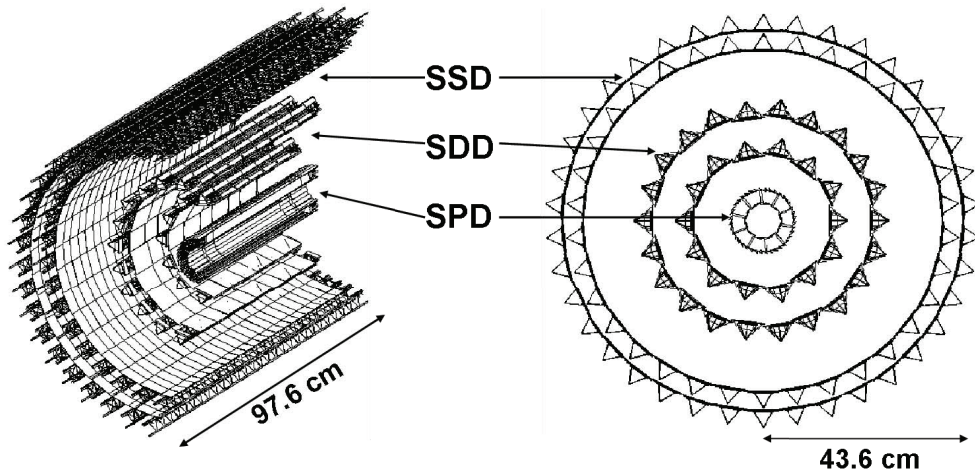
Figure 4.7: Schematic view of the ITS.

The ITS [65] is a cylindrically-shaped silicon tracker that surrounds the interaction region. As shown schematically in Fig. 4.7 it consists of six layers with radii between 3.9 cm and 43 cm and covers the pseudo-rapidity range $|\eta| < 0.9$. The two innermost layers have an extended pseudo-rapidity coverage ($|\eta| < 2$ and $|\eta| < 1.4$ for the first and second layer, respectively) that allows, together with the FMD (see Section 4.2.3), for a continuous measurement of charged particles multiplicity ($-3.4 < \eta < 5$). The number, position and segmentation of the layers were optimized for efficient track finding and high secondary vertex resolution. In particular, the outer radius is determined by the necessity to match tracks with those from the TPC, and the inner radius is the minimum allowed by the radius of the beam pipe (3 cm). The main tasks of the ITS are to reconstruct the primary vertex with a resolution better than 100 μm; to identify secondary vertices from

---

[4]High-resolution silicon pixel (SPD), drift (SDD) and strip (SSD) detectors

the decays of hyperons and heavy flavored hadrons (B and D mesons) with a resolution well below 100 μm due to the mean proper decay lengths of $c\tau \sim 100 - 500$ μm; to track and identify particles with momentum below 200 MeV/c; to improve the position, angle, and momentum resolution for tracks reconstructed in the TPC (see next section). By combining different silicon detector technologies, ITS features the high granularity and excellent spatial precision needed to achieve all the above requirements. Because of the high particle density expected in heavy-ion collisions (up to 50 particles per cm^2 have been predicted for the inner layer), the two innermost layers are equipped with Silicon Pixel Detectors (SPD), and the following two layers with Silicon Drift Detectors (SDD). For the outer two layers, where the track densities are below 1 cm^{-2}, double-sided Silicon micro-Strip Detectors (SSD) were chosen.

The SPD is based on hybrid silicon pixels, consisting of a two-dimensional sensor matrix (sensor ladder) of silicon detector diodes with a thickness of 200 μm bump-bonded to 5 readout chips. The sensor matrix has 256×160 cells, each measuring 50 μm by 425 μm. The number of readout chips is 1200 for a total of 9.8×10^6 channels. The readout is binary [5], thus SPD does not contribute to PID. But each chip provides a Fast-OR digital pulse when at least one pixel is hit, so SPD can be used as Level 0 trigger (see Section 4.2.4). The trigger signal is integrated over 100 ns by the SPD corresponding to one bunch crossing for heavy ions, or four bunch crossing in pp, therefore a coincidence between SPD and another detector (e.g. the V0) is needed to resolve the bunch crossing ambiguity.

The SDD was produced from a homogeneous high-resistivity 300 μm thick silicon. Each module is divided into two drift regions where electrons move in opposite directions under a drift field of ≈ 500 V/cm. In this way SDD exploits the measurement of the transport time of the charge deposited by a traversing particle to localize the impact point in one of the dimensions, thus enhancing resolution and multi-track capability at the expense of speed. All its 133000 channels have analog readout, thus the SDD can be used for PID via dE/dx measurement.

Table 4.2 summarizes some of the geometrical parameters of the layers (radial position, length along beam axis, number of modules, spatial resolution, and material budget). Another 1.3% of radiation length coming from thermal shielding and supports installed between different layers should be added to the values reported in the table, thus making the total material budget for straight tracks perpendicular to the detector surface equal to $\sim 7.66\%$ of X$_0$.

To achieve the precision requirements on the track parameters the misalignment spread in a given direction should be around 70% of the intrinsic sensor resolution along that direction. Using the intrinsic precisions listed in Table 4.2, the target residual misalignment spreads are: for SPD, 8 μm in x and 70 μm in z; for SDD, 25 μm in x and 18 μm in z; for SSD, 14 μm in x and 500 μm in z. Here x and z are the local coordinates of the sensor plane (see Appendix B). The first alignment was done using survey measurements as well as reconstructed tracks from cosmic ray events, about 10^5 charged tracks from cosmic rays that have been collected during summer 2008, with the ALICE solenoidal magnet switched

---

[5]A signal above a set threshold results in a logical 1.

Layer	Type	Number of modules	r (cm)	$\pm z$ (cm)	Resolution $r\phi \times z$ (μm^2)	Material budget X/X_0 (%)
1	pixel	80	3.9	14.1	12×100	1.14
2	pixel	160	7.6	14.1	12×100	1.14
3	drift	84	15	22.2	35×25	1.13
4	drift	176	23.9	29.7	35×25	1.26
5	strip	748	38.0	43.1	20×830	0.83
6	strip	950	43.0	48.9	20×830	0.86

Table 4.2: Characteristics of the ITS layers [53].

off and a special SPD trigger [66]. For SSD the residual misalignment after applying the survey corrections is negligible with respect to the intrinsic spatial resolution (about 20 μm) since the effective position resolution for a single point is estimated to be $\approx$ 18 μm. In the SPD case the effective spatial resolution was estimated to be about 14 μm compared to the intrinsic resolution of about 11 μm extracted from simulations with the ideal geometry of the ITS. This shows that the ITS alignment is comparable with the target values.

Time Projection Chamber (TPC)

The TPC [67, 68] is the main tracking detector of ALICE in the central barrel. It also provides particle identification using the specific energy loss. A detailed description including some of the design considerations, the layout, and the physics processes is given in Chapter 5.

Transition Radiation Detector (TRD)

The main purpose of the TRD [69] is to discriminate electrons from pions with high efficiency for momenta above 1 GeV/c. At the same time it contributes to tracking and can provide a trigger signal for charged particles with high momentum. The detector is based on the transition radiation (TR) that arises when a charged particle traverses the boundary of media with different dielectric constants. TR depends strongly on the particle's Lorentz factor γ, so only electrons produce TR for $1 < p < 100$ GeV/c. TR is photons with wavelengths in the soft X-rays region $(2 - 40$ keV) emitted at an angle approximately $1/\gamma$ with respect to the momentum vector.

TRD covers $|\eta| < 0.84$ and fills the radial space from 2.9 m to 3.68 m with an active length of 7 m in the longitudinal (z) direction. Following the segmentation in azimuthal angle of the TPC there are 18 sectors each with a 5-fold segmentation along z and 6 layers in radius ($18 \times 5 \times 6 = 540$ detector modules). A TRD module is illustrated in Fig. 4.8. Each module consists of a radiator of 48 mm thickness, a drift section of 30 mm thickness, and a multi-wire proportional chamber section (7 mm) with pad readout. The chambers are filled with a Xe/CO_2 gas mixture (85/15). Each chamber has 144 pads in ϕ and
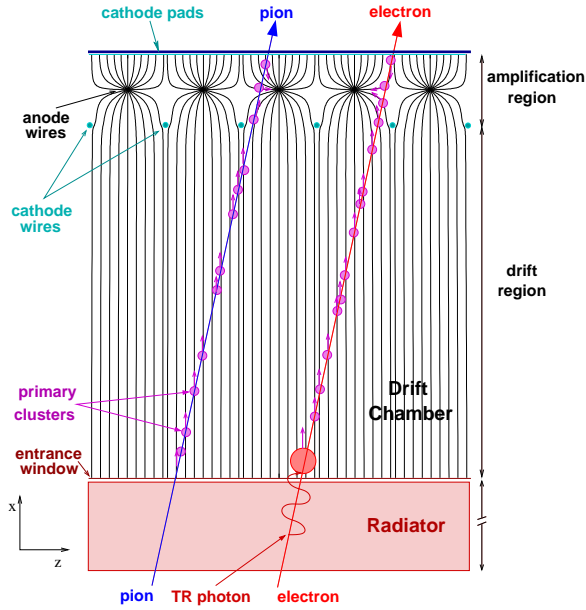
Figure 4.8: Sketch of a TRD module together with the clusters produced by a pion and electron track. The TR produced in the radiator is also illustrated [53].
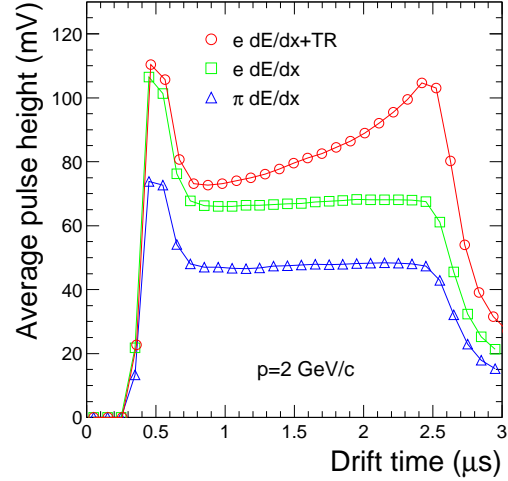
Figure 4.9: Average pulse height as a function of drift time for pions (blue triangles), electrons without TR (green squares), and electrons with TR (red circles). For the nominal drift field of 0.7 kV/cm, the detector signal is spread over about 2 μs [53].

between 12 and 16 pads rows in z which leads to a total of 1.18×10^6 readout channels. The TR produced in the radiator is efficiently converted by the high-Z counting gas (Xe) at the beginning of the drift region into an electron cluster which is subsequently detected. Figure 4.9 presents the measured average signals as a function of drift time for pions and electrons (with and without radiator) from test beam data (beam momentum of 2 GeV/c). The peak at small drift times originates from the amplification region, while the plateau is from the drift region. For the electrons, the contribution of TR, which is preferentially absorbed at the entrance of the detector (see Fig. 4.8), is evident when using a radiator (red circles). The position resolution is 400 μm ($r\phi$) and 2 mm (z) for momenta around 1 GeV/c and the momentum resolution is around 2.5-3% for momenta below 2 GeV/c [53].

Time-of-Flight Detector (TOF)

The TOF [70] covers $|\eta| < 0.9$ and is inscribed in a cylindrical shell with an inner radius of 3.7 m and an outer one of 3.99 m and a length of 7.41 m (active region). It consists of 18 sectors in ϕ each having 5 segments in z ($18 \times 5 = 90$ modules) of Multi-gap Resistive Plate Chambers (MRPCs). The MRPC (Fig. 4.10) is a double-stack of resistive glass plates separated by gas gaps defined by nylon fishing line. The central anode is a 122 cm long and 13 cm wide strip with two rows of pickup pads of 2.5×3.5 cm^2. Both
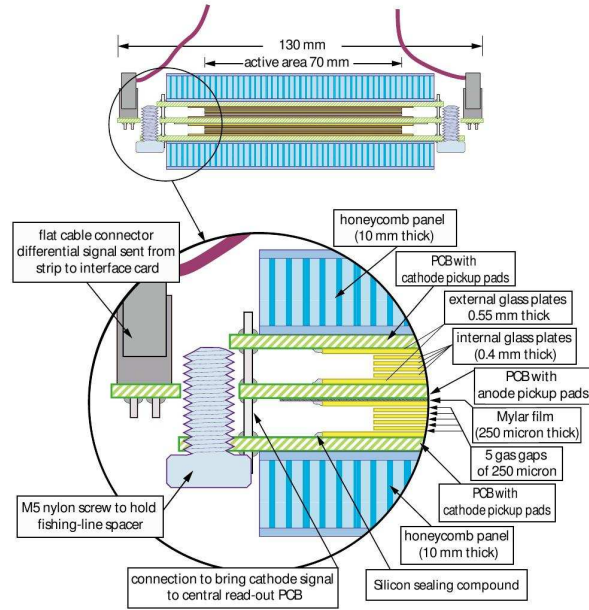
Figure 4.10: Schematic cross section of a 10-gap double-stack MRPC strip.
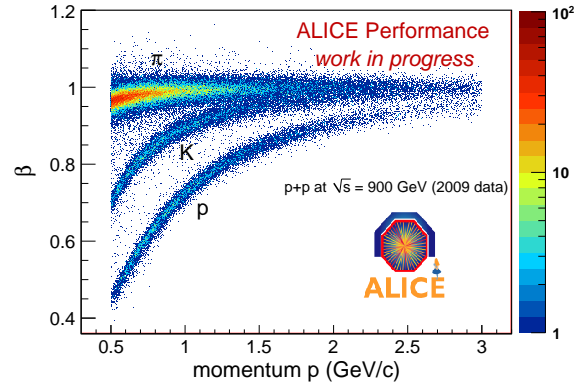
Figure 4.11: Particle velocity measured by TOF as a function of momentum from pp data collected during 2009.

outermost conductive plates serve as voltage cathodes; all non-conductive electrodes are floating (they achieve the correct voltage by electrostatic effect). When a charged particle passes the gaps, it produces clusters of primary ionization; due to the strong electric field, each of these clusters starts an avalanche. Since the intermediate resistive electrodes are transparent for the fast signals, the resultant signal is formed by the sum of all avalanches in the gaps. In order to minimize sparks and to maximize the probability for a particle to trigger an avalanche, the MRPC is filled with $C_2H_2F_4/C_4H_{10}/SF_6$ (90/5/5) gas mixture. The TOF detector has an active area of 140 m^2 and 157248 readout channels.

The detector is responsible for PID at the intermediate momentum range through time measurements matched with momentum of the particles. Using the difference between the arrival time of the particles in the detector and the time of the collision determined by T0 (see Section 4.2.3), a π/K (K/p) separation better than 3σ for $p < 2.5$ GeV/c ($p < 4$ GeV/c) was obtained for simulated data [71]. This separation is achieved due to its time resolution better than 40 ps (the overall resolution, including other uncertainties (e.g. the interaction time uncertainty) is better than 100 ps). Together with ITS and TPC, TOF will provide track-by-track identification of pions, kaons, and protons at low and intermediate momenta.

The identification of hadrons using TOF results from the difference in time-of-flight (t) for particles with the same momentum (p), but different mass (Fig. 4.11). The tracks reconstructed by ITS-TPC are propagated to TOF. TOF will give the time when the tracks are reaching the detector, while the track lengths (l) are calculated from momentum.

Knowing the collision time, the velocity of the tracks can be determined which permits the particle mass to be calculated as: $m^2 = p^2(\frac{t^2}{l^2} - 1)$.

High-Momentum Particle Identification Detector (HMPID)

The HMPID [72] is one of the detectors with partial acceptance and is dedicated to inclusive measurements of identified hadrons at $p_T > 1$ GeV/c. It is located at a radius of 5 m and covers $|\eta| < 0.6$ and $1.2° < \phi < 58.8°$ (5% of the central barrel geometry space). The detector consists of 7 modules of proximity-focusing Ring Imaging Cherenkov (RICH) counters with a total surface of about 11 m^2 which makes it the largest scale application of this technique. The principle of these detectors comes from the fact that a particle passing through a dielectric medium with a speed (β) greater than the speed of light in that medium will emit Cherenkov radiation in a cone at an angle of $\cos\theta = 1/n\beta$ (n is the refractive index of the medium) relative to the track direction. The correlation between the angle and the momentum allows for PID. HMPID extends ALICE's PID capability of π/K and K/p discrimination, on a track-by-track basis, up to 3 GeV/c and 5 GeV/c, respectively. Due to the small coverage this applies only for a small subset of tracks.

PHOton Spectrometer (PHOS)

The PHOS [73] is a high-resolution electromagnetic calorimeter with a limited acceptance at central rapidity. It allows ALICE to test the properties of the initial phase of the collision through low p_T direct photon measurements and the study of jet quenching by measuring high p_T π^0 and γ-jet correlations. The energy resolution is around $\sigma_E/E \approx 4\%$ for 1 GeV photons and the position resolution is measured to be $\sigma_{x,y}[\text{mm}] = \sqrt{3.26^2/\text{E(GeV)} + 0.44^2}$ [73]. The detector is situated in the bottom part of the ALICE setup, at 4.6 m from the interaction point, and covers $|\eta| < 0.12$ and $220° < \phi < 320°$ (3.7% of the available geometry space in the central region after its final installation). The PHOS is made of lead-tungstate crystals (PbWO$_4$) and readout by Avalanche Photo-Diodes (APD). In order to reject charged particles, a set of multi-wire proportional chambers is placed in front of the calorimeter at a distance of about 5 mm. This is called the Charged-Particle Veto (CPV) detector.

ElectroMagnetic CALorimeter (EMCal)

The EMCal [74] is a large Pb-scintillator sampling calorimeter located at a radius of ~ 4.5 m from the beam line. It covers $|\eta| < 0.7$ and $\Delta\phi = 107°$ (around 23% of the barrel geometry space), and is positioned approximately opposite in azimuth to the PHOS. It was added later to the experiment and its size was constrained by the available free space and the maximum weight which can be supported by the space frame (construction began in 2008). The detector measures direct and decay photons like the PHOS and enables ALICE to explore in detail the physics of jet quenching over a large kinematic range in heavy-ion collisions. The energy resolution of EMCal is measured to be $11\%/\sqrt{\text{E(GeV)}} \oplus 1.7\%$ and the

electromagnetic shower position resolution is described by $1.5\,\text{mm} \oplus 5.3\,\text{mm}/\sqrt{\text{E(GeV)}}$ [75]. The EMCal can provide a fast and efficient trigger (L0, L1) for hard jets, photons, and electrons based on sums of deposited energy (towers) in regions of the detector.

ALICE COsmic Ray DEtector (ACORDE)

The ACORDE is an array of 60 plastic scintillators placed on top of the L3 magnet at a radius of 8.5 m (Fig. 4.5). It covers $|\eta| < 1.3$ and $-60° < \phi < 60°$. The detector provides a fast L0 trigger signal, when atmospheric muons are crossing it, for the commissioning, calibration and alignment of the tracking detectors. Furthermore, it allows high-energy cosmic rays to be studied by detecting, in combination with the TPC, TRD and TOF, single atmospheric muons and multi-muons events (so-called muon bundles).

4.2.2 Muon Spectrometer

The Muon Spectrometer [76] was designed to measure the complete spectrum of quarkonia (i.e. J/ψ, ψ', Υ, Υ', Υ''), as well as the ϕ meson, in the $\mu^+\mu^-$ decay channel. In order to resolve the Υ states a resolution of 100 MeV/c^2 in the 10 GeV/c^2 dimuon invariant mass region is needed. In addition to vector mesons, the unlike-sign dimuon continuum can be investigated up to masses of around 10 GeV/c^2. At LHC energies the continuum will be dominated by muons from open charm and beauty decays, thus the production of open (heavy) flavors can also be studied with the muon spectrometer.

The spectrometer covers the polar angular range $171° < \theta < 178°$ which corresponds to the pseudo-rapidity range of $-4.0 < \eta < -2.5$ and has full azimuthal coverage for muons with $p > 4$ GeV/c (see Fig. 4.5). The momentum cut-off is due to the front absorber made predominantly of carbon and concrete to reduce the track density by absorbing hadrons and photons from the interaction vertex and which muons have to pass through to reach the spectrometer. The muons are measured by five tracking stations of two planes of high-granularity cathode pad chambers each and triggered by two stations with two planes of resistive plate chambers. A dipole magnet with a nominal magnetic field of 0.67 T (3 Tm integrated magnetic field) allows to evaluate the muon's momentum. Two tracking chambers are placed before the dipole magnet, one inside the magnet (in its center), and two behind. The trigger chambers, the last components of the spectrometer, are further protected by the muon filter, an iron wall of 1.2 m thick.

4.2.3 Forward Detectors

Forward Multiplicity Detector (FMD)

The FMD [77] consists of five rings of silicon strip detectors located at $z = 3.2$ m, 0.83 m, 0.75 m, -0.63 m, and -0.75 m. Its main task is to measured the charged-particle multiplicity in the pseudo-rapidity range $-3.4 < \eta < -1.7$ and $1.7 < \eta < 5.0$, in full

azimuth. Additionally, it allows to determine the reaction plane for each event in heavy-ion collisions and to study the multiplicity fluctuations on an event-by-event basis (due to the azimuthal and radial segmentation).

V0 Detector

The V0 [77] provides minimum bias triggers for the detectors located in the central barrel, estimates the centrality of the collision, rejects beam-gas events, and participates in the measurement of the luminosity. It is a small angle detector consisting of two arrays of scintillator counters, labeled V0A and V0C, segmented into 32 individual counters each arranged in four rings and eight sectors of 45°. The V0A is situated at $z = 3.4$ m ($2.8 < \eta < 5.1$) and the V0C at $z = -0.9$ m ($-3.7 < \eta < -1.7$), in front of the muon absorber. The time resolution is better than 1 ns and each counter provides time-of-flight and signal charge information.

T0 Detector

The T0 [77] was designed to measure the real time of the collision (needed by TOF to calculate the time-of-flight) and to determine the vertex position with a precision of about 1.5 cm. If the vertex position is within some preset values (where the interactions are expected) a L0 trigger is issued, whereas a vertex position outside these values is used to discriminate against beam-gas interactions. Furthermore, it can generate minimum bias and multiplicity triggers.

The detector is made of two arrays of twelve Cherenkov counters with quartz radiator each (called T0A and T0C) which are installed on either side of the ALICE interaction point. T0C is located at $z = -0.73$ m ($-3.28 \leq \eta \leq -2.97$), while T0A at $z = 3.75$ m ($4.61 \leq \eta \leq 4.92$). In the radial (transverse) direction both T0 arrays are placed as close to the beam pipe as possible to maximize triggering efficiency. The detector has a time resolution of about 50 ps (37 ps each counter) giving a vertex position resolution of 1.3 cm.

Photon Multiplicity Detector (PMD)

The PMD [78] measures the multiplicity and spatial ($\eta - \phi$) distribution of photons in the forward region ($2.3 \leq \eta \leq 3.7$, full azimuth). These measurements also provide estimations of the reaction plane in heavy-ion collisions on an event-by-event basis. The detector is situated at $z = 3.64$ m and consists of two gas proportional chambers (having a honeycomb structure and wire readout) with a lead converter in between them. The detector plane in front of the converter is used for vetoing charged particles and the other one, called pre-shower, is used to identify photons by their conversion in the lead plate.

Zero Degree Calorimeter (ZDC)

The ZDC [79] detects the number of spectator nucleons in heavy-ion collisions which is related to the energy carried in the forward direction (at 0° relative to the beam direction).

Thus the number of participant nucleons can be estimated as $N_{participants} = A - N_{spectators}$ and hence the centrality of the collision can be determined. ZDC, being a position-sensitive detector, can also give an estimate of the reaction plane in heavy-ion collisions. Finally, it can provide L1 triggers. The detector consists of two hadronic calorimeters, ZN (to measure neutrons) and ZP (to measure protons), and an electromagnetic calorimeter (ZEM). The hadronic calorimeters are located at 116 m on either side from the nominal interaction point. At this distance the spectator protons are spatially separated from neutrons by the magnets in the beam line; thus ZN is placed between the beam pipes at 0° relative to the LHC axis and ZP is placed externally to the outgoing beam pipe. ZEM is situated at $z = 7$ m ($4.8 < \eta < 5.7$) and allows to distinguish between central and peripheral heavy-ion events by measuring the total forward energy (since this energy is expected to increase monotonically with centrality).

4.2.4 Trigger System

ALICE has two trigger layers: the Central Trigger Processor (CTP) and the High-Level Trigger (HLT) [80]. CTP is a hardware trigger that combines information from different detectors in order to select events having a variety of different features at rates which can be scaled down to suit physics requirements and the restrictions imposed by the bandwidth of the Data Acquisition (DAQ) system. HLT is a logically hierarchical commodity cluster which can perform full event reconstruction. While CTP is responsible for the readout of the detectors, HLT is able to process the raw data in real time.

Central Trigger Processor (CTP)

The CTP is an electronic system which decides whether an event should be accepted (read out and saved) or rejected by combining inputs from different detectors. The input to the CTP is signals from triggering detectors (i.e. detectors which contribute with signals to the trigger) and the output by a command to read out detectors. The readout command signals are distributed to the detectors using the Local Trigger Unit (LTU). Due to the nature of the trigger inputs and the different event processing speed of various detectors, the ALICE trigger inputs are divided into three levels which have different associated latencies. The first level (L0) is delivered 1.2 μs after the collision takes place, the second one (L1) after 6.5 μs, and the final trigger (L2) after 100 μs, a value imposed by the TPC drift time. An event is finally stored only after a L2 accept trigger. Note that the CTP decisions are made in 100 ns, with the rest of the L0 latency coming from the generation time for the trigger input signals and from the cable delays.

The CTP can handled up to 24 L0, 24 L1, and 12 L2 trigger inputs; it means that 24 cables can physically be connected to the CTP (for the L0 trigger inputs propagation). But the trigger logic requires some restrictions, since a simple enumeration of all outcomes (look-up table approach) is not feasible, and only up to 50 trigger *classes* (logical conditions demanded for the inputs) can be defined. In addition to trigger classes, the CTP can handle up to 6 detector *clusters*. Each cluster contains a subset of the ALICE detectors and can

be defined at any time. The advantage is that while the slow detectors, e.g. TPC, are constrained to relatively low event rates, the fast detectors, e.g. SPD, can record events at much higher rates. For more informations see [80].

Other features of the trigger system are the continuous check of time separation of events and a dynamic suppression of common triggers.

The first one is achieved through the so-called *past-future protection* which limits/avoids pile-up events. So if there are some critical number of other events in some past or future time interval of the actual event, the event can be vetoed by the CTP. As different detectors are busy for widely different periods following a valid trigger, the past-future protection setting (a specified time window in which pile-up is recognized) depends on the detectors from the read-out cluster as well as the collision system. For example in heavy-ion collisions, for clusters in which the TPC is included only 2 additional peripheral events and no additional semi-central events are allowed in a time window of ± 88 μs centered on the event under consideration [53]. In *pp* collisions the pile-up in the TPC is inevitable and more pile-up events are tolerable due to the lower multiplicities than in heavy-ion collisions. However, a past-future protection for the ITS becomes useful as it provides a way to select the right events in the TPC (since ITS is only sensitive to events in a time window of 100 ns).

The second feature is fulfilled by adjusting the rates at which different trigger classes (running concurrently) are read out. The reduction of these rates can be done by applying downscaling factors to the trigger classes individually, i.e. only every nth event should be read out. Studies of the behavior of the trigger and DAQ systems have shown that temporary data storage in the DAQ can become saturated which affects rare processes. In order to avoid this problem all trigger classes are classified into common and rare triggers and a prioritization scheme is put in place: when the occupancy of the DAQ buffers exceeds a given threshold (high water mark), only rare triggers are accepted, and the common trigger are again enabled when the available temporary storage drops below the threshold (low water mark).

High-Level Trigger (HLT)

In order to meet the requirements regarding the luminosity, maximum detector readout rate, and limited storage rate and capacity a new trigger layer (HLT) sitting logically between the L2 and the event building was introduced. HLT is a PC farm of up to 1000 multi-processor computers which processes the data in parallel and allows an online analysis of the events. Based on this analysis a trigger decision is derived and the events can be accepted or rejected. Furthermore, HLT can reduce the stored data volume by selecting regions of interest (relevant parts of the event through a partial readout) and by applying compression algorithms on the accepted and selected data.

The HLT has a hierarchical structure for processing the data. The first layer receives the raw data of all ALICE detectors. Layer 2 performs basic calibration and extracts hits and clusters. Layer 3 reconstructs the event for each detector individually. The global reconstruction of the event is done by layer 4 which combines the processed and calibrated

information of all detectors. Layer 5 performs the selection of the events or regions of interest and, if the trigger decision is positive, the data is compressed and stored.
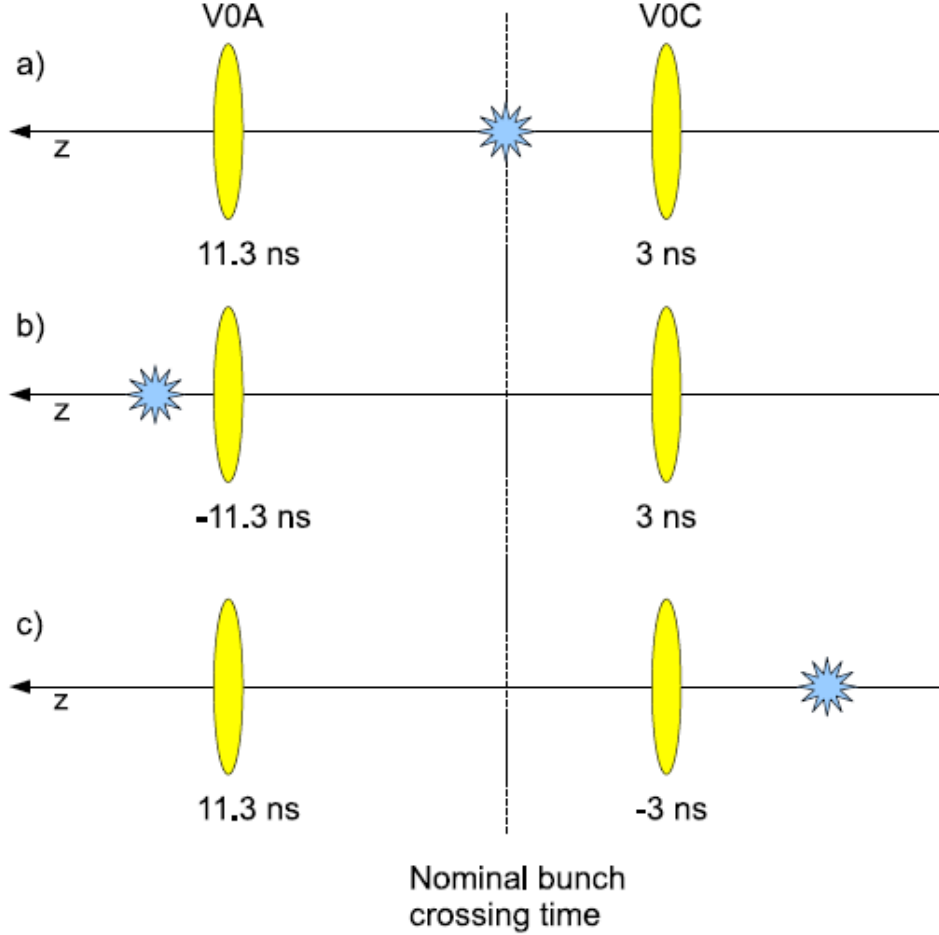
Figure 4.12: Beam-gas detection in V0. The particle arrival times on both sides of V0 are indicated with respect to the nominal bunch crossing time for normal interaction (a), beam gas events (b and c). The figure is taken from [81].

Minimum Bias Triggers

As discussed above different trigger classes can be configured by the CTP. All the events (simulated or real) used in this thesis were recorded using the minimum bias trigger MB1 (see below). Minimum bias triggers are designed to select all types of inelastic interactions with the requirement that they should impose the minimal bias on the event selection compared to all inelastic collisions. In ALICE, the SPD and V0 detectors are used to form the most effective minimum bias triggers [53]:

- MB1 = (V0or $\oplus$ SPDor) $\odot$ $\overline{\text{BEAMGASor}}$.

- MB2 = V0or $\odot$ SPDor $\odot$ $\overline{\text{BEAMGASor}}$.

- MB3 = V0and $\odot$ SPDor $\odot$ $\overline{\text{BEAMGASor}}$.

where the symbols $\oplus$ and $\odot$ indicate OR and AND, respectively and:

- V0or means a hit in the appropriate time window in either V0A or V0C.

- V0and means hits in the appropriate time window in both V0A and V0C.

- SPDor means at least one hit in the SPD.

- $\overline{\text{BEAMGASor}}$ indicates that a beam gas collision (collision between the particles of the beam and the molecules or atoms of the residual gas in the vicinity of the detector) was detected in the corresponding time windows for such collision on either side of V0 (see Fig. 4.12).

4.2.5   Offline Computing Framework

The ALICE offline framework (AliRoot) [82] is designed to handle all aspects of simulation, reconstruction, and data analysis in both pp and heavy ions environments. AliRoot is based on Object-Oriented technology and depends on the ROOT system [83]. It is entirely written in C++, with some external programs still in FORTRAN. The development of the ALICE computing framework started in 1998. It has extensively been used to optimize the design of the ALICE subsystems and to evaluate the physics performance of the full ALICE detector through simulation studies.
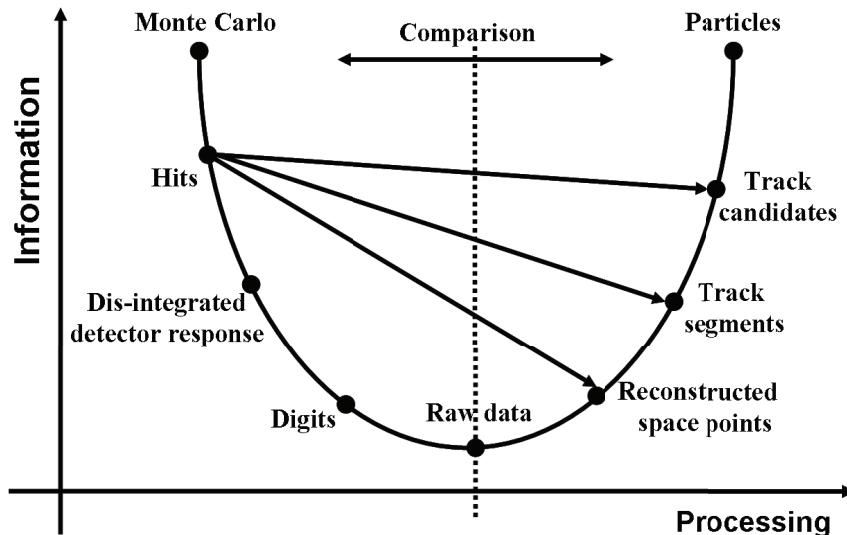
Figure 4.13: Data processing framework.

The functionality of the AliRoot framework is shown schematically in Fig. 4.13. Simulated data are generated via Monte Carlo (MC) event generators interfaced with AliRoot

(e.g. PYTHIA [31], PHOJET [84], HIJING [85]) which produce a set of "particles" with type, momentum, charge, and mother-daughter relationship forming the "kinematic tree". The generated particles are then transported through the detectors via detector simulation packages interfaced with AliRoot (e.g. GEANT3 [86], GEANT4 [87], FLUKA [88]) that produce "hits" (energy deposition at a given point and time) which are stored for each detector. The information is complemented by the so called "track references" corresponding to the location where the particles are crossing user defined reference planes. The hits are then transformed into ideal detector responses ("summable digits") which are further "digitized" by taking into account the associated electronics response function (noise). The transition from hits/tracks to digits/detectors is marked on the picture as "dis-integrated detector response"; only the labels are carrying the MC information now. Finally, the data is stored in the specific hardware format of each detector (raw data). From here on the processing of real or simulated data is indistinguishable. Now the reconstruction chain is activated. The detectors perform the clusterization (a local reconstruction done on the signals left in several parts or time bins of the detector by particles interacting with it) and then using a seeding procedure the particle trajectory is determined. The primary and secondary vertices are also found at this step. By comparing the reconstructed particles from simulated events with the MC generated ones, the software and the detector performance can be evaluated and the correction factors determined.

The output of the reconstruction is the Event Summary Data (ESD) containing the position of the primary vertex, the reconstructed charged particle tracks together with their PID information, secondary vertex candidates, particles reconstructed in the calorimeters. Subsequent data reduction to Analysis Object Data (AOD) will be performed. AODs are the objects that eventually will be used for analysis and can be standard (standard content condensed from ESDs) or specific to a given set of physics objectives (specific analysis). In this thesis the ESDs are used for analysis.

In a nominal running year ALICE should record 10^9 pp events and 10^8 heavy-ion collisions with an average raw size per event of ~ 1 MB (pp) and ~ 14 MB (PbPb) leading to a total raw data volume of 2.5 PB. The average size of an ESD is 40 kB for a pp event and 3 MB for a PbPb event. In order to understand the data a similar number of simulated events is expected (a factor 10 less for PbPb). The raw size for a simulated pp event is 400 kB and for PbPb is 300 MB; the ESD size per simulated event is 90 kB (pp) and 6 MB (PbPb). So the magnitude of the computing resources needed to store and process the data is such that it can not be concentrated in a single computing center. Therefore data storage and processing is distributed onto several computing centers located worldwide. But these distributed computing resources should work as an integrated computing center. This task is not easy and the solution was found to be the concept of the Grid [89]. At present around 90 centers, spread in more than 30 countries, are part of the ALICE Grid. All these centers are linked together by an ALICE specific Grid Middleware (software that implements the Grid concept) called AliEn [90]. The user interacts with the ALICE Grid via the AliEn User Interface, and services are provided by a combination of ALICE specific services offered by AliEn and basic services from the Middleware installed on the center.

4.2.6   ALICE Configuration during Data Taking, 2009-2010

During December 2009 and 2010 ALICE recorded pp collisions at $\sqrt{s} = 900$ GeV and $\sqrt{s} = 7$ TeV. At this stage most of the detectors were fully installed except the TRD (7/18 modules), EMCal (4/12 modules), PHOS (3/5 modules). Also HLT was only 60% equipped. In this configuration ALICE had full capabilities for hadrons and muons and partial for electrons and photons. Figure 4.14 shows a pp interaction at $\sqrt{s} = 7$ TeV recorded by the ALICE central barrel detectors on March 30, 2010.
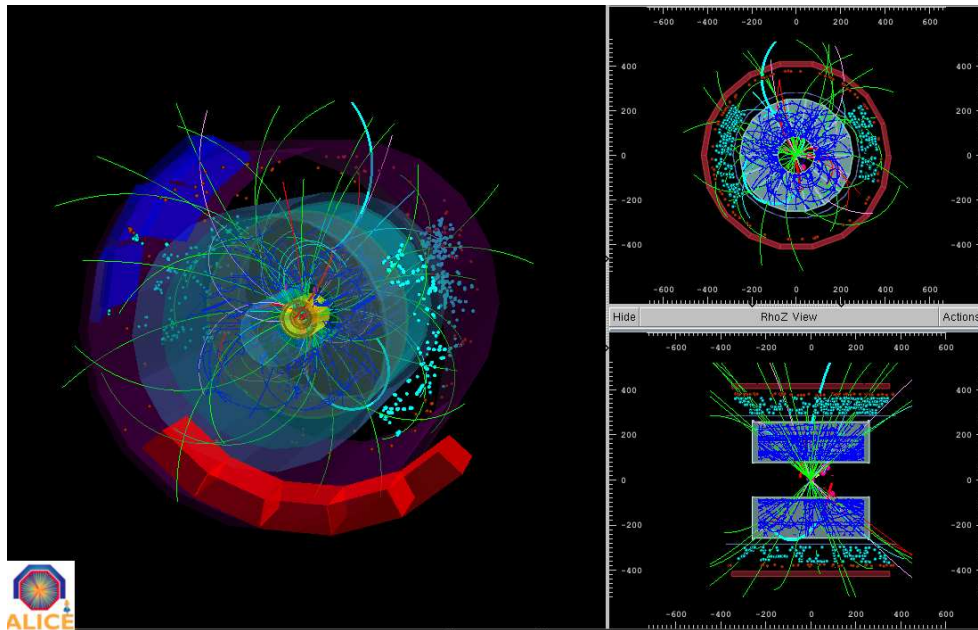
Figure 4.14: ALICE 3D and 2D views of the central barrel detectors of a real data event at $\sqrt{s} = 7$ TeV. The event was recorded on 30.03.2010 (run 114783, event 126).

Chapter 5

ALICE TPC

This chapter describes the ALICE Time Projection Chamber in detail. It is the main device for tracking of charged particles in the central part of the ALICE experiment. The design considerations, layout, and functional principle will be presented first. Then the focus will be on reconstruction and performance: the tracking procedure, how the signal is obtained, and the momentum determination.

5.1 Layout of the TPC

The TPC design was dictated by the extreme charged particle multiplicity predicted for central PbPb collisions at LHC energy, $dN_{ch}/d\eta = 8000$, which would result in about 20000 tracks (including secondaries) in the TPC acceptance. This implied a p_T resolution better than 1% (2.5%) for momenta below 2 (4) GeV/c, a dE/dx resolution better than 8%, and a two track resolution capable of separating tracks with a relative momentum difference below 5 MeV. The TPC is optimized to measure the tracks of the charged particles through the ionization electrons created when the particles are traversing a gas volume [67, 68]. As a consequence, particles lose an amount of energy per unit track length. Since the energy loss of the particles is type specific, the TPC can do PID through dE/dx measurements. By moving in a magnetic field, the momentum of the particles can be determined from the curvature of the tracks; the charge of the particles can also be deduced. Furthermore, the TPC can provide the interaction vertex.

The TPC is a cylindrical chamber with a volume of 90 m^3, filled with a Ne/CO$_2$/N$_2$ (85.7/9.5/4.8) gas mixture. Its active volume is defined by an inner radius of about 85 cm, an outer radius of about 250 cm, and an overall length along the beam direction of 500 cm. It covers the full azimuth (except 10% dead zones) and $|\eta| < 0.9$ for tracks with full radial track length (matches in other barrel detectors) and up to $|\eta| < 1.5$ for 1/3 radial length (at reduced momentum resolution and without matching with the outer detectors). The axis is aligned with the beams from the LHC and is parallel to the solenoidal magnetic field. The TPC has two main components: the field cage and the readout chambers (ROCs). The material budget of the TPC is around 3.5% of a radiation length near $\eta = 0$. A simplified
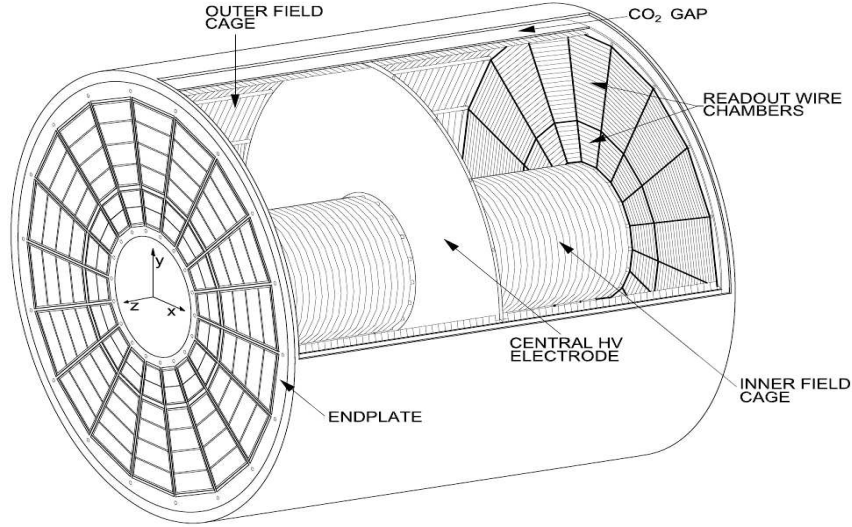
Figure 5.1: Layout of the TPC.

layout of the detector is shown in Fig. 5.1.

The field cage has a high voltage electrode in the middle of the detector and two opposite axial potential dividers. In this way a uniform electrostatic field needed by the ionization electrons to drift towards the ROCs without significant distortions (below 10^{-4}) is created. By applying a negative voltage of 100 kV on the central electrode, an electric field of 400 V/cm is obtained (the electric field runs parallel to the axis of the cylinder).

The ROCs are multi-wire proportional chambers (MWPCs) with a segmented cathode pad ('pad plane') (see Fig. 5.2). They are mounted into 18 trapezoidal sectors at each endplate. To account for the radial dependence of the track density ($\sim \frac{1}{r^2}$), the readout is segmented radially into inner (IROC) and outer (OROC) readout chambers with different pad sizes as well as wire geometries. The radial range of the active area is from 84.1 cm to 132 cm (IROC) and from 134.6 cm to 246.6 cm (OROC). By aligning the inactive areas between neighboring IROCs and OROCs the momentum precision for detected high p_T tracks is increased, but in 10% of the azimuthal angle the detector is non-sensitive. The total active area of the ALICE TPC readout chambers is 32.5 m^2 .

The MWPC has three wire planes: anode wires, cathode wires, and gating grid. All wires run in the azimuthal direction. The wire geometry as seen from the wire direction is depicted in Fig. 5.3. The anode wires are 20 μm thick and are set to a positive voltage of 1350 V (IROC) and 1550 V (OROC). The cathode plane separates the drift volume from the amplification region. It collects the ions produced during the avalanche, so the uniform drift electric field will not be distorted. The gating grid is an activation grid that allows the electrons from the drift volume to reach the amplification region when all the wires are held at the same potential V_G (the open gate mode). When is biased with a bipolar field ($V_G \pm \Delta V$) (the close gate mode) the drifted electrons can not reach the amplification volume and the ions created in the avalanche processes of previous events are trapped inside the MWPC region. The gating grid is normally closed and is opened only
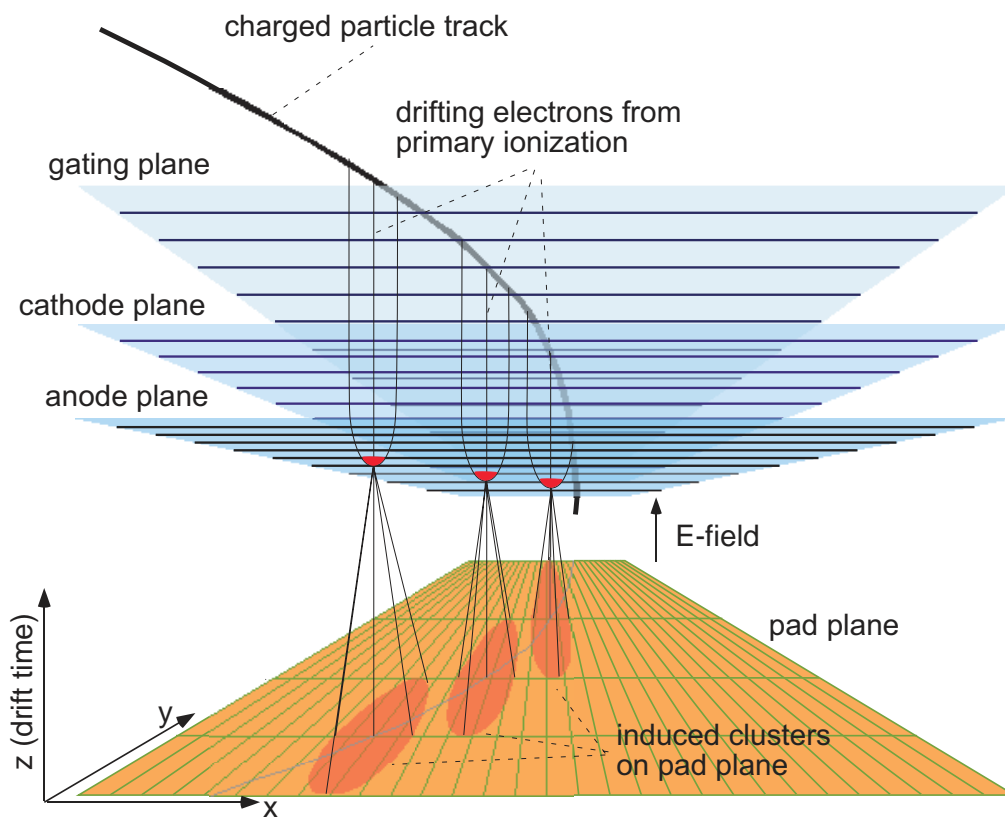
Figure 5.2: Schematic illustration of the working principle of a multiwire proportional chamber with segmented cathode.
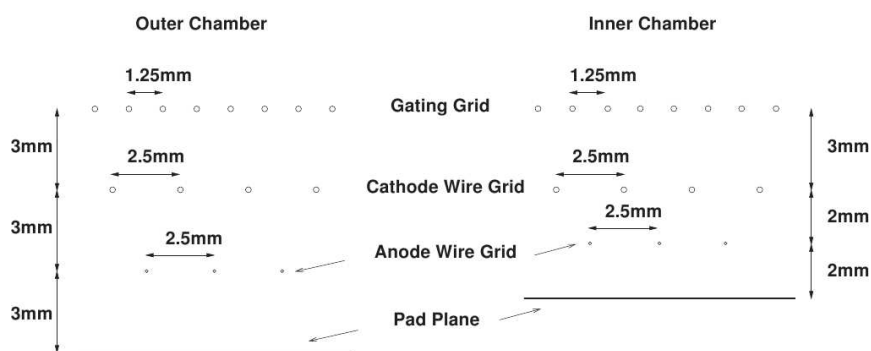
Figure 5.3: The wire geometry with respect to the pad planes for the outer (left) and inner (right) readout chambers [68].

by a L1 trigger (see Section 4.2.4) for the duration of one drift time interval, i.e. of about 90 μs.

The pad plane is a three layer printed circuit board with the pad structure etched onto its front side. The pads are connected by traces and plated trough holes to microconnectors on the opposite side of the board. It order to keep the occupancy as low as possible and to ensure the necessary dE/dx, position, and two track resolution, each sector has three pad sizes. The pads characteristics are given in Table 5.1. The pad size increases with radius in two steps following the radially decreasing track density. A pad row is defined as the pads at the same local x coordinate (see Appendix B).

Pad Type	Pad size (mm^2)	Number of rows	Number of pads per row
IROC (81.1 - 132.1 cm)	4×7.5	63	5504
OROC (134.6 - 198.6 cm)	6×10	64	5952
OROC (198.6 - 246.6 cm)	6×15	32	4072
Total		159	557568

Table 5.1: Characteristics of the TPC pad plane [68].

The drift gas was optimized for drift speed, low diffusion, low multiple scattering, small space-charge effect, stability properties. The Ne/CO_2 mixture is known to have a good electron mobility at high electrics fields, and is non-flammable. The drawback of this mixture is that the drift velocity (≈ 2.7 cm/μs) is strongly dependent on gas temperature, pressure, exact mixture at the nominal drift voltage. This makes it necessary to maintain a thermal stability of less than 0.1 K across the full volume of the TPC in order to exhaust the intrinsic detector resolution and to meet the desired physics performance. The N_2 was added to improve the stability of the readout chambers since it allows higher maximum gains (see next section). Furthermore, N_2 has a larger photon absorption cross section than CO_2 at the main excitation state of Ne; so N_2 supports CO_2 to quench this excited state. The O_2 impurity is about 1 ppm which implies that the absorption of electrons over the long drift length is minimum. The CO_2 and N_2 fractions are kept stable to 0.1% to ensure stable drift velocity and gas gain.

5.2   Functional Principle

A charged particle traversing the gas volume ionizes gas atoms along its flight path. The electrons created by the ionization process will drift in the electric field towards the pad planes. But the electrons are interrupted by collisions with gas molecules in their paths which limits the electron velocity to

$$u = \frac{eE}{m}\tau = \mu E \tag{5.1}$$

where e is the electron charge, m the electron mass, τ the average time between collision, E the electric field, and μ the electron mobility. This discontinuous motion appears macroscopically as a constant drift with the velocity u which results in a maximum drift time of about 90 μs. Another process that affects the electrons is the diffusion. A detailed description of drift properties in gases can be found in Appendix C.

When the drifted electrons are in the vicinity of the anode wire, as the the electric field close to the wire is proportional to $1/r$, they are accelerated to ionization energies, thereby secondary electrons are created. The released electrons themselves cause further ionizations, so an avalanche process starts and the number of electrons is increased by four orders of magnitude (2×10^4). This amplification, called *gas gain*, needs to be as stable as possible for the energy loss measurement. The avalanche and the ion movement induces a signal on the pads which is proportional to the number of primary electrons (since the MWPCs are operated in proportional mode). The signal is integrated over a characteristic period of time dictated by the time constants of the amplifier (chosen to match the time characteristic of the incoming cloud) and the signal voltage is measured at each time sample, called time bin. The location of the avalanche can be obtained from the induced signal. The x and y coordinates are given by the coordinate of readout pad where the signal was induced, while the z coordinate is determined by sampling the time distribution of the pad signal (knowing the drift velocity of electrons in the gas u and the drift time t, the z component is calculated as $z = u \cdot t$). A more precise measurement of the location of the avalanche can be obtained using an appropriate center of gravity (COG) algorithm. The resulting two-dimensional pulse height distribution in pad-time space is called a *cluster* (see Section 5.3.1).

5.3 Reconstructing Tracks in the TPC

In general, there are two large groups of tracking methods with advantages and inconveniences each: global and local methods.

The global methods (e.g. combinatorial methods, Hough transformation, templates, conformal mappings) require a precise global track model since all the track measurements are treated simultaneously and the selection of a track candidate is operated only after all the information about the track in known. The advantages of these methods are the stability with respect to noise and mismeasurements and the fact that they can operate directly on raw data. On the other hand, such track models are hard to determine (or even do not exist) because of the physical factors that can perturbate the model. In ALICE, they are used in the HLT software [91].

The local methods (e.g. Kalman filter) always estimate the track parameters 'locally' at a given point in space and the selection of a track candidate is performed using the information from that point or the information coming from the previous points in the iterative 'history' of this track. In this way all the local track peculiarities are taken into account and no global track model is needed. The disadvantages come from the space point reconstruction algorithms that the local methods rely on.

As discussed in Section 4.2 a good track-finding efficiency and reconstruction precision at very low p_T ($p_T \approx 100$ MeV/c) is required in ALICE. There are also rather big dead radial zones between the tracking detectors which complicates the extrapolation of a track from one detector to the other. Some of the ALICE tracking detectors (ITS, TRD) have a significant material budget, so the energy losses or the multiple scattering can not be neglected in the reconstruction. For all these reasons, ALICE has adopted for reconstruction the Kalman filtering approach.

The general strategy is to start with the cluster finding in all central detectors. Using the clusters reconstructed in SPD the position of the primary vertex is estimated and the track finding begins from the outer radius of the TPC where the track density is minimal. First, the track candidates ('seeds') are found and the tracking proceeds towards the smaller TPC radii in a Kalman filter way (see Section 5.3.2). When all the seeds are extrapolated to the inner limit of the TPC, the ITS takes over and tries to assign reconstructed ITS clusters to the TPC track candidates by prolonging them as close as possible to the primary vertex. When this is over, a special ITS standalone tracking procedure is applied to the remaining ITS clusters, trying to find the tracks that were missed by the TPC. At this point the tracking is repeated in the opposite direction (from primary vertex to the outer wall of the TPC) and the tracks are extrapolated to the TRD, TOF, HMPID, PHOS, and EMCal. Finally, all the tracks are refitted with the Kalman filter backwards to the primary vertex (or to the innermost possible radius, in the case of the secondary track).

The tracking in the TPC will be detailed in the following [1].

5.3.1   Cluster Finding in the TPC

As mentioned previously, before the tracking itself, two-dimensional clusters in the pad-row/time plane have to be found. The cluster finder algorithm loops over pads and time bins for any given pad row and searches for the local maxima in pad and time.

If there is only one local maximum, the algorithm assigns a region of 5×5 bins in z (time bin) and y (pad) directions around this maximum. The selected region is bigger than the typical size of a cluster ($\sigma \sim 0.75$ bins in both directions). The position of the corresponding space points, which is interpreted as the crossing point between the tracks projection and the centers of the pad rows, is reconstructed as its COG. In this way the local y and z coordinates are determined, while the x coordinate is given by the center of the pad row. If there are several local maxima (overlapped clusters), an unfolding procedure based on the fast spline method is applied by requiring charge conservation.

But the accuracy of COG as representing the track coordinate depends on diffusion, angular effect, gas gain fluctuation, and secondary ionization fluctuation. The diffusion smears out the position of the electron cloud according to a two dimensional Gaussian distribution with $\sigma_y^2 = D_T^2 L_{Drift}$ for the transverse direction and $\sigma_z^2 = D_L^2 L_{Drift}$ for the longitudinal direction (see Appendix C). The angular effect comes from the ionization electrons being uniformly distributed along the particle trajectory which implies that the

---

[1]The local coordinate system (see Appendix B) is used throughout this section.

projection itself must be uniformly distributed with a width L_a (valid for y and z positions since x is fixed to the middle of a pad row). The contribution to the cluster variance is given by the pad length L_{pad} and the angle α (resp. β):

$$L_a = L_{pad} \tan \alpha, \tag{5.2}$$

where α is the inclination angle between the track and the readout plane, while β is the angle between the tangent to the track projection to the pad plane and the pad rows (see Fig. 5.2). So the angles α, β give the track direction with respect to the pad plane and the pad orientation.

Considering the gas gain fluctuation factor G_g, the secondary ionization factor $G_{Lfactor}$, the electronic noise σ_{noise} and neglecting $\mathbf{E} \times \mathbf{B}$ [2] and unisochronity [3] effects (simulation indicates that these distortions are negligible compared with the others), the COG resolution parametrization appears as [92]:

$$\sigma^2_{z_{COG}} = \frac{D_L^2 L_{Drift}}{N_e} G_g + \frac{\tan^2 \alpha L_{pad}^2 G_{Lfactor}(N_{e_{prim}})}{12 N_{e_{prim}}} + \sigma^2_{noise} \tag{5.3}$$

$$\sigma^2_{y_{COG}} = \frac{D_T^2 L_{Drift}}{N_e} G_g + \frac{\tan^2 \beta L_{pad}^2 G_{Lfactor}(N_{e_{prim}})}{12 N_{e_{prim}}} + \sigma^2_{noise} \tag{5.4}$$

where N_e is the total number of electrons in the cluster (Landau distributed) and $N_{e_{prim}}$ is the number of primary electrons in the cluster (described by a Poisson distribution). One needs both values since not all the electrons produced in the same cluster are collected in the same pad row, because of diffusion. The factor $1/12$ comes from the variance of the uniform distribution of the electrons along the track.

In order to use Eqs. 5.3 and 5.4, the number of electrons should be estimated from their proportionality to the total measured charge A in the cluster. But an empirical parametrization of the factors $G(N)/N = G(A)/(kA)$ gives better results [92]. The error parametrization becomes:

$$\sigma^2_{z_{COG}} = \frac{D_L^2 L_{Drift}}{A} \cdot \frac{G_g(A)}{k} + \frac{\tan^2 \alpha L_{pad}^2}{12A} \cdot \frac{G_{Lfactor}(A)}{k_{prim}} + \sigma^2_{noise} \tag{5.5}$$

$$\sigma^2_{y_{COG}} = \frac{D_T^2 L_{Drift}}{A} \cdot \frac{G_g(A)}{k} + \frac{\tan^2 \beta L_{pad}^2}{12A} \cdot \frac{G_{Lfactor}(A)}{k_{prim}} + \sigma^2_{noise} \tag{5.6}$$

Here k and k_{prim} are free parameters.

Finally, a simple additional correction for the cluster shape and overlap factor is used:

$$\sigma_{COG} \rightarrow \sigma_{COG}(A) \times \left(1 + const \times \frac{RMS_m - RMS_e}{RMS_e} \right), \tag{5.7}$$

where $\sigma_{COG}(A)$ is calculated according to Eqs. 5.5 and 5.6, RMS_m is the measured r.m.s., and RMS_e is the expected parametrized r.m.s. of the cluster (see Ref. [92]).

---

[2]Discussed in Appendix C

[3]Different arrival times of electrons at the wires owing to different trajectory lengths near the wires depending on the arrival position.

5.3.2   Kalman Tracking in TPC

Since the x coordinate of the intersection point of a track and a pad row is fixed to the center of that pad row, the y and z coordinates can be expressed as [91, 92]:

$$y(x) = y_0 - \frac{1}{C}\sqrt{1 - (Cx - \eta)^2} \tag{5.8}$$

$$z(x) = z_0 - \frac{\tan\lambda}{C}\arcsin(Cx - \eta) \tag{5.9}$$

where C is the curvature of the track projection on the pad plane, thus the radius is $R = 1/C$ (see Fig. 5.4), λ is the angle of the trajectory with respect to the pad plane (the so-called 'dip' angle), (x_0, y_0) are the coordinates of the center of the curvature of the track projection on the pad plane, z_0 is defined as $z_0 \equiv z(x_0)$, and $\eta \equiv Cx_0$.

The track is regarded as a dynamical system, which evolves from point to point. So the filter uses starting track candidates with a few parameters (seeds) and tries to associate new track points to these candidates with the help of the determined parameters. Whenever possible, the track parameters are more and more refined as the tracking progresses. The main component of the filter is the so-called 'state vector'. The state vector used in the Kalman-filter calculations performed for TPC tracking is:

$$\mathbf{x} = (y,\ z,\ C,\ \tan\lambda,\ \eta). \tag{5.10}$$

This is the starting point of the tracking algorithm. The Kalman filter estimates the state vector and predicts the next coordinate measurement (within a certain error) and the covariance matrix. Let $\mathbf{x}_k$ be the state vector evaluated at pad row k. The state vector varies according to a evolution equation:

$$\mathbf{x}_k = f_k(\mathbf{x}_{k-1}) + \boldsymbol{\epsilon}_k, \tag{5.11}$$

where f_k is a linear transformation since the TPC measurements are discrete and $\boldsymbol{\epsilon}_k$ is an error vector which has a zero mean value ($\langle \boldsymbol{\epsilon}_k \rangle = 0$) and a known covariance matrix ($\mathrm{cov}(\boldsymbol{\epsilon}_k) = \mathbf{Q}_k$). Bold letters denote vectors and large bold letters denote matrices. Generally, the measurement performed by the detector is only a function of the state vector (a projection). This function is assumed to be a linear transformation of the state vector, denoted by the matrix $\mathbf{H}_k$, and the measurement at a given point $\mathbf{m}_k$ is corrupted by the error vector $\boldsymbol{\delta}_k$:

$$\mathbf{m}_k = \mathbf{H}_k\mathbf{x}_k + \boldsymbol{\delta}_k. \tag{5.12}$$

Again, the error vector is supposed to be unbiased ($\langle \boldsymbol{\delta}_k \rangle = 0$) and have a definite covariance matrix ($\mathrm{cov}(\boldsymbol{\delta}_k) = \mathbf{V}_k$). The filter estimates the state vector using a given number of intersection points. This estimation depends on the accuracy of the determination of the cluster positions. If the track points were identified precisely, the filter is then able to effectively predict the state vector at the next intersection point, using the covariance matrices and the calculated linear transformations. The only components of the state vector which will change as the track is propagated from one pad row to another are the

local track position y and z; C, $\tan\lambda$, η are track specific. It should also be noted that when a track is leaving one sector and is entering another, the coordinate system is rotated by $20°$, thus changing the y, z and η components of the state vector.

Considering $\mathbf{x}_k$ the true state vector at pad row k and $\widetilde{\mathbf{x}}_k^i$ the estimated state vector at pad row k evaluated using data from pad rows 0 to i, two cases that characterize the Kalman filter can be applied to the TPC:

- Prediction ($i < k$): the state vector at next pad rows is predicted using information from all the previous pad rows. This is used to limit the search area for a following track point, and for propagation of a given track into another TPC sector.

- Filtering/Update ($i = k$): the state vector is evaluated at any given pad row using the information from all the previous pad rows. In this case $\widetilde{\mathbf{x}}_k^k \equiv \widetilde{\mathbf{x}}_k$.

Let $\widetilde{\mathbf{C}}_k^i = \mathrm{cov}(\widetilde{\mathbf{x}}_k^i - \mathbf{x}_k)$ be the covariance matrix of the difference between the estimated state vector and the true vector at a given pad row and $\mathbf{R}_k^i = \mathrm{cov}(\mathbf{r}_k^i)$ the covariance matrix of the measurement residual defined as $\mathbf{r}_k^i = \mathbf{m}_k - \mathbf{H}_k\widetilde{\mathbf{x}}_k^i$ (the difference between the predicted measurement vector at pad row k and the obtained one at the given intersection point). For $i = k - 1$, all $k - 1$ pad rows are used, the predicted state vector at pad row k can be evaluated together with the covariance matrix by means of formulas:

$$\widetilde{\mathbf{x}}_k^{k-1} = f_k(\widetilde{\mathbf{x}}_{k-1}) \tag{5.13}$$

$$\widetilde{\mathbf{C}}_k^{k-1} = \mathbf{F}_k\widetilde{\mathbf{C}}_{k-1}\mathbf{F}_k^T + \mathbf{Q}_k, \quad \mathbf{F}_k = \frac{\partial f_k}{\partial\mathbf{x}_{k-1}}. \tag{5.14}$$

Using the predicted measurement residual and the corresponding covariance matrix,

$$\mathbf{r}_k^{k-1} = \mathbf{m}_k - \mathbf{H}_k\widetilde{\mathbf{x}}_k^{k-1} \tag{5.15}$$

$$\mathbf{R}_k^{k-1} = \mathrm{cov}(\mathbf{r}_k^{k-1}) = \mathbf{V}_k + \mathbf{H}_k\widetilde{\mathbf{C}}_k^{k-1}\mathbf{H}_k^T \tag{5.16}$$

the predicted χ^2 increment can also be calculated:

$$\left(\chi^2\right)_k^{k-1} = \left(\mathbf{r}_k^{k-1}\right)^T \left(\mathbf{R}_k^{k-1}\right)^{-1} \mathbf{r}_k^{k-1}. \tag{5.17}$$

When the intersection point between the track and the TPC in pad row k is predicted and the results of the state vector measurement are also known (filtering), the estimation of the state vector improves according to:

$$\widetilde{\mathbf{x}}_k = \widetilde{\mathbf{x}}_k^{k-1} + \mathbf{H}_k\left(\mathbf{m}_k - \mathbf{H}_k\widetilde{\mathbf{x}}_k^{k-1}\right) \tag{5.18}$$

$$\widetilde{\mathbf{C}}_k = \mathrm{cov}(\widetilde{\mathbf{x}}_k - \mathbf{x}_k) = \widetilde{\mathbf{C}}_k^{k-1} - \mathbf{K}_k\mathbf{H}_k\widetilde{\mathbf{C}}_k^{k-1} \tag{5.19}$$

where $\mathbf{K}_k = \widetilde{\mathbf{C}}_k^{k-1}\mathbf{H}_k^T \left(\mathbf{V}_k + \mathbf{H}_k\widetilde{\mathbf{C}}_k^{k-1}\mathbf{H}_k^T\right)^{-1}$ is the Kalman gain matrix. The transformation (Eq. 5.18) needs to correct the update of the predicted state vector, so that the

mean square error of the state vector components is minimized which is the standard fitting requirement. This implies that the covariance matrix given by Eq. 5.19 should be minimized.

The measurement residual after the filtering and the corresponding covariance matrix,

$$\mathbf{r}_k = \mathbf{m}_k - \mathbf{H}_k \widetilde{\mathbf{x}}_k \tag{5.20}$$

$$\mathbf{R}_k = \mathbf{V}_k - \mathbf{H}_k \widetilde{\mathbf{C}}_k \mathbf{H}_k^T \tag{5.21}$$

allow the determination of the filtered χ^2 increment:

$$\chi_k^2 = (\mathbf{r}_k)^T (\mathbf{R}_k)^{-1} \mathbf{r}_k. \tag{5.22}$$

The dimension of the vector $\mathbf{m}_k$ gives the number of degrees of freedom. It can be shown that the predicted χ^2 value is equal to the filtered one: $(\chi^2)_k^{k-1} = \chi_k^2$. In this way one can simultaneously do tracking and fit the track. By rejecting track points with a χ^2 increment above a certain threshold both tracking and fitting are improved. So, for a given track, the number of found clusters can differ from the number of the assigned clusters.
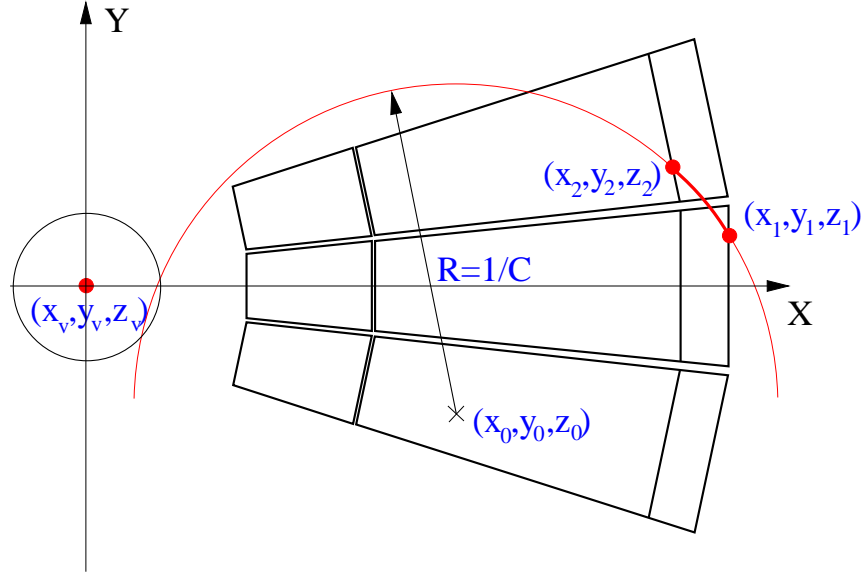
Figure 5.4: Schematic view of the seeding with the vertex constraint. The track finding coordinate system as well as track parameters are also visible. Figure taken from [91].

Seed Finding

In order to do reasonable tracking using the Kalman filter a good initial approximation for the track variables of the state vector is needed. These initial points are called seeds and the TPC is the only detector in ALICE able to provide them properly. There are two different seeding strategies: with and without primary vertex constraint.

The seed finding with vertex constraint is done first. A schematic illustration of the algorithm is depicted in Fig. 5.4. It starts with a search for pairs of clusters in two pad rows, numbered i and j ($i - j \approx 20$) with initial track parameters allowing to be projected to the primary vertex. For each point in the outer pad row i there is a limited search area in the inner pad row j; the area is defined by a p_T cut which gives a search window in the (x, y) plane and by the requirement of pointing to the primary vertex which gives a window in the z direction. In this way the number of possible combinations is significantly reduced. The primary vertex is reconstructed with high precision from hits in the SPD.

When two reasonable points are found, the algorithm calculates the parameters of a helix going through these points and the primary vertex (see Fig. 5.4) which are used to search for another cluster near the crossing point of this helix and a middle pad row $k = j + (i - j)/2$. If this is found, the parameters are used as initial state vector for the potential track and the corresponding covariance matrix is evaluated by using the point pair errors and applying big errors to the position of the primary vertex. The Kalman filter starts from the outer point of the pair to the inner one. If at least half of the pad rows between i and j contains track points which are successfully associated with this track candidate, it is saved as a seed and another pair of initial points is searched.

Although the algorithm is very efficient for primary tracks (around 90% for primaries with $p_T > 200 \, \text{MeV/c}$ [91]), it suppresses secondary tracks. For these tracks, two algorithms without vertex constraint have been developed. Only one will be presented here; the second one is described in Ref. [91]. For each cluster at a given pad k, the algorithm finds the two nearest clusters at the pad rows $k - 1$ and $k + 1$ and does a linear fit. This line is prolonged to the pad rows $k + 2$ and $k - 2$ and the clusters nearest to the fitted line are found. When seven clusters are assigned to the track candidate, the linear fit is replaced by polynomial and continues until the pad rows i and j are reached. If more than a half of the possible clusters are found, the track candidate is saved as a seed, later to be Kalman filtered starting from the outermost pad row inwards.

A quality parameter defined by the normalized χ^2 and the ratio of the found clusters to the possible clusters (possible clusters are the track crossings with the pad rows when the track is not in a dead zone) is introduced for the reconstructed tracks. A distribution of the quality parameter is then obtained and the mean value and the sigma is calculated. If the quality parameter of a given track falls within 3σ from the mean value, the clusters associated with this track can not be used in the subsequent seedings.

Track Following

After seeding, several track candidates are tracked in parallel using the following procedure:

- The prolongation to the next pad row is found for each track candidate according to the actual estimation of the track parameters. Multiple scattering and mean energy loss assuming that the actual particle is a pion are also taken into account during this step.

- The nearest cluster is found on this pad row by defining a 'window' along the pad direction with the width set to $\pm 4\sigma$ (σ is calculated taking into account the track and cluster position errors) and comparing the clusters within the window.

- Estimate the cluster position errors from the track and cluster parameters and accept it if the residuals in both directions are smaller than the estimated 3σ.

- Update the track parameters and their covariance matrix. If the track enters another TPC sector the track parameters and the covariance matrix are recalculated (rotated) in order to be always expressed in the local coordinate system of the sector containing the track.

- Stop tracking not active candidates.

- Follow down to the innermost TPC pad row or until the seeded track is lost.

- Remove track candidates which share too many clusters using the 'track overlap factor' defined as the ratio of the clusters shared between two track candidates and the number of all clusters. If the overlap factor is bigger than a certain value, the track candidate with the higher χ^2 or lower number of assigned clusters is removed.

5.4   The TPC Signal

5.4.1   Energy Loss of Charged Particles

Electrically charged particles traversing a gas lose their energy mainly by ionization or excitation of electrons of the atoms in the gas. The mean rate of energy loss (or stopping power) is given by the Bethe-Bloch formula [9]:

$$-\left\langle \frac{dE}{dx} \right\rangle = K z^2 \frac{Z}{A} \frac{1}{\beta^2} \left[\frac{1}{2} \ln \frac{2 m_e c^2 \beta^2 \gamma^2 T_{max}}{I^2} - \beta^2 - \frac{\delta(\beta\gamma)}{2} \right], \tag{5.23}$$

where $K = 4\pi N_A r_e^2 m_e c^2$, r_e and m_e are the classical radius and mass of the electron, N_A Avogadro's number, Z and A the atomic number and atomic mass of the material, z and β the electric charge and the relativistic velocity of the incident particle, $\gamma = 1/\sqrt{1 - \beta^2}$, I the mean ionization potential of the material, T_{max} the maximum kinetic energy that can be given to a free electron in a single collision which, for a particle of mass M, is given by

$$T_{max} = \frac{2 m_e c^2 \beta^2 \gamma^2}{1 + 2\gamma m_e/M + (m_e/M)^2} \tag{5.24}$$

and becomes $T_{max} = 2 m_e c^2 \beta^2 \gamma^2$ for $M \gg m_e$ (the so-called "low-energy" approximation).

The term $\delta(\beta\gamma)$ represents a density effect correction and is relevant for particles with $\beta\gamma \gg 3$. It arises due to the polarization of the atoms along particle path which shields the field of the traveling particle [9]. So the electrons far from the path of the particle

will therefore contribute less to the total energy loss and this must be corrected for. The density effect correction $\delta(\beta\gamma)$ is given by the Sternheimer formula [93]:

$$\delta = \begin{cases} 0 & X < X_0 \\ 4.6052X + C + a(X_1 - X)^m & X_0 < X < X_1 \\ 4.6052X + C & X > X_1 \end{cases}, \tag{5.25}$$

where $X = \log_{10}(\beta\gamma)$. The quantities X_0, X_1, C, a and m depend on the material, the corrections being larger for condensed materials than lighter substances such as gases [9]. This comes from the fact that the parameter C scales with the plasma frequency of the material $h\nu_p$

$$C = - \left(2\ln\frac{I}{h\nu_p} + 1 \right) \tag{5.26}$$

which is proportional to the density of electrons N_e:

$$\nu_p = \sqrt{\frac{N_e e^2}{\pi m_e}}, \qquad N_e = \frac{N_A \rho Z}{A}. \tag{5.27}$$

Even though a small dependence on M is introduced through T_{max} at high energies, for all practical purposes the dE/dx given by Eq. 5.23 depends on β only. Conventionally it is a function of $\beta\gamma = p/Mc$. Equation 5.23 is valid for $0.1 \lesssim \beta\gamma \lesssim 1000$ since at the lower limit the velocity of the incident particle becomes comparable with the atomic electron "velocity" and at the upper limit radiative losses start to be important (1% at around 10 Gev for muons) [9].

The mean energy loss for muons, pions, and protons in different materials measured as a function of the particle momentum and $\beta\gamma$ is shown in Fig. 5.5. As can be seen from the figure at low velocities dE/dx is dominated by the overall $1/\beta^2$ factor and is steeply decreasing with increasing velocity until about $\beta \approx 0.97$, where a minimum is reached. Note that the broad minima around $\beta\gamma \simeq 3$ is roughly independent of material. Particles in this region are usually termed "minimum ionizing particles" (MIPs). As the momentum increases beyond this point, the term $1/\beta^2$ is almost constant and dE/dx grows as $\ln\beta\gamma$ since T_{max} increases as $\beta^2\gamma^2$ due to (rare) large energy transfers to a few electrons. This region is known as the *relativistic rise*. Restricting the energy transfer to $T \leq T_{cut} \leq T_{max}$, so excluding events with large energy transfers, the truncated mean energy loss reads:

$$-\left.\frac{dE}{dx}\right|_{T<T_{cut}} = Kz^2\frac{Z}{A}\frac{1}{\beta^2}\left[\frac{1}{2}\ln\frac{2m_e c^2 \beta^2\gamma^2 T_{cut}}{I^2} - \frac{\beta^2}{2}\left(1 + \frac{T_{cut}}{T_{max}}\right) - \frac{\delta}{2}\right]. \tag{5.28}$$

In this case the $\beta\gamma$ term producing the relativistic rise is replaced by a constant (T_{cut} replaces T_{max}), and $dE/dx|_{T<T_{cut}}$ reaches a constant value, the so-called *Fermi plateau*. As $T_{cut} \to T_{max}$, the truncated mean energy loss (Eq. 5.28) approaches the Bethe-Bloch function (Eq. 5.23).

The dE/dx in a thin material as given by Eq. 5.23 is governed by large fluctuations due to the limited number of ionizations, excitations, and large energy transfer events. Even
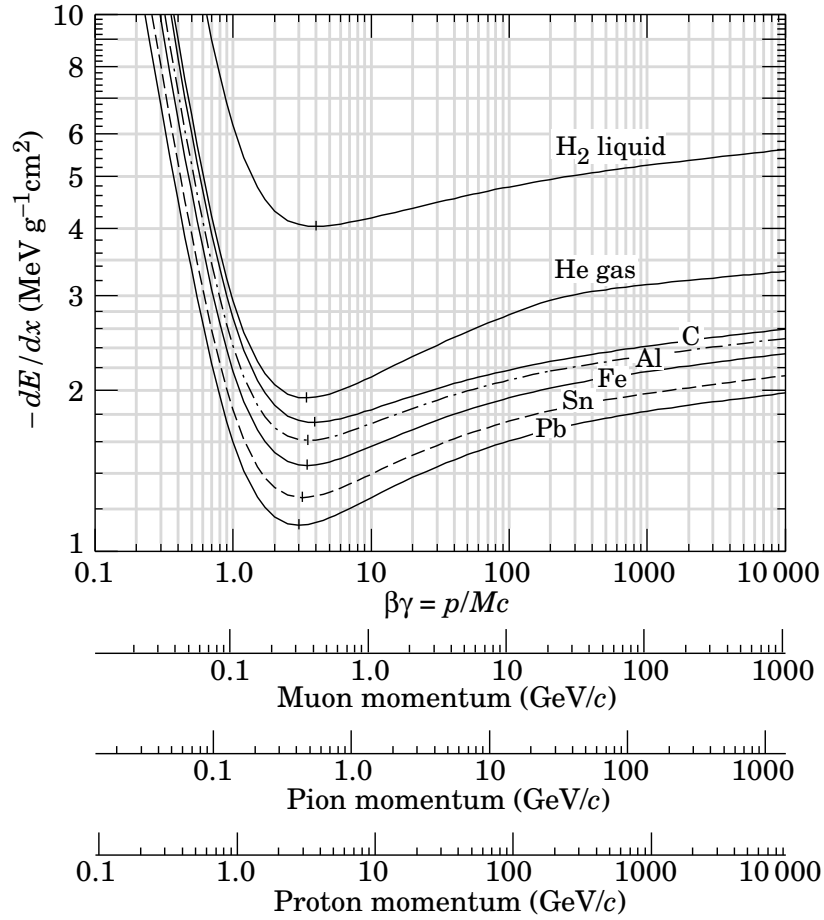
Figure 5.5: Mean energy loss as a function of $\beta\gamma$ for pions, muons, and protons in different materials (omitting radiative effects) [9].

with hundreds of dE/dx samples measured in a track a proper value for the mean energy loss can not be determined. These fluctuations are not Gaussian but are asymmetric with a high energy loss tail due to the large single-collision energy transfers discussed above, giving rise to a Landau distribution [94]. Different methods have been investigated to overpass this difficulty and the best and easiest way is to calculate the most probable energy loss (usually its value is below the mean given by the Bethe-Bloch equation).

Considering Δ the energy losses of a particle traversing a gas volume of thickness x, the energy loss probability distribution $f(\Delta; \beta\gamma, x)$, customarily called "straggling function", is given by:

$$f(\Delta; \beta\gamma, x) = \frac{\phi(\lambda)}{\xi}, \tag{5.29}$$

where $\xi = (K/2) \langle Z/A \rangle (x/\beta^2)$ and the Landau distribution $\phi(\lambda)$:

$$\phi(\lambda) = \frac{1}{\pi} \int_0^\infty e^{-u\ln u - u\lambda} \sin \pi u\, du \approx \frac{1}{\sqrt{2\pi}} e^{-\frac{1}{2}(\lambda + e^{-\lambda})}, \quad \lambda = \frac{\Delta - \Delta_{MP}}{\xi}. \tag{5.30}$$

Here λ is defined to be the normalized deviation from the most probable energy loss, Δ_{MP} [95]:

$$\Delta_{MP} = \xi \left[\ln \frac{2mc^2\beta^2\gamma^2}{I} + \ln \frac{\xi}{I} + j - \beta^2 - \delta(\beta\gamma) \right]. \tag{5.31}$$

The parameter j is 0.200 [95] and Δ_{MP}/x scales as $a\ln x + b$ [96].

5.4.2 Signal Determination

The ALICE TPC can perform PID through the measurement of the ionization of the charged particles traversing the gas volume. The dE/dx for a given track must be extracted from the number of clusters, n_{cl}, assigned to the particle track ($50 < n_{cl} < 159$) [68]. The charge deposited in the clusters is related to the dE/dx and the maximal charge Q_{max} (the highest ADC value) or the total charge Q_{tot} can be determined for each cluster. The question of whether the dE/dx information should be extracted from Q_{max} or Q_{tot} is still under discussion. Results presented here are based on evaluations from Q_{tot}, but for the high multiplicity environment expected in heavy-ions collisions Q_{max} may be more adequate since it is less sensitive to the cluster overlaps.

The cluster charge straggling function is determined for each track, but its mean value is not a good estimator due to the fluctuations of long tail towards higher energy losses as could be seen from the previous section. The truncated mean distribution, S, also called the TPC signal, is used instead. At present, S is derived track by track by discarding 2% of the smallest cluster charge values and 40% of the largest ones and averaging the remaining cluster charges [97], but different values used in the determination of S were investigated in the past (see Section 8.2.3). The distribution of S for many particles of the same $\beta\gamma$ is almost a perfect Gaussian distribution. The variance of the Gaussian distribution of S is called the energy loss resolution, $\sigma_{dE/dx}$, and depends on the number of clusters in a track. From now the TPC signal from a track, S (the truncated mean), will be called dE/dx of a detected particle.

The dE/dx Parametrization

Figure 5.6 shows the TPC signal of charged particles versus their rigidity from the $\sqrt{s} = 900$ GeV data. Characteristic bands for electrons, pions, kaons, protons, deuterons can clearly be observed. Different parametrizations can be used to describe the dE/dx. ALICE has adopted the parametrization proposed by the ALEPH experiment of the form [98]:

$$f(\beta\gamma) = \frac{P_1}{\beta^{P_4}} \left(P_2 - \beta^{P_4} - \ln \left(P_3 + \frac{1}{(\beta\gamma)^{P_5}} \right) \right), \tag{5.32}$$
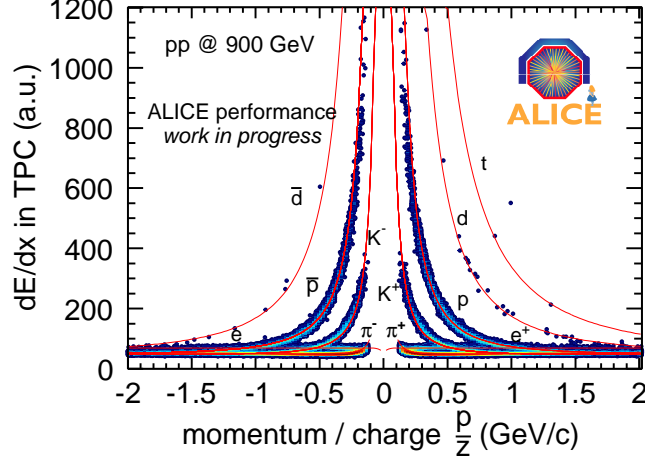
Figure 5.6: dE/dx for charged particles versus the rigidity from the $\sqrt{s} = 900$ GeV data. The curves correspond to the ALEPH parametrizations of the dE/dx (see text).

where β can be expressed using $\gamma = 1/\sqrt{1 - \beta^2}$ as

$$\beta = \frac{\beta\gamma}{\sqrt{1 + (\beta\gamma)^2}}. \tag{5.33}$$

The ALEPH parametrizations for each particle type are shown as lines in Fig. 5.6. For the ALICE TPC, the parameters were found to be: $P_1 = 0.028$, $P_2 = 26.34$, $P_3 = 5.041 \times 10^{-11}$, $P_4 = 2.125$, $P_5 = 4.887$. These parameters are different from the ALEPH TPC ones since the Ne-based gas mixture used by ALICE differs from the gas mixture of the ALEPH TPC (90% Ar and 10% CH_4). They are determined from a fit with the best possible precision. The fit procedure is presented in [99]. But other, simple parametrizations are often used.

The dE/dx Resolution

The important quantity for PID purposes is the energy loss resolution, $\sigma_{dE/dx}$. For a perfect gain calibration, it depends on the number of clusters, n_{cl}, the pad length, l, and the gas pressure, p. The resolution is not expected to depend drastically on the pad length, as long as the total length of the measured track, i.e. $n_{cl} \times l$, is constant. The width of the ionization distribution (which together with the cluster size defines the energy loss distribution) is inversely proportional with the product lp [68]. For the n_{cl} dependence a statistical scaling according to the law $\sigma_{dE/dx} \propto 1/\sqrt{n_{cl}}$ is expected. This will not be the case since the straggling functions are subject to large fluctuations due to the high energy loss tails. Allisson and Cobb [100] proposed an empirical relationship between dE/dx resolution and n_{cl} and l:

$$\frac{\Delta dE/dx}{dE/dx} = \frac{0.96}{2.35} n_{cl}^{-0.46} l^{-0.32}. \tag{5.34}$$

In addition, systematic uncertainties will also influence the dE/dx measurements. Therefore, the overall resolution is assumed to be [68]

$$\sigma^2_{dE/dx}(n_{cl}) = \sigma^2_{syst} + \frac{\sigma^2_{stat}}{n_{cl}}.$$ (5.35)

The dE/dx resolution dependence on the number of clusters assigned to cosmic tracks is shown in Fig. 5.7. As can be seen from the figure, $\sigma_{dE/dx}$ reaches 5% for cosmic tracks with 159 clusters, which is slightly better than the design value of 5.5% as specified in the TPC Technical Design Report (TDR) [67]. More details on how the $\sigma_{dE/dx}$ is extracted can be found in [99].
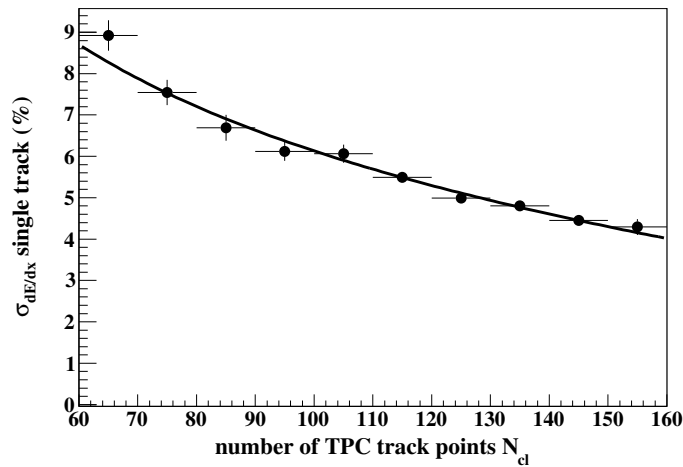
Figure 5.7: $\sigma_{dE/dx}$ dependence on the number of clusters assigned to cosmic tracks. The solid line is a fit of the function defined by Eq. 5.35. Picture taken from [68].

5.5 Momentum Measurement

Since the TPC is embedded in a magnetic field B parallel to the electric field, the transverse momentum of any charged particle traversing the gas volume can be determined through the curvature C of the track projection on the pad plane provided by the x and y coordinates measured by the readout chambers (see Section 5.3.2), according to:

$$p_T \text{ (GeV/c)} = 0.3 \cdot \frac{B}{C} \text{ (Tm)}$$ (5.36)

The transverse momentum error is given by the azimuthal resolution of a single space point, $r\delta\varphi$, calculated in the local frame which approximates the particle trajectory with a parabola. It can be described by [101]:

$$\frac{\Delta p_T}{p_T^2} = \frac{r\delta\varphi}{0.3 \cdot B \cdot L^2}\sqrt{\frac{720}{n_{cl} + 4}}$$ (5.37)

where L is the total visible track length and n_{cl} denotes the number of track points. Whereas B and L are given by the overall design of the ALICE TPC, the azimuthal position resolution $r\delta\varphi$ is influenced by [98]:

- The amount of ionization contributing to the individual space point measurements.

- The diffusion broadening of the electron cloud during drift.

- Fluctuations in the gas amplification of single electrons, which effectively enhance the delocalization caused by diffusion by a factor $\sqrt{2}$.

- $\mathbf{E}$ and $\mathbf{E}\times\mathbf{B}$ effects due to the non-homogeneity and non-parallelism of the fields.

All these effects will disturb the momentum resolution. Also a poor track point determination, as will be the case for high momentum particles, leads to a worse momentum resolution. For a perfect track of 1.5 m length, creating track points in every pad row (159) with an uncertainty $r\delta\varphi = 1$ mm and propagating in a magnetic field of 0.5 T, Eq. 5.37 gives $\Delta p_t/p_t^2 \approx 0.007$ (GeV/c)$^{-1}$. The transverse momentum resolution of the TPC determined from cosmic ray tracks by comparing the momenta for the first and second half of each track is depicted in Fig. 5.8. As can be seen from the figure, a transverse momentum resolution of better than 7% is reached at 10 GeV.
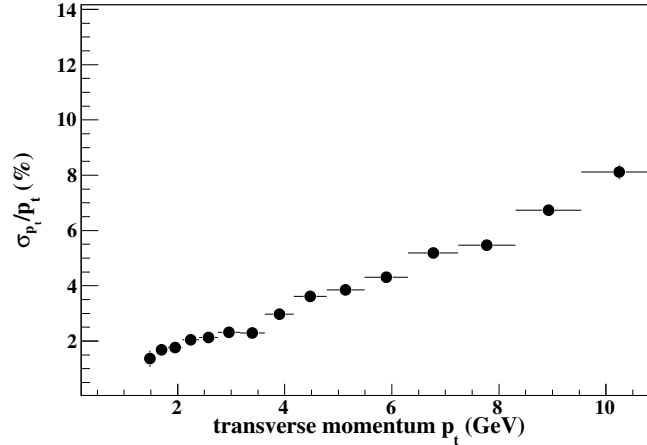

Figure 5.8: Transverse momentum resolution measured with cosmic rays. Figure taken from [68].

Chapter 6

Heavy Stable Hadrons

This chapter is devoted to the motivation to search for heavy stable particles predicted by some extensions of SUSY. These particles could be sufficiently long-lived as to be directly detected at colliders. The chapter starts with a brief review of the theoretical motivations for performing such a search and a description of the available scenarios. Then the production mechanisms at LHC energies will be addressed. The techniques used in heavy stable particle searches and the existing mass limits are described in the end.

6.1 SUSY Prediction for LHC

Chapter 2 has shown that SUSY is an attractive theory which can solve the hierarchy problem, unify the coupling constants, and give a viable dark matter candidate. But it should also be clear that SUSY parameter space is vast and many theoretical scenarios are available in the SUSY framework. In most of these models, the suggested new physics searches focus on the decay products of short-lived SUSY particles and the weakly interacting dark matter candidates, assumed stable, appear only as missing energy signatures. However, several extensions of SUSY predict the existence of exotic, heavy long-lived particles, which can be directly detected through their interactions with matter. In this thesis a heavy stable particle is a particle which does not decay during its passage through the detector. Although heavy stable particles recur in many extensions of the SM, the emphasis will be on SUSY models and only a short description of other scenarios will be presented here. An excellent review of the theoretical models in which such states appear can be found in Ref. [102].

Before going into the description of concrete scenarios, let's briefly address the possible mechanisms behind the stability of new heavy particles and the best way to do this is to look at the SM. It provides different types of stable or long lived particles (electrons, muons, protons, neutrons) which illustrate various ways of stability mechanisms:

- Conservation of quantum numbers.

- Suppressed coupling.

• Limited (or absent) decay phase space.

The electron can not decay to neutrinos due to the conservation of the electric charge, while the proton decay is forbidden by the conservation of lepton and baryon number. In the second mechanism metastability comes about through small couplings to kinematically allowed decay products. This is the case of muon whose long lifetime arises due to the hierarchy between the muon mass and weak scale ($\Gamma_\mu \propto m_\mu^5/m_W^4$). The long lifetime of the neutron is explained by the big difference between the neutron mass and the available kinetic energy of 0.8 MeV to decay. Clearly all these mechanisms can be used to provide heavy stable particles. In addition, other mechanisms that are not seen in the SM have been proposed: topological defects, like cosmic strings or magnetic monopoles. The most used way to induce stability is done implying a new state that carries a new conserved (or almost conserved) global symmetry. The lightest state will be stable and one or more higher states may also be stable or meta-stable.

6.2   Theoretical Scenarios with Heavy Stable Hadrons

6.2.1   SUSY Models

Due to the large parameter space, the general MSSM allows for any sparticle to be a heavy stable particle. However, more specific models have individual heavy stable candidates. In AMSB scenarios the chargino has usually been considered as a heavy particle. Due to the gaugino mass hierarchy ($M_2 \ll M_1 \ll M_3$), the lightest neutralino, wino-like, becomes the LSP and the lightest chargino, also dominantly wino, can be long-lived [103]. A phenomenological study of the minimal AMSB model can be found in Ref. [104]. In GMSB and SUGRA models, the gravitino is the LSP and any sfermion Next-to-Lightest Supersymmetric Particle (NLSP) should decay to the gravitino, and may thus naturally be metastable due to the small effective coupling to the gravitino. As discussed in Section 2.5, the GMSB suppression is given by the effective SUSY breaking scale, while in SUGRA models the suppression is set by the reduced Planck mass ($M_P = 2.4 \times 10^{18}$ GeV/c^2). This leads to a great range of possible decay lengths for a sfermion NLSP. In GSMB scenarios the decay length of a slepton NLSP is [25]

$$c\tau_{NLSP} = 0.1 \left(\frac{100\text{GeV}}{m_{NLSP}}\right)^5 \left(\frac{m_{\widetilde{G}}}{2.4\text{eV}}\right) \text{mm}, \tag{6.1}$$

with $m_{\widetilde{G}}$ given by Eq. 2.22. For Planck scale SUSY breaking the lifetime of the NLSP is obtained by substituting $m_{\widetilde{G}}$ with $\sqrt{3}m_{3/2}M_P$ in the above equation. A SUGRA model with a long-lived $\tilde{\tau}$ can be found in Ref. [105]. In some extensions of the GMSB scenario the gluino becomes light, and often the LSP [106]. There are also string inspired models in which the gluino is the LSP, the so-called O-II orbifold model [107].

Split SUSY is an interesting model that has gained a lot of interest in the past years, since it predicts a long-lived gluino. A gluino can only decay via squarks, but as the squark
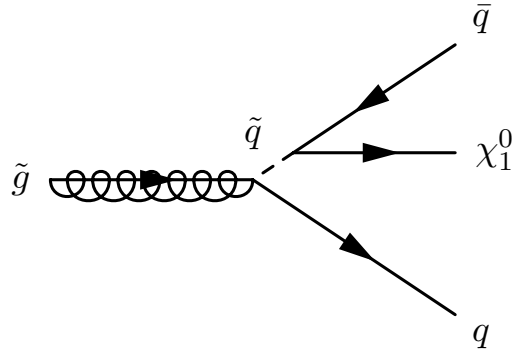
Figure 6.1: Schematic illustration of the gluino decay into a quark-antiquark pair and the LSP through a virtual squark in Split SUSY scenarios.

is very heavy in Split SUSY ($m_{\tilde{q}} \gg 1$ TeV/c^2) and the gluino is much lighter than the squark ($m_{\tilde{g}} \ll 1$ TeV/c^2) the gluino decay is suppressed and can only happen via a virtual squark (to preserve color). In this situation gluinos can undergo 3-body decays into two quarks plus a neutralino or chargino (see Fig. 6.1) or radiative 2-body decays to a gluon and a neutralino. Explicit calculations of the decay width and branching ratios of the gluino in Split SUSY can be found in Ref. [108]. A very simplified treatment of the gluino lifetime will be given next having as starting point the generic Feynman diagram illustrated in Fig. 6.1.

Lets consider p the 4-momentum of the gluino, k_1 and k_2 the 4-momenta of the quarks, k_3 the 4-momentum of the neutralino, and Q the momentum transferred to the virtual squark. At the vertices there are factors $\sim g_s C_1$, $\sim g_{\tilde{f}} C_2$, while the propagator is $1/(Q^2 - m_S^2)$. Here C_1, C_2 are constants, g_s is the strong coupling constant, $g_{\tilde{f}}$ is the coupling constant between the neutralino and the quark. The momentum given to the virtual squark will not be larger than the mass of the gluino, since it provides all the energy for the decay, so Q^2 is very small compared to m_S^2 and can be neglected. This leads to the amplitude:

$$M \simeq \frac{C}{m_S^2}, \tag{6.2}$$

where C is a constant that combines C_1, C_2, g_s, and $g_{\tilde{f}}$.

The decay rate for a particle at rest is given by [8]:

$$d\Gamma = \frac{1}{2m_i} \left(\prod_f \frac{d^3 p_f}{(2\pi)^3} \frac{1}{2E_f} \right) |M(m_i \to p_f)|^2 (2\pi)^4 \delta^{(4)}(p_i - \sum p_f), \tag{6.3}$$

where the p_i and m_i is the momentum and the mass of the initial particle, respectively; p_f and E_f the momentum and energy of the final states.

In order to estimate $d\Gamma_{\tilde{g}}$, the absolute square of the matrix element summed and averaged over spins, $\overline{|M|^2}$, is needed. Since M is dimensionless, $\overline{|M|^2} = C^2 m_{\tilde{g}}^4/m_S^4$. Thus the

gluino decay rate reads:

$$d\Gamma_{\tilde{g}} = \frac{1}{(2\pi)^5} \frac{C^2 m_{\tilde{g}}^4}{2m_{\tilde{g}} m_S^4} \delta^{(4)}(p - k_1 - k_2 - k_3) \frac{d^3 k_1}{2k_1^0} \frac{d^3 k_2}{2k_2^0} \frac{d^3 k_3}{2k_3^0}. \tag{6.4}$$

To get the full width the phase space integration should be performed. The integral over $\delta^{(4)} d^3 k_1/k_1^0 d^3 k_2/k_2^0 = 2\pi$ and $d^3 k_3 = k_3^2 dk_3 d\Omega_{k_3}$ ($k_3 dk_3 = k_3^0 dk_3^0$). Then

$$d\Gamma_{\tilde{g}} = \frac{1}{(2\pi)^4} \frac{C^2 m_{\tilde{g}}^3}{16 m_S^4} k_3^0 dk_3^0 d\Omega_{k_3}. \tag{6.5}$$

Assuming no angular dependence for $\vec{k_3}$, $\int d\Omega_{k_3} = 4\pi$, and that the maximum neutralino energy is $m_{\tilde{g}}/2$, so $\int_0^{m_{\tilde{g}}/2} k_3^0 dk_3^0 = m_{\tilde{g}}^2/8$, the total width is given by:

$$\Gamma_{\tilde{g}} \approx \frac{C^2}{256\pi^3} \frac{m_{\tilde{g}}^5}{m_S^4}. \tag{6.6}$$

Thus the lifetime of the gluino becomes very long, of order [28]

$$\tau = \frac{1}{\Gamma_{\tilde{g}}} \simeq (4\pi)^3 \frac{m_S^4}{m_{\tilde{g}}^5} \simeq \left(\frac{m_S}{10^{13} \text{ GeV}}\right)^4 \left(\frac{1 \text{ TeV}}{m_{\tilde{g}}}\right)^5 0.4 \text{ Gyr}, \tag{6.7}$$

where the the SUSY breaking scale m_S may vary from 10^7 GeV/c^2 up to GUT scale and the gluino mass $m_{\tilde{g}}$ may range from 100 GeV/c^2 to 1 TeV/c^2. Inserting these numbers in the above equation one obtains a gluino lifetime in between 10^{-6} s and the age of the Universe (see Fig. 6.2). For a phenomenology study, see [109].

There are also models with long-lived squarks and the main candidate is the stop eigenstate $\tilde{t}_1$ since it is expected to be the lightest scalar quark (from renormalization group equations one expects that due to the strong Yukawa coupling between top/stop and Higgs fields the soft SUSY breaking masses m_Q, $m_{\bar{u}}$, and $m_{\bar{d}}$ of the 3rd generation sfermions are smaller than those of the 1st and 2nd generation and gives rise to large mixing) [21]. An interesting scenario with a long-lived $\tilde{t}_1$ can be found in Ref. [110]. In this model the mass difference between the LSP $\tilde{\chi}_1^0$ and the NLSP $\tilde{t}_1$ is small due to the non-universal squark mass terms, while the chargino is kept too heavy for the decay $\tilde{t}_1 \to b\tilde{\chi}_1^+$ to occur.

6.2.2   Other BSM Models

SUSY is not the only theory with heavy stable particle candidates. Other BSM scenarios also predict heavy stable states. The same stability mechanisms as in the SM or SUSY are responsible for these new states: a new conserved quantum number or the decays are suppressed by kinematics or couplings. For example, in Universal Extra Dimensions theories all the SM fields are allowed to propagate freely in all dimensions (not only in the 3+1 normal dimensions, but also in the new ones). Due to the compactification of the extra dimensions, the momentum components along these dimensions become discrete and, as
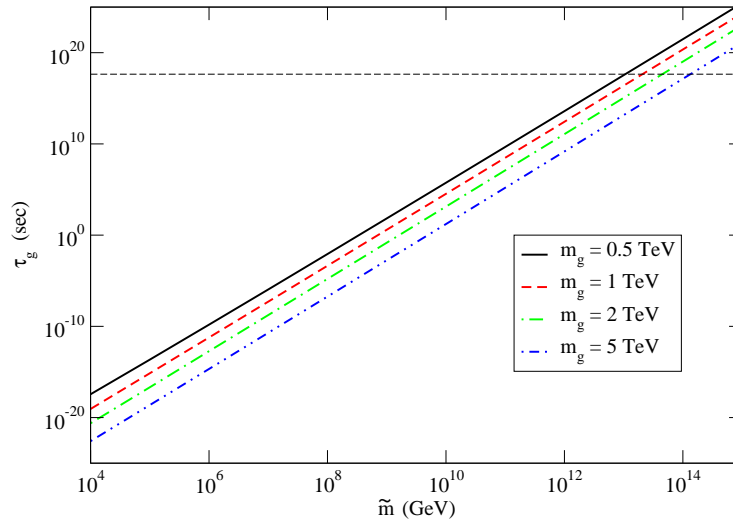
Figure 6.2: The gluino lifetime $\tau_{\tilde{g}}$ in Split SUSY as a function of the sfermion mass $\widetilde{m}$ for $\tan\beta = 2$ and $\mu > 0$. The dashed horizontal line represents the age of the Universe $\tau_U = 14$ Gyr. The figure is taken from [108].

they contribute to the effective mass of the particles propagating in all dimensions, heavy Kaluza-Klein (KK) towers appear in the effective 4D theory. Momentum conservation in the extra dimensions leads to very long-lived KK excitations of quarks and gluons, which will hadronize into stable states [111]. This requirement has an important phenomenological consequence: the KK modes will be pair-produced through reactions as $gg \to g_{KK}g_{KK}$ or $q\bar{q} \to g_{KK}g_{KK}$. So as signature one should look for events with two heavy, stable back-to-back particles traversing the detector. More exotic theories like models with leptoquarks [112], certain unification models [113], fourth generations fermions [114] can also give rise to heavy stable particles depending on the parameters.

6.3 Heavy Stable Hadrons in SUSY at LHC

The focus in this section will be the heavy stable colored particles predicted by the different SUSY scenarios in term of a stable gluino or squark. At LHC, the squarks and gluons would be produced through the following partonic reactions [115]:

$$
\begin{aligned}
\tilde{q}\bar{\tilde{q}} \text{ production}: \quad & q_i + \bar{q}_j \to \tilde{q}_k + \bar{\tilde{q}}_l \\
& g + g \to \tilde{q}_i + \bar{\tilde{q}}_i \\
\tilde{q}\tilde{q} \text{ production}: \quad & q_i + q_j \to \tilde{q}_i + \tilde{q}_j \text{ and } c.c. \\
\tilde{g}\tilde{g} \text{ production}: \quad & q_i + \bar{q}_i \to \tilde{g} + \tilde{g} \\
& g + g \to \tilde{g} + \tilde{g} \\
\tilde{q}\tilde{g} \text{ production}: \quad & q_i + g \to \tilde{q}_i + \tilde{g} \text{ and } c.c.
\end{aligned}
$$

where the indices $i - l$ indicate the flavors of the quarks (q) and squarks ($\tilde{q}$) and charge-conjugates processes (*c.c.*) are also possible.

The relevant Feynman diagrams are displayed in Fig. 6.3. Squarks final states require quark-antiquark (a), gluon-gluon (b), quark-pair (c), quark-gluon (f) initial states; gluinos are produced from quark-antiquark (d), gluon-gluon (e), quark-gluon (f) collisions. All these processes are strong, and therefore depends on the squark and gluino masses as well as on the strong coupling constant. Using these Feynman diagrams the total partonic cross sections can be calculated from the squared matrix elements of each process (see Chapter 3). For masses where large x partons are required quark diagrams typically dominate, while in the case of low x partons the gluon diagrams dominate. But the relative yields of squarks and gluinos in the final states are strongly correlated with their masses: if squarks are lighter than gluinos, the valence partons give the dominant yield of squark-antisquark/squarks pairs; the gluinos will be copiously produced if they are the lighter. A detailed calculation of the gluino and squark cross sections can be found in [115].

Figure 6.4 shows the leading order and next-to-leading order gluino, squark, neutralino, chargino production cross section predictions at the LHC as a function of the average final state mass. The cross sections were computed with Prospino2.0 [115, 116]. As can be seen from the figure the gluino cross section is much higher than the stop one. This has strong implications for ALICE since around 10^9 pp collisions will be recorded per year (see Section 4.2.5), so large cross sections for new physics are needed. Due to this requirement, only stable gluinos were considered in this thesis (see next chapter).

The squarks and gluinos, being colored particles, will pass through a hadronization stage during which they pick up quarks or gluons to form a color singlet state: *R-hadron*. "R" refers to the fact that they are stable only if the R-parity is conserved. Different R-hadron types can be formed from an exotic color triplet C_3 or color octet C_8: "mesons" $C_3\bar{q}$ or $C_8 q_1 \bar{q}_2$, "baryons" $C_3 q_1 q_2$ or $C_8 q_1 q_2 q_3$, "glueballs" $C_8 g$. A brief description of the hadronization of the colored heavy object within the Lund string fragmentation model [30] (discussed in Section 3.3) will be given below.

For a color triplet C_3 (or $C_{\bar{3}}$), located at the endpoint of a string, the $\bar{q}$ or $q_1 q_2$ (in a color antitriplet state) from a light quark-antiquark or diquark-antidiquark pair created by the breakup of the string can combine with the C_3 to form a singlet. For a color octet C_8, the picture is more complicated as it is attached to two string pieces that can individually break as above. One will give a quark or an antidiquark and the other an antiquark or diquark. The new quarks can combine with the C_8 to form an *R-meson* or *R-baryon*. In addition, a gg pair may be produced which leads to the formation of an *R-glueball*, while the remaining gluon attaches to the two string pieces. Since no normal glueballs were observed, the probability to form a R-glueball is a free parameter and is set to 0.1 in PYTHIA. By neglecting the fraction of R-glueballs and since the R-hadron production occurs predominantly by the $C_{3,8}$ picking up u and d quarks, roughly 50% of the produced states will be charged (due to the $u - d$ charge difference); around 1% of the charged R-hadrons will have charge $+2e$. Also most of the produced R-hadrons will be R-mesons (R-baryons contribute less than 10%). As no $C_{3,8}C_{3,8}$ bound states are considered the R-hadrons are always produced in pairs.
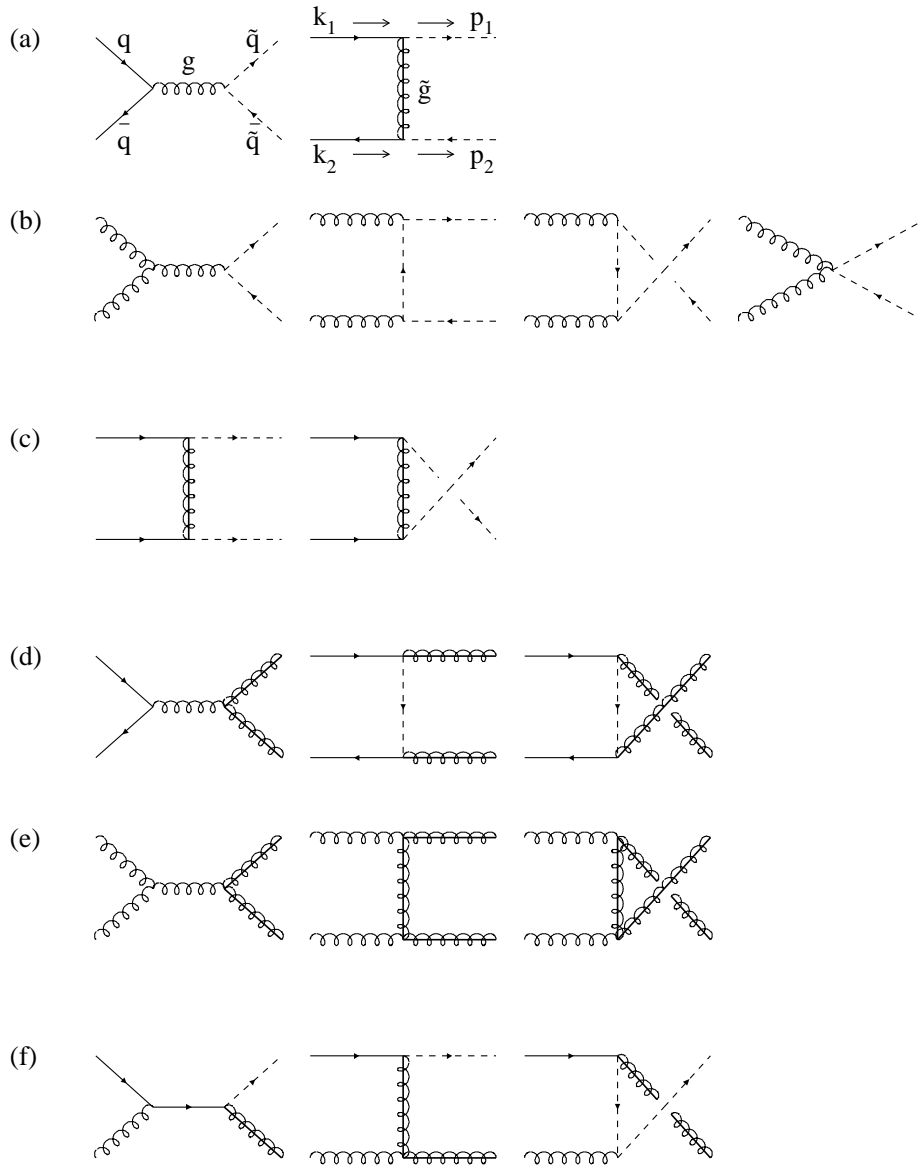
Figure 6.3: Squark and gluino production at LHC. Squarks are produced through the diagrams (a), (b), (c), and (f), while gluino through (d), (e), and (f). The k_1 and k_2 are the momenta of the initial partons, p_1 and p_2 those of the particles in the final states. Figure taken from [115].
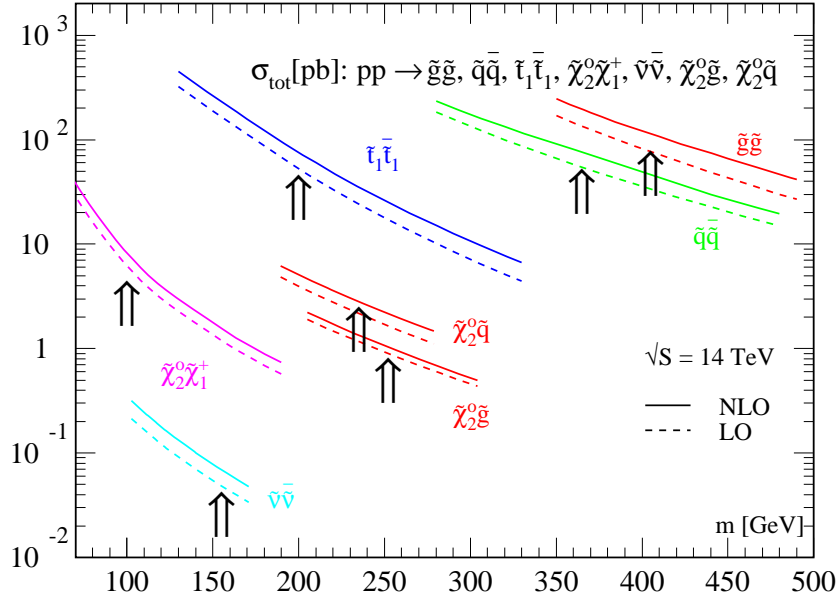
Figure 6.4: Leading order and next-to-leading order production cross section predictions at the LHC maximum energy. A typical SUGRA scenario is indicated by the arrows. The figure is taken from [117].

PYTHIA does not only perform the hadronization, but also allows to study the kinematics of the heavy particles produced in collisions. The η distribution for gluino R-hadrons for different values of $m_{\tilde{g}}$ is depicted in Fig. 6.5. The particles are produced more central for higher gluino masses as is shown by the narrowing of the η distribution as a function of $m_{\tilde{g}}$ which follows logically as the available phase space decreases for higher masses. The p_T (left) and β (right) distributions as a function of the gluino mass are illustrated in Fig. 6.6, while $\eta_R - \eta_{R^{p_T^{max}}}$ and $\phi_R - \phi_{R^{p_T^{max}}}$ distributions for different values of $m_{\tilde{g}}$ are shown in Fig. 6.7. A few things are noteworthy. First of all, the p_T distribution is broad and it can be a challenge for ALICE to reconstruct the momentum with sufficient precision for making PID because of the low magnetic field (maximum of 0.5 T). Second, looking at the β distribution ($\beta = \frac{p}{E}$), it can be seen that the R-hadrons have an average velocity significantly smaller than one. So R-hadrons are very different from SM particles with the same momentum: the slow R-hadrons will ionize like "soft" protons and will have a large time-of-flight. It is this difference that can be exploited in order to identify heavy stable particles and which can also give limitations for ATLAS and CMS since they can only trigger on (and associate all detector information for) tracks with $\beta > 0.7$ because the LHC bunch spacing is so short (25 ns) [1]. Third, the R-hadrons are seen to be produced approximately back-to-back in ϕ.

---

[1]Note also that if ATLAS and CMS can not detect the slow R-hadrons, the identification has to rely on their hadronic reactions (see below) which might be very sensitive to model assumptions.
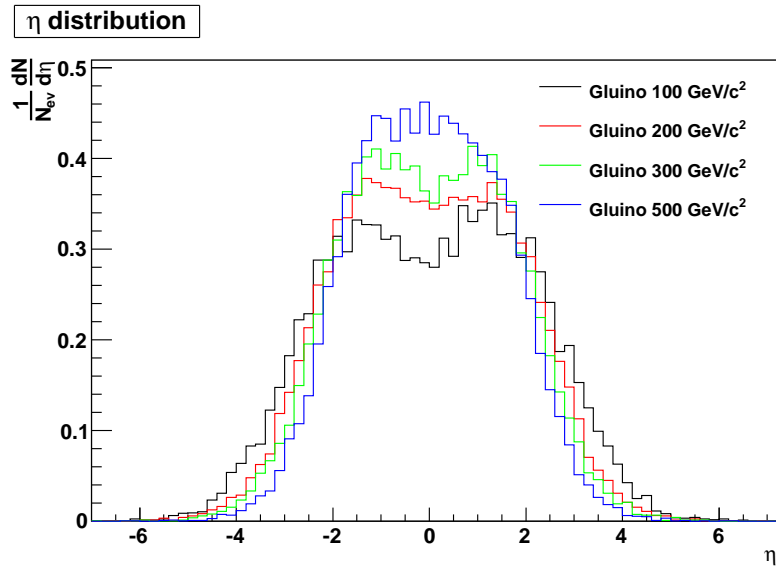
Figure 6.5: Pseudo-rapidity distributions normalized to the number of simulated events, N_{ev}, for gluino R-hadrons for different values of $m_{\tilde{g}}$ as predicted by PYTHIA ($\sqrt{s} = 14$ TeV).
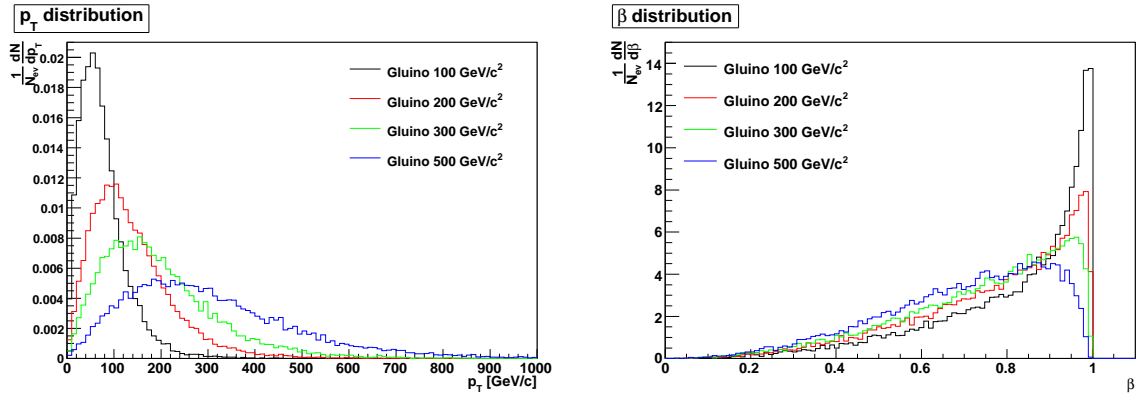

Figure 6.6: Transverse momentum (left) and β (right) distributions normalized to the number of simulated events, N_{ev}, for gluino R-hadrons for different values of $m_{\tilde{g}}$ as predicted by PYTHIA ($\sqrt{s} = 14$ TeV).
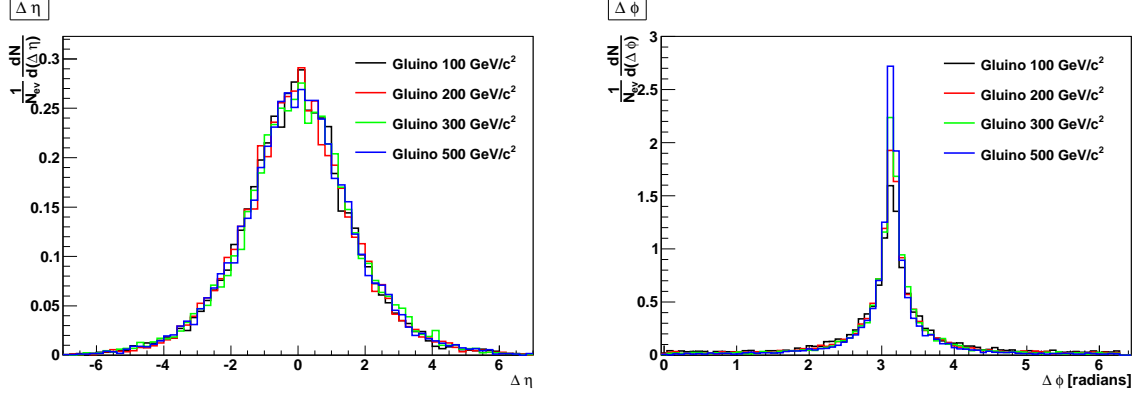
Figure 6.7: $\Delta\eta$ (left) and $\Delta\phi$ (right) distributions normalized to the number of simulated events, N_{ev}, for gluino R-hadrons for different values of $m_{\tilde{g}}$ as predicted by PYTHIA ($\sqrt{s} = 14$ TeV).

In order to establish a search strategy, the mass splittings are crucial: the lightest state should be dominantly present in the detector. A complete mass calculation can be found in [118] and only a brief outline will be given here.

The mass of the produced R-hadrons can be approximated by the mass formula of the lowest level hadronic states with no radial or angular excitation [119]:

$$m_{hadron} \approx \sum_{i} m_i - k \sum_{i \neq j} \frac{(\mathbf{F_i} \cdot \mathbf{F_j})(\mathbf{S_i} \cdot \mathbf{S_j})}{m_i m_j}. \tag{6.8}$$

The summation is over the partons i inside the hadrons, m_i are the parton constituent masses, F_i represents the color $SU(3)$ matrices, S_i the spin $SU(2)$ matrices (for parton i), and k a parameter with dimension (mass)^3. The second term of Eq. 6.8 gives the mass splittings; terms involving a heavy parton in the denominator can be safely neglected due to the big difference between constituent masses and heavy parton mass. The $\pi - \rho, K - K^*, D - D^*, B - B^*$ masses and mass splittings are reproduced reasonably well using $k \approx 0.043$ GeV^3, while in the baryon sector the masses are obtained using $k \approx 0.026$ GeV^3. The mass splittings for R-hadrons are then found to be less than the order of 100 MeV/c^2 [118].

Other important aspects for a search strategy are the R-hadron interactions with "normal" matter when propagating through a medium. The dominant interactions are the electromagnetic and strong ones. As the ionization energy loss of charged particles was already discussed in Section 5.4.1, only the nuclear interactions will be shortly addressed in the following.

The nuclear interactions of the R-hadrons are not well understood and different phenomenological approaches [118, 120] were developed to describe the R-hadron nuclear scattering processes. The model proposed in [118] uses a constant geometrical cross section and phase space arguments in order to predict all possible $2 \rightarrow 2$ and $2 \rightarrow 3$ processes, while the energy losses are determined by implementation of the model into GEANT3 [118] or GEANT4 [121]. The second approach [120] is a Regge-based model which was extended and

implemented in GEANT4 [122]. Only small differences in terms of the predicted energy loss and scattering cross sections between the two GEANT4 approaches were observed [122].

Although the models are using different assumptions some features are common among them. Since the probability that the parton $C_{3,8}$ will interact perturbatively with the quarks in the target nucleon is small (these interactions are suppressed by the squared inverse mass of the parton), the heavy state $C_{3,8}$ is considered as a non-interacting spectator, acting as a reservoir of kinetic energy and surrounded by a cloud of interacting quarks that determine the charge of the R-hadron. Thus the interaction cross section will be typical of that of a meson. The energy loss per interaction is predicted to be low (few GeV [121]) and expected to be dominated by losses occurred in inelastic collisions. This implies that the fraction of R-hadrons which would be stopped during their traversal of a typical detector is negligible. Another feature is the conversion of one species of R-hadron to another. This can be done through baryon number and charge exchange. In the first process, an inelastic R-meson-nucleon interaction results in the release of a pion for which the reverse reaction is suppressed (phase space and the relative absence of the pions) [118]. Thus most R-mesons will convert early to baryons due to the nuclear scatterings in passing through calorimeters and remain as baryons. In [118, 121] most of the created R-baryons are charged, but this assumption is now disputed in the case of gluino R-baryons [122]. Charge exchange may arise in any meson-to-meson, meson-to-baryon, or baryon-to-baryon process and is expected to form a substantial contribution to all interactions. The charge and baryon flip is one of the signals that ATLAS and CMS are relying on in their search for R-hadrons.

6.4 Experimental Search Techniques

As could be seen from Section 6.2 heavy stable particles are predicted in a broad range of models. As their signatures are determined by interactions with materials, these particles can be identified using various experimental techniques that will be described next. The most common search techniques include the use of ionization energy loss (dE/dx) and Time of Flight (ToF).

From Section 5.4.1 one could see that the ionization energy loss depends on $\beta\gamma$. This has crucial implications in searches for heavy stable particles at collider since these particles will look like muons (penetrate calorimeters) and their momenta ($p = M\beta\gamma$) can be determined from the curvature of its track in a magnetic field.

Several issues should be taken into account when using this search technique. The main problem is related with the $\langle dE/dx \rangle$ not being Gaussian, but rather described by a Landau distribution. The solution, as discussed in Chapter 5, is to calculate the most probable energy loss. The background sources are:

- The positively charged ions from secondary interactions in the detector material produced by primary particles.

- Finite resolution of the tracking chamber that causes, for example, two very close tracks to be reconstructed with a highly ionizing signal.

- Secondary highly ionizing particles from collisions between the beams and the gas inside the beam pipe.

- Combinatorial mistakes when combining ionization and momentum informations (more probable when they are provided by different detectors). This will not be the case for ALICE since both ionization and momentum are given by the TPC.

The second most used method of heavy stable particles identification is the ToF measurement. At actual energies, all the stable or metastable SM particles will have a velocity of $\beta \approx 1$, while the new massive particles will be produced with smaller velocity and thus will have a large ToF. As for the dE/dx case, the correlation of momentum (measured from a different detector) and velocity leads to a measurement of the mass ($M = p/\beta\gamma$) with an accuracy given by

$$\left(\frac{\Delta M}{M}\right)^2 = \left(\frac{\Delta p}{p}\right)^2 + \left(\gamma^2 \frac{\Delta\beta}{\beta}\right)^2 . \tag{6.9}$$

Here the uncertainties of the momentum and velocity are assumed to be uncorrelated. Also the uncertainty of the velocity is given by the uncertainty of the ToF t ($\Delta\beta/\beta = \Delta t/t$). As background sources one can have combinatorial mistakes when combining momentum and time-of-flight informations.

6.5   Existing Searches and their Limitations

The last part of this chapter will overview some of the various searches for heavy stable particles. A detailed review of limits on massive particles can be found in Ref. [102], while for an exhaustive list of all results the curious reader should consult Ref. [9].

The most direct way to look for new particles is by using colliders. The best current collider constraints (in terms of masses and cross sections) have been obtained at e^+e^- (LEP) and $p\bar{p}$ (Tevatron) facilities, but searches at e^-p collider (HERA) have also been carried out. The lower mass bounds are typically the result of a comparison between the predicted pair-production cross section of a massive particle in a particular model, and a limit on the number of events with particles reconstructed above a certain mass from the experiment. As discussed in Section 6.4, due to their large mass these particles would have anomalously high dE/dx, so the primary experimental observable used is the dE/dx measurement. Simple topological cuts are also used to look for such candidates.

The OPAL experiment at LEP, adopting the above approach, searched for long-lived massive particles of charge $\pm e$ or fractional charge $\pm 2/3e$, $\pm 4/3e$, $\pm 5/3e$ [123]. The data for this study were collected by the OPAL detector between $1995-2000$ (the so-called LEP-2 period) at center-of-mass energies from 130 GeV to 209 GeV, with a total integrated luminosity of 693.1 pb^{-1}. The massive particles, denoted by $X^{\pm}$, with $m_X > m_Z/2$ were assumed to be pair-produced in the reaction $e^+e^- \to X^+X^-$ and not to interact strongly. Since no evidence for the production of such particles was observed, model independent upper limits on the pair-production cross section for weakly interacting scalar and spin

1/2 particles were extracted at 95% confidence level (C.L.), combining the results from all center-of-mass energies and assuming s-channel production. For spin 0 particles with charge $\pm e$ the 95% C.L. upper bound on the pair-production cross sections varies from 0.005 to 0.028 pb in the mass range $45 < m_X < 101$ GeV. Translated into sparticle masses this implies a lower mass limit of 98.0 GeV/c^2 and 98.5 GeV/c^2 for the mass of right- and left-handed smuons and staus, respectively. Note that this bound does not translate to selectrons, as their cross section depends on other sparticle parameters in t-channel production. For spin 1/2 particles with charge $\pm e$, the 95% C.L. upper limit varies from 0.005 to 0.024 pb in the mass range $45 < m_X < 100$ GeV/c^2 which gives a low mass limit for charginos and leptons of 102 GeV. For fractional charge $\pm 2/3e$, $\pm 4/3e$, $\pm 5/3e$ particles, the cross section limits lie between 0.005 and 0.020 pb at 95% C.L. in the range $45 < m_X < 95$ GeV/c^2.

Searches for stable colored particles have also been performed by the ALEPH experiment at LEP [124]. Data from LEP-1 and LEP-2 have been used in this analysis and it is assumed that the LSP is either the gluino or squark, in the context of the MSSM with R-parity conservation. For a stable gluino hypothesis, the dominant production process is $e^+e^- \rightarrow q\bar{q}\tilde{g}\tilde{g}$, where a radiated gluon splits into a pair of stable gluinos. Data collected by ALEPH at LEP-1, at center-of-mass energies around the Z resonance, were considered for this process (about 4.5 million hadronic Z decays). This search results in a low mass limit of 26.9 GeV/c^2 at 95% C.L. for a gluino LSP. For stable stops and sbottoms, ALEPH was investigating the process $e^+e^- \rightarrow \tilde{q}\bar{\tilde{q}}$ with LEP-2 data, using dE/dx measurements. Due to the mixing of the left- and right-handed states of the stop (or sbottom), a conservative assumption was made here: the mixing angles were taken such that the stop and sbottom couplings to the Z disappear. This allowed for stable hadronizing stop (sbottom) to be excluded up to masses of 95 (92) GeV/c^2 at 95% C.L.

The CDF experiment at the Tevatron has also looked for long-lived charged massive particles [125]. Limits for weakly interacting and strongly interacting stable massive particles were set with 1 fb^{-1} of $p\bar{p}$ collisions at center-of-mass energy of 1.96 TeV collected with a high transverse momentum p_T muon trigger. Using a ToF detector to calculate the masses of the particles from their measured velocity and momentum, long-lived massive particle candidates have been isolated. Two scenarios were considered in this analysis: the production of a single stable massive particle and a benchmark model for top-squark pair production in the reference volume. The first one is largely model independent, while the results of the second one could generally be applied to all stable $\tilde{t}$ production models. SM backgrounds are estimated from the mass resolution on muon-like particles found in a control-region, and no excess of events is found for masses above 100 GeV/c^2. Model independent upper limits on the production cross section of $\sigma < 10$ fb and $\sigma < 48$ fb at 95% C.L. for weakly and strongly interacting stable massive particles were found for candidates with $p_T > 40$ GeV/c, $|\eta| < 0.7$, $0.4 < \beta < 0.9$, and a measured mass $m > 100$ GeV/c^2. From the above limits a lower stop mass bound of 249 GeV/c^2 at 95% C.L. was inferred.

The other Tevatron experiment, D0, performed a similar analysis based on 1.1 fb^{-1} data [126]. In this study stable tau sleptons, gaugino-like charginos, and higgsino-like charginos produced directly in pairs were considered, so di-muons triggers were used to

collect data. The ToF technique was used to separate the candidates from the SM particles. No evidence of a signal was found and an upper limit on stau production cross section was set at 95% C.L. This varies from 0.31 pb to 0.04 pb for stau masses between 60 GeV/c^2 and 300 GeV/c^2. For the chargino, mass limits of 206 GeV/c^2 and 171 GeV/c^2, for a wino- and higgsino-like chargino, respectively, is given at the 95% C.L.

No stable gluinos were considered in the Tevatron work, but a limit on the gluino mass, in the case when it fragments into a stable neutral hadron that remain neutral throughout the detector, was set from Tevatron Run I limits on stable charged particles and anomalous mono-jet production to $m_{\tilde{g}} \gtrsim 170$ GeV/c^2. This limit could be increased to $m_{\tilde{g}} \lesssim 430$ GeV/c^2 with a luminosity of 2 fb^{-1} collected by Run II [109].

Chapter 7

R-hadron Search with the ALICE Detector

The preceding chapter illustrates the arguments for heavy stable particle searches. This chapter presents a Monte Carlo study at $\sqrt{s} = 14$ TeV outlining the ALICE discovery potential of R-hadrons. It concerns both PYTHIA and ALICE detector response simulations. Gluino R-hadron was chosen as an example of a candidate, and cross sections and kinematic properties were obtained from PYTHIA simulations for various gluino masses ($100 - 500$ GeV/c^2). Detailed detector response simulations of the most important signatures for R-hadron identification in the ALICE central barrel were performed for 100 GeV/c^2 R-hadron mass. Only the electromagnetic interactions were considered in this study due to the low material budget that ALICE has. This implies that the results and conclusions apply to all heavy charged particles - ALICE can not separate between R-hadrons and other heavy stable charged particles. The work presented here was previously described in Refs. [127, 128].

7.1 PYTHIA Event Generation

Events were generated using PYTHIA 6.4.10 [31]. The gluino production was enabled through the processes $gg \to \tilde{g}\tilde{g}$ and $f\bar{f} \to \tilde{g}\tilde{g}$ (Subprocesses 244 and 243). For moderate gluino masses ($m_{\tilde{g}}$ up to ~ 1400 GeV/c^2), the channel $gg \to \tilde{g}\tilde{g}$ is dominating when considering $pp \to \tilde{g}\tilde{g}$. The processes allowing for $f\bar{f} \to \tilde{g}\tilde{\chi}_n$ (Subprocesses $237 - 242$) were disabled in order to minimize the model dependence. The $gg \to \tilde{g}\tilde{g}$ cross section depends only on the gluino mass, while the $f\bar{f} \to \tilde{g}\tilde{g}$ cross section depends on the mixing in the squark sector and is therefore subject to model assumptions. In PYTHIA the dominating part of the cross section is the gg term. In the present study, the gluino hadronization is performed using custom code taken from the example R-hadron program on the PYTHIA homepage [129].

Gluino masses of 100, 200, 300, and 500 GeV/c^2 were investigated. For each gluino mass, 10000 events were generated in order to ensure enough statistics for the study of
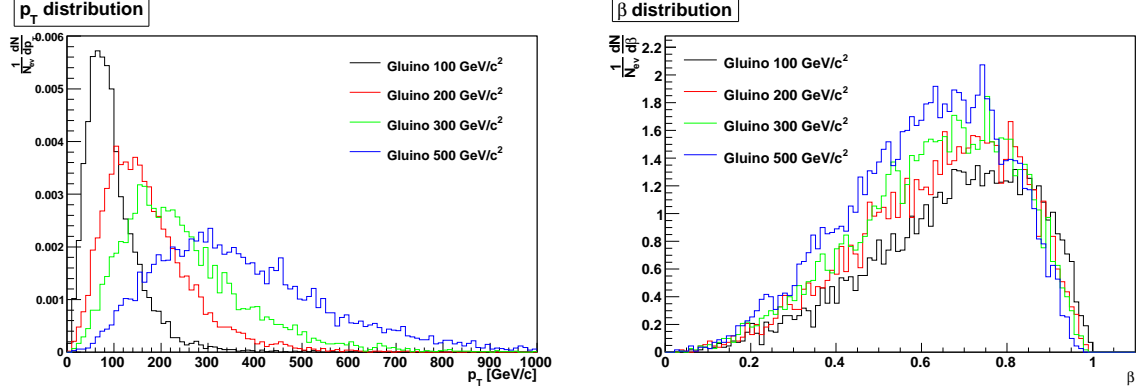
Figure 7.1: Transverse momentum (left) and β (right) distributions normalized to the number of simulated events, N_{ev}, for charged and neutral R-hadrons for different values of $m_{\tilde{g}}$ for $|\eta| < 1$ ($\sqrt{s} = 14$ TeV).

Mass [GeV/c^2]	$\sigma_{\tilde{g}\tilde{g}}$ [mb]		Acceptance		Rate$_{\text{charged}}$	
	7 TeV	14 TeV	7 TeV	14 TeV	7 TeV	14 TeV
100	1.2×10^{-5}	5.6×10^{-5}	0.36	0.31	4.7×10^{-8}	1.6×10^{-7}
200	3.2×10^{-7}	2.2×10^{-6}	0.42	0.36	1.5×10^{-9}	0.7×10^{-8}
300	2.9×10^{-8}	2.8×10^{-7}	0.45	0.38	1.5×10^{-10}	1.0×10^{-9}
500	8.4×10^{-10}	1.6×10^{-8}	0.51	0.44	5×10^{-12}	0.7×10^{-10}

Table 7.1: Rate (see text) of charged R-hadrons for $\sqrt{s} = 7$ TeV and $\sqrt{s} = 14$ TeV.

the detector response. In order to see how many R-hadrons would have nearly full length tracks in the TPC, a cut in pseudo-rapidity $|\eta| < 1$ was used.

The kinematics of the physics processes generated were investigated first. Figure 7.1 shows the p_T and β distributions inside the TPC acceptance as a function of the gluino mass. The p_T distribution is broad. As already discussed in Section 6.3, the R-hadrons have low velocities due to their large mass. This can also be seen from the right panel of Fig. 7.1 which illustrates that the centrally produced R-hadrons are slower than the forward produced ones since they have a β between 0.3 and 0.9 with a mean around 0.7.

Having established the kinematic properties of the R-hadrons in the TPC acceptance, the number of R-hadrons that pass the η acceptance cut (Fig. 7.2) was estimated. Events where neither one of the two generated R-hadrons could be detected, events with one R-hadron in the TPC acceptance, but also events where both R-hadrons ended up inside the TPC acceptance have been found. The low fraction of events containing two R-hadrons shows that an ALICE analysis can not rely exclusively on events with two R-hadrons, but also should look for events with single tracks. It can be observed that the particles are produced more centrally for higher gluino masses as is shown by the increase in the number of R-hadrons which falls in the η cut.
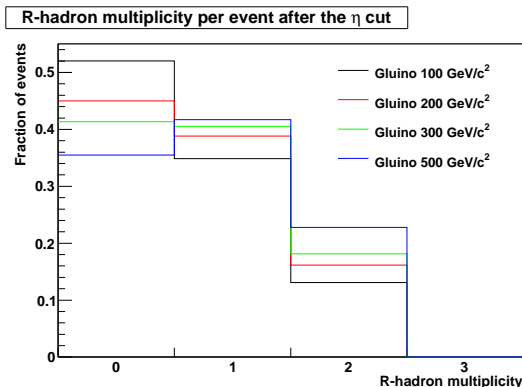
Figure 7.2: Number of charged and neutral R-hadrons per simulated event inside the TPC acceptance ($|\eta| < 1$) for different values of $m_{\tilde{g}}$ ($\sqrt{s} = 14$ TeV).
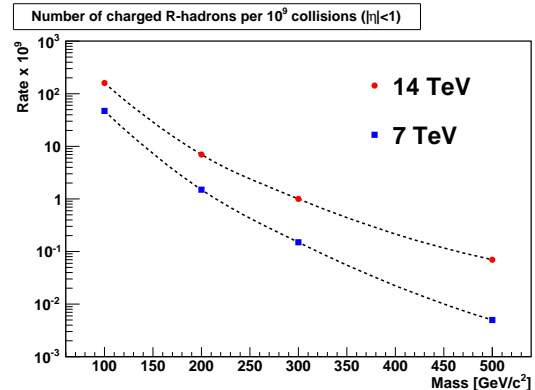
Figure 7.3: Mean number of charged R-hadrons as a function of the gluino mass per ALICE nominal annual pp run (10^9 events) for $\sqrt{s} = 7$ TeV (blue squares) and $\sqrt{s} = 14$ TeV (red circles).

Next step was to estimate the number of R-hadrons which can be detected by the ALICE experiment per pp minimum bias collision. This quantity was called "rate". The equation used to determine the rate is:

$$Rate = 2 \times \frac{\sigma_{\tilde{g}\tilde{g}}}{\sigma_{pp}} \times Acceptance$$

where:

- $\sigma_{\tilde{g}\tilde{g}}$ is the LO cross section given by PYTHIA (2nd column of Table 7.1).

- $\sigma_{pp} \sim 110$ mb ($\sqrt{s} = 14$ TeV) and $\sigma_{pp} \sim 90$ mb ($\sqrt{s} = 7$ TeV) is the total pp cross section [130]. The values are quite uncertain and subject for further investigations and experimental verification.

- Acceptance is the ratio between the number of R-hadrons in the TPC acceptance and the number of generated R-hadrons in the global picture (3rd column of Table 7.1).

- factor 2 appears because the R-hadrons are always produced in pairs.

The last column of Table 7.1 gives the rate for charged R-hadrons (remember that half of the R-hadrons are neutral). Since the available energy for the next 18-24 months will be 7 TeV [63], the expected rate at this energy was also estimated. Figure 7.3 shows the mean number of charged R-hadrons for a nominal annual pp run in ALICE where 10^9 events are accumulated for $\sqrt{s} = 7$ TeV (blue squares) and $\sqrt{s} = 14$ TeV (red circles). As can be seen from the figure, the low number of collisions per year makes it very unlikely that ALICE can discover R-hadrons with mass above 200 GeV/c^2 at $\sqrt{s} = 7$ TeV and above 300 GeV/c^2 at $\sqrt{s} = 14$ TeV even if they exist.

7.2   AliRoot Simulations

In this section the AliRoot simulation results based on the PYTHIA output files will be presented. Two different configurations were adopted: one with TPC standalone (TPC should be fully calibrated and internally aligned from the first day of running) and in the other configuration both ITS and TOF were introduced in the simulation. In the TPC standalone case the ITS was kept in the simulation, but was removed from the reconstruction. Charged R-hadrons with the mass fixed to 100 GeV/c^2, based on the PYTHIA simulation of 100 GeV/c^2 gluinos, were simulated and reconstructed. Note that, while these R-hadrons have the largest cross sections, they are the most difficult to identify because they are faster (Fig. 6.6 right). In the TPC standalone configuration both charge $+e$ and $+2e$ were investigated for the charged R-hadrons. The results of the R-hadron simulation were compared with the results of pion, proton, and muon simulations with exactly the same momentum distribution. When ITS and TOF have been included in the simulation the charge $+e$ R-hadrons were compared with protons. Simulations for fractional charge R-hadrons ($+2/3e$, $+4/3e$) were also run even though this is not predicted by any of the SUSY models, but this could of course be a signature of free (heavy) quarks. The simulation results were compared with the ones for charge $+e$ R-hadrons and protons with exactly the same momentum distribution. The magnetic field used was 0.5 T. Only tracks with at least 50 TPC clusters, a distance to the vertex less than 0.2 cm in the transverse direction, and not flagged as kink daughter were required (see Section 9.2). Furthermore, a cut in pseudo-rapidity $|\eta| < 0.9$ and another one in momentum $p > 10$ GeV/c were added on top of the track selection (to be in a region of optimal performance for the TPC).

7.2.1   TPC Standalone Simulation - Integer Charge R-hadrons

The reconstruction efficiency per track was found to be 85% for charge $+e$ R-hadrons and 78% for charge $+2e$ R-hadrons.

Figure 7.4 shows the momentum distribution for charge $+e$ R-hadrons. The mean $p_{Rec} - p_{MC}$ is depicted in Fig. 7.5 (the systematic offset from 0 for momenta $p_{MC} >$ 100 GeV/c shows that at the time of the simulations there were some problems with the momentum reconstruction in the TPC standalone case). As could be seen from Section 5.3, the estimation of the track parameters depends strongly on the vertex position as well as the number of track points. Since the TPC alone was used in the reconstruction the vertex position is not well determinated. Also at these high momenta the tracks have almost straight trajectories and the TPC track points will not be enough to get a good approximation of the curvature. This leads to a poor estimation of the track parameters (recall from Section 5.5 that $\sigma_{p_T}/p_T \propto 1/L^2$). The momentum resolution is presented in Fig. 7.6. However, the momentum resolution is still adequate to separate high momentum R-hadrons from low momentum (slow) SM particles which might otherwise give a background signal.

Figure 7.7 illustrates the energy loss (dE/dx) as a function of the reconstructed momentum ($p_{Rec} > 10$ GeV/c) for charge $+e$ R-hadrons (blue), pions (black), protons (red),
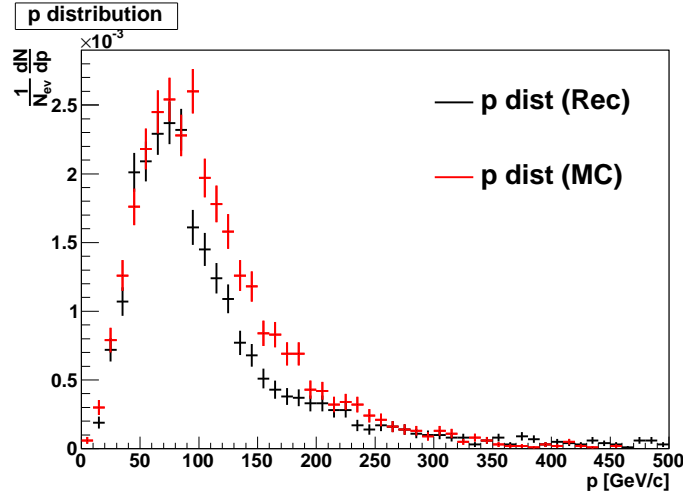
Figure 7.4: Momentum distribution normalized to the number of simulated events, N_{ev}, for charge $+e$ R-hadrons. Red points represent the input distribution and black points represent the reconstructed momentum.
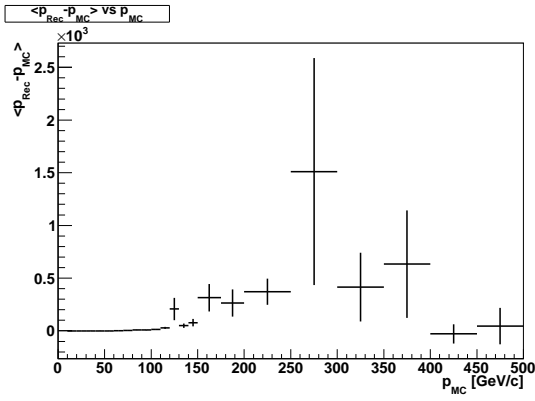

Figure 7.5: Mean $p_{Rec} - p_{MC}$ as a function of the MC momentum for charge $+e$ R-hadrons.
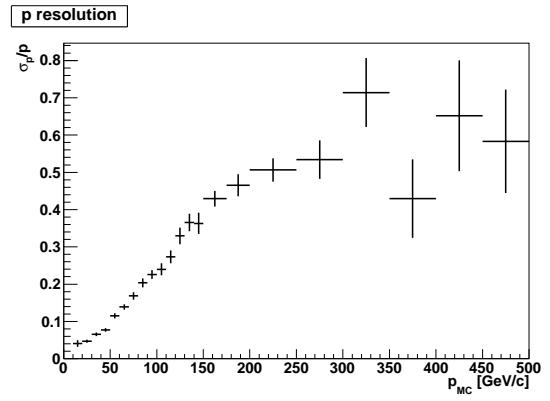

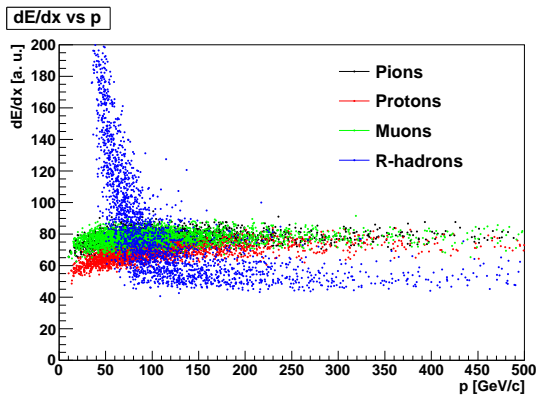Figure 7.6: Momentum resolution as a function of the MC momentum for charge $+e$ R-hadrons.

Figure 7.7: dE/dx as a function of the reconstructed momentum ($p_{Rec} > 10$ GeV/c) for charge $+e$ R-hadrons (blue), pions (black), protons (red), and muons (green). The pions and muons overlay completely, so only muons can be seen in the figure.
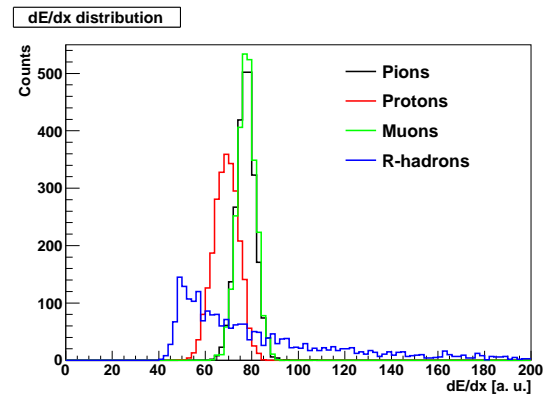

Figure 7.8: dE/dx distribution for charge $+e$ R-hadrons (blue), pions (black), protons (red), and muons (green) for $p_{Rec} > 10$ GeV/c.
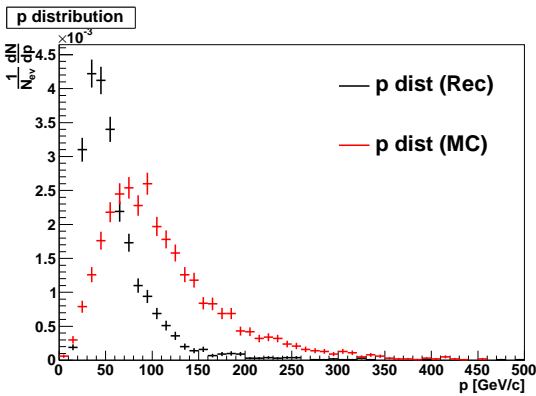

Figure 7.9: Momentum distribution normalized to the number of simulated events, N_{ev}, for charge $+2e$ R-hadrons. Red points represent the input distribution and black points represent the reconstructed momentum. The momentum is half of the input because the reconstruction algorithm assumes charge $+e$ particles.
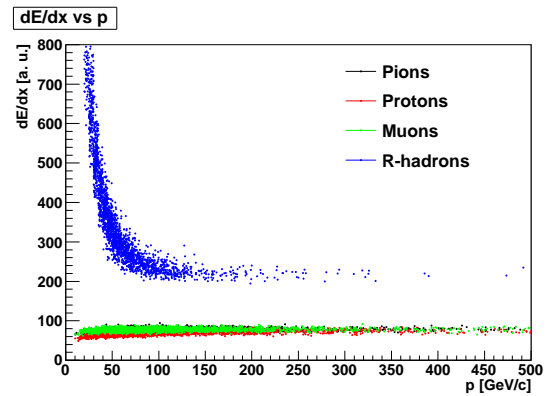

Figure 7.10: dE/dx as a function of the reconstructed momentum ($p_{Rec} > 10$ GeV/c) for charge $+2e$ R-hadrons (blue), pions (black), protons (red), and muons (green). Charge $+2e$ R-hadrons are completely separated from the SM particles.

and muons (green). The color coding used is the same throughout this section. Since the pions and muons overlay completely, only muons can be seen in the figure. As expected the dE/dx for charge $+e$ R-hadrons lies in the region of $1/\beta^2$ while the dE/dx for pions, protons, and muons are on the relativistic rise/plateau (remember the β distribution for R-hadrons from the previous section). Figure 7.8 shows the dE/dx distribution for charge $+e$ R-hadrons, pions, protons, and muons. As can be seen from both figures slow R-hadrons are well separated from pions, protons, and muons. The number of these R-hadrons was estimated. In order to do this a cut in reconstructed momentum ($p_{Rec} > 10$ GeV/c) and in the energy loss ($dE/dx > 100$) was applied which corresponds to a 5.5 σ separation from pions and muons. This resulted in 31% of R-hadrons being in this region. The remaining R-hadrons can not be separated from other charged particles by the TPC on an event by event basis, but only statistically which is not likely to be feasible because of the low yield.

Charge $+2e$ R-hadrons were also investigated even though the model predicts only a small fraction (1%) of R-hadrons with such a charge. The model prediction is based on the low energy QCD hadronic spectrum and is uncertain. Figure 7.9 shows the momentum distribution for charge $+2e$ R-hadrons. As can be observed from the figure, the reconstructed momentum is half of the input for this type of R-hadrons because the reconstruction algorithm assumes charge $+e$ particles. The energy loss for charge $+2e$ R-hadrons compared with the response from pions, protons, and muons as a function of the reconstructed momentum is depicted in Fig. 7.10. The R-hadrons with charge $+2e$ are completely separated from the SM particles. There could be a background from high momentum ^{3}He, but because of the momentum cut of $p_{Rec} > 10$ GeV/c this should be negligible as this would require the formation of protons and one neutron, all close in momentum phase space, and all with momenta above ~ 7 GeV/c (^3He can also be rejected by the TOF).

7.2.2 ITS+TPC+TOF Simulation - Integer Charge R-hadrons

In this section the ITS and TOF were included in the simulation. Charge $+e$ R-hadrons were compared to protons with the same momentum distribution. The reconstruction efficiency for ITS and TPC was found to be 83%. When a TOF signal is required the reconstruction efficiency drops to 65%.

The momentum distribution (Fig. 7.11), the mean $p_{rec} - p_{MC}$ (Fig. 7.12) and the momentum resolution (Fig. 7.13) were investigated first. All the figures show that the ITS greatly improves the momentum determination. The momentum resolution is below 5% at $p_{MC} = 100$ GeV/c for this configuration.

Surprisingly the momentum resolution is dominated by multiple scattering (MS) out to $p_{MC} = 50$ GeV/c, see Fig. 7.13. One can try to understand this from a simple argument. The spread in angles by multiple scattering goes as, $\sigma_{\theta(\text{MS})} \propto 1/(p\beta)$, while the bending angle is inversely proportional to the momentum: $\theta \propto 1/p$. One therefore finds that $\sigma_{p(\text{MS})}/p \sim \sigma_{\theta(\text{MS})}/\theta \propto 1/\beta$, so that even though the multiple scattering for an R-hadron with a similar velocity as a proton is smaller, the effect on the momentum resolution only depends on β.

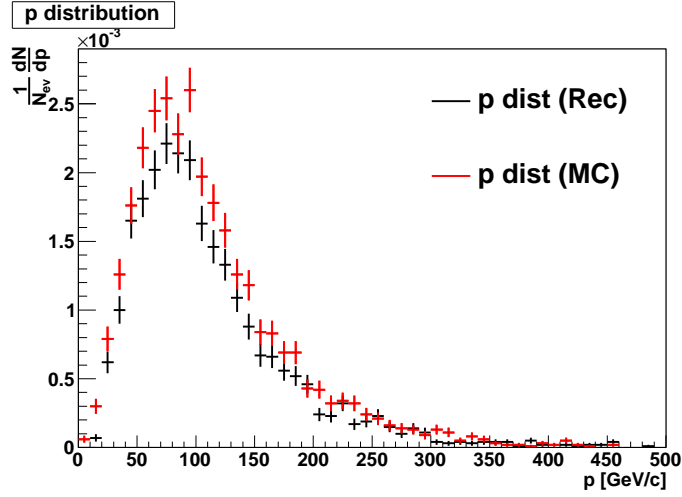Figure 7.14 shows the dE/dx in ITS as a function of the reconstructed momentum

Figure 7.11: Momentum distribution normalized to the number of simulated events, N_{ev}, for charge $+e$ R-hadrons with ITS included in the reconstruction. Red points represent the input distribution and black points represent the reconstructed momentum.
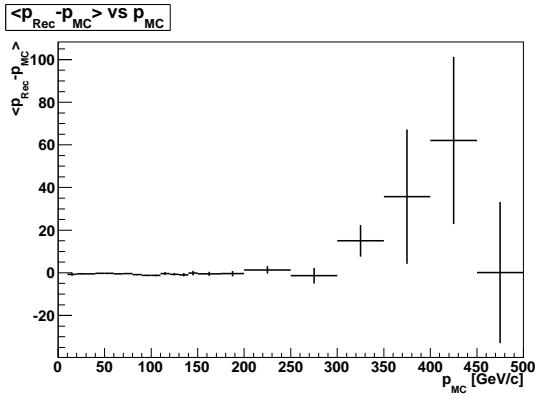

Figure 7.12: Mean $p_{Rec} - p_{MC}$ as a function of the MC momentum for charge $+e$ R-hadrons with ITS included in the reconstruction.
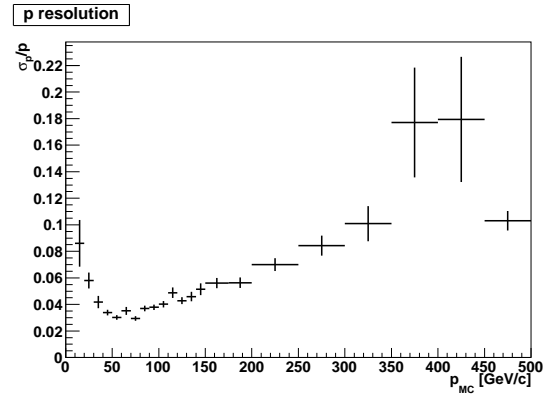

Figure 7.13: The momentum resolution as a function of the MC momentum for charge $+e$ R-hadrons with ITS included in the reconstruction.
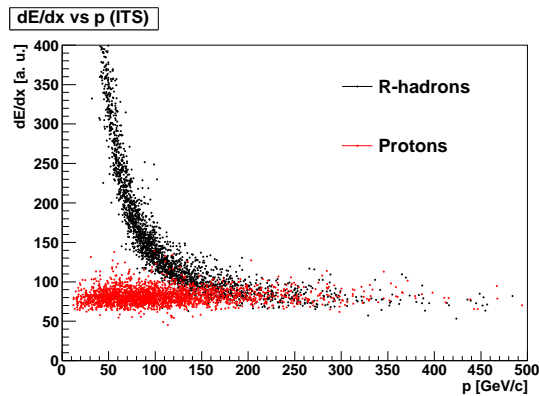
Figure 7.14: dE/dx in the ITS as a function of the reconstructed momentum ($p_{Rec} > 10$ GeV/c) for charge $+e$ R-hadrons (black) and protons (red).
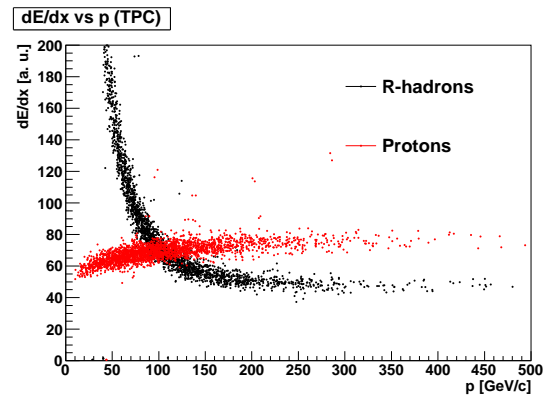
Figure 7.15: dE/dx in the TPC as a function of the reconstructed momentum ($p_{Rec} > 10$ GeV/c) for charge $+e$ R-hadrons (black) and protons (red).

($p_{Rec} > 10$ GeV/c) for R-hadrons (black) and protons (red). As can be observed from the figure, in the ITS detector one can separate R-hadrons up to higher momenta ($p_{Rec} < 100$ GeV/c). However, the dE/dx resolution is worse than for the TPC and might give a large background. The improved momentum resolution gives a sharper correlation between dE/dx in the TPC and momentum (Fig. 7.15).

From the TOF signal one can determine β. Figure 7.16 depicts $1/\beta$ as a function of momentum for charge $+e$ R-hadrons (black) and protons (red). As expected the protons have a $1/\beta$ distribution around 1 (they are ultra-relativistic), while for R-hadrons $1/\beta$ first approaches 1 at very high momenta ($p > 250$ GeV/c). For $p_{Rec} > 10$ GeV/c and $1/\beta > 1.04$ (which corresponds to a 5 σ separation from protons), 99% of R-hadrons are in this region. Figure 7.17 indicates that the mass of R-hadrons can be measured directly.

The total probability for reconstruction and PID is 65% with this setup. Even with the lower reconstruction probability the PID capabilities are much better than in the TPC standalone case since combining information from different detectors enhance the separation power between R-hadrons and SM particles. For example, one can remove proton up to $p_{Rec} \sim 200$ GeV/c which will almost cut the R-hadrons free in the TPC. One should also note that since detailed response simulations were done with the lowest mass (100 GeV/c^2), any higher mass will be better separated from the SM hadrons than this lightest R-hadron.

7.2.3 ITS+TPC+TOF Simulation - Fractional Charge R-hadrons

Some models also predict stable massive particles with fractional charge ($\pm 1/3e$, $\pm 2/3e$, $\pm 4/3e$) [112, 131, 132]. Two types of R-hadrons with fractional charge ($+2/3e$, $+4/3e$) were chosen here. The reconstruction efficiency for ITS and TPC was found to be around 80% for both charge $+2/3e$ R-hadrons and charge $+4/3e$ R-hadrons. When a signal in the
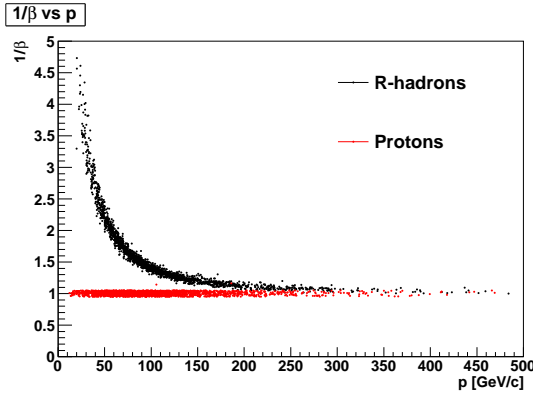
Figure 7.16: $1/\beta$ as a function of the recon-
structed momentum ($p_{Rec} > 10$ GeV/c) for
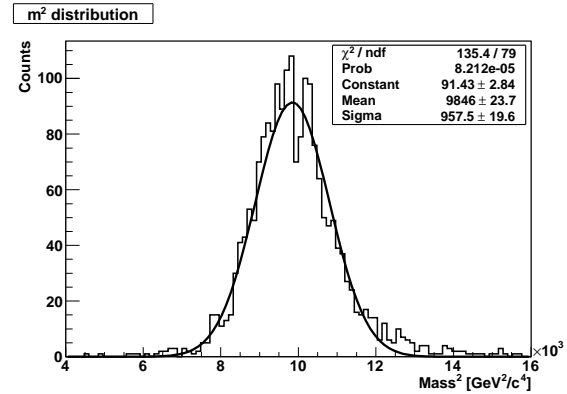charge $+e$ R-hadrons (black) and protons
(red).

Figure 7.17: Mass squared distribution for
charge $+e$ R-hadrons.

TOF detector is required the reconstruction efficiency drops to 62% in both cases.

The momentum distribution for charge $+2/3e$, charge $+e$, and charge $+4/3e$ R-hadrons is presented in Fig. 7.18 (the color coding used is the same throughout this section). As can be seen from the figure the momentum for R-hadrons with fractional charge is not well reconstructed (same reason as for charge $+2e$ R-hadrons).

Figure 7.19 and Figure 7.20 show the energy loss in the ITS and TPC, respectively as a function of the reconstructed momentum ($p_{Rec} > 10$ GeV/c) for charge $+2/3e$ (black), charge $+e$ (red), charge $+4/3e$ (green) R-hadrons, and protons (blue). The dE/dx for charge $+2/3e$ should be 4/9 times the dE/dx of charge $+e$ R-hadrons, while the dE/dx for charge $+4/3e$ should be 16/9 times the dE/dx for charge $+e$ R-hadrons because $dE/dx \propto q^2$. As can be observed from the figures, this seems like the case for both detectors. In the ITS case one can not distinguish between fractional and integer charge R-hadrons for momenta $p_{Rec} < 150$ GeV/c; the charge $+4/3e$ R-hadrons are complete separated from protons. In the TPC case a good separation between fractional and integer charge R-hadrons with $p_{Rec} > 100$ GeV/c was found; the charge $+2/3e$ R-hadrons are very well separated from protons for $p_{Rec} > 110$ GeV/c. Using velocity and momentum correlations one should be able to separate the R-hadrons with different charges at low momenta.

7.3   Discussions

In this section the possibility for ALICE to discover heavy stable charged particles based on the studies of the previous sections will be addressed.

At the nominal LHC design luminosity ATLAS and CMS will have 10^9 collisions per second which is as much as ALICE hopes to have in one year. While their triggering efficiency might be low, this is clearly outweighed by this much larger rate of collisions.
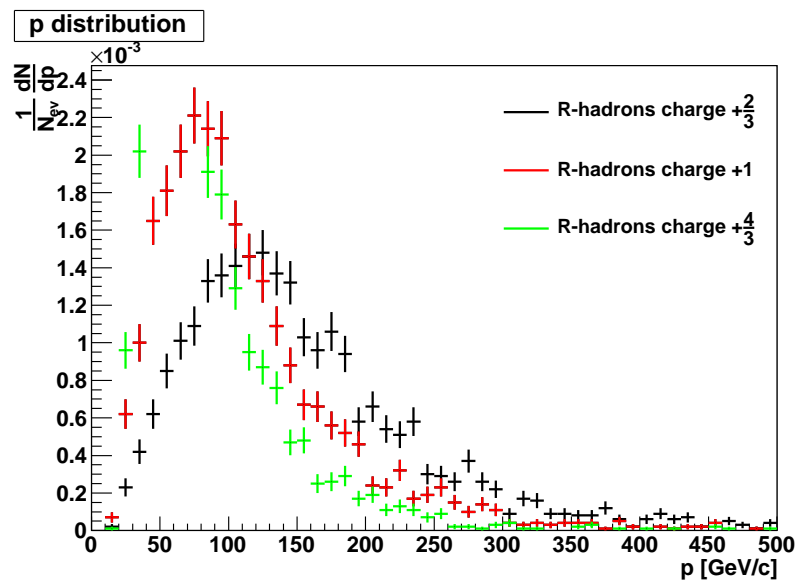
Figure 7.18: Momentum distribution for R-hadrons with fractional and integer charges. The difference in the momentum distributions appears because the reconstruction algorithm assumes charge $+e$ particles and is difficult to know from data which charge is correct.
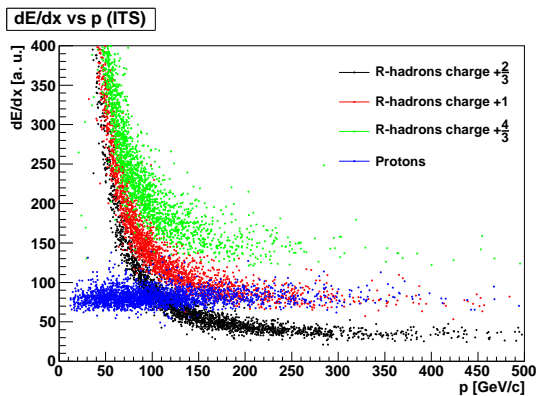

Figure 7.19: dE/dx in the ITS as a function of the reconstructed momentum ($p_{Rec} > 10$ GeV/c) for charge $+2/3e$ (black), charge $+e$ (red), charge $+4/3e$ (green) R-hadrons, and protons (blue).

Figure 7.20: dE/dx in the TPC as a function of the reconstructed momentum ($p_{Rec} > 10$ GeV/c) for charge $+2/3e$ (black), charge $+e$ (red), charge $+4/3e$ (green) R-hadrons, and protons (blue).
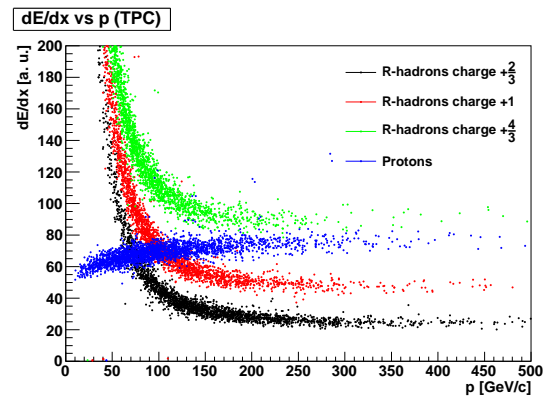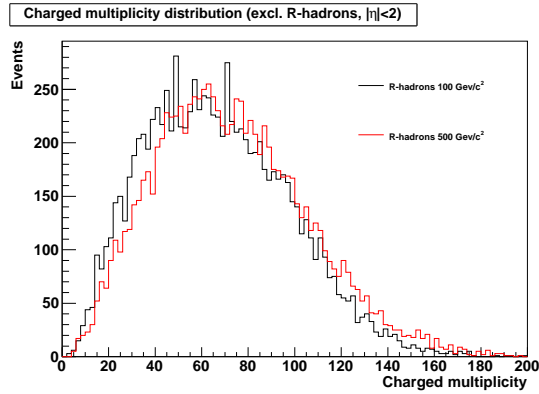
Figure 7.21: Charged particle multiplicity distribution for events with R-hadrons (excluding R-hadrons) for different values of $m_{\tilde{g}}$ as predicted by PYTHIA ($|\eta| < 2$) ($\sqrt{s} = 14$ TeV).
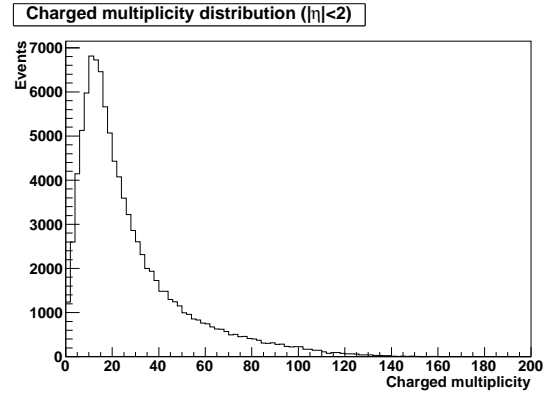
Figure 7.22: Charged particle multiplicity distribution for minimum bias events as predicted by PYTHIA ($|\eta| < 2$) ($\sqrt{s} = 14$ TeV).

However, at the start up of LHC the luminosity will be lower and the difference between the number of events for ATLAS, CMS and ALICE will be smaller and this might provide a window of opportunity for ALICE to make this exciting discovery.

ALICE has a high triggering efficiency and for events with R-hadrons where the associated charged particle multiplicity is large, see Fig. 7.21, one expect no trigger efficiency losses. Rather, in the case where ALICE has to downscale the trigger rates, it seems feasible to use the SPD fast multiplicity trigger to enhance the R-hadron sample. Figure 7.21 illustrates the charged particle multiplicity distribution (excluding R-hadrons) in the SPD acceptance ($|\eta| < 2$) for 10000 events with R-hadrons for 100 GeV/c^2 (black) and 500 GeV/c^2 gluino mass. Figure 7.22 shows the distribution of charged particles in the SPD acceptance for 100000 minimum bias events generated with the same version of PYTHIA used for the R-hadron study. The trigger fractions obtained for the two charged multiplicity distributions discussed above are presented in Fig. 7.23 and Fig. 7.24, respectively. The trigger fraction was computed by dividing the integral of each multiplicity bin by the total integral of the multiplicity histogram (for both minimum bias and R-hadron cases). Dividing the R-hadron trigger fraction histogram by the minimum bias one, the trigger enhancement is obtained (Fig. 7.25). For example, requiring more than 50 charged particles only ∼15% minimum bias events are accepted (see Fig. 7.24), while ∼67% (∼73%) R-hadron events for 100 GeV/c^2 (500 GeV/c^2) gluino mass pass the trigger cut (see Fig. 7.23). This effectively enhances the R-hadron sample by a factor 4 (5) for 100 GeV/c^2 (500 GeV/c^2) gluino mass (see Fig. 7.25).

Another option to enhance the number of R-hadron events is to use of the p_T trigger provided by the TRD. Two trigger scenarios have been considered: looking at the maximum p_T in each event and at the second largest p_T in each event ($|\eta| < 0.9$). In order to do this, 100000 minimum bias PYTHIA events were generated in the TRD acceptance
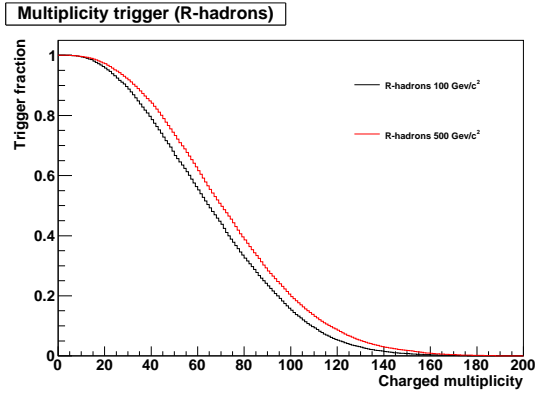
Figure 7.23: Trigger fraction distribution for events with R-hadrons for different values of $m_{\tilde{g}}$ in the SPD acceptance ($|\eta| < 2$).
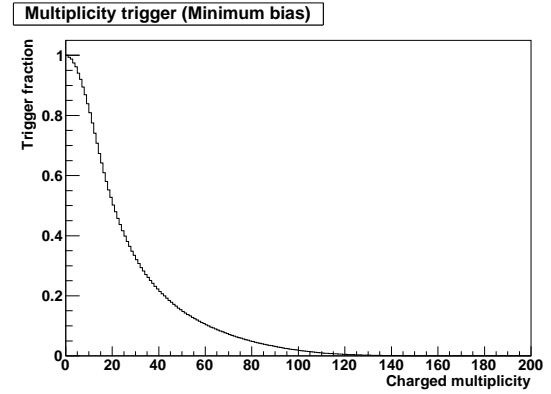
Figure 7.24: Trigger fraction distribution for minimum bias events in the SPD acceptance ($|\eta| < 2$).
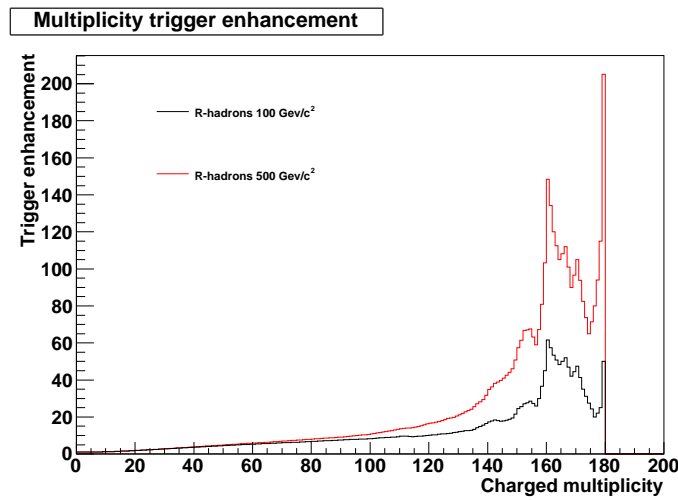

Figure 7.25: Multiplicity trigger enhancement for different values of $m_{\tilde{g}}$ in the SPD acceptance ($|\eta| < 2$). The sharp cut at 180 comes from the fact that no minimum bias events with multiplicity greather than this value were found in the simulated sample.
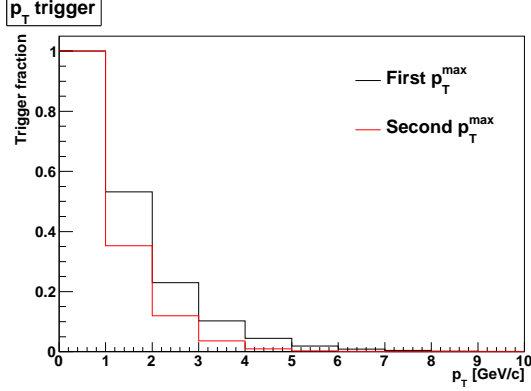
Figure 7.26: p_T trigger fraction distribution for minimum bias events for maximum p_T in the event (black) and the second largest p_T in the event (red) in the TRD acceptance ($|\eta| < 0.9$).
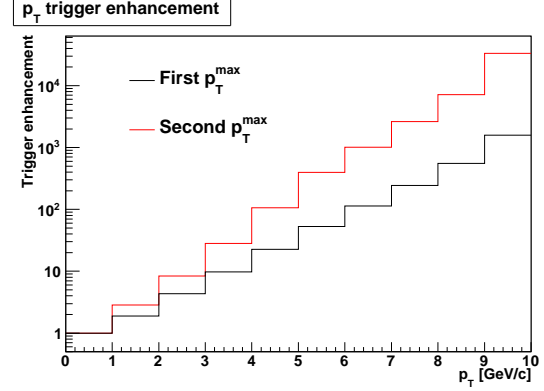
Figure 7.27: p_T trigger enhancement for maximum p_T in the event (black) and the second largest p_T in the event (red) in the TRD acceptance ($|\eta| < 0.9$).

($|\eta| < 0.9$). The trigger fractions are presented in Fig. 7.26 and the trigger enhancement, given by inverting the trigger fraction since all R-hadron events have a higher momentum, is depicted in Fig. 7.27. For the nominal TRD trigger limit ($p_T > 3$ GeV/c), a factor 10 enhancement is found for the first scenario (the max p_T in the event), but this is increased to 30 in the second scenario (the second largest p_T in the event). These number are given for the full TRD and additional investigations are required due to the limited number of TRD modules available.

While the TPC in standalone mode has some interesting possibilities in searching for this kind of new physics, to make a discovery one probably needs to have at least one "golden event" where two high p_T tracks approximately back-to-back with dE/dx consistent with high masses in ITS, TPC, and a time-of-flight indicating that the particles are slow are measured. To estimate the number of "golden events" (and one track events) in 10^9 collisions an η cut of $|\eta| < 1$ on the MC information together with the requirement that $p_{MC} > 10$ GeV/c and $1/\beta > 1.04$ (R-hadrons should be separable in the TOF barrel) were introduced. The number of events with one R-hadron or two R-hadrons that are reconstructed and identified are then determined from Eq. 7.1 and Eq. 7.2, respectively. In the estimation of the number of events with one R-hadron, the events with two R-hadrons where only one is reconstructed/identified were also included. The number of events with one or two R-hadrons per annual pp run in ALICE at $\sqrt{s} = 14$ TeV are listed in Table 7.2.

$$\text{One R-hadron} = 10^9 \times \frac{\sigma_{R-hadron}}{\sigma_{pp}} \times (P \times Fraction1 + (2P - 2P^2) \times Fraction2) \quad (7.1)$$

$$\text{Two R-hadrons} = 10^9 \times P^2 \times \frac{\sigma_{R-hadron}}{\sigma_{pp}} \times Fraction2 \quad (7.2)$$

where:

- $\sigma_{\mathrm{R-hadron}}$ is taken from Table 7.1.

- $\sigma_{pp} \sim 110$ mb (see Section 7.1).

- *Fraction*1 is the ratio between the number of events with one R-hadron which survives after the cuts ($|\eta| < 1$, $p_{MC} > 10$ GeV/c, $1/\beta > 1.04$) and the total number of events which are generated.

- *Fraction*2 is the ratio between the number of events with two R-hadrons which survives after the cuts and the total number of events which are generated.

- the factor 10^9 is the annual pp collisions recorded by ALICE.

- $P = 0.5 \times 0.65 = 0.325$ is the probability for a R-hadron to be charged and to be reconstructed (and identified) in ITS, TPC, and TOF.

Mass [GeV/c^2]	Fraction1	Fraction2	One R-hadron	Two R-hadrons
100	0.35	0.13	59+33	6.7
200	0.39	0.16	2.6+1.6	0.34
300	0.41	0.18	0.34+0.20	4.9×10^{-2}
500	0.42	0.23	$(2.0 + 1.7) \times 10^{-2}$	4.0×10^{-3}

Table 7.2: Number of events with at least one or two R-hadrons at $\sqrt{s} = 14$ TeV ($|\eta| < 1$, $p_{MC} > 10$ GeV/c, $1/\beta > 1.04$) per 10^9 events (the ALICE nominal annual pp run). For the One R-hadron case, the events with two R-hadrons where only one is reconstructed/identified are also included.

It is important to consider the background for this kind of study, as this will presumably be the biggest problem for at least single track events. The background could come from a high p_T track associated with a wrong TOF hit from a slow particle, or from wrong measurements by the TPC.

The background was considered in the following. The simulated data used for this study has been produced in the Physics Data Challenge 2006 (PDC06) and consists of 2100000 minimum bias events. The same cuts as the ones used in the R-hadron study were applied (see Section 7.2). Figure 7.28 shows that only 2289 tracks with momentum $p > 10$ GeV/c are found from the 2.1 million analyzed events. For the TPC dE/dx one lonely point with a dE/dx close to 100 was found, see Fig. 7.29. Figure 7.30 illustrates the $1/\beta$ as a function of momentum for 2065 tracks, but as can be seen from Fig. 7.31, here two particles have $1/\beta > 1.04$ which is the PID cut for R-hadrons.

A similar background analysis was performed for around 27.5 millions triggered events recorded at the center-of-mass energy of 7 TeV. An event with a reconstructed vertex position, vtx$_z$, was accepted if $|\text{vtx}_z - \text{vtx}_0| < 10$ cm. Only primary tracks with at least 70 TPC clusters, a χ^2 per cluster less than 4, at least one cluster in the SPD, and not flagged

Figure 7.28: Momentum distribution normalized by the number of events, N_{ev}, for particles with $p > 10$ GeV/c from PDC06 data.
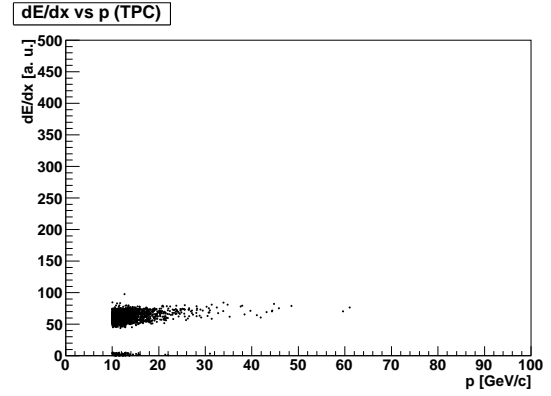
Figure 7.29: dE/dx in the TPC as a function of the momentum for particles with $p > 10$ GeV/c from PDC06 data.

Figure 7.30: $1/\beta$ as a function of momentum for particles with $p > 10$ GeV/c from PDC06 data.

Figure 7.31: $1/\beta$ distribution for particles with $p > 10$ GeV/c from PDC06 data.

as kink daughter were required. A p_T dependent cut on the distance to closest approach (d_0) to the reconstructed event vertex in the transverse direction was also applied: tracks were rejected if $d_0 > 0.35$ mm $+ 0.42$ mm $\cdot p_T^{-0.9}$. All these cuts are detailed in Sections 9.1 and 9.2.
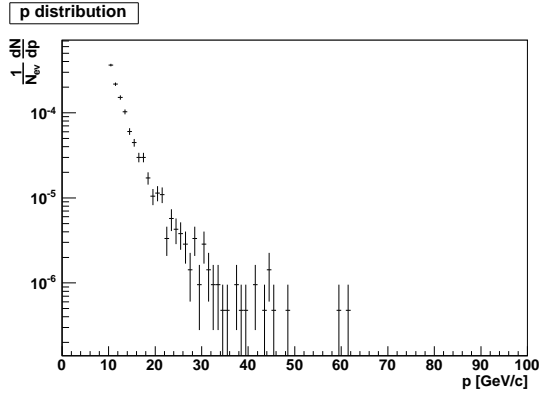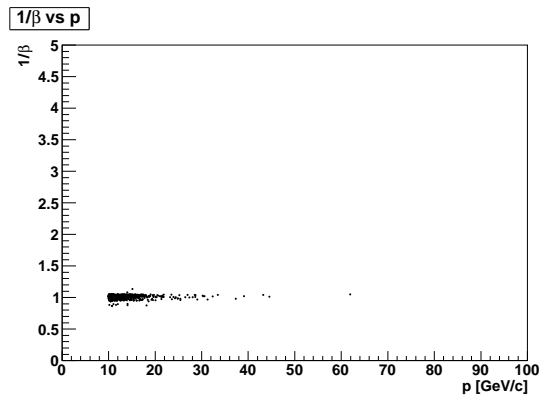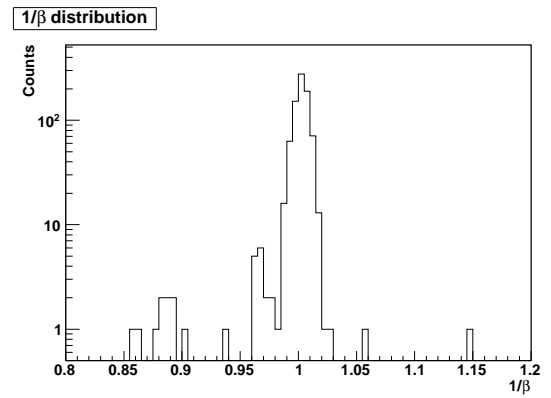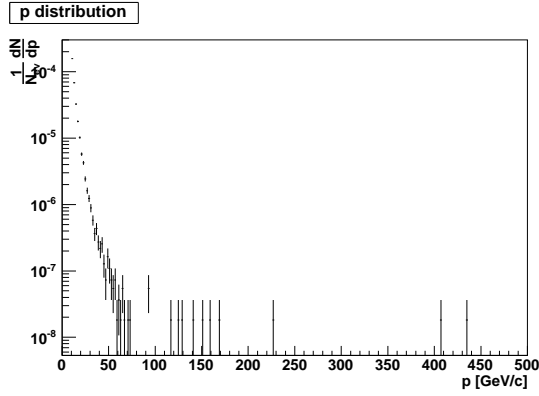

Figure 7.32: Momentum distribution normalized by the number of events, N_{ev}, for particles with $p > 10$ GeV/c from 27.5 millions events recorded at $\sqrt{s} = 7$ TeV.

Figure 7.33: dE/dx in the TPC as a function of the momentum for particles with $p > 10$ GeV/c from 27.5 millions events recorded at $\sqrt{s} = 7$ TeV.

Figure 7.32 shows the momentum distribution for tracks with $p > 10$ GeV/c; 16792 tracks fulfill this cut. When the TPC dE/dx was correlated with the momentum, 18 tracks with $dE/dx > 100$ and $p > 10$ GeV/c were found (see Fig. 7.33). Figure 7.34 presents the $1/\beta$ as a function of momentum for 8805 tracks, but as can be seen from Fig. 7.35, neither one passes our PID cut for R-hadrons ($1/\beta > 1.04$).

Figure 7.34: $1/\beta$ as a function of momentum for particles with $p > 10$ GeV/c from 27.5 millions events recorded at $\sqrt{s} = 7$ TeV.

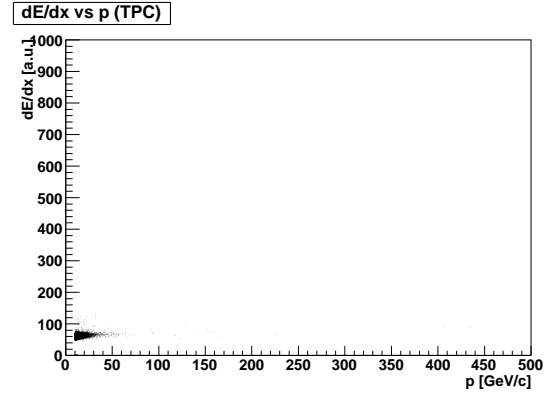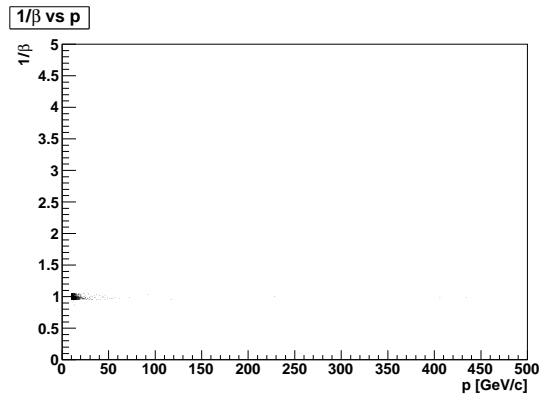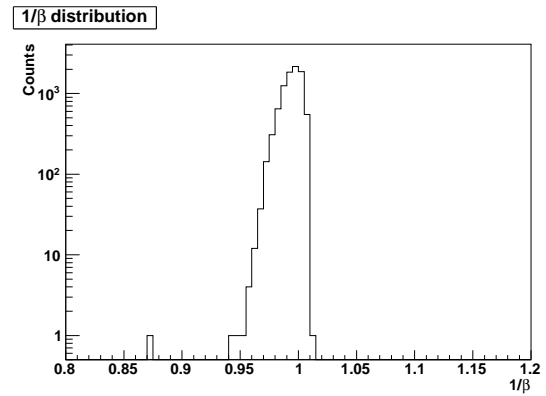Figure 7.35: $1/\beta$ distribution for particles with $p > 10$ GeV/c from 27.5 millions events recorded at $\sqrt{s} = 7$ TeV.

7.4   Conclusions

With the start-up of the LHC, the discovery of physics beyond the Standard Model through heavy stable charged particles is a possibility also for ALICE. Using the tracking system and the TOF detector, ALICE has two techniques for identification of heavy stable charged particles: the dE/dx method and the TOF method. The TPC dE/dx can very easily separate new particles from SM ones if they have charge $q \geq 2e$. At the nominal TPC gas gain, ALICE can also detect and in some cases separate particles of charge $2/3e$ from charge $+e$ high momentum particles. The ALICE TOF detector can not only separate the slow particles from the faster SM ones, but can also, together with the momentum information from the tracking, give an estimate for the mass of these particles.

The main ALICE advantage comes from its excellent particle identification capabilities which implies that one "golden event" will be enough to discover these particles. Figure 7.36 shows a simulated "golden event" where two gluinos produced approximately back-to-back hadronized into two charged R-hadrons with high p_T, dE/dx consistent with high masses in ITS, TPC, and a time-of-flight indicating that the particles are slow.

No attempts were done for now to search for these particles in the available data sample collected at $\sqrt{s} = 7$ TeV as the momentum resolution of the TPC needs more investigations at the expected R-hadrons momenta. Also the number of expected charged R-hadrons at this energy is low.
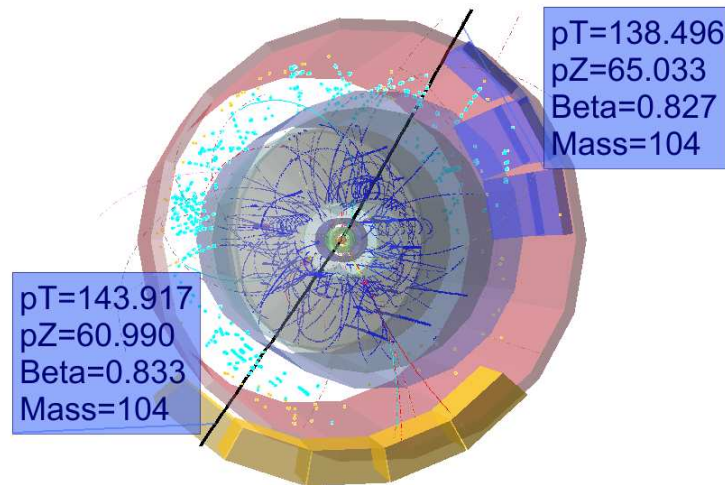

Figure 7.36: A fully simulated R-hadron event generated with PYTHIA in the ALICE central barrel at $\sqrt{s} = 14$ TeV. Two 100 GeV gluinos are produced back-to-back and form two charged R-hadrons. The velocity and mass is determined from the time-of-flight, the track length and the momentum.

Chapter 8

PID using the TPC dE/dx

This chapter describes an early study based on ALICE simulated data done to understand how and to what precision identified particle yields can be obtained on the relativistic rise when the average energy loss, $\langle dE/dx \rangle$, and resolution, $\sigma_{dE/dx}$, are known. Two methods have been compared for this: R_π (STAR approach for statistical PID) and Δ_π (the simplest approach). The Δ_π method was found to be more suitable in the case of ALICE.

8.1 Introduction

The STAR experiment at RHIC has demonstrated that with a dE/dx resolution of 8 % statistical PID is feasible on the relativistic rise ($\beta\gamma > 4$, $p_T > 3$ GeV/c) [133, 134, 135]. Figure 8.1 shows the measurement of the p/π^+ and $\bar{p}/\pi^-$ ratios as a function of transverse momentum for particles identified with the TOF ($p_T < 3$ GeV/c) and the TPC ($p_T > 3$ GeV/c) detectors at STAR.

In principle statistical PID of π, K, and p can be done up to 50 GeV/c or more, because the energy loss rises logarithmically from $\beta\gamma \sim 3.6$ (MIP) to $\beta\gamma \sim 1000$ (the plateau) (see Section 5.4.1). As $\beta\gamma = p/m$, one will have an almost constant separation between particles with different mass proportional to $log(p/m_1) - log(p/m_2) = log(m_2/m_1)$ so that the separation between π and K is much larger than the separation between K and p.

The challenge of using the TPC dE/dx for STAR (and ALICE) is that the separation between particles is not clean, so that the particle yield has to be extracted statistically, e.g. from a fit to the dE/dx distribution. The dE/dx measured in a momentum interval can be fit with a sum of 3 Gaussians (π, K, and p) with a total of 9 parameters: 3 yields, 3 mean positions, and 3 widths. The main point of the study in this chapter is therefore to constrain as many parameters as possible. If the TPC dE/dx is well calibrated the $\langle dE/dx \rangle$ should only depend on $\beta\gamma$. If one can extract $\sigma_{dE/dx}$ from the data then one can in principle constrain the mean and the width, i.e. 6 of the 9 parameters.

In STAR, the Bichsel function from Photo Absorption Ionization (PAI) energy loss calculations [96] has been adopted as a prediction for the dE/dx, i.e., to constrain the mean position of the Gaussians. We have previous to this study done a comparison between
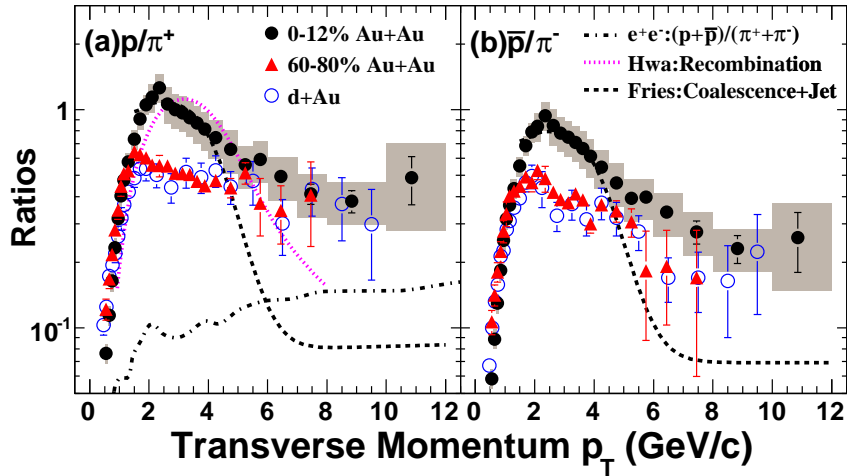
Figure 8.1: Measurements by STAR of the p/π^+ (left) and $\bar{p}/\pi^-$ (right) ratios from dAu and AuAu collisions at $\sqrt{s_{NN}} = 200$ GeV compared with the $(p + \bar{p}/(\pi^+ + \pi^-)$ ratio from light quark jets in e^+e^- collisions at $\sqrt{s} = 91.2$ GeV (dotted-dashed line) and model calculations (dotted and dashed lines). Figure is taken from [134].

energy loss calculations by Bichsel and GEANT4 to results from an ALICE TPC test beam and it was found that the two PAI calculations disagree somewhat and that GEANT4 gives the best description of the data (because Bichsel includes sub-threshold energy loss in his calculation which produces little or no ionization) [136]. Even in the best case the energy loss and resolution is modified by detector effects, so therefore it seems more likely that the $\langle dE/dx \rangle$ curve will have to be extracted from data.

The focus in the next sections is not on how the parametrizations for $\langle dE/dx \rangle$ and $\sigma_{dE/dx}$ are obtained from real data, but rather on how and to what precision the yields can be extracted once these functions are known. The methods are applied to real data in Chapter 9.

8.2   Mean dE/dx and Resolution from MC Data

8.2.1   Input Data and Cuts

The simulated data used for this study has been produced in the Physics Data Challenge 2009 (PDC09) and consists of nine runs (81590 to 81599) from the LHC09a4 production (1149000 minimum bias PYTHIA events). The data reflects the status of the alignment and the installed detectors as of May 2009. The energy used in the simulation was 10 TeV and the magnetic field was 0.5 T. Only triggered events with a reconstructed vertex were

analyzed [1]: 977906 events fulfilled these requirements.

Only primary tracks with at least 50 TPC clusters, a χ^2 per cluster of less than 3.5, a distance to the vertex less than 3 cm in both z and transverse directions, and not flagged as kink daughter were required (see Section 9.2). Furthermore, a cut in pseudo-rapidity, $|\eta| < 0.9$, and in transverse momentum, $p_T > 0.5$ GeV/c, were added on top of the primary track selection (to be in a region of optimal performance for the TPC). In order to have a pure sample, only tracks with a MC info as pions, kaons, or protons were accepted.
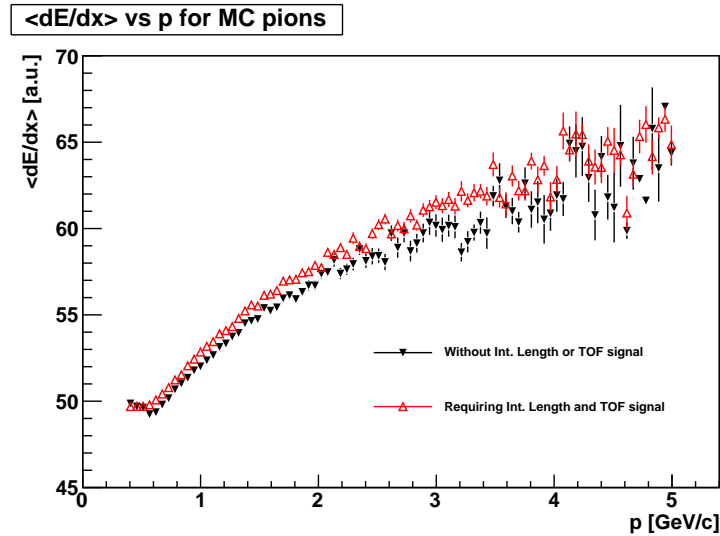

Figure 8.2: $\langle dE/dx \rangle$ as a function of the momentum for MC pions. The black filled triangles represent tracks that do not reach TOF and the red open triangles tracks that reach and have TOF signal.

A first observation from the reconstructed data was a systematic shift between data with and without TOF signal. Figure 8.2 shows this shift for MC identified pions.

To understand the origin of this discrepancy the $\eta - \phi$ correlations (Fig. 8.3) were investigated for tracks that do not reach TOF (left) and tracks that reach and have TOF signal (right). As can be seen from Fig. 8.3 the tracks that do not reach TOF are mostly at the edges (TOF coverage) and inside a region defined by $|\eta| < 0.2$ and $4 < \phi < 6$ (looks like a problem with one of the TOF modules), while the ones with TOF signal are uniformly distributed within the available acceptance.

It seems likely that the origin of the problem is the large topological differences between the tracks with and without TOF signals that are not properly corrected for. As this effect deteriorate the dE/dx resolution, only tracks with TOF signals were used from now on.

Figure 8.4 shows that there are tracks with a TOF signal and assigned TPC clusters ($N_{TPC\ clusters} > 50$) without a TPC signal ($dE/dx \approx 0$). The problem may be related with the gaps between TPC sectors as the $\eta - \phi$ correlations for these tracks present a structure

---

[1]The MB2 trigger condition detailed in Section 4.2.4 was used to select events.
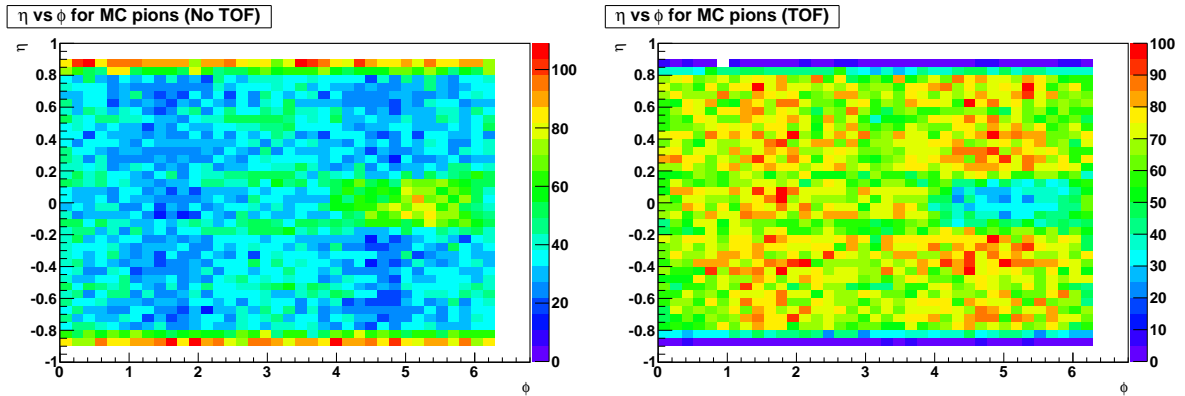
Figure 8.3: $\eta - \phi$ correlations for MC identified pions that do not reach TOF (left) and pions that reach TOF and have a TOF signal (right).

compatible with these gaps (see Fig. 8.5). All tracks with $dE/dx < 20$ were removed from the analysis.
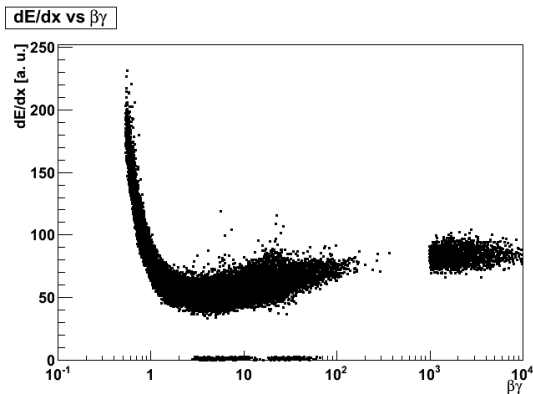
Figure 8.4: dE/dx as a function of the $\beta\gamma$ for all MC identified particles.
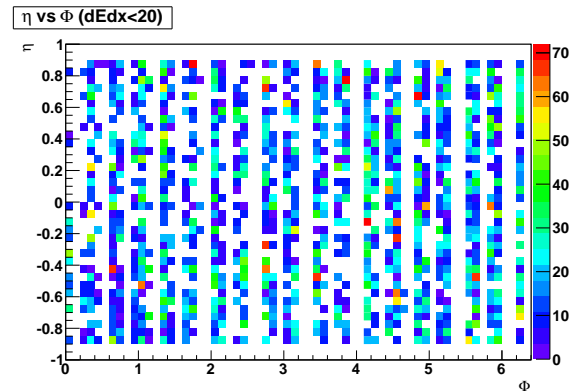
Figure 8.5: $\eta - \phi$ correlations for tracks with $dE/dx < 20$.

8.2.2   Extracting the Mean dE/dx Curve

Figure 8.6 shows the $\langle dE/dx \rangle$ as a function of $\beta\gamma$ for all MC identified particles. The zoom in Fig. 8.7 shows that a jump occurs around $\beta\gamma \sim 3$ which is the point where the pions are above the momentum cut. Figure 8.8 shows the same curve, but for π and K separately. It is clear that there is not a single curve, but rather two curves (three curves if protons are also included).

In order to understand this bias, the mean number of TPC clusters (Fig. 8.9) and at the ratio between $N_{TPC\ clusters}$ and $N_{TPC\ clusters\ findable}$ (Fig. 8.10) for pions (black circles) and kaons (red squares) were plotted. Here the $N_{TPC\ clusters}$ represents the number of assigned
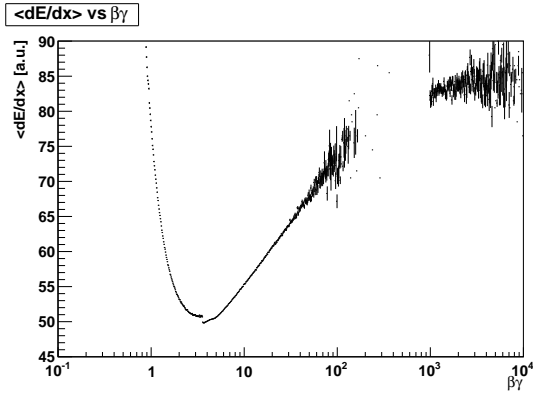
Figure 8.6: $\langle dE/dx \rangle$ for all MC identified particles as a function of $\beta\gamma$.
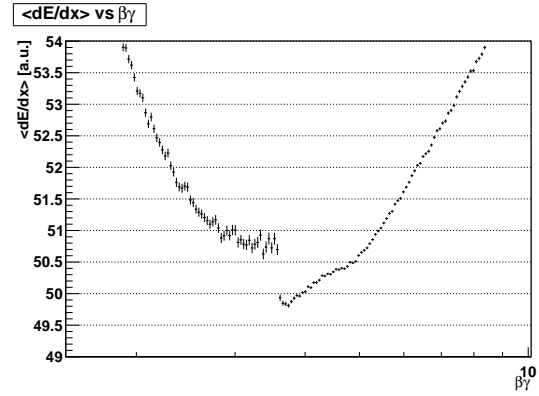
Figure 8.7: A zoom into $\langle dE/dx \rangle$ for all MC identified particles in the minimum ionization region as a function of $\beta\gamma$.

clusters to the track, while the $N_{TPC\ clusters\ findable}$ is the number of found clusters for the given track (see Section 5.3.1). Figure 8.9 shows a clear difference between pions and kaons and it seems the cluster loss only depends on dE/dx. But Fig. 8.10 indicates that the cluster efficiency is almost the same. The origin of this difference can be the different topology as well as a problem with the track length correction. For a given $\beta\gamma = p/m$ the different particles have quite different momentum and therefore the track segment length over the pads, Δx, is different.

In the following three curves were therefore used to describe the $\langle dE/dx \rangle$, one for each particle specie.
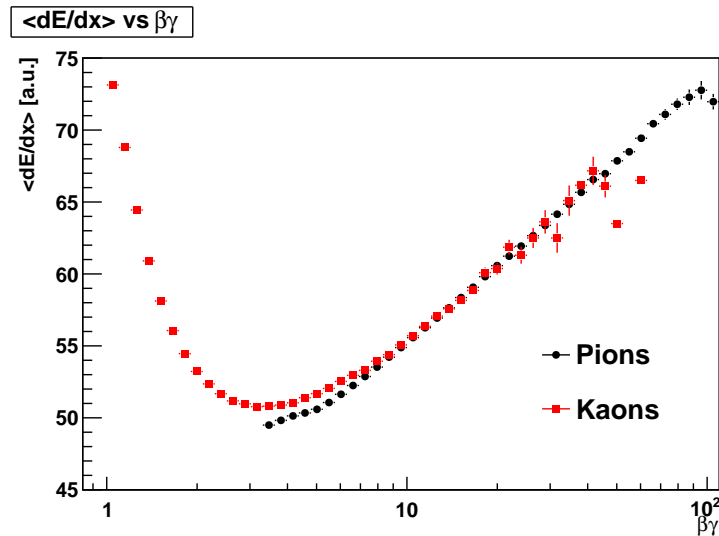
Figure 8.8: $\langle dE/dx \rangle$ as a function of $\beta\gamma$ for MC π (black circles) and K (red squares).
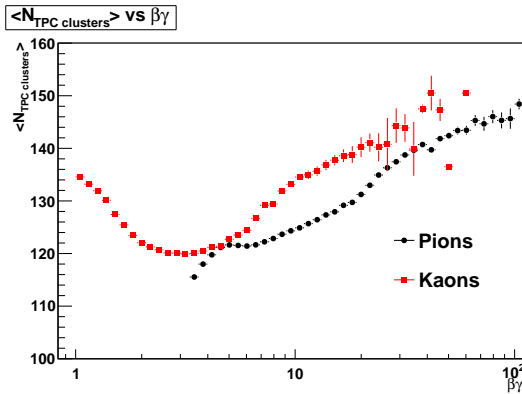
Figure 8.9: Mean number of TPC clusters per track as a function of $\beta\gamma$ for MC π (black circles) and K (red squares).
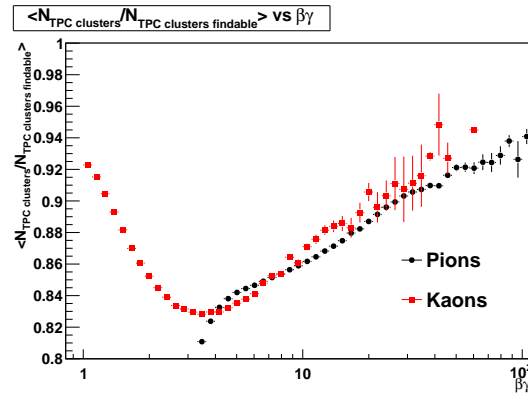
Figure 8.10: Ratio between $N_{TPC\ clusters}$ and $N_{TPC\ clusters\ findable}$ as a function of $\beta\gamma$ for MC π (black circles) and K (red squares).

The $\langle dE/dx \rangle$ resolution, $\sigma_{dE/dx}$, is 5-6 %, or around 3-4 ADC ch. To determine the $\langle dE/dx \rangle$ with a much better precision than this requires a precise fit. Figure 8.11 shows the fit to the $\langle dE/dx \rangle$ curve for MC identified pions. The functional shape of the fit was approximated by:

$$\langle dE/dx \rangle = k_0 \cdot \left(\frac{1}{x^{k_3}} + 1\right) \cdot \frac{x^{k_1}}{k_2 + x^{k_1}} \tag{8.1}$$

where $x = \beta\gamma$ and k_0, k_1, k_2, and k_3 are constants obtained from the fit.

Figure 8.12 illustrates the mean after the fit has been subtracted. It is clear that even with MC truth and a fit that looks reasonable the precision of $\langle dE/dx \rangle$ is not great because one will have systematic shifts of 0.05-0.1 σ. The discrepancy is also revealed by the reduced χ^2 for the fit, so that one can try to find a fit function that describes the data with higher precision.

8.2.3   Extracting the dE/dx Resolution

The dE/dx is obtained as the truncated mean of up to 159 clusters (see Section 5.4.2). One should be able to get a rough estimate from the energy loss data of the track itself. The dE/dx is calculated with the truncated mean algorithm as the mean of the 70 % [2] lowest charges. If one would also determine the RMS, one would expect that the resolution should be:

$$\sigma_{dE/dx} = \frac{\text{RMS}}{\sqrt{N_{TPC\ clusters}}}. \tag{8.2}$$

However, because there are strong positive correlations between the charge of neighboring hits on the track, due to diffusion and pad row couplings, one will in general underestimate the resolution with this method, i.e. the resolution would be too good.

---

[2]This was the value used in the simulations performed in 2009.
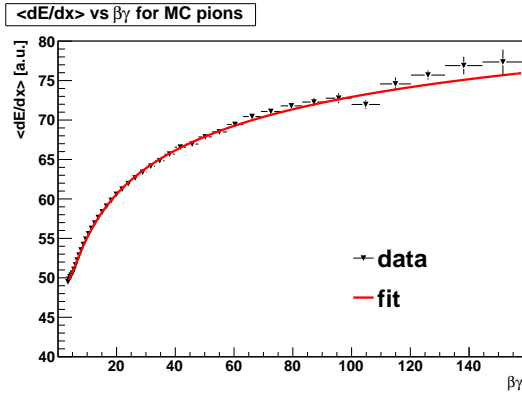
Figure 8.11: $\langle dE/dx \rangle$ as a function of $\beta\gamma$ for MC identified pions (black triangles) fitted with Eq. 8.1 (red line).
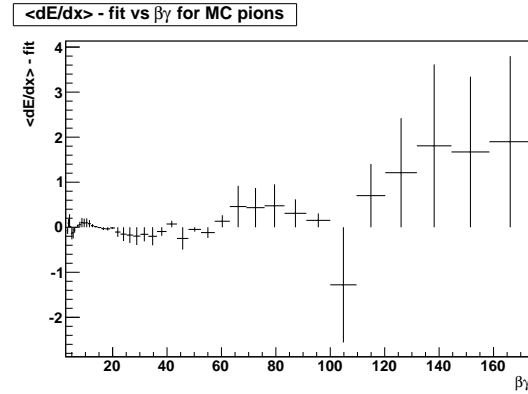
Figure 8.12: The results of the fit subtraction from $\langle dE/dx \rangle$ (pions) as a function of $\beta\gamma$.

Instead one will have to extract the dE/dx resolution from the data and parametrize it. One expects that the dE/dx resolution can be parametrized as:

$$\sigma_{dE/dx} = \sigma_0 \cdot dE/dx^a \cdot \left(\frac{159}{N_{TPC\ clusters}} \right)^b , \tag{8.3}$$

where $N_{TPC\ clusters}$ is the number of TPC clusters on the track and the constants are expected to be: $\sigma_0 \approx 0.05$, $a \approx 1$, and $b \approx 0.5$.

Figure 8.13 presents the mean number of clusters per track for all MC identified particles. The minima for protons and kaons follow the minima for dE/dx implying that the gain in the simulation is so low that MIP particles loose clusters because the charge goes below threshold. It is important that this bias is properly handled if it is present in the experimental ALICE data. At the moment, the gain of the TPC is higher than that in this MC data set, see [137, 138], and one could hope that the higher gain will remove this bias.

For the MC data a multi-dimensional histogram was constructed with dE/dx as a function of MC PID, $N_{TPC\ clusters}$, and momentum p. By projecting dE/dx versus p and fit the dE/dx distribution for narrow intervals in momentum, the $\langle dE/dx \rangle$ and $\sigma_{dE/dx}$ can be determined. In this way a large data set is extracted and can be described with Eq. 8.3. In order to estimate the constants in the parametrization, at least on the average, the dependence on dE/dx and $N_{TPC\ clusters}$ should be removed. The constants were found to be $\sigma_0 = 5.1$ %, $a = 1$ and $b = 0.7$. Figure 8.14 depicts the fitted resolution divided by the parametrized resolution as a function of $\langle dE/dx \rangle$ (left) and $N_{TPC\ clusters}$ (right). This shows that the parametrization to a large degree corrects for the dependence on these variables.

While σ_0 and a are as expected, $b = 0.7$ is different from the expectation of $b = 0.5$ (square root dependence). This suggests that the parametrization is not optimal. It is clear from Fig. 8.13 that the dE/dx and $N_{TPC\ clusters}$ are correlated, so that it is a bit

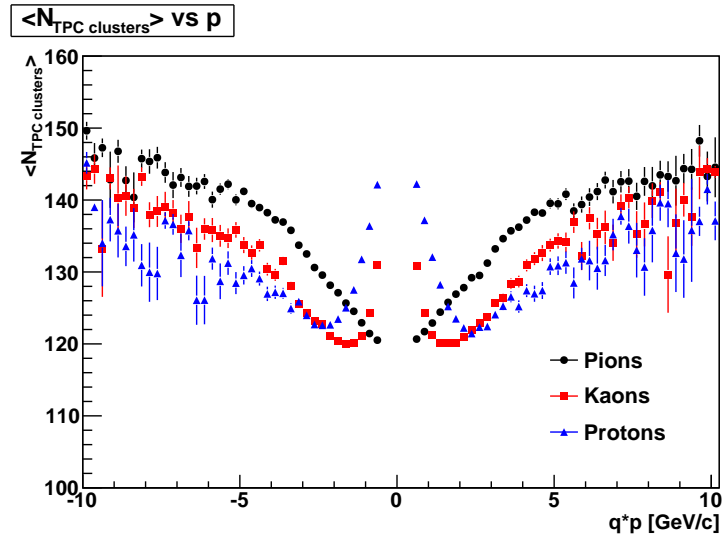Figure 8.13: Mean number of TPC clusters per track as a function of the rigidity for MC identified π (black circles), K (red squares), and p (blue triangles).
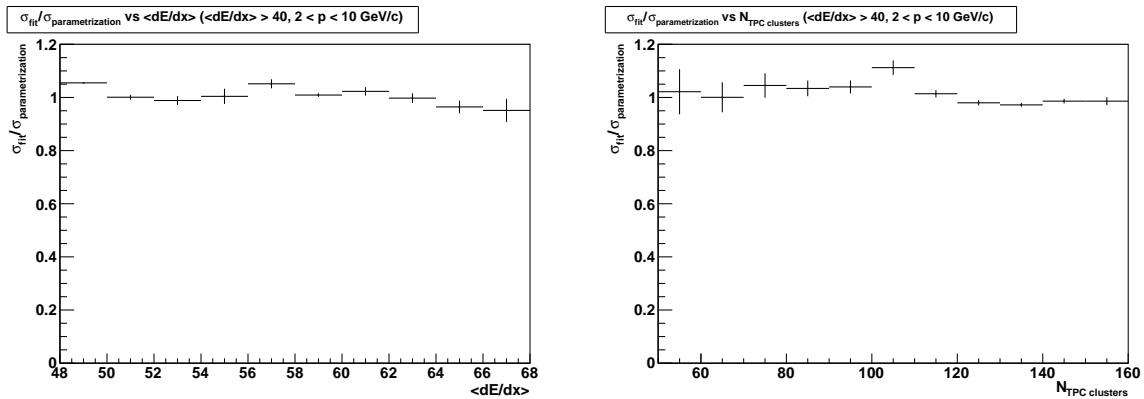

Figure 8.14: The fitted resolution divided by the parametrized resolution as a function of $\langle dE/dx \rangle$ (left) and $N_{TPC\ clusters}$ (right) ($dE/dx > 40$ and $2 < p < 10$ GeV/c).

uncertain where the problem is. It might also be that the track length should be used instead of $N_{TPC\ clusters}$ as this takes into account both the η-variation and the difference between short, medium and long pads. For now, the expression found will be used.

8.3 Determination of the Identified Particle Yields

The focus in this section is on the determination of the yields of π, K, and p in a narrow momentum interval using the $\langle dE/dx\rangle$ and $\sigma_{dE/dx}$ found in the last section.

This means that no full p_T spectra will be constructed, but rather the MC and reconstructed yields will be compared directly since the rest of the analysis should be very similar to the one that will be used to construct charged p_T spectra.

8.3.1 Two Different PID Approaches

The STAR method has been presented in several papers [139, 140]. The idea is for each momentum interval to study the quantity, R_π, defined as:

$$R_\pi = \frac{dE/dx - \langle dE/dx\rangle_\pi}{\sigma_{dE/dx}}, \tag{8.4}$$

where $\langle dE/dx\rangle_\pi$ is the expected energy loss for a pion and the energy loss resolution, $\sigma_{dE/dx}$, varies track-by-track [3].

From the definition of R_π one expects that the pions will be described roughly by a Gaussian with the mean position, $\mu = 0$, and the width, $\sigma = 1$. On the other hand, as the $\sigma_{dE/dx}$ is varying track-by-track, the K and p peaks will also vary track-by-track, and so the K and p distributions do not have to be Gaussian and do not have to have small widths. No information is gained to constrain the width of K and p and even the locations of the K and p peaks rely on the specific sample properties (resolution distribution).

An alternative to the STAR method is to study:

$$\Delta_\pi = dE/dx - \langle dE/dx\rangle_\pi \tag{8.5}$$

where $\langle dE/dx\rangle_\pi$ is the expected energy loss for a pion.

The method is simpler than R_π, but it does not have to give Gaussian distributions as one folds Gaussian distributions with different widths. Also in this case no additional information to constrain the widths and means of K and p is achieved (even the width of π is not constrained now).

8.3.2 Toy Model

In order to study which method is better, a toy model was developed. In this model the R_π and Δ_π distributions are generated track-by-track using random p and $N_{TPC\ clusters}$,

---

[3]The STAR experiment uses $\log dE/dx$ and $\log\langle dE/dx\rangle$ to get a Gaussian distribution. This also affects $\sigma_{dE/dx}$ which then supposedly does not depend on dE/dx.

the ALICE $\langle dE/dx \rangle$ and $\sigma_{dE/dx}$ parametrizations found in Section 8.2.3. The separation between particles is given as:

$$S_{AB} = \frac{|\mu_A - \mu_B|}{\sqrt{\sigma_A \sigma_B}} \qquad (8.6)$$

where A, B can be π, K, and p, $\mu_{A,B}$ and $\sigma_{A,B}$ are the mean position and width of the R_π (Δ_π) distribution, respectively.

For each track, a random flat momentum distribution between 0 and 20 GeV/c and a random flat $N_{TPC\ clusters}$ distribution between 50 and 159 were generated. Knowing the momentum and assuming the PID, the $\beta\gamma$ could be calculated. From $\beta\gamma$ and the ALICE $\langle dE/dx \rangle$ parametrization, one can get the $\langle dE/dx \rangle$. From the just calculated $\langle dE/dx \rangle$ and $N_{TPC\ clusters}$ on the track, the $\sigma_{dE/dx}$ could be obtained. Assuming a Gaussian distribution, random dE/dx signals could be generated considering the track to be a pion, kaon, and proton, and histograms with R_π and Δ_π are filled. Fitting R_π and Δ_π with Gauss functions one can get the mean position, μ, and the width, σ, used in Eq. 8.6.

Two different cases have been considered: an "ideal" scenario when the $\sigma_{dE/dx}$ is based only on the number of TPC clusters and $\langle dE/dx \rangle$ and a "realistic" case when the $\sigma_{dE/dx}$ is calculated from the number of TPC clusters and dE/dx. So in the "ideal" scenario, knowing the particle type, one can use $\sigma_{dE/dx}$ for that particle, e.g. assuming a pion the $\sigma_{dE/dx}$ for a pion will be used. But if the particle type is not known, $\sigma_{dE/dx}$ should be calculated from the "realistic" scenario. The separation for πK, πp, and $K p$ was determined by using Eq. 8.6. Figure 8.15 shows the separation from R_π and Δ_π methods for both scenarios. As can be seen from the figure in the "ideal" case the R_π method gives a better separation than Δ_π, while in the "realistic" case the Δ_π method is better.

Having the toy model predictions, the separations obtained from the ALICE simulated data were also investigated. The πK, πp, and $K p$ separations were computed for MC identified particles using Eq. 8.6. The results are depicted in Fig. 8.16. The two methods (R_π and Δ_π) seem to perform similarly, even though R_π provides a slightly worse separation for πp and $K p$ for $p > 3$ GeV/c.

8.3.3 Constructing the Expected Shape

The problem observed in the Section 8.3.1 was that in both methods one did not obtain the shape of the dE/dx distribution for K and p. In this section the shape distribution will be "generated" track-by-track using p, $N_{TPC\ clusters}$, the $\langle dE/dx \rangle$ and $\sigma_{dE/dx}$ parametrizations.

The method is as follows. For each track, random dE/dx signals are generated assuming that it is a pion, kaon, and proton, and fill histograms with R_π and Δ_π. To generate the signals, $\beta\gamma$ is obtained from the momentum of the track assuming the PID (mass). Knowing the $\beta\gamma$, the $\langle dE/dx \rangle$ is determined. From $\langle dE/dx \rangle$ and $N_{TPC\ clusters}$, the $\sigma_{dE/dx}$ is calculated. Assuming a Gaussian distribution, 10 values of dE/dx can then be generated. Also the $\sigma_{dE/dx}$ can be recalculated using the generated dE/dx and $N_{TPC\ clusters}$. Then one can fill R_π and Δ_π distributions.

This method means that a large statistics prediction for what the shape of π, K, and p should be given *our specific* data sample (in particular the distribution of number of TPC
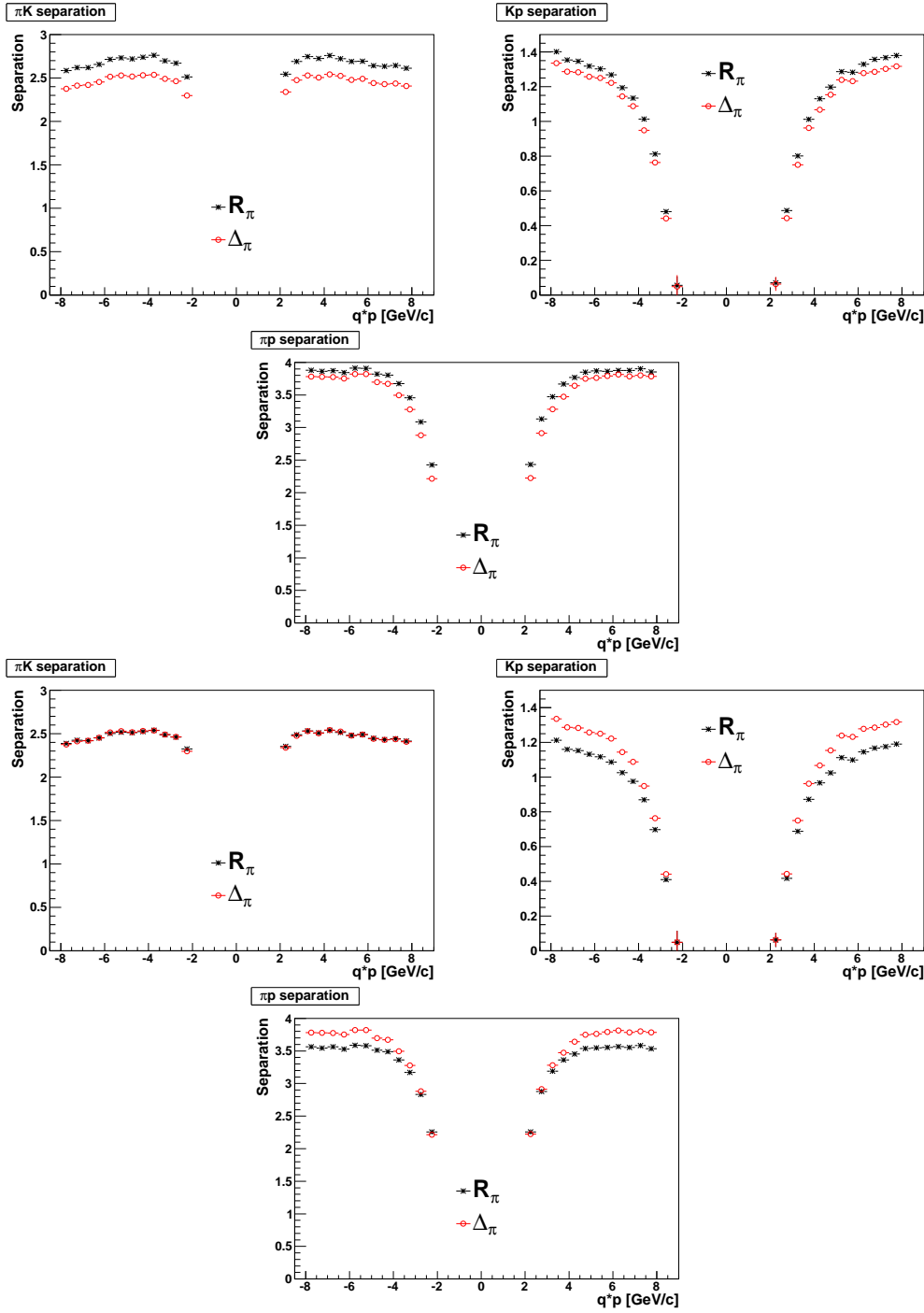
Figure 8.15: The πK (left), πp (middle) and Kp (right) separations as a function of the rigidity from the "ideal" (upper) and "realistic" (lower) toy model. The black stars represent the results from the R_π method and the red open circles the results from the Δ_π method.
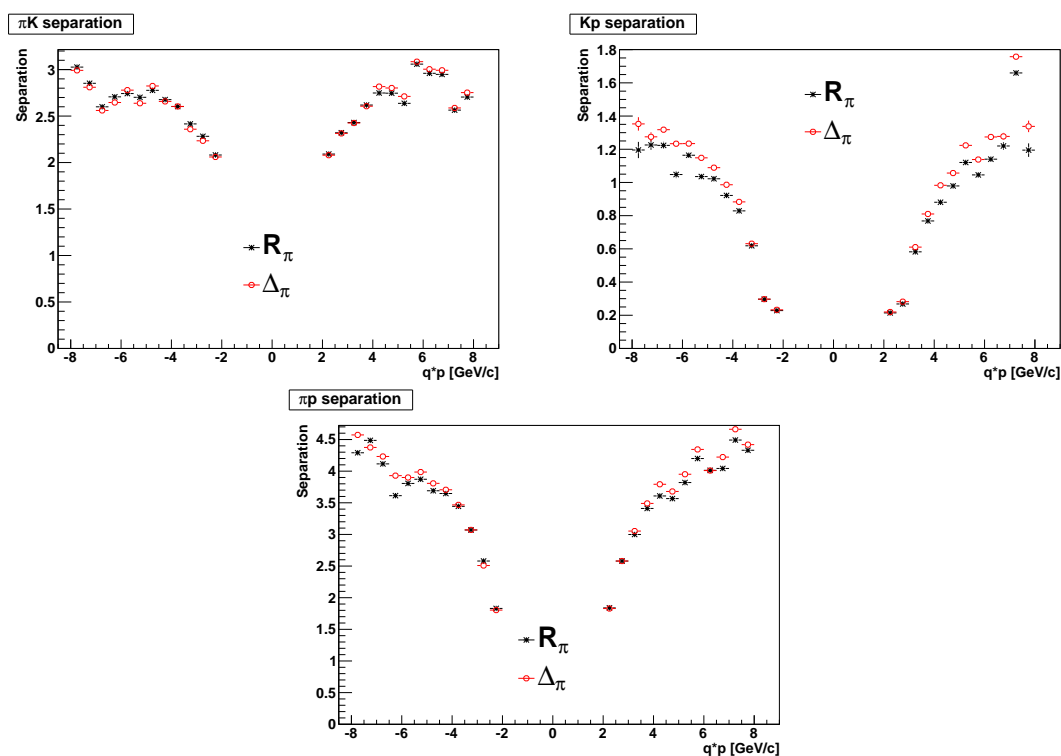
Figure 8.16: The πK (left), πp (middle) and Kp (right) separations as a function of the rigidity for MC identified particles from ALICE simulated data. The black stars denote the R_π method results, while the Δ_π method results are given by the red open circles.
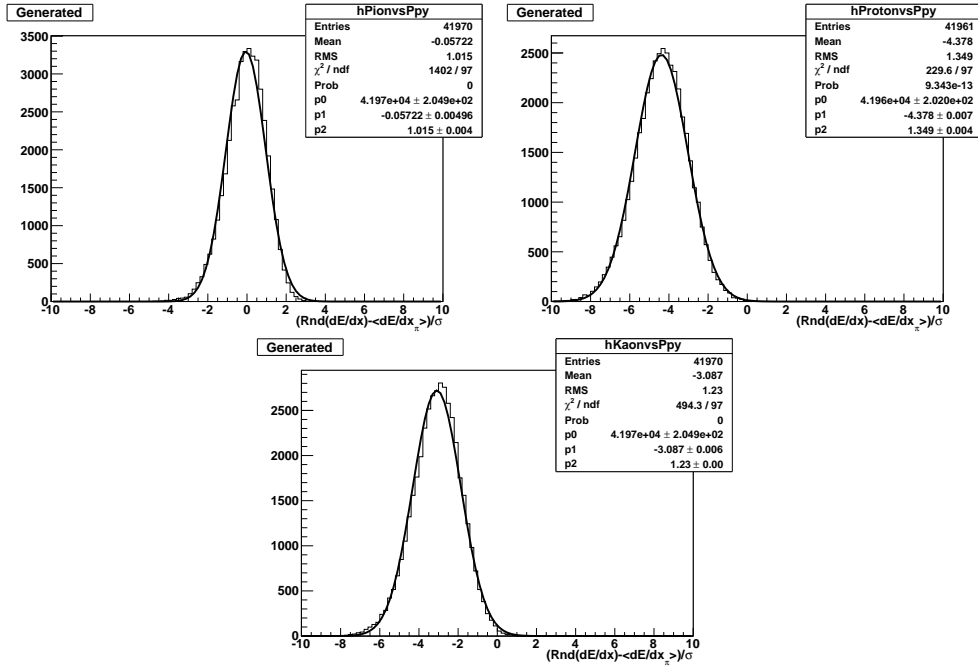
Figure 8.17: Generated shapes for π (left), K (middle), and p (right) fitted by Gauss distributions in a narrow momentum interval for the R_π method ($4 < p < 4.5$ Gev/c).
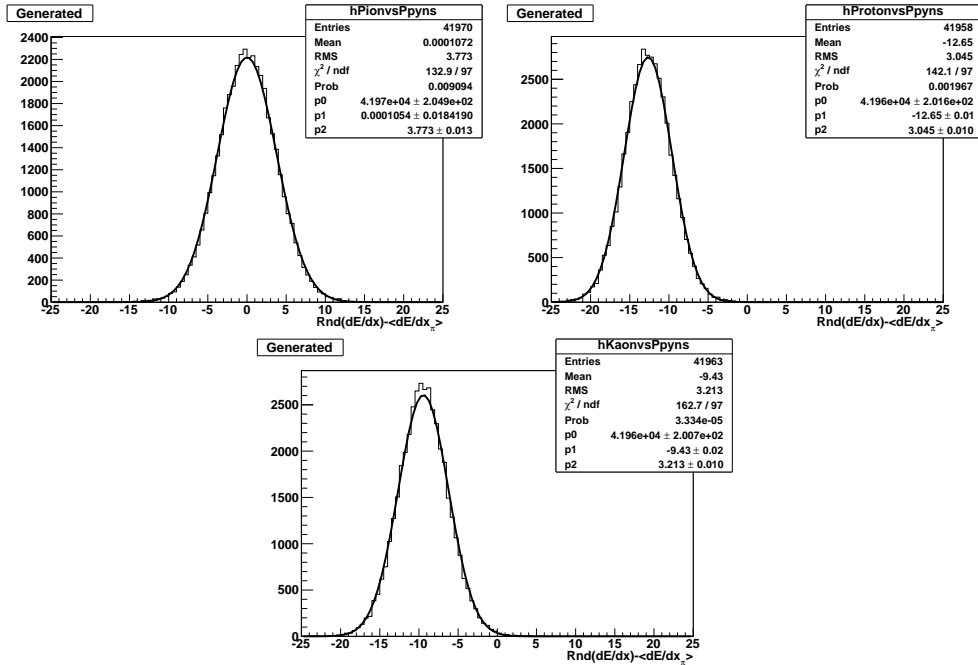
Figure 8.18: Generated shapes for π (left), K (middle), and p (right) fitted by Gauss distributions in a narrow momentum interval for the Δ_π method ($4 < p < 4.5$ Gev/c).

clusters) is determined. From Fig. 8.13 it is clear that some bias is introduced in the way the expected shapes are generated. Take e.g. $p = 4$ GeV/c. The bias is always towards pions because they are produced in large quantities. As they have more clusters than kaons and protons at this momentum, the estimated resolution gets too good for kaons and protons. These shapes will be used for now since no easy way to avoid the bias was found.

Figure 8.17 shows the generated shapes for π (left), K (middle), and p (right) for R_π; the shapes from Δ_π are depicted in Fig. 8.18. The plots are for a narrow momentum interval ($4 < p < 4.5$ Gev/c). As can be seen from the figures in the R_π case the distributions are not quite Gaussian (the asymmetry comes from $\sigma_{dE/dx}$ used to generate the shapes not being symmetric, but larger for bigger dE/dx), while the Δ_π method gives nicely Gaussian distributions.

Figure 8.19 illustrates a comparison between the mean position, μ, (left plot) and the width, σ, (right plot) obtained from the generated shapes (filled markers) and ALICE simulated data (open markers) as a function of the rigidity for the R_π method; the Δ_π results are presented in Fig. 8.20. A good agreement between the generated shapes and the ALICE simulated data distributions is found, so this implies that one can use the μ and σ of the generated distributions to fix the means and widths for π, K, and p.

Figure 8.19: The mean position, μ, (left) and the width, σ, (right) distributions obtained from the generated shapes (filled markers) and ALICE simulated data (open markers) as a function of the rigidity for the R_π method.

8.4   Results

The results for R_π and Δ_π methods will be presented next. In order to extract the yields, the R_π and Δ_π calculated for a narrow momentum interval were fitted with a sum of 3 Gaussians (π, K, and p). This gives 9 parameters: 3 yields, 3 means, and 3 widths. But using the generated distributions from Section 8.3.3, the means and the widths are constrained, i.e 6 of the 9 parameters.
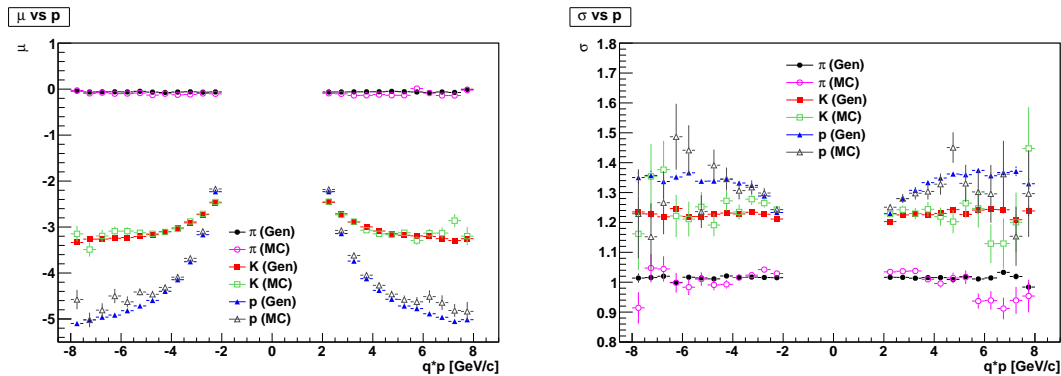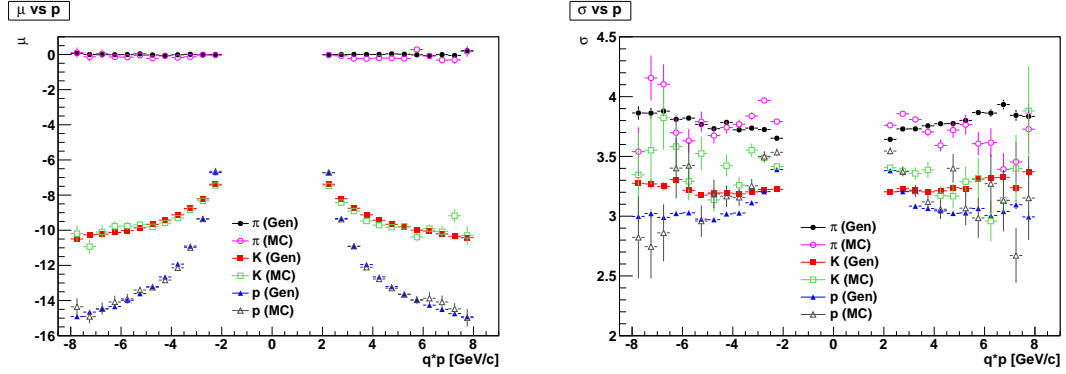
Figure 8.20: The mean position, μ, (left) and the width, σ, (right) distributions obtained from the generated shapes (filled markers) and ALICE simulated data (open markers) as a function of the rigidity for the Δ_π method.
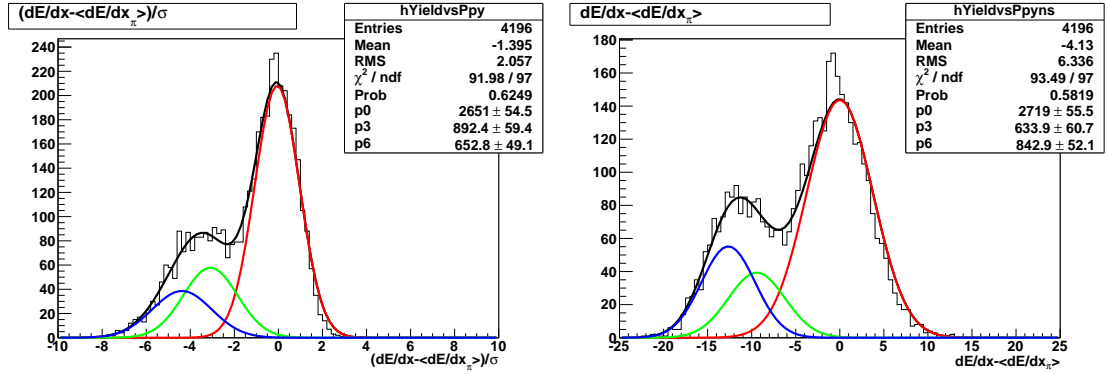
Figure 8.21: An example of the R_π (left) and Δ_π (right) distributions, the fitting function (black) and the corresponding particle species distributions: π (red), K (green), and p (blue). The means and the widths are constrained by the values of the generated shapes. The results are for $4 < p < 4.5$ GeV/c.

Figure 8.21 shows an example of the R_π (left) and Δ_π (right) distributions, in this case for $4 < p < 4.5$ GeV/c. The fit (black curve) fails in both cases the pion peak, but otherwise describes the data well. The big surprise is that the estimates for the kaons and protons are significantly different for the same data and parametrizations with the two methods. For R_π 250 more kaons than protons were found, while for Δ_π 200 more protons than kaons. This means that even if the constructed estimates of the μ and σ of the Gaussians are very good, as can be seen from Fig. 8.19 and Fig. 8.20, the extraction of the yields from the fits has very large uncertainties. This was also found in the case where the actual ALICE simulated data values for μ and σ were used, so it seems that neither of the methods is very stable because the separation between kaons and protons is so small.

A comparison between the reconstructed and the MC truth yields (ALICE simulated data) for R_π (black stars) and Δ_π (red open circles) methods is depicted in Fig. 8.22 (left

Figure 8.22: Ratio of the reconstructed and MC truth yields for R_π (black stars) and Δ_π (red open circles) for π (left), K (middle), and p (right) as a function of the rigidity. The means and the widths are constrained by the values of the generated shapes.

plot shows the ratio of the reconstructed and MC π yield, the middle figure presents the K results, and the right one the p results). We got a very good estimation of pions yield for all momenta. The kaons and protons yields are not precisely determined (particularly for $p < 5$ GeV/c); however the yields improve at higher momenta.

An attempt to extract the yields by constructing similar quantities as Eq. 8.4 and Eq. 8.5 for kaons and protons and do a simultaneous fit was also tried. This approach did not improve significantly the results because the fundamental problem is that kaons and protons are not very well separated.

Strong correlations between the extracted number of kaons and protons were found when looking at the correlations between the fitted yields from the covariance matrix (Fig. 8.23). This explains the poor estimation of the K and p yields (the correlations also follow the separation presented in Section 8.3.2).

Having the estimated yields in momentum bins, narrow transverse momentum intervals were also investigated (as STAR is doing). The same procedure as before was used, so to constrain the means and the widths the distributions had to be generated. The results are depicted in Fig. 8.24. The pion yield is again precisely recovered, while the kaon and proton yields are poorly determined.

A good agreement between reconstructed and MC truth yields for all particles was found when the actual ALICE simulated data values for μ and σ were used. The results
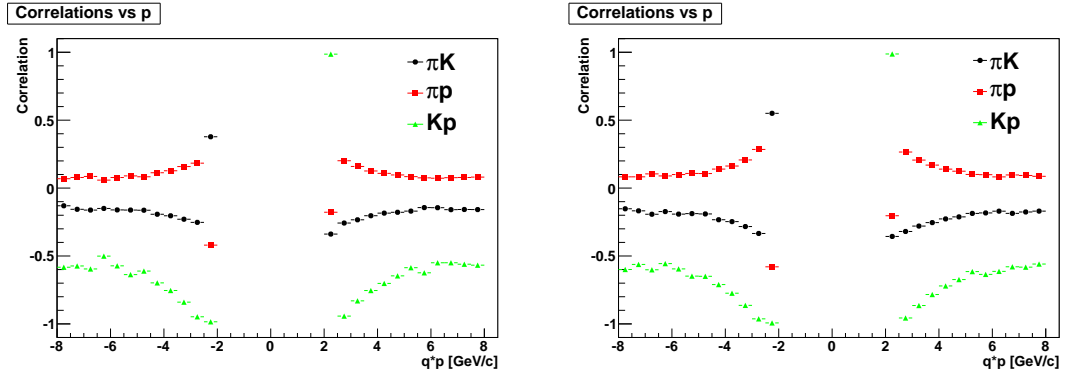
Figure 8.23: Correlations between the fitted yields from the covariance matrix for R_π (left) and Δ_π (right) as a function of the rigidity: πK (black circles), πp (red squares), and Kp (green triangles).
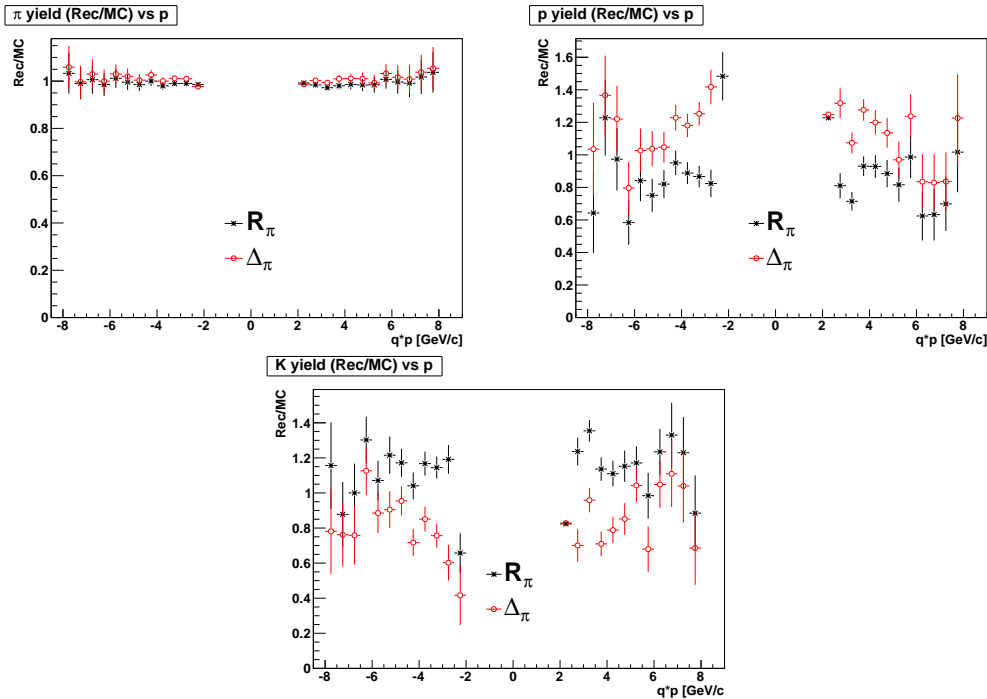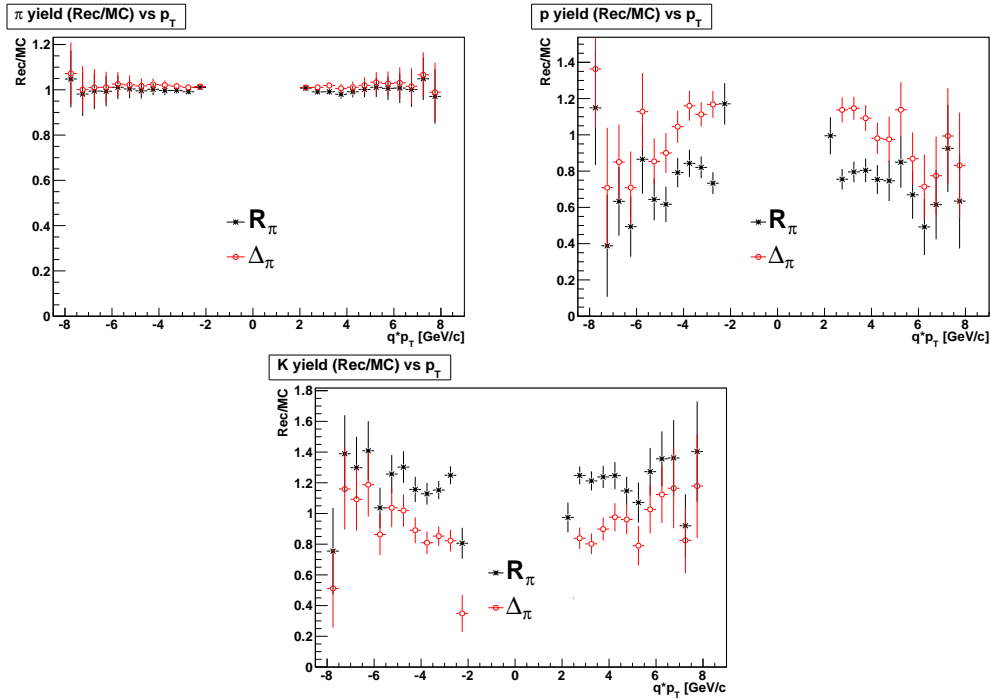

Figure 8.24: Ratio of the reconstructed and MC truth yields for R_π (black stars) and Δ_π (red open circles) for π (left), K (middle), and p (right) as a function of the transverse momentum multiplied with charge sign. The means and the widths are constrained by the values of the generated shapes.

are presented in Fig. 8.25. As can be seen from the figure, both methods estimate very well the particle yields.

The reason for the better estimation of the particle yields for p_T is related with both physics and topology. One expects dN/dp_T to be almost independent of y/η in a region around midrapidity. However, this means that dN/dp is not invariant, so that the actual shape is very sensitive to the η cut and actually we will bias mostly towards large η (because dN/dp_T is decreasing). So not only that dN/dp is biased towards large η, but it could have also be seen in Section 8.2 that dE/dx is not equally well calibrated over the full acceptance. The combination of these two effects can be the cause of the above problems in extracting the yields.

The discrepancy between the two p_T results arises from the generated shapes not providing the right values and the strong correlations between kaons and protons (Fig. 8.23). A comparison between the μ (left) and σ (right) obtained from the generated shapes and ALICE simulated data for the R_π method is shown in Fig. 8.26. The similar behavior could be observed for Δ_π method. So a better way to generate the expected shapes should be found.

Figure 8.25: Ratio of the reconstructed and MC yields for R_π (black stars) and Δ_π (red open circles) for π (left), K (middle), and p (right) as a function of the transverse momentum multiplied with charge sign. The means and the widths are constrained by the actual ALICE simulated data values.
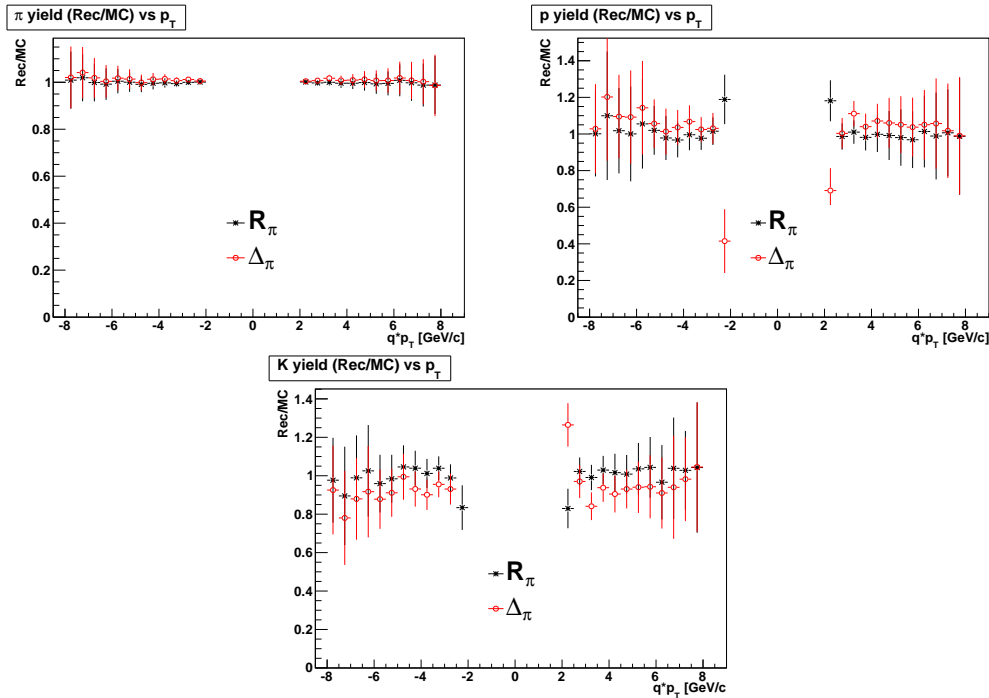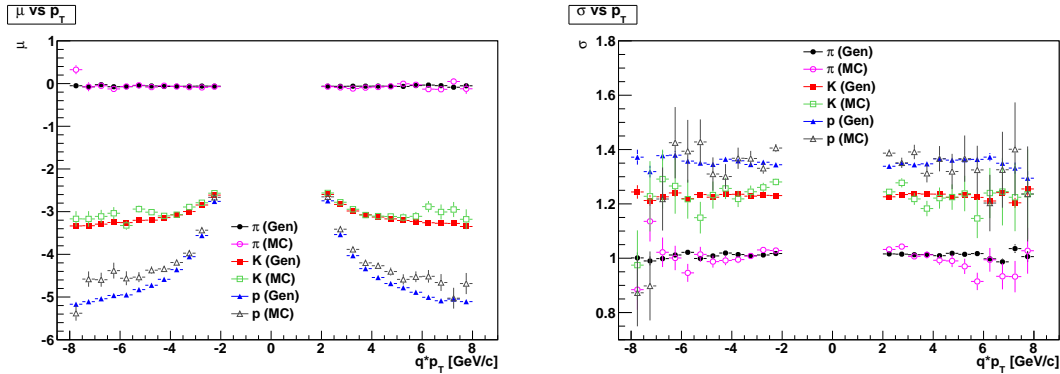
Figure 8.26: The mean position, μ, (left) and the width, σ, (right) obtained from the generated shapes (filled markers) and ALICE simulated data (open markers) as a function of the transverse momentum multiplied with charge sign for the R_π method.

8.5 Conclusions

In this study two approaches, R_π (STAR method) and Δ_π (the simplest method), were investigated to obtain identified particle yields at high p_T. Both methods provide similar separation between particles as could be seen from the constructed toy model. The same conclusion was drawn from the ALICE simulated data. In order to fix the means and the sigmas in the 3 Gaussian fit used to extract the yields, a new approach to generate the expected shapes for π, K, and p was developed. In the case of ALICE, the STAR method does not give Gaussian distributions, while Gaussian shapes were obtained for Δ_π method. The Δ_π method was chosen for data analysis in the next chapter.

Trying to extract the yields in narrow momentum intervals the methods could only precisely determine the π yield, while the K and p yields are strongly correlated and very difficult to obtain. But everything changed when the yields were determined in narrow transverse momentum intervals: the yields were very well estimated for all particles since dN/dp_T is almost independent of y/η in a region around midrapidity.

The reach in momentum in the analysis is statistically limited because, as can be seen from Fig. 8.19 and Fig. 8.20, the separation between π, K, and p is increasing with momentum. This suggests that one could extend this analysis up to 20 GeV/c or higher.

The methods could be studied and refined using π and p from Λ^0 and K^0 decays, identified by their displaced decay vertex. Also identified particles by TOF and/or HMPID detectors could be used for trimming the procedures.

Chapter 9

Identified Charged Pion Spectra

The previous chapter has shown that the identification capability of charged hadrons could be extended by employing the TPC dE/dx information. It could also be seen that the Δ_π method (see Section 8.3.1) gave the best results in the ALICE case. In this data analysis, the Δ_π method was used to extract the π^+ and π^- spectra at high transverse momentum ($p_T > 2.5$ GeV/c) in pp collisions at $\sqrt{s} = 900$ GeV and $\sqrt{s} = 7$ TeV. Data from around 3.8 ($\sqrt{s} = 900$ GeV) and around 28 ($\sqrt{s} = 7$ TeV) million inelastic pp collisions, recorded during May and March-April 2010 LHC runs, were used for this analysis. The events were recorded with positive magnetic field polarity (+0.5 T) for $\sqrt{s} = 900$ GeV and with both magnetic field polarities (±0.5 T) for $\sqrt{s} = 7$ TeV.

9.1   Event Selection

The event samples used in this analysis were collected with the MB1 trigger condition (see Section 4.2.4). The trigger efficiency at $\sqrt{s} = 900$ GeV is 96% [141], while at $\sqrt{s} = 7$ TeV it is 93% [142]. The events were in coincidence with signals from two beam pick-up counters, one on each side of the interaction region, indicating the presence of passing bunches. In order to remove beam induced background events, an offline event selection is applied for both data samples as described in [141, 143]. The beam-gas or beam-halo events are rejected using the timing information from the V0 detector by removing events with negative arrival time (see Fig. 4.12). In addition, at both energies, correlations between the number of clusters of pixel hits and the number of tracklets (short track segments in the SPD) are also used for background rejection since background events typically have a large number of pixel hits than for collisions [144]. This selection gives 3785370 and 28007959 events for the $\sqrt{s} = 900$ GeV and $\sqrt{s} = 7$ TeV data samples, respectively.

Furthermore, only events with a reconstructed primary vertex within ±10 cm along the beam axis (z direction) are required for this analysis since, from Monte Carlo simulations, the vertex reconstruction efficiency is practically independent of the vertex $z-$position in this region [141]. The fraction of triggered events with a reconstructed primary vertex after background rejection is 95% (98.5%), resulting in a 900 GeV (7 TeV) sample of

133

3589472 (27625589) events from which 3145349 (27491686) events have $|z| < 10$ cm. The distribution of the interaction vertices along the beam axis reconstructed by associating pairs of hits in the two SPD layers is depicted in Fig. 9.1. The vertex distribution has an estimated r.m.s. of 6.5 cm and 3.2 cm for the 900 GeV and 7 TeV data samples, respectively.

After these selections, the remaining background in the samples is below 0.01% and can be neglected. The cosmic-ray contamination is also found to be negligible in both data samples.
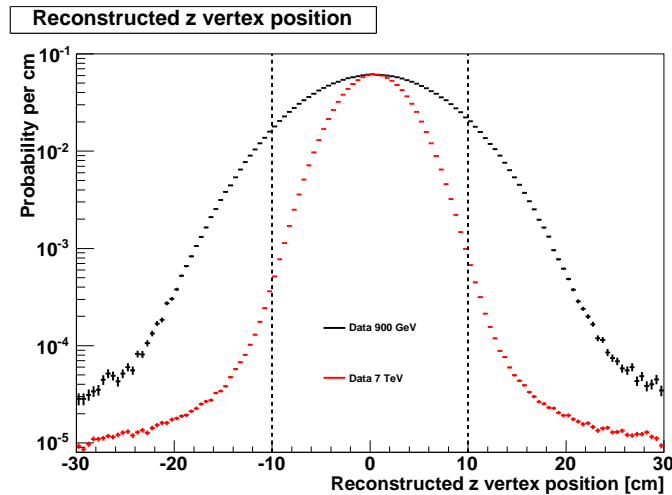
Figure 9.1: Reconstructed longitudinal vertex distributions obtained from hit correlations in the two SPD layers for the 900 GeV (black) and 7 TeV (red) data samples. The events selected for the present analysis are the ones that falls in the region delimited by the vertical dashed lines ($|z| < 10$ cm).

9.2 Track Selection

To obtain the π^+ and π^- yields, primary charged particles are selected in the pseudorapidity range $|\eta| < 0.8$. In this way tracks have full projected track length in the TPC and the efficiency losses due to detector boundaries are minimal. Note that primary particles are here defined as all particles produced in the collision, including products of strong and electromagnetic decays as well as weak decays of charmed and beauty particles, but excluding products from strange weak decays, conversions and secondary hadronic interactions in the detector material which are referred to by secondary particles in the following.

Additional quality cuts are applied to ensure low secondary and fake track contamination as well as good track reconstruction efficiency. A track is accepted if it has at least 70 clusters in the TPC, a maximum χ^2 per cluster of less than 4 in the track fitting, and at least two hits in the ITS with at least one in the SPD. Furthermore, the track is not allowed to be flagged as a kink daughter. Here kink means a sudden change in the

Figure 9.2: Mean number of tracks that passed the selection as a function of event time stamp for the 900 GeV (left) and 7 TeV (right) samples.

particle's trajectory which arises when a charged particle decays inside the detector, for example $K^+ \to \mu^+ \nu_\mu$. In the reconstruction the K^+ is flagged as kink mother and μ^+ as kink daughter. A p_T dependent cut on the dis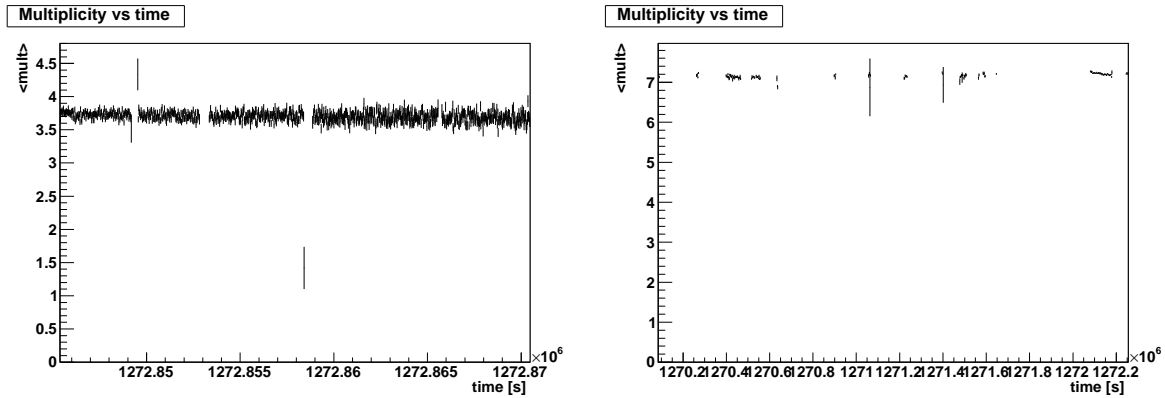tance to closest approach (d_0) to the reconstructed event vertex in the transverse direction is also applied: tracks were rejected if $d_0 > 0.35$ mm $+ 0.42$ mm $\cdot p_T^{-0.9}$, with p_T in GeV/c. This cut is tuned to minimize the contributions from secondary particles and to select primary particles with high efficiency. Tracks with $p_T < 0.2$ GeV/c are omitted for the 900 GeV sample. For the 7 TeV sample, tracks with $p_T > 2$ GeV/c and a small set of tracks with $0.4 < p_T < 0.6$ GeV/c and $40 < dE/dx < 60$ (the cuts defined a small region around the MIP position (see Section 5.4.1), called MIP region next) are considered.

In order to verify the quality of the data that passed the selection, the mean number of tracks is plotted as a function of event time stamp for the 900 GeV and 7 TeV samples (see Fig. 9.2). As can be seen from the figure flat mean multiplicity distributions are obtained for both data samples.

In addition to the above cuts, tracks close to the TPC sector edges are removed by employing a cut on the track ϕ angle. In this way, the tracks with a low number of TPC clusters, i.e. worse dE/dx resolution, are removed and only tracks with the proper number of TPC clusters will be used in the present analysis. The advantage of using this cut is an increased separation between particles even though the number of tracks is reduced. Figure 9.3 shows the correlations between the number of TPC clusters, $N_{TPC\ clusters}$, and the ϕ modulo $\pi/9$ (since a TPC sector covers around 20° in azimuth) before (left) and after (right) the cut for positive (up) and negative (down) tracks with $p_T > 2$ GeV/c for the 900 GeV data sample. In terms of $N_{TPC\ clusters}$, the results are presented in Fig. 9.4. As can be seen from the figure, most of the tracks with $N_{TPC\ clusters} < 100$ are removed by this cut: around 17% of tracks with $p_T > 2$ GeV/c are lost, while around 25% of all tracks are rejected. The same cut is applied to the 7 TeV data sample and a similar percentage of rejected tracks is found. One should note that the cut is not only charge dependent, but also depends on the magnetic field polarity.
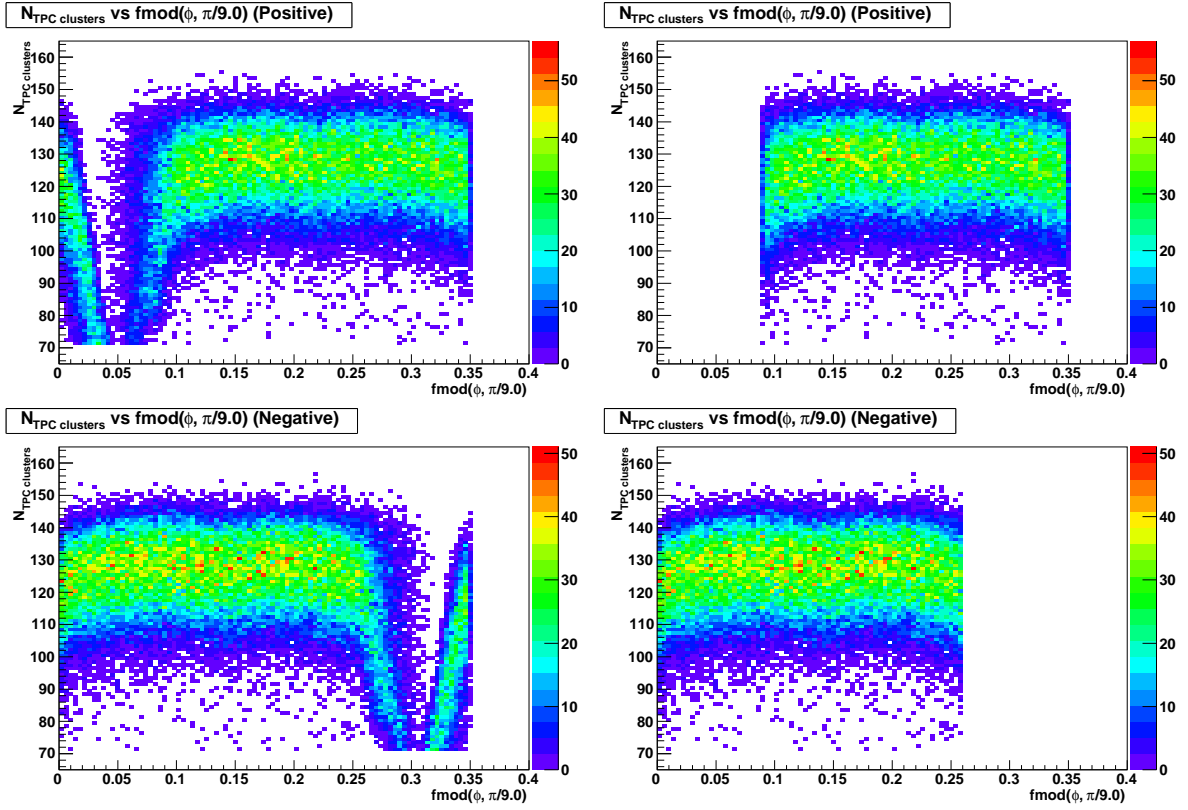
Figure 9.3: Correlations between the number of TPC clusters, $N_{TPC\ clusters}$, and the ϕ modulo $\pi/9$ (since a TPC sector covers around 20° in azimuth) before (left) and after (right) the cut for positive (up) and negative (down) tracks with $p_T > 2$ GeV/c for the 900 GeV data sample.
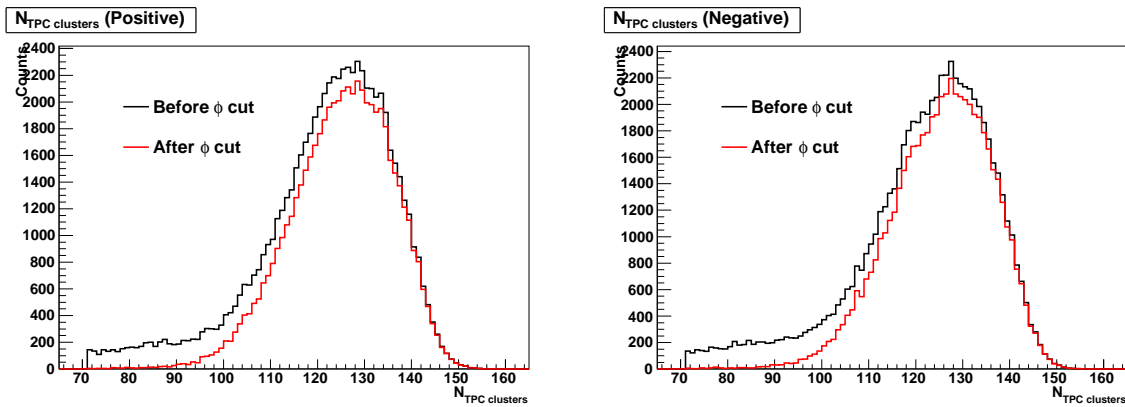
Figure 9.4: TPC cluster distributions before (black) and after (red) the ϕ cut for positive (left) and negative (right) tracks with $p_T > 2$ GeV/c for the 900 GeV data sample.

Using this selection, the acceptance and reconstruction efficiency for primary charged particles and the remaining contamination from secondaries as a function of the transverse momentum are estimated from PYTHIA combined with detector simulation and reconstruction. The procedure estimates losses due to the tracking inefficiency, absorption and secondary interactions of the detector. The acceptance and reconstruction efficiency for primary charged particles is shown in the left panels of Fig. 9.5. It reaches around 60% for $p_T > 1$ GeV/c. Since $p_T > 2.5$ GeV/c is the low limit of the momentum range that this analysis is interested in, an 0.5 bin size in p_T is considered here. For a proper evaluation of the acceptance and reconstruction efficiency at low p_T, one should use a smaller segmentation in p_T. The losses at low p_T are mainly due to energy loss in the detector material and to track bending in the magnetic field. The contamination from secondary particles is illustrated in the right panels of Fig. 9.5. As the contamination is around 1% at $p_T \sim 2.5$ GeV/c and drops for larger p_T, it is small enough not to affect the results within the expected statistical error at this stage. So the final results are not corrected for the secondary contamination. Note that the efficiency and secondary contamination are slightly different for positive and negative particles, mainly due to larger absorption of negative particles and isospin effects in secondary interactions.

9.3 Correction Factor and Normalization

The acceptance and reconstruction efficiency from the previous section is converted to p_T dependent correction factors. They are used to correct the raw p_T spectrum. The correction factor used in the present analysis is a multiplication between two ratios: the ratio between the trigger efficiency (see Section 9.1) and the p_T dependent correction factors and the ratio between events with a reconstructed vertex and events with a reconstructed vertex with $|z| < 10$ cm. This simple correction factor arises from the following assumptions (remember that only particles with $p_T > 2.5$ GeV/c are considered in this analysis):

- Events that have not triggered have no high p_T yield.

- Events with no reconstructed vertex have no high p_T yield.

- No background from diffractive events.

The normalization here is a multiplication between the number of triggered events N_{ev}, the η bin size $\Delta_\eta = 1.6$, and the p_T bin size $\Delta_{p_T} = 0.5$.

In order to test the correction factor and normalization (excluding particle identification), the fully corrected p_T spectra are compared with data recently published by ALICE [145] and CMS [146] (see Fig. 9.6). For 900 GeV sample, good agreement between this analysis and ALICE data is obtained for $p_T > 2$ GeV/c, while at low p_T, as the secondary contamination is not corrected for in the present analysis, a small difference can be observed. A slight discrepancy can also be seen between this analysis and ALICE points for the 7 TeV sample; it comes from the fact that a different reconstructed data sample
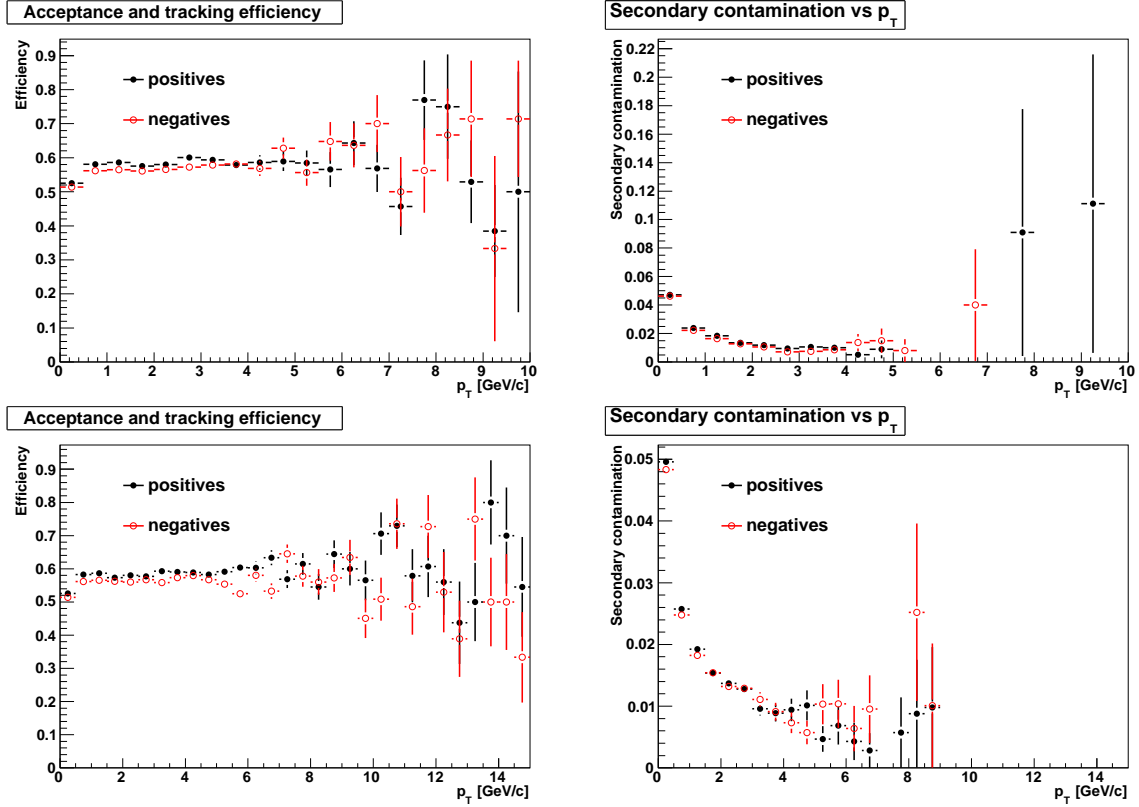
Figure 9.5: Acceptance and reconstruction efficiency for primary charged particles (left) and contamination from secondary particles (right), separately for positive and negative particles in $|\eta| < 0.8$ as a function of p_T for 900 GeV (upper panels) and 7 TeV (lower panels) samples. The secondary contamination is not corrected for in the present analysis.
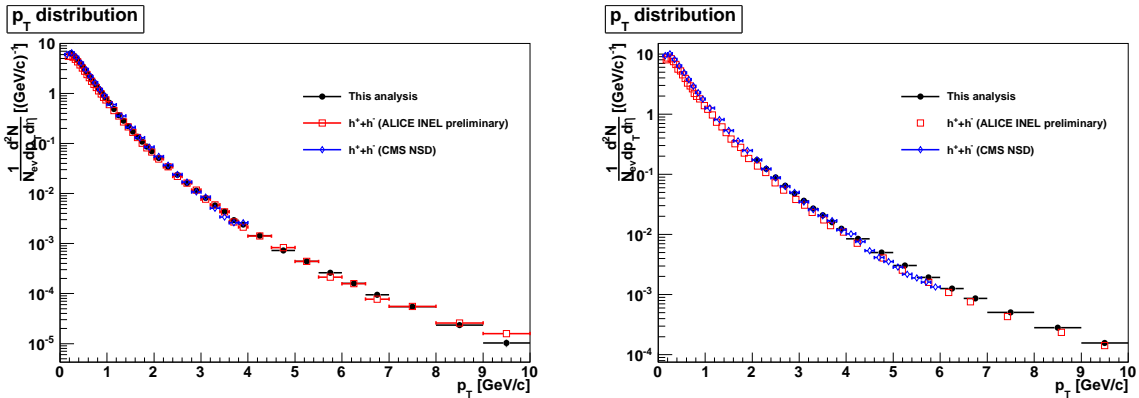
Figure 9.6: Comparison between the corrected p_T spectra from the present analysis (black full circles) and the ALICE inelastic (red open squares) and CMS non single-diffractive (blue open diamond) data for the 900 GeV (left) and 7 TeV (right) samples. A pseudo-rapidity window $|\eta| < 0.8$ is used in the present/ALICE analysis, while $|\eta| < 2.4$ in the CMS one.
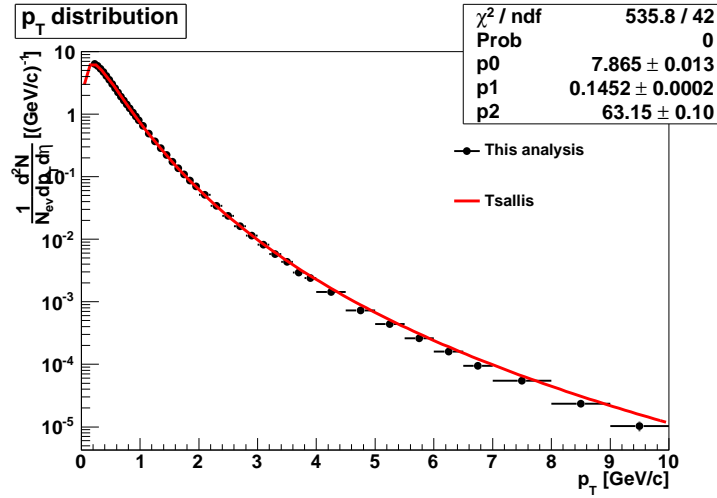
Figure 9.7: Corrected p_T spectrum from the present analysis fitted by the Tsallis function ($\sqrt{s} = 900$ GeV).

Figure 9.8: Left: $dE/dx - \eta$ correlations for tracks with $0.4 < p < 0.6$ GeV/c and $40 < dE/dx < 60$ fitted by second degree polynomials (black lines). Right: Corrected dE/dx as a function of η; the same functions are used to cross check the corrections and that the MIPs are positioned at 50 ADC. The results are for the $\sqrt{s} = 900$ GeV data set selected for this analysis.

is used in the ALICE analysis. The difference between CMS and ALICE/this analysis is related to the different event classes (non single-diffractive for CMS and inelastic for ALICE/this analysis) as well as different pseudo-rapidity windows ($|\eta| < 2.4$ for CMS and $|\eta| < 0.8$ for ALICE/this analysis) considered in the analyzes. In addition, the corrected p_T spectrum obtained from the 900 GeV sample is fitted by the Tsallis function [147]

$$\frac{d^2 N_{ch}}{d\eta dp_T} \propto p_T \left(1 + \frac{E_T}{nT} \right)^{-n}, \tag{9.1}$$

where $E_T = \sqrt{m_\pi^2 + p_T^2} - m_\pi$ is the transverse kinetic energy (m_π is the pion mass and assumed for all tracks), n and T are fit parameters (see Fig. 9.7). Integrating, the pseudo-rapidity density is found to be $dN_{ch}/d\eta = 3.5$ compared to $dN_{ch}/d\eta = 3.02$ published by ALICE [141]. The difference is related with the data points from this analysis being slightly higher than the ALICE ones for $p_T < 2$ GeV/c (see above) as well as with the fit not describing the data at high p_T (see Fig. 9.7). The same cross check can not be performed for the 7 TeV sample due to the transverse momentum cut ($p_T > 2$ GeV/c) used to select tracks.

A new correction and normalization procedure that matches the strategy described in [81] is under study. Due to time constraints, it could not be used in this thesis. So the results from Sections 9.5.2 and 9.5.3 are corrected and normalized using the approach presented earlier.

9.4   Mean dE/dx and Resolution

9.4.1   The dE/dx Pseudo-rapidity Dependence

Tracks with $0.4 < p < 0.6$ GeV/c and $40 < dE/dx < 60$ were selected to evaluate the dE/dx calibration. Since (almost) no momentum dependence of dE/dx is expected for this region, ideally there should be no pseudo-rapidity dependence if the dE/dx is properly calibrated. Figure 9.8 presents the $dE/dx - \eta$ correlations for the MIP region from the $\sqrt{s} = 900$ GeV data sample. As can be seen from the left panel of Fig. 9.8 the calibration is not optimal (at least for MIPs there are residual effects that are not properly taken into account). Second degree polynomials were used to correct the η dependence of the dE/dx and to position the MIPs at 50 ADC (see the right panel of Fig. 9.8). A similar η dependence was also found for the data sample selected at $\sqrt{s} = 7$ TeV (see Fig. 9.9).

9.4.2   Extracting the Pion Mean dE/dx Curve

In order to extract the $\langle dE/dx \rangle_\pi$, a triple Guassian fit in narrow momentum intervals was tried as a first approach, but it did not give a continuos curve. Since the mean values of these fits should follow a single curve ($\langle dE/dx \rangle (\beta\gamma)$), a two dimensional triple Gaussian fit in dE/dx and momentum was used to fit all the momentum intervals at the same time by requiring a fixed relation between the means (see below). In this way the $\langle dE/dx \rangle_\pi$
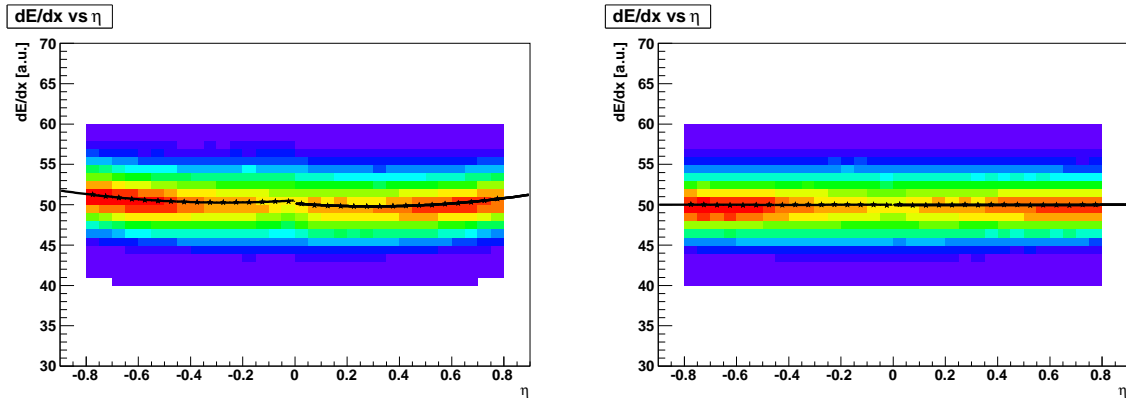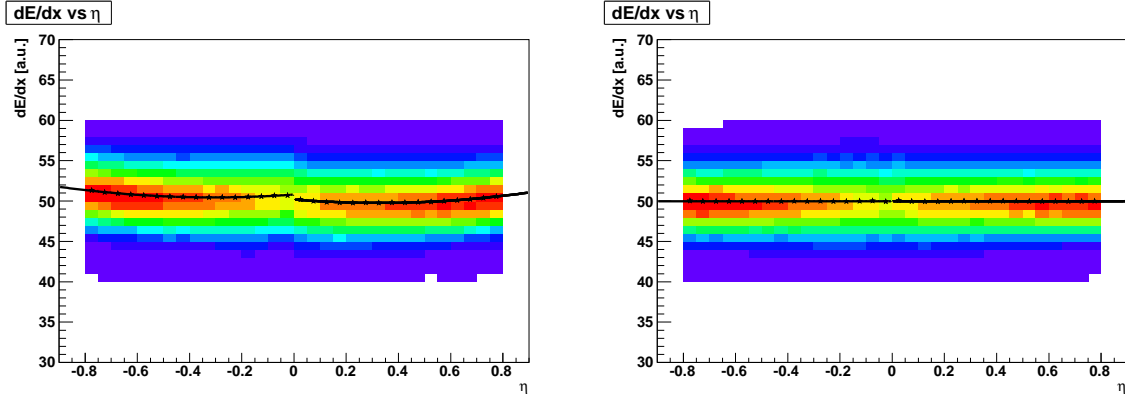
Figure 9.9: Left: $dE/dx - \eta$ correlations for tracks with $0.4 < p < 0.6$ GeV/c and $40 < dE/dx < 60$ fitted by second degree polynomials (black lines). Right: Corrected dE/dx as a function of η; the same functions are used to cross check the corrections and that the MIPs are positioned at 50 ADC. The results are for the $\sqrt{s} = 7$ TeV data sample selected for this analysis.
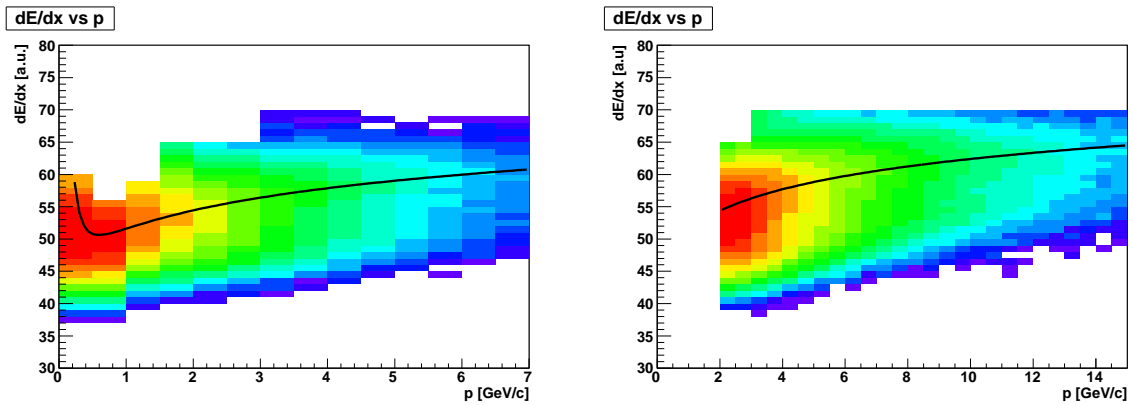
Figure 9.10: The dE/dx distribution as a function of the momentum together with the fit to the $\langle dE/dx \rangle_\pi$ (black line) for the 900 GeV (left) and 7 TeV (right) data samples.

and the particle yields were obtained simultaneously. The same procedure was folowed on Monte Carlo data and it described the data well (see Sections 9.5.2 and 9.5.3). Due to time constraints, the $\langle dE/dx \rangle_\pi$ could not be cross checked with clean samples from Λ^0 and K^0 decays.

The $\langle dE/dx \rangle_\pi$ was parametrized as

$$\langle dE/dx \rangle_\pi = b_0 \frac{1 + x^2}{x^2} + b_1 \log(1 + x), \tag{9.2}$$

where $x = p/m_\pi$, b_0 and b_1 are constants obtained from the fit. A triple Guassian fit was used in each momentum interval to extract the pion, kaon, and proton yields by fixing their mean positions to the values approximated by Eq. 9.2 (scaled for kaons and protons) and using the same width, σ, for each particle species. So the fit has three global parameters (b_0, b_1, σ) and three parameters for each momentum interval (π, K, p yields). The dE/dx distribution as the function of the momentum together with the fit to the $\langle dE/dx \rangle_\pi$ (black line) is depicted in Fig. 9.10 for the 900 GeV (left) and 7 TeV (right) data samples considered in this analysis.

9.4.3   Extracting the dE/dx Resolution
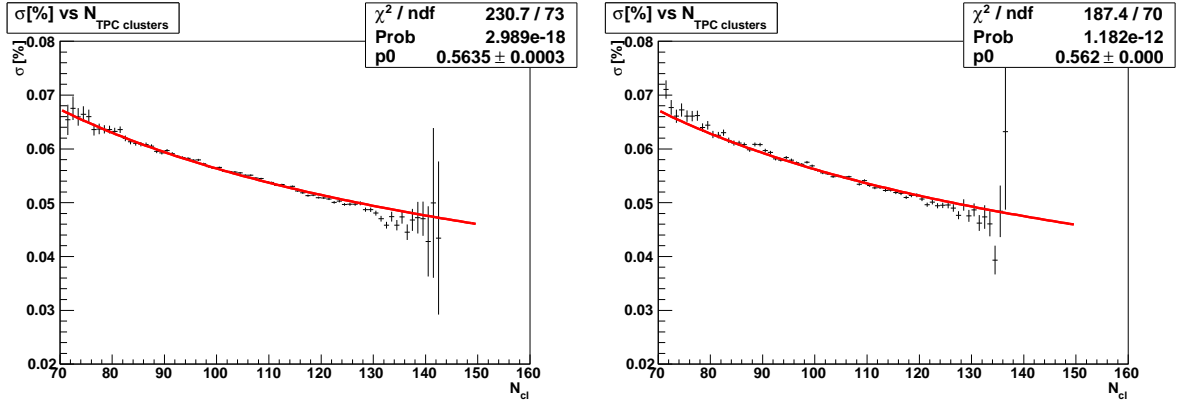
Figure 9.11: $\sigma_{dE/dx}$ as a function of the $N_{TPC\ clusters}$ fitted with Eq. 9.3 (red line) for the 900 GeV (left) and 7 TeV (right) data sets considered in this analysis.

The dE/dx resolution, $\sigma_{dE/dx}$, was obtained from the MIP region by fitting the dE/dx in narrow $N_{TPC\ clusters}$ intervals with Gauss distributions. For each $N_{TPC\ clusters}$ interval, the $\sigma_{dE/dx}$ and $\langle dE/dx \rangle$ were determined and the $\sigma_{dE/dx}$ in percentage can be calculated. Figure 9.11 shows the fit to the $\sigma_{dE/dx}$ for the 900 GeV (left) and 7 TeV (right) data samples considered in this analysis. The functional shape of the fit was approximated by

$$\sigma_{dE/dx} = \frac{c_0}{\sqrt{N_{TPC clusters}}}, \tag{9.3}$$

where c_0 is a constant obtained from the fit. No η dependence of the $\sigma_{dE/dx}$ was found here.

9.5 Determination of the Identified Pion Yields

As already discussed in the previous chapter, the $\Delta_\pi = dE/dx - \langle dE/dx \rangle_\pi$ method was chosen to extract the π^+ and π^- yields. The Δ_π distribution determined for narrow transverse momentum intervals was fitted with a sum of 2 (3) Gaussians (π, $K + p$ (π, K, p)) with a total of 6 (9) parameters: 2 (3) yields, 2 (3) mean positions, 2 (3) widths. A slightly modified approach to construct the expected shapes for pions, kaons, and protons as the one presented in Section 8.3.3 was used to constrain some parameters: two for the double Gaussian fit (the mean position and width of pions) and six for the triple Gaussian fit (the mean positions and widths of pions, kaons, and protons).

9.5.1 Constructing the Expected Shape

Figure 9.12: The mean position, μ, (left) and the width, σ, (right) obtained from the generated shapes for positive (upper) and negative particles (lower) for the 900 GeV data.

From Section 8.3.3, one could see that a bias was introduced in the way the expected shapes are generated because the $\sigma_{dE/dx}$ depends on dE/dx, i.e. depends on the particle type. In order to remove this bias, a slightly modified approach to "generate" predictions for pion, kaon, and proton shapes was developed based on the $\langle dE/dx \rangle_\pi$ and $\sigma_{dE/dx}$ parametrizations found in the previous sections and the number of TPC track points.

First of all, the $\langle dE/dx \rangle_K$ and $\langle dE/dx \rangle_p$ are determined from the $\langle dE/dx \rangle_\pi$. The dE/dx of each track is checked to be within ± 3 ADC around $\langle dE/dx \rangle_\pi$ or $\langle dE/dx \rangle_K$ or $\langle dE/dx \rangle_p$. Knowing the particle type (from the above selection) and the $N_{TPC\ clusters}$, the $\sigma_{dE/dx}$ is

Figure 9.13: The mean position, μ, (left) and the width, σ, (right) obtained from the generated shapes for positive (upper) and negative particles (lower) for the 7 TeV data.

calculated (don't forget that $\sigma_{dE/dx}$ is in percent now). Assuming a Gaussian distribution, 20 (or more) values of the dE/dx can be generated. Then the Δ_π distribution can be filled.

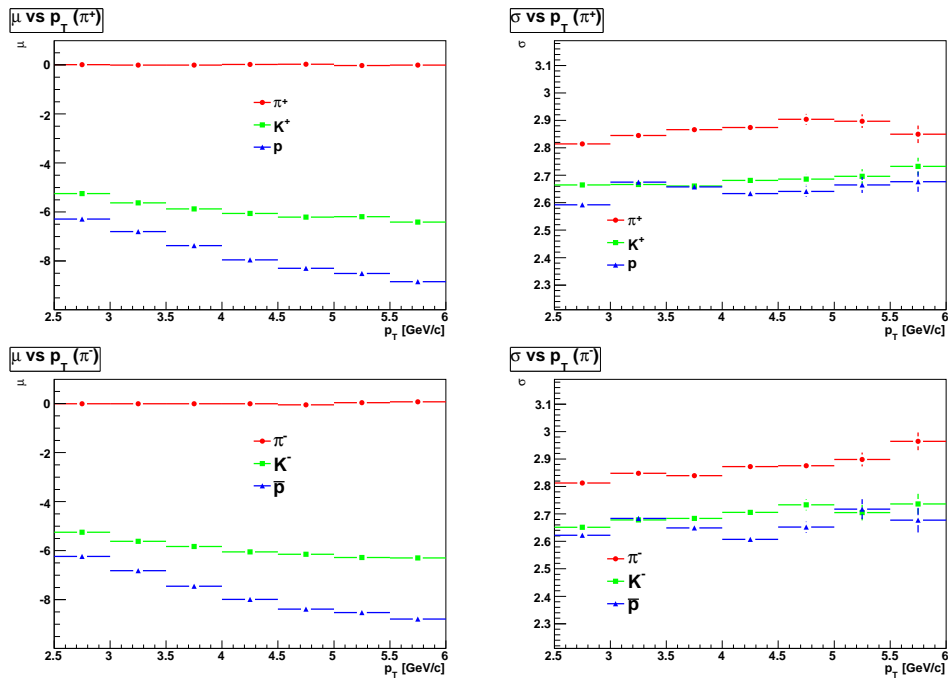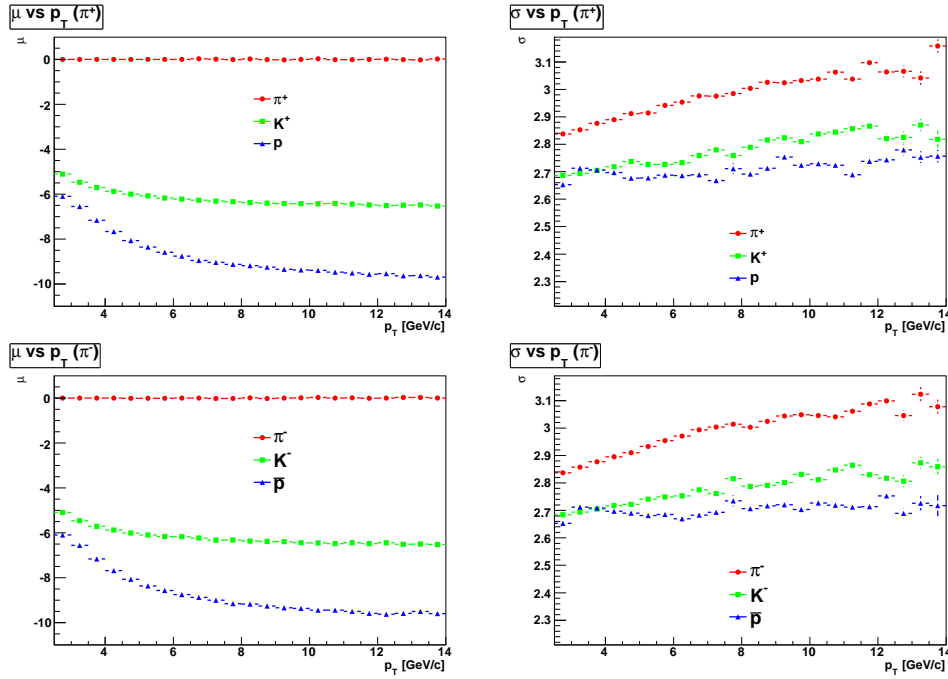Figure 9.12 presents the mean position, μ, (left) and the width, σ, (right) obtained from the generated shapes for positive (upper) and negative particles (lower) for the 900 GeV data, while the results for the 7 TeV data are depicted in Fig. 9.13. As can be seen from the figures the separation between particles increases with the momentum. Furthermore, the separation between kaons and protons is so small for the first p_T bins and the triple Gaussian fits will not be very stable (see Appendices D and E). The width is also increasing with the momentum which is expected since σ is proportional to the dE/dx.

9.5.2   Pion Yields at 900 GeV Center-of-Mass Energy

Figure 9.14 shows examples of Δ_π distributions for positive (upper) and negative (lower) particles together with the double (left) and triple (right) Gaussian fits. The results are for $4 < p_T < 4.5$ GeV/c. All the Δ_π distributions fitted with a sum of 2 (3) Gaussians are presented in Appendix D. The fits (black curves) describe the data well even though there are some differences between the Δ_π distributions for positive and negative particles. The discrepancy will influence the estimation of the yields in some p_T bins (see below).

The uncorrected pion yields are presented in Fig. 9.15. Good agreement between the two methods (double and triple Gaussian fits) is found (also see Fig. 9.16). Additional cross checks are performed before the spectra are fully corrected. Figure 9.17 shows the
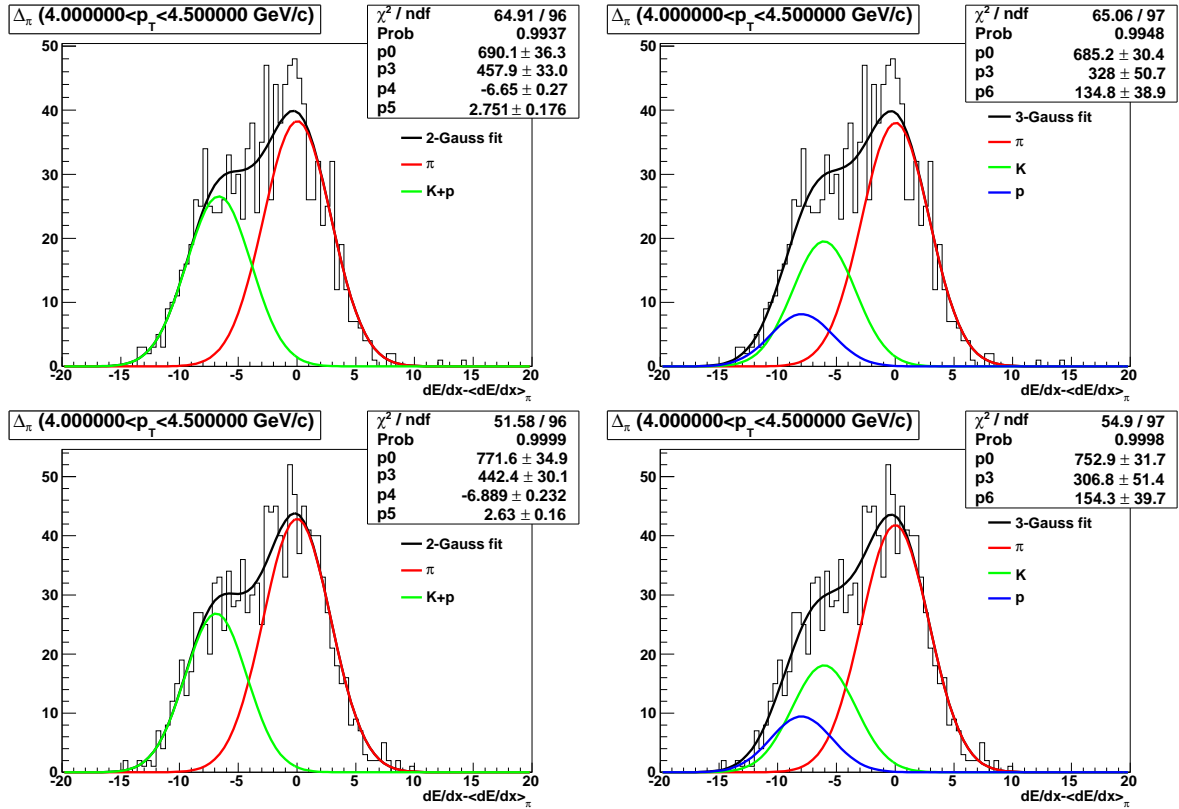
Figure 9.14: Examples of the Δ_π distributions for positive (upper) and negative (lower) particles together with the double (left) and triple (right) Gaussian fits for $4 < p_T < 4.5$ GeV/c. The means and widths are constrained by the values of the generated shapes for triple Gaussian fits, while only the mean and width of pions are constrained by the values of the generated shapes for double Gaussian fits ($\sqrt{s} = 900$ GeV).
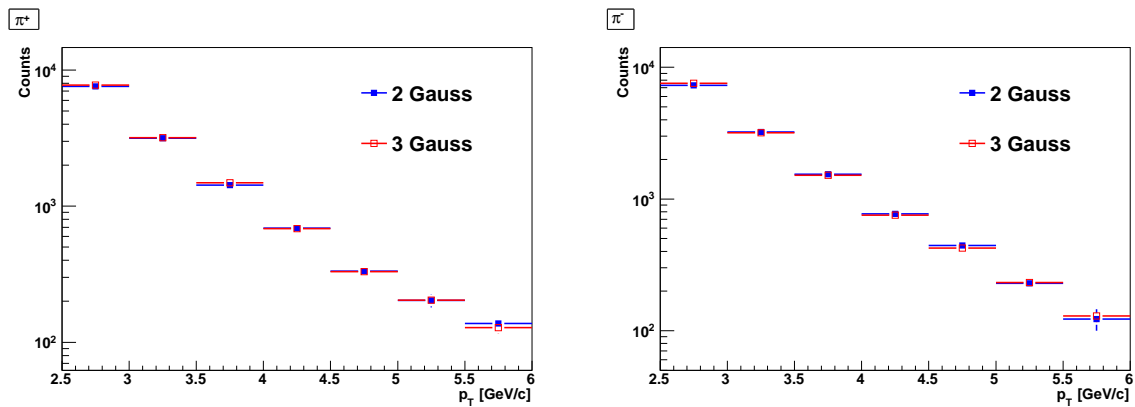
Figure 9.15: Uncorrected π^+ (left) and π^- (right) yields from the double (full blue squares) and triple (open red squares) Gaussian fits as a function of the transverse momentum ($\sqrt{s} = 900$ GeV).
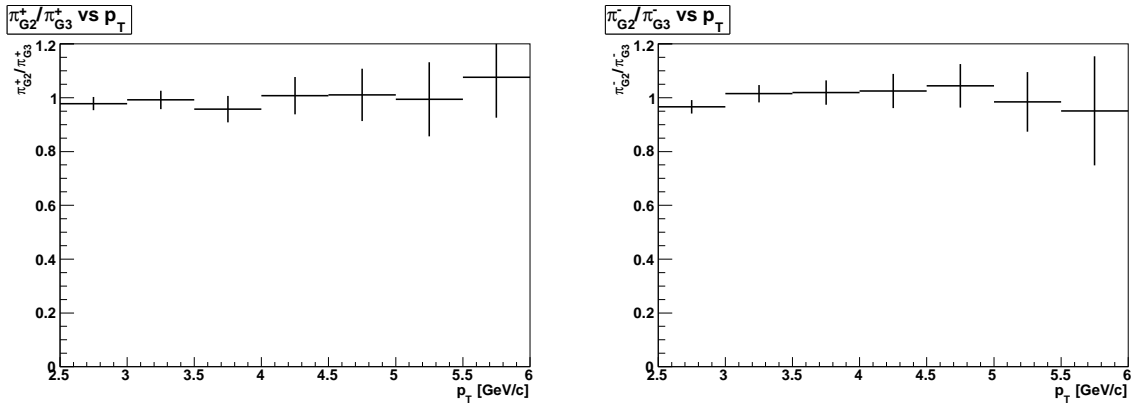
Figure 9.16: The ratio between the results of the two methods for π^+ (left) and π^- (right) as a function of transverse momentum ($\sqrt{s} = 900$ GeV).
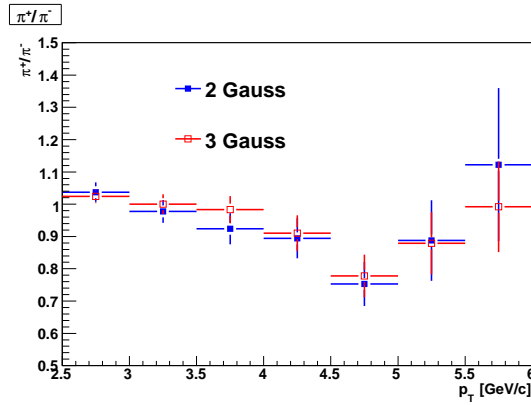
Figure 9.17: π^+/π^- ratio as a function of transverse momentum ($\sqrt{s} = 900$ GeV).
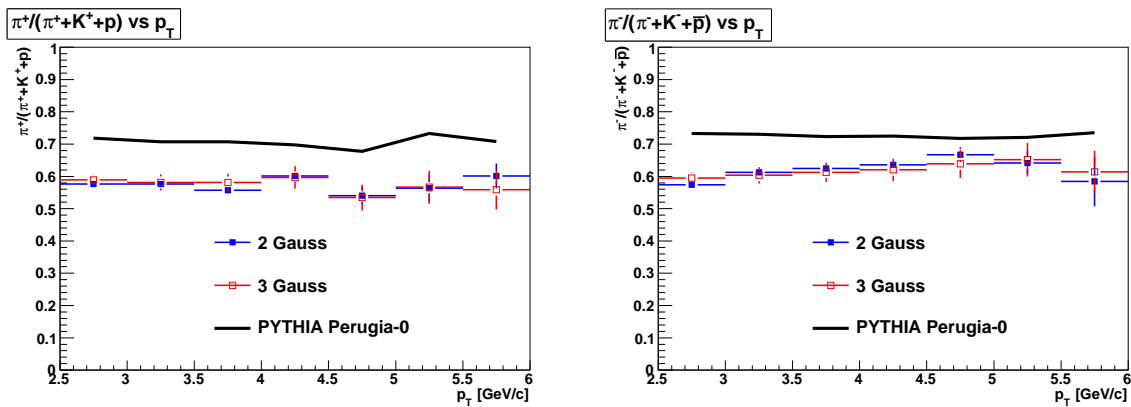
Figure 9.18: Pion to charged particle ratio for positive (left) and negative (right) particles as a function of the transverse momentum. The PYTHIA 6 Perugia-0 tune predictions are shown as the solid black lines ($\sqrt{s} = 900$ GeV).

Figure 9.19: Corrected π^+ (left) and π^- (right) spectra compared with the ALICE preliminary results and PYTHIA 6 Perugia-0 tune predictions ($\sqrt{s} = 900$ GeV).
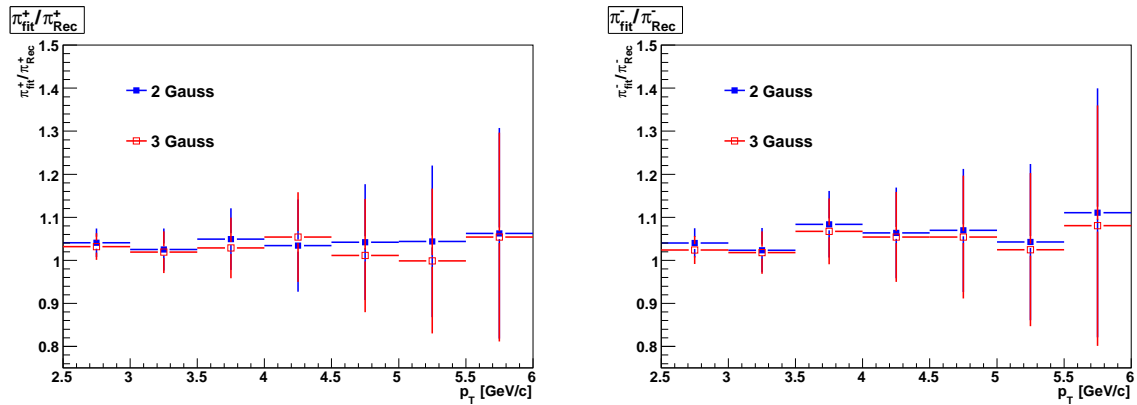
Figure 9.20: Systematic uncertainties for π^+ (left) and π^- (right) yields for the two methods, estimated from ALICE simulated data ($\sqrt{s} = 900$ GeV).

π^+/π^- ratio as a function of p_T for both methods. Except one p_T bin ($4.5 < p_T < 5$ GeV/c), the number of π^+ estimated by the two methods is close to the one of π^-. The problem arises due to the fact that the Δ_π distributions are quite different in this p_T bin. It looks like the pion mean dE/dx obtained in Section 9.4.2 fails for positive particles or the calibration is not properly performed for this bin. Since nothing like this can be seen for the 7 TeV sample (see next section), it may be a statistical fluctuation and no more effort to understand this was put here. The $\pi^+/(\pi^+ + K^+ + p)$ (left) and $\pi^-/(\pi^- + K^- + \bar{p})$ (right) ratios compared with PYTHIA 6 Perugia-0 tune [148] predictions are depicted in Fig. 9.18. The data indicate that 60% of the charged particles are charged pions, while PYTHIA 6 Perugia-0 tune overestimates the charged pion fractions with around 10%.

The corrected pion spectra are shown in Fig. 9.19. They follow nicely the ALICE preliminary charged particle transverse momentum spectrum [145]. The small discrepancy between the data from this analysis and ALICE preliminary π^+ and π^- spectra at lower momenta obtained from a combined analysis using the ITS, TPC, and TOF [149] is related to the different correction and normalization procedures used in the two analyzes. The PYTHIA 6 Perugia-0 tune slightly overpredicts the pion yields as was also seen in the ratios above.

Systematic Uncertainties

In order to estimate the systematic uncertainties, the above analysis was repeated on ALICE simulated data (the same data set used to obtain the acceptance and reconstruction efficiency). Figure 9.20 shows the ratio between the number of pions found using the methods and the number of reconstructed pions as a function of the transverse momentum. The methods estimate the pion yields within 5-10%; this is the methods uncertainty. More statistics is needed for a more accurate evaluation. The systematic uncertainty on the p_T spectrum for inelastic events was found to be 3.0-7.1% [145]. Adding quadratically the two values, the total systematic uncertainty is 6-12%.

9.5.3   Pion Yields at 7 TeV Center-of-Mass Energy

The results obtained from the 7 TeV sample will be presented in the following using the same procedure as for the 900 GeV data set. Figure 9.21 shows examples of Δ_π distributions for positive (upper) and negative (lower) particles together with the double (left) and triple (right) Gaussian fits. The results are for $4 < p_T < 4.5$ GeV/c. The distributions for positive and negative particles are similar in this case and the fits describe the data well (see Appendix E).

The uncorrected pion yields are depicted in Fig. 9.22. The methods agree very well over the full p_T range (also see Fig. 9.23). The same cross checks as the ones done for the 900 GeV sample are also performed here. Figure 9.24 shows the π^+/π^- ratio as a function of p_T for both methods. The same number of π^+ and π^- is found by the two methods for $p_T < 8$ GeV/c, while for $8 < p_T < 14$ GeV/c the limited statistics influences the fits and the yields are estimated within 10%. The $\pi^+/(\pi^+ + K^+ + p)$ (left) and $\pi^-/(\pi^- + K^- + \bar{p})$ (right) ratios
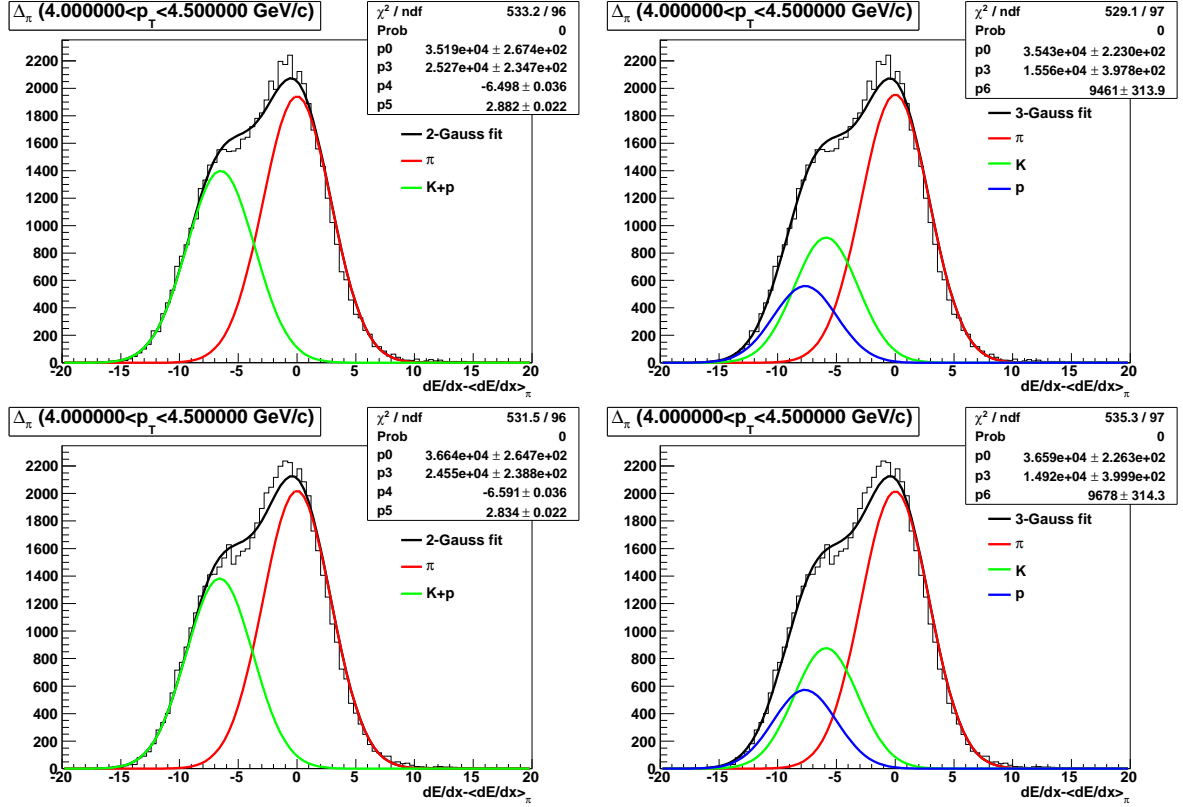
Figure 9.21: Examples of the Δ_π distributions for positive (upper) and negative (lower) particles together with the double Gaussian (left) and triple Gaussian (right) fits for $4 < p_T < 4.5$ GeV/c. The means and widths are constrained by the values of the generated shapes for triple Gaussian fits, while only the mean and width of pions are constrained by the values of the generated shapes for double Gaussian fits ($\sqrt{s} = 7$ TeV).
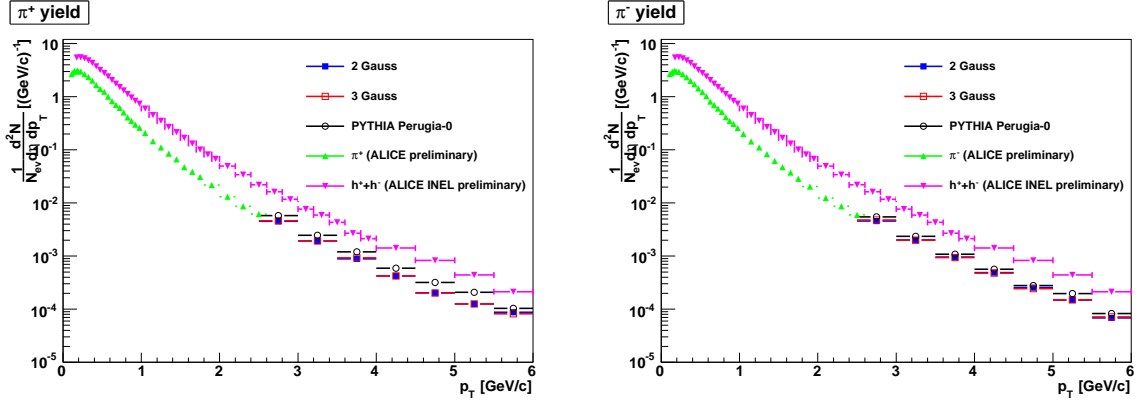
compared with PYTHIA 6 Perugia-0 tune predictions are presented in Fig. 9.25. As can be seen from the figure the charged pion fractions are slightly increasing with the transverse momentum. PYTHIA 6 Perugia-0 tune overpredicts the charged pion fractions with 5-10% for $p_T < 8$ GeV/c, while at higher p_T more statistics is needed to draw conclusions.

The corrected pion spectra are shown in Fig. 9.26. A good agreement between the π^+ and π^- spectra and the ALICE preliminary π^0 spectrum measured with a completely different method is found. Also the pion spectra follow nicely the charged particle transverse momentum spectrum. The PYTHIA 6 Perugia-0 overestimates the pion yields.

Systematic Uncertainties

In order to estimate the systematic uncertainties, the analysis was repeated on ALICE simulated data (the same data set used to obtain the acceptance and reconstruction efficiency). Figure 9.27 shows the ratio between the number of pions found using the methods and the number of reconstructed pions as a function of the transverse momentum. For
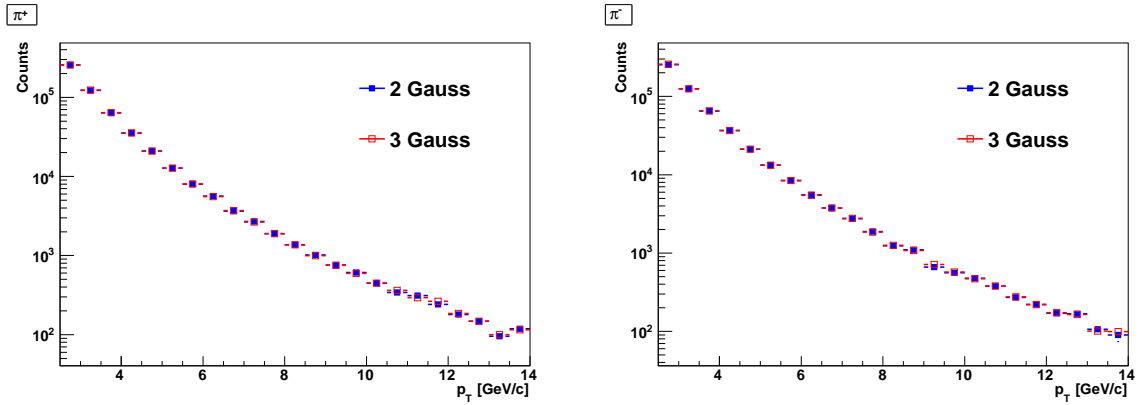
Figure 9.22: Uncorrected π^+ (left) and π^- (right) yields from the double (full blue squares) and triple (open red squares) Gaussian fits as a function of the transverse momentum ($\sqrt{s} = 7$ TeV).
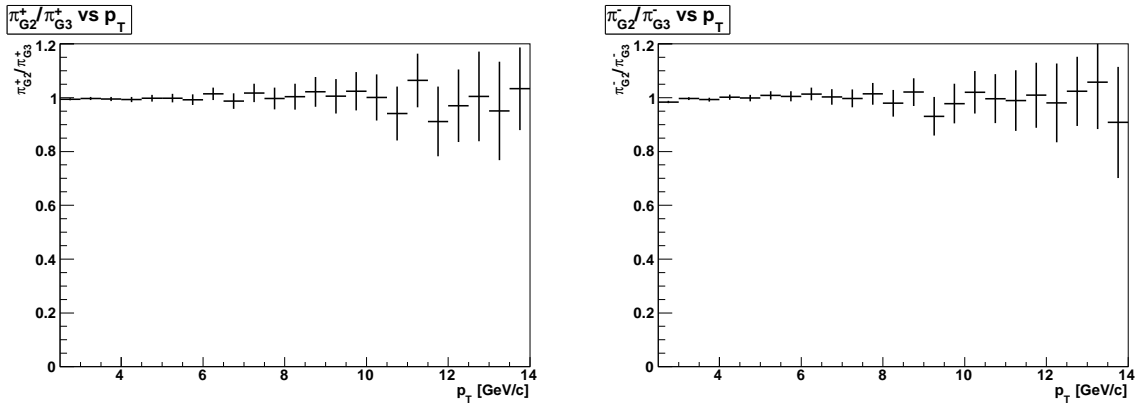
Figure 9.23: The ratio between the results of the two methods for π^+ (left) and π^- (right) as a function of transverse momentum ($\sqrt{s} = 7$ TeV).
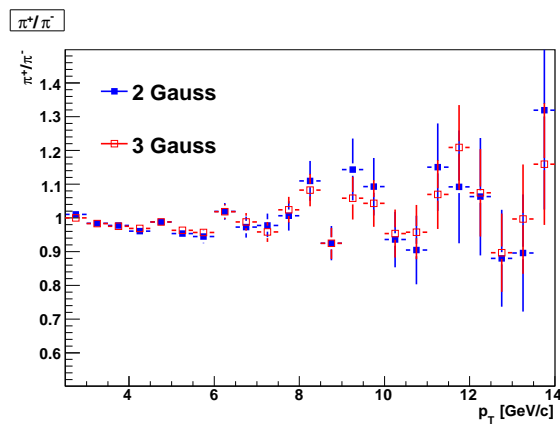
Figure 9.24: π^+/π^- ratio as a function of transverse momentum ($\sqrt{s} = 7$ TeV).
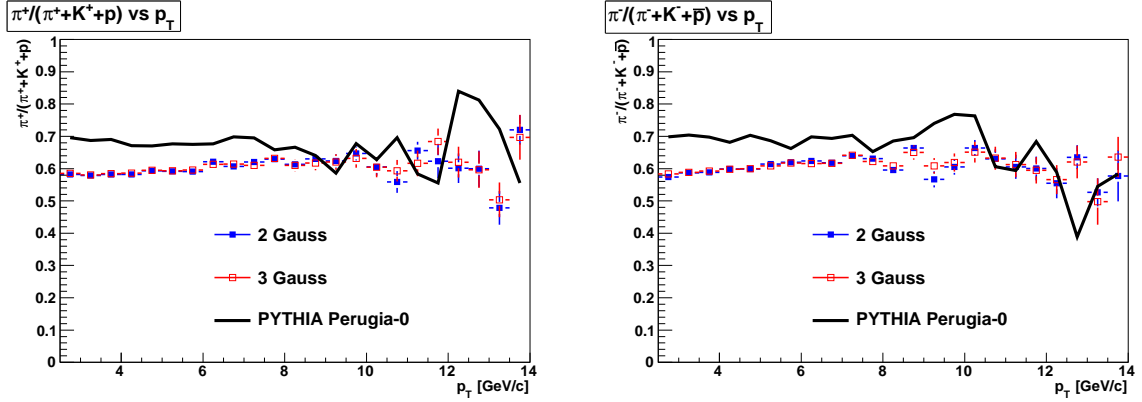
Figure 9.25: Pion to charged particle ratio for positive (left) and negative (right) particles as a function of the transverse momentum. The PYTHIA 6 Perugia-0 tune predictions are shown as the solid black lines ($\sqrt{s} = 7$ TeV).
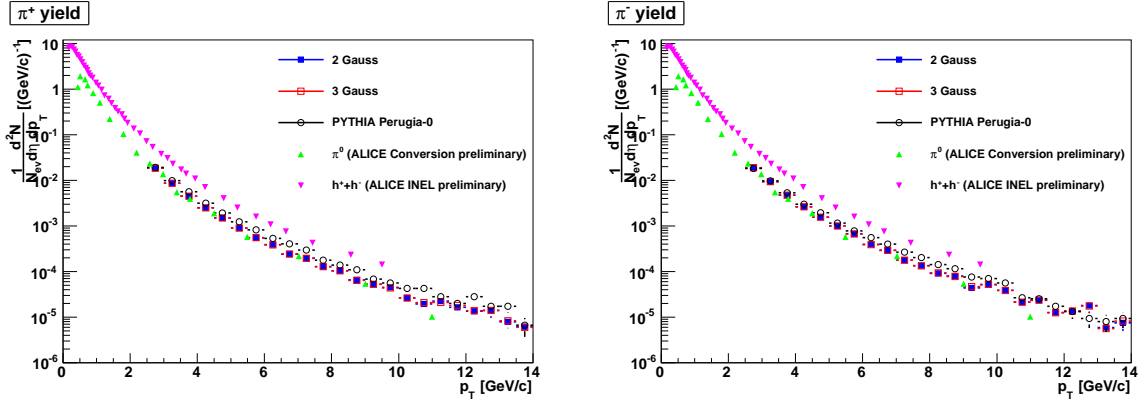
Figure 9.26: Corrected π^+ (left) and π^- (right) spectra compared with the ALICE preliminary results and PYTHIA 6 Perugia-0 tune predictions ($\sqrt{s} = 7$ TeV).
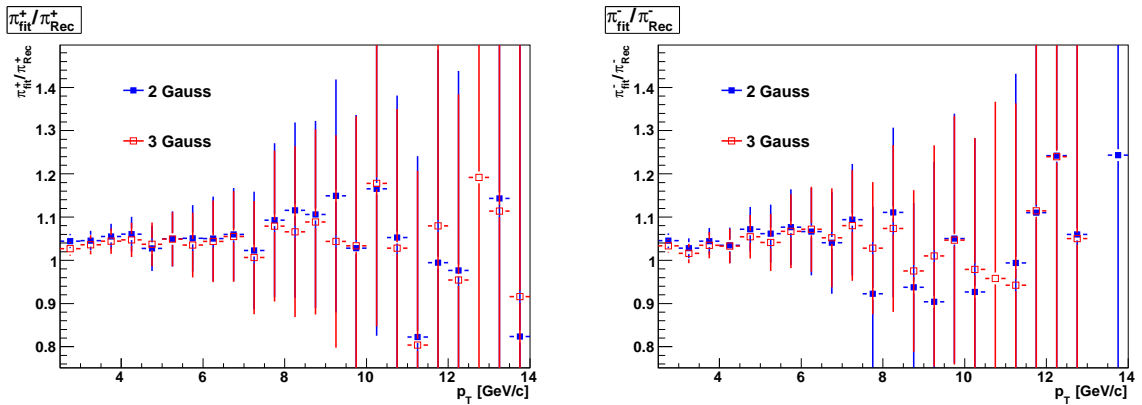
Figure 9.27: Systematic uncertainties for π^+ (left) and π^- (right) yields for the two methods, estimated from ALICE simulated data ($\sqrt{s} = 7$ TeV).

$p_T < 8$ GeV/c the methods estimate the pion yields within 5-10%, while the limited statistics at $p_T > 8$ GeV/c does not allow a quantitative evaluation of the systematic uncertainty (also for $p_T < 8$ GeV/c more statistics is needed). The systematic uncertainty on the p_T spectrum for inelastic events is not yet determined for this energy, so the total systematic uncertainty can not be estimated in this case.

9.6   Final Remarks

The analysis presented here, even though in an early stage, has shown that particle identification at intermediate and high p_T is feasible by employing the TPC dE/dx. Charged pion spectra could be extracted up to 6 GeV/c and 14 GeV/c for the 900 GeV and 7 TeV samples, respectively. The reach in momentum is statistically limited because, as can be seen from Fig. 9.12 and Fig. 9.13, the separation between pions, kaons, and protons is still increasing with momentum.

More developments are expected to happen or are already pursued for this analysis. Some of them will be presented in the following. First of all, the analysis could be refined using π and p from Λ^0 and K^0 decays, identified by their displaced decay vertex, for experimental calibration of the $\langle dE/dx \rangle (\beta\gamma)$ curve. Furthermore, the generated expected shapes for π and p could be cross checked with the obtained dE/dx distributions. Also identified particles by TOF and/or HMPID detectors could be used for trimming the procedures. As already pointed out, a new correction and normalization procedure is already under investigation. A fit function that describes better the data than Eq. 9.3 could be used to extract the $\sigma_{dE/dx}$. Also the momentum resolution needs to be taken into account. The main challenge will be to extract the K and p spectra due to the strong correlations between the obtained number of kaons and protons observed in Section 8.4.

Chapter 10

Summary

In this thesis the ALICE discovery potential of signals beyond the SM in pp collisions has been presented. The heavy stable charged particles predicted by some theoretical models are good candidates for such searches since the ALICE detector has excellent particle identification capabilities. The focus has been on gluino R-hadrons which are stable hadronized gluinos, arising in Split Supersymmetry scenarios. First steps towards identified charged particle spectra at intermediate and high transverse momentum (p_T) were also taken in this thesis. Using the TPC specific ionization energy loss (dE/dx), the charged pion spectra have been extracted in pp collisions at $\sqrt{s} = 900$ GeV and $\sqrt{s} = 7$ TeV (the maximum LHC energy available in this initial phase).

The analysis presented in Chapter 7 has illustrated that the discovery of new physics through heavy stable charged particles is a possibility also for ALICE. It showed for the first time detailed ALICE detector response simulations of the most important signatures for R-hadron identification in the ALICE central barrel. The TPC dE/dx can very easily separate charge $2e$ R-hadrons from SM particles and in some cases the fractional charge R-hadrons from integer charge high momentum particles. Only charge $+e$ R-hadrons with high dE/dx and low β can be separated from other charged particles by the TPC on an event by event basis. The TOF detector can not only separate the slow R-hadrons from the faster SM particles, but can also together with the momentum information from the tracking give an estimate for the mass of these particles. In order to have evidence for R-hadrons probably one needs at least one "golden event" where two approximately back-to-back high p_T tracks with dE/dx consistent with high masses in ITS, TPC, and a time-of-flight indicating that the particles are slow are measured. Furthermore, two trigger scenarios are considered in this study to enhance the number of R-hadron events. PYTHIA simulations performed at $\sqrt{s} = 7$ TeV show that it is very unlikely that ALICE can discover R-hadrons, even if they exist, with mass above 200 GeV/c^2 at this energy due to the low number of nominal annual ALICE collisions (10^9 events). No evidence of particles that pass the R-hadron selection criteria in the ITS, TPC, and TOF can be observed in around 27.5 million pp events at $\sqrt{s} = 7$ TeV. Clearly this is a long shot for ALICE, and if no heavy stable charged hadrons are observed, any cross section limit would quickly be superseded by ATLAS and CMS, but it is also sure that if we don't look for

them we won't find them.

The second topic of this thesis was particle identification (PID) at intermediate and high p_T using the TPC dE/dx. As this analysis can be used for different studies (e.g. high p_T R_{AA}, p/π anomaly), it seems worthwhile to develop it although the ALICE reconstruction and calibration software is still in an early phase. A study based on the ALICE simulated data done to understand how and to what precision identified charged particle spectra can be obtained on the relativistic rise is described in Chapter 8. Two approaches, R_π (STAR method for statistical PID) and Δ_π (the simplest method), were investigated here. The Δ_π method was found to be more suitable in the case of ALICE and was used in Chapter 9 to extract the charged pion spectra at high p_T in inelastic pp collisions at $\sqrt{s} = 900$ GeV and $\sqrt{s} = 7$ TeV. Two different methods, double and triple Gaussian fits, were used to extract the yields. A new approach to generate the expected shapes for π, K, and p was introduced to constrain as many parameters as possible in the fits. The methods gave similar results for π^+ and π^- yields at both energies. The high p_T charged pion spectra could be extracted up to 6 GeV/c and 14 GeV/c for the 900 GeV and 7 TeV samples, respectively. The reach in momentum in the analysis is statistically limited since the separation between pions, kaons, and protons is still increasing with momentum. This is a truly unique ALICE capability at LHC that has the promise of delivering many exciting physics results.

Appendix A

Variables

For any particle of momentum $p = (p_x, p_y, p_z)$ and mass m one has:

$$E = \sqrt{p^2 + m^2} \tag{A.1}$$

$$p_T = \sqrt{p_x^2 + p_y^2} \tag{A.2}$$

$$m_T = \sqrt{m^2 + p_T^2} \tag{A.3}$$

$$\beta = \frac{v}{c} = \frac{pc}{E} \tag{A.4}$$

$$\gamma = \frac{1}{\sqrt{1 - \beta^2}} = \frac{E}{mc^2} \tag{A.5}$$

The longitudinal momentum p_z is usually expressed in terms of the rapidity y:

$$y = \frac{1}{2} \ln \frac{E + p_z}{E - p_z}. \tag{A.6}$$

The rapidity has the nice property of being invariant under a boost transformation (along the beam axis), since it changes by an additive constant (the rapidity of the moving frame of reference):

$$y' = \frac{1}{2} \ln \frac{E' + p_z'}{E' - p_z'} = \frac{1}{2} \ln \frac{\gamma(1 - \beta)(E + p_z)}{\gamma(1 + \beta)(E - p_z)} = \frac{1}{2} \ln \frac{E + p_z}{E - p_z} + \frac{1}{2} \ln \frac{1 - \beta}{1 + \beta} = y - y_\beta \tag{A.7}$$

The following relations can be useful:

$$E = m_T \cosh(y) \tag{A.8}$$

$$p_z = m_T \sinh(y) \tag{A.9}$$

In the limit when $p_T \gg m$, the rapidity reduces to the pseudo-rapidity η:

$$y = \frac{1}{2} \ln \frac{E + p_z}{E - p_z} \sim \frac{1}{2} \ln \frac{p + p_z}{p - p_z} = \frac{1}{2} \ln \frac{1 + \cos\theta}{1 - \cos\theta} = -\ln\left(\tan\frac{\theta}{2}\right) \equiv \eta \tag{A.10}$$

η is often used when the mass is unknown.

For any collision between the projectile (energy E_1, momentum p_1, mass m_1) and the target (energy E_2, momentum p_2, mass m_2) , the center of mass (CM) energy $\sqrt{s}$ is given by:

$$\sqrt{s} = \sqrt{(E_1 + E_2)^2 - (p_1 + p_2)^2} \tag{A.11}$$

When the projectile and the target have the same energy and equal and opposite momenta, $\sqrt{s}$ is simply the sum of the two energies.

For a collision in the 'laboratory system', where the target is at rest:

$$s = m_1^2 + m_2^2 + 2E_1 m_2 \tag{A.12}$$

In this case the rapidity y_{CM} is:

$$y_{CM} = \cosh^{-1} \frac{E_1 + m_2}{\sqrt{s}} \tag{A.13}$$

Another useful quantity is y_{beam}, the rapidity of the incident particle in the laboratory system

$$y_{beam} = \cosh^{-1} \frac{E_1}{m_1} \tag{A.14}$$

and for the same mass

$$y_{CM} = y_{beam}/2 \tag{A.15}$$

In the case of ion collisions, the total CM energy is $\sqrt{s} = A \cdot \sqrt{s_{NN}}$ for symmetric AA collisions, where $\sqrt{s_{NN}}$ is the nucleon pair CM energy.

Appendix B

ALICE Coordinate System
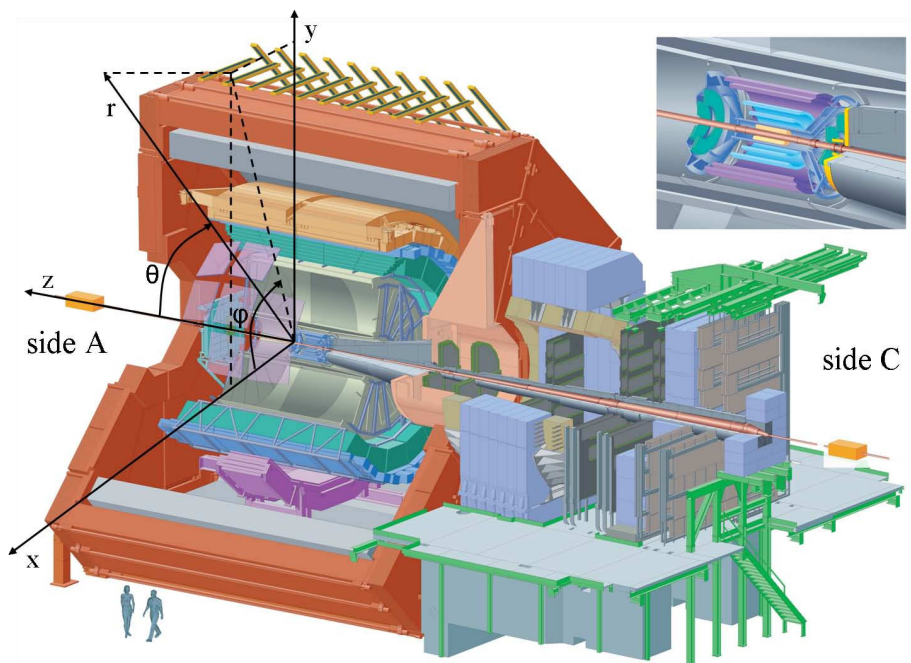
Figure B.1: The ALICE coordinate system.

ALICE has a global and local coordinate systems. The global coordinate system [150] is a right-handed orthogonal Cartesian system with the origin at the beam interaction point. The parameters are defined as:

- **x axis** is lying in the local horizontal accelerator plane, perpendicular to the mean local beam direction and pointing towards the center of the LHC ring. The side with positive x values (from the point of origin toward the accelerator center) is labeled as Inside (I), the opposite as Outside (O);

- **y axis** is perpendicular (vertical) to the x axis and the mean local beam direction, pointing upward;

- **z axis** is parallel to the mean local beam direction, pointing towards the 'side A'. The muon arm is at negative z ('side C');

- **azimuthal angle** ϕ increases counter-clockwise from x ($\phi = 0$) to y ($\phi = \pi/2$) to x ($\phi = 2\pi$) with the observer looking from side A towards side C;

- **polar angle** θ increases from z ($\theta = 0$) to xy plane ($\theta = \pi/2$) to $-z$ ($\theta = \pi$).

A sketch of the global coordinate system is given in Fig. B.1.

Due to the azimuthal segmentation of the central tracking detectors (ITS, TPC, and TRD) the reconstruction software uses a local coordinate system related to a given sub-detector (TPC sector, ITS module, etc.). The local coordinate system is a right-handed Cartesian system with the same origin and z axis as the global system and the x axis perpendicular to the subdetector 'sensitive plane' (TPC pad row, ITS ladder, etc.). Therefore the local and global systems can be transformed into each other by a simple rotation of the angle α around the z axis.

Appendix C

Drift Properties in Gases

The understanding of the motion of the electrons and ions in gases is very important for ionization detectors (e.g. a TPC with its long drift lengths) since these factors crucially influence their behavior. Moreover, the detectors are located in electric and magnetic fields which complicates the picture even more. Two processes are of particular importance: the drift velocity and the diffusion.

C.1 Drift Velocity

A charged particle traversing a gas frees electrons and ions which in the presence of an electric field $\mathbf{E}$ are accelerated along the field lines. This acceleration is limited by collisions with the gas molecules and the average velocity attained is known as the *drift velocity*. When a magnetic field $\mathbf{B}$ is also applied, the drift of charged particles can be expressed in terms of an equation of motion with a friction term [98]

$$m\frac{d\mathbf{u}}{dt} = e\mathbf{E} + e[\mathbf{u} \times \mathbf{B}] - K\mathbf{u}, \tag{C.1}$$

where m and e are the mass and electric charge of the particle with the velocity vector $\mathbf{u}$, and K describes a frictional force experienced by the particle in the gas.

As the ratio m/K has the dimension of a characteristic time it can be interpreted as the average time between collisions τ:

$$\tau = \frac{m}{K}. \tag{C.2}$$

For $t \gg \tau$, $d\mathbf{u}/dt = 0$ (the drift velocity is constant) and Eq. C.1 becomes:

$$\frac{1}{\tau}\mathbf{u} - \frac{e}{m}[\mathbf{u} \times \mathbf{B}] = \frac{e}{m}\mathbf{E}. \tag{C.3}$$

Introducing the cyclotron frequency $\boldsymbol{\omega} = \frac{e}{m}\mathbf{B}$ and $\boldsymbol{\epsilon} = \frac{e}{m}\mathbf{E}$, Eq. C.3 can be expressed in the

form of the matrix equation

$$M\mathbf{u} = \boldsymbol{\epsilon}, \quad M = \begin{bmatrix} 1/\tau & -\omega_z & \omega_y \\ \omega_z & 1/\tau & -\omega_x \\ -\omega_y & \omega_x & 1/\tau \end{bmatrix} \tag{C.4}$$

with the solution obtained by inverting M:

$$\mathbf{u} = M^{-1}\boldsymbol{\epsilon}$$

$$M^{-1} = \begin{bmatrix} 1 + \omega_x^2\tau^2 & \omega_z\tau + \omega_x\omega_y\tau^2 & -\omega_y\tau + \omega_x\omega_z\tau^2 \\ -\omega_z\tau + \omega_x\omega_y\tau^2 & 1 + \omega_y^2\tau^2 & \omega_x\tau + \omega_y\omega_z\tau^2 \\ \omega_y\tau + \omega_x\omega_z\tau^2 & -\omega_x\tau + \omega_y\omega_z\tau^2 & 1 + \omega_z^2\tau^2 \end{bmatrix} \times \frac{\tau}{1 + \omega^2\tau^2}, \tag{C.5}$$

where $\omega^2 = \omega_x^2 + \omega_y^2 + \omega_z^2 = \left(\frac{e}{m}\right)^2 B^2$. Equation C.5 can be written as:

$$\mathbf{u} = \frac{e}{m}\tau|\mathbf{E}|\frac{1}{1 + \omega^2\tau^2}\left(\hat{\mathbf{E}} + \omega\tau[\hat{\mathbf{E}} \times \hat{\mathbf{B}}] + \omega^2\tau^2(\hat{\mathbf{E}} \cdot \hat{\mathbf{B}})\hat{\mathbf{B}}\right), \tag{C.6}$$

where $\hat{\mathbf{E}}$ and $\hat{\mathbf{B}}$ denote the unit vectors in the direction of the fields. Equation C.6 shows that the drift direction is governed by the dimensionless parameter $\omega\tau$.

For $\omega\tau = 0$, $\mathbf{u}$ along $\mathbf{E}$, the above relation reads:

$$\mathbf{u} = \frac{e}{m}\tau\mathbf{E} = \mu\mathbf{E}. \tag{C.7}$$

Here μ is the electron mobility and defined as

$$\mu = \frac{e}{m}\tau. \tag{C.8}$$

For positive ions, the drift velocity is low due to their large mass and was found to depend linearly on the ratio E/p (called the reduced electric field) up to relatively high electric fields [151]. Here p denotes the pressure. This implies that the mobility μ is a constant at a fixed pressure. For a given E, it is also evident that μ varies as the inverse of the pressure. The drift velocity of positive noble gas ions in their own gas as a function of the reduced electric field is shown in the left panel of Fig. C.1. As can be seen from the figure, $\mu \propto E$ at low electric fields, while $\mu \propto \sqrt{E}$ at high fields. For electrons, the mobility is much greater than for ions since they are much lighter and is found to be a function of E [151]. The computed electron drift velocity in several gases at normal temperature and pressure (NTP: 20°, 1 atm) is depicted in right panel of Fig. C.1.

For $\omega\tau \gg 0$ and $e > 0$, $\mathbf{u}$ is along $\mathbf{B}$. If $\hat{\mathbf{E}} \cdot \hat{\mathbf{B}} = 0$, $\mathbf{u}$ will be in the direction of $\hat{\mathbf{E}} \times \hat{\mathbf{B}}$, independently of the charge sign. Changing the $\mathbf{B}$ polarity, the $\hat{\mathbf{E}} \times \hat{\mathbf{B}}$ component changes its sign. The $\mathbf{E}$ and $(\hat{\mathbf{E}} \cdot \hat{\mathbf{B}})\hat{\mathbf{B}}$ components will change sign when reversing the charge of the particle.
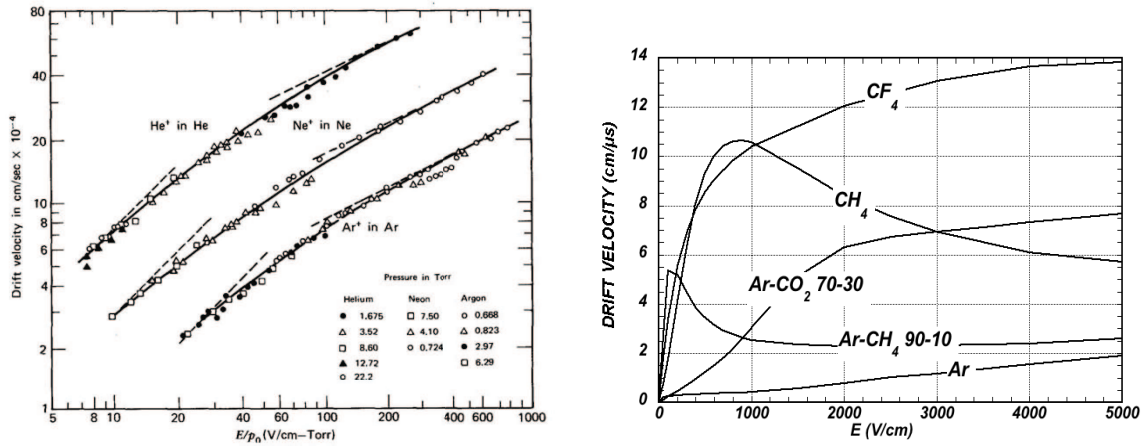
Figure C.1: Left: Drift velocity of positive noble gas ions in their own gas as a function of the reduced electric field. The dashed lines represent the limiting behavior at low ($\mu \propto E$) and high ($\mu \propto \sqrt{E}$) electric fields [98]. Right: Computed electron drift velocity as a function of the electric field in several gases at NTP (20°, 1 atm) [9].

When **E** and **B** are almost parallel, using Eq. C.6 and considering $\mathbf{E} = (0, 0, E_z)$, $\mathbf{B} = (B_x, B_y, B_z)$ $(B_x, B_y \ll B_z)$ the drift velocity components are given by:

$$\frac{u_x}{u_z} = \frac{-\omega\tau B_y + \omega^2\tau^2 B_x}{(1 + \omega^2\tau^2) B_z} \tag{C.9}$$

$$\frac{u_y}{u_z} = \frac{\omega\tau B_x + \omega^2\tau^2 B_y}{(1 + \omega^2\tau^2) B_z} \tag{C.10}$$

But as soon as the magnetic field is not parallel to the electric field, the drift velocity vector is not anymore parallel to **E** and this gives rise to displacements in the x and y directions (due to the Lorentz force) of the size $\delta_x = Lu_x/u_z$ and $\delta_y = Lu_y/u_z$ (L is the drift length). This effect is known as the $\mathbf{E} \times \mathbf{B}$ effect and must be corrected for. The correction is calculated from the ALICE field map and can be compared to measurements with laser tracks taken with and without magnetic field.

C.2 Diffusion

In the absence of the electric and magnetic fields, electrons and ions liberated by the moving particle spread uniformly outward. They suffer multiple collisions with the gas molecules and lose their initial energy, thus come quickly into thermal equilibrium and eventually recombine. At thermal energies, $\epsilon_T = 3/2kT$, the charges velocities are given by:

$$v = \sqrt{\frac{8kT}{\pi m}}, \tag{C.11}$$

where k is the Boltzmann's constant, T the temperature, and m the mass of the particle. At room temperature, the electron speed is a few times 10^6 cm/s, while the positive ion velocities are on the order of 10^4 cm/s [151].

In this simplest picture an electron cloud after diffusing a time t will have a Gaussian density distribution,

$$n = \left(\frac{1}{\sqrt{4\pi Dt}}\right)^3 \exp\left(-\frac{r^2}{4Dt}\right), \tag{C.12}$$

r being the distance from the point of the origin and D the *diffusion constant*. The width of the distribution, σ, in one dimension is thus

$$\sigma = \sqrt{2Dt}. \tag{C.13}$$

From kinetic theory, it can be shown that the diffusion constant is given by:

$$D = 1/3v\lambda, \tag{C.14}$$

where λ is the mean free path of the electron or ion in the gas which, for a classical ideal gas, reads:

$$\lambda = \frac{1}{\sqrt{2}}\frac{kT}{\sigma_0 p}, \tag{C.15}$$

where σ_0 is the total cross section for a collision with a gas molecule, p the pressure, T the temperature, and k the Boltzmann's constant. Substituting Eq. C.11 and Eq. C.15 into Eq. C.14 gives

$$D = \frac{2}{3\sqrt{\pi}}\frac{1}{p\sigma_0}\sqrt{\frac{(kT)^3}{m}} \tag{C.16}$$

which illustrates the dependence of D on the various gas parameters.

Applying an electric field breaks the isotropy of Eq. C.12. The three diffusion constants are anisotropic now, with a different component in the z direction than in the xy plane:

$$n = \left(\frac{1}{\sqrt{4\pi D_l t}}\right)\left(\frac{1}{\sqrt{4\pi D_t t}}\right)^2 \exp\left(-\frac{x^2+y^2}{4D_t t}-\frac{(z-ut)^2}{4D_l t}\right), \tag{C.17}$$

with u the drift velocity, D_l and D_t the longitudinal and transverse diffusion constants.

Averaging over a large number of collisions, the diffusion constant can be expressed as

$$D = \frac{2}{3}\frac{\epsilon}{m}\tau \tag{C.18}$$

and using Eq. C.8 and the thermal energy ϵ_T, one can deduce the *Nernst-Townsend formula*, or the *Einstein formula*:

$$\frac{D}{\mu} = \frac{kT}{e}. \tag{C.19}$$

The width of the electron cloud (Eq. C.13) that has traveled the distance $L = ut = \mu Et$ becomes:

$$\sigma = \sqrt{2Dt} = \sqrt{\frac{2DL}{u}} = \sqrt{\frac{2DL}{\mu E}} = \sqrt{\frac{4\epsilon L}{3eE}}. \tag{C.20}$$

Inserting Eq. C.19 into the above formula a lower limit to the width of the distribution, called the *thermal limit*, is obtained:

$$\sigma = \sqrt{\frac{2kTL}{eE}}.\tag{C.21}$$

Standard deviations for longitudinal (σ_l) and transverse (σ_t) diffusion scaled with the square root of the drift distance are used to quantify the diffusion in a gas:

$$D_L = \frac{\sigma_l}{\sqrt{L}} = \sqrt{\frac{2D_l t}{L}} = \sqrt{\frac{2D_l}{u}} = \sqrt{\frac{2D_l}{\mu E}}\tag{C.22}$$

$$D_T = \frac{\sigma_t}{\sqrt{L}} = \sqrt{\frac{2D_t t}{L}} = \sqrt{\frac{2D_t}{u}} = \sqrt{\frac{2D_t}{\mu E}},\tag{C.23}$$

in units of $\mu m/\sqrt{cm}$. Since the diffusion is inversely related with the drift velocity, fast-counting gases are needed for small diffusion. Fast gases mixtures are achieved by adding polyatomic gases (usually CH_4 or CO_2) to the noble gases, since the former ones have large inelastic cross section at moderate energies and in this way "cooling" the electrons. This gives a reduction in both the total electron scattering cross-section and the electron energy, so a large increase of the electron drift velocity. Figure C.2 shows the results for Ar and Ne gas mixtures with CH_4 and CO_2; the thermal limit is also marked on the figure. As can be seen from the figure, CO_2 gas mixture has a lower diffusion constant than CH_4 gas mixture. In order to achieve a high track resolution over the full drift length, the large TPC should be operated with CO_2 gas mixture.
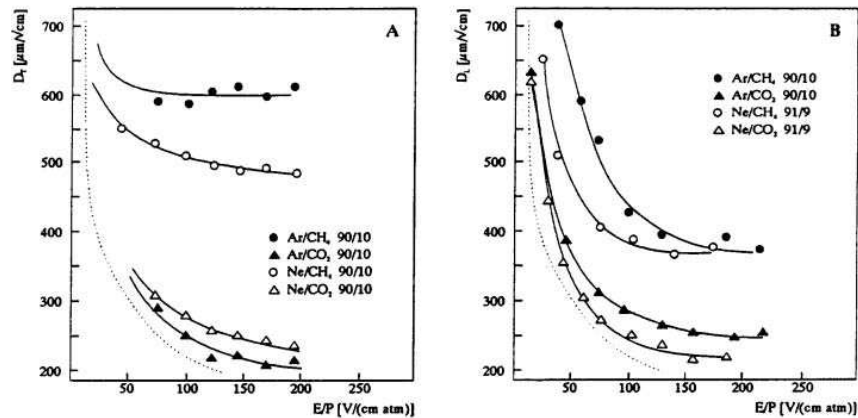

Figure C.2: Transverse (left) and longitudinal (right) diffusion constants as a function of the reduced field E/p for different gas mixtures. The thermal limit is denoted by the dotted line [152].

C.3 Avalanche Multiplication

The drifted electrons approaching an anode wire see the electric field

$$E = \frac{\lambda}{2\pi\epsilon_0 r},$$
(C.24)

where ϵ_0 is the permittivity, λ the linear charge density on the anode wire, r distance to the anode wire. At a certain distance, the electrons experienced large enough fields in order to undergo ionizing collisions with the gas molecules. The resulting secondary electrons then produce tertiary ionization and an avalanche is formed.

Lets consider λ_i to be the mean free path of the electron for a secondary ionizing collisions. Above a gas-dependent threshold, λ_i decreases exponentially with the field. Its inverse, $\alpha = 1/\lambda_i$ is the probability for an ionization per unit path length or better known as the *first Townsend coefficient* (see Fig. C.3). If there are n electrons, then in a path dx, there will be

$$dn = n\alpha dx$$
(C.25)

new electrons created in a uniform electric field. Integrating, one gets:

$$n = n_0 \exp(\alpha x),$$
(C.26)

where n_0 is the initial number of electrons.
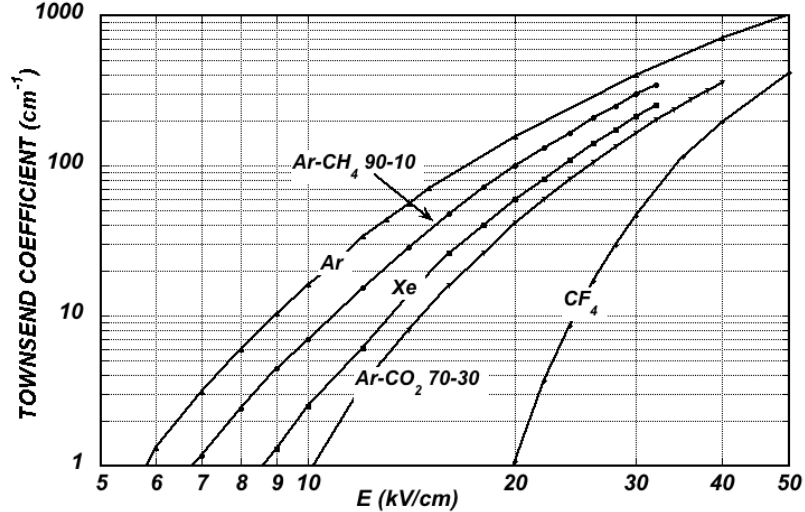

Figure C.3: Computed first Townsend coefficient α as a function of the electric field in several gases at NTP (20°, 1 atm) [9].

The multiplication factor or *gas gain* is then

$$n/n_0 = \exp(\alpha x).$$
(C.27)

The gas gain is limited to 10^8 or $\alpha x < 20$ which is known as Raether limit.

An early model for calculating α gives [153]:

$$\frac{\alpha}{p} = A \exp\left(\frac{-Bp}{E}\right),$$ (C.28)

where A and B are constants depending on the gas, p is the pressure, E the electric field, and α the first Townsend coefficient.

The voltage on the anode wires is chosen such that the number of electron-ion pairs in the avalanche is direct proportional to the number of primary electrons, resulting in a proportional amplification of the current. The proportionality is given as long as the field of the produced ions is negligible compared to that of the anode which is valid when the linear charge density on the wire λ is much larger than the charge density in the avalanche. As can be seen from Eq. C.24 the electric field is strongest near the anode wire, so most of the avalanche growth occurs very quickly and almost entirely within a few radii of the anode. Electrons are immediately after the avalanche absorbed by the anode and do not (or only marginally) participate in the signal creation. So the largest fraction of the detected signal is due to the motion of ions receding from the anode and drifting towards the cathode wire. This determines the characteristic shape of the detected signals in proportional mode, with a fast rise followed by a gradually slower increase. By differentiating the signal, the so-called ion tail that limits the time resolution of the detector is usually removed.

Appendix D

Double and Triple Gaussian Fits (900 GeV)

Figure D.1: Double Gaussian fits for positive particles ($\sqrt{s} = 900$ GeV).

Figure D.2: Triple Gaussian fits for positive particles ($\sqrt{s}$ = 900 GeV). The fits describe very well the pions, while the kaons and protons are poor estimated due to the strong correlations presented in Section 8.4. Also the method fails to describe the kaons and protons for the first bins because the separation between particles is not clean (see Fig. 9.12).

Figure D.3: Double Gaussian fits for negative particles ($\sqrt{s} = 900$ GeV).

Figure D.4: Triple Gaussian fits for negative particles ($\sqrt{s} = 900$ GeV). The fits describe very well the pions, while the kaons and antiprotons are poor estimated due to the strong correlations presented in Section 8.4. Also the method fails to describe the kaons and antiprotons for the first bins because the separation between particles is not clean (see Fig. 9.12).
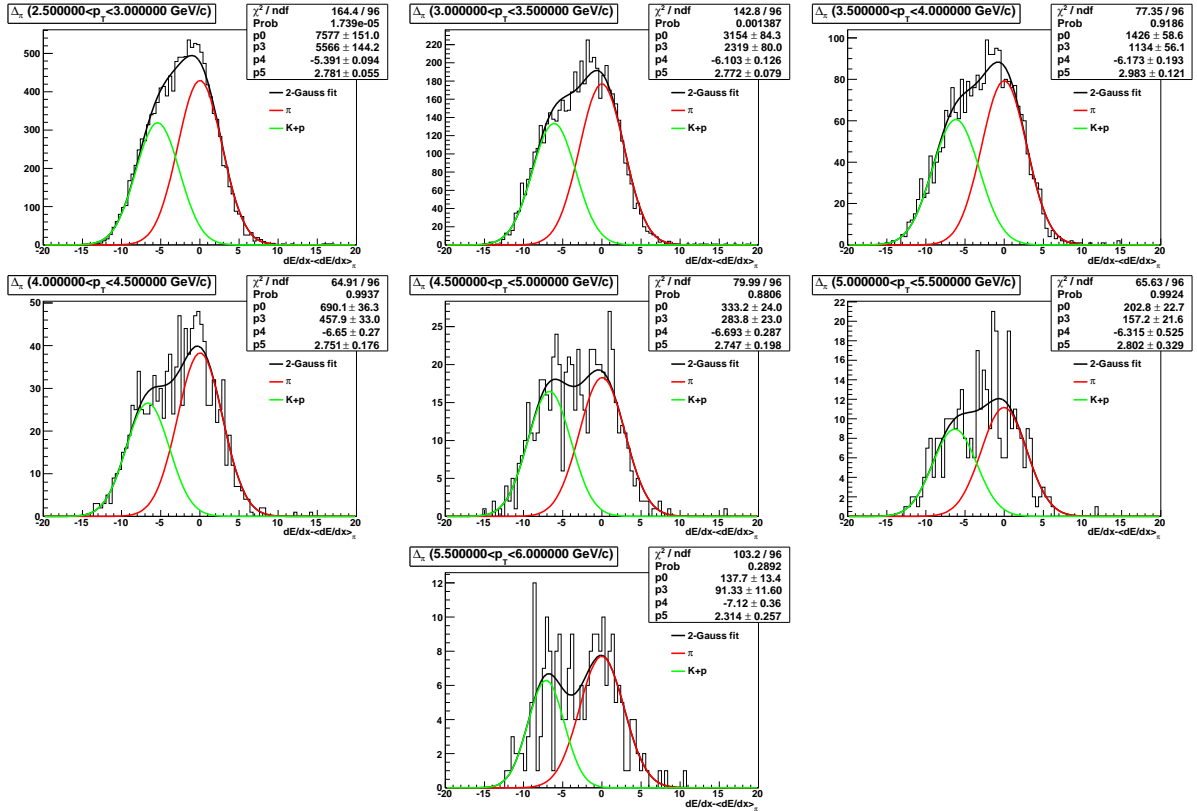
Appendix E

Double and Triple Gaussian Fits (7 TeV)
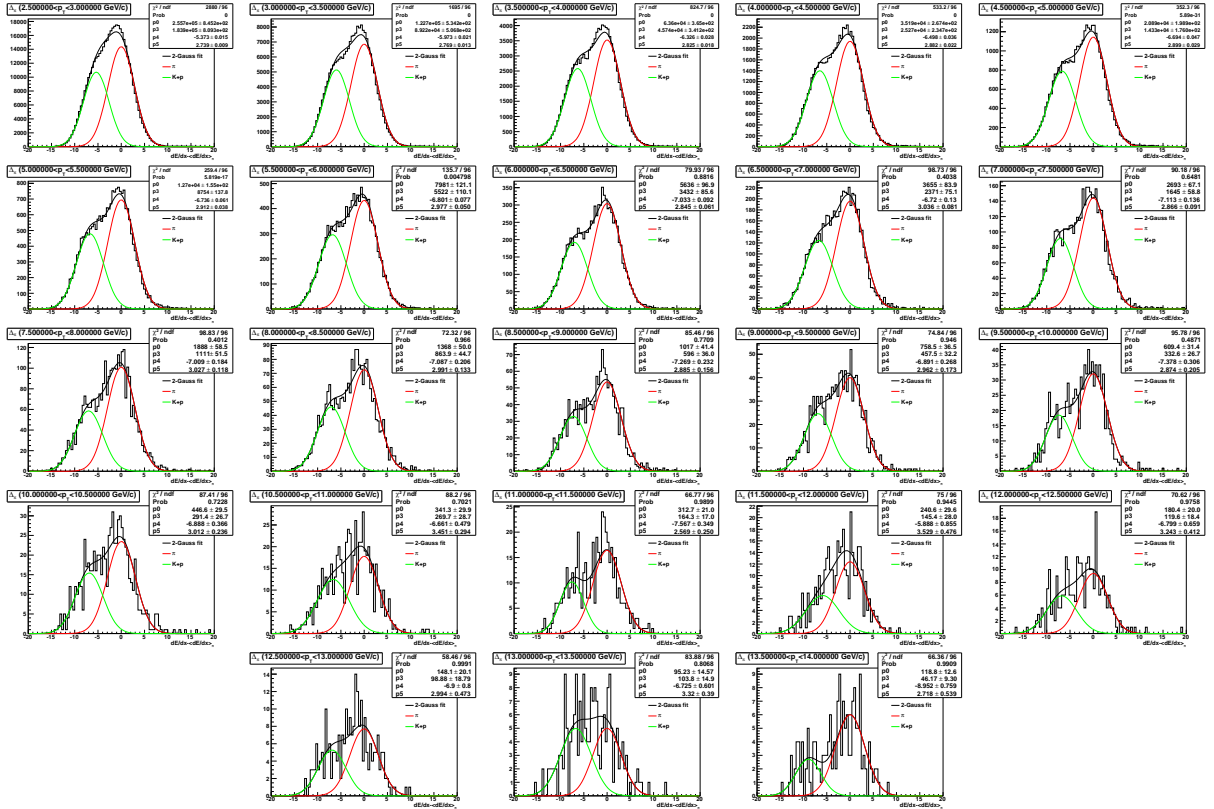
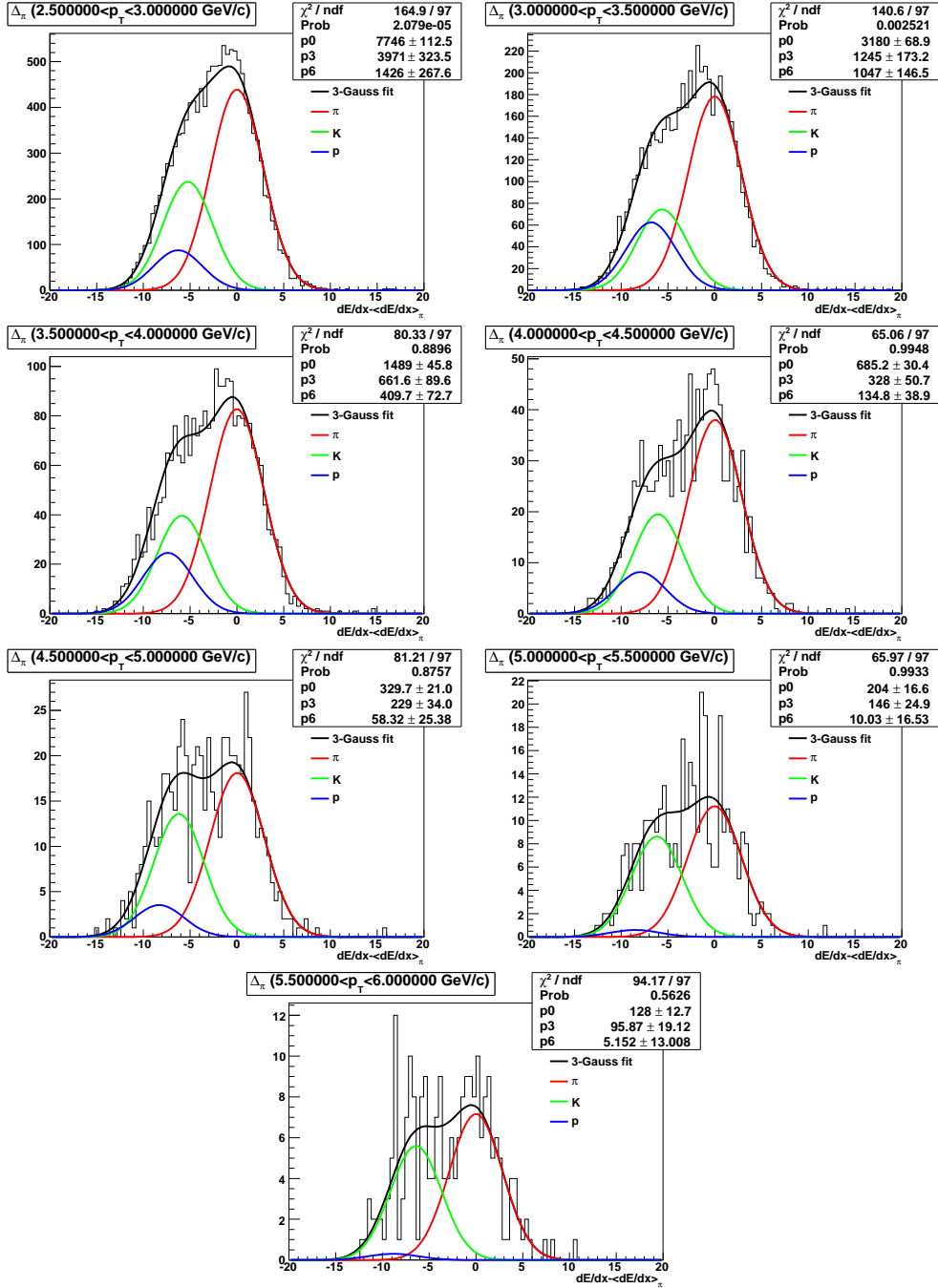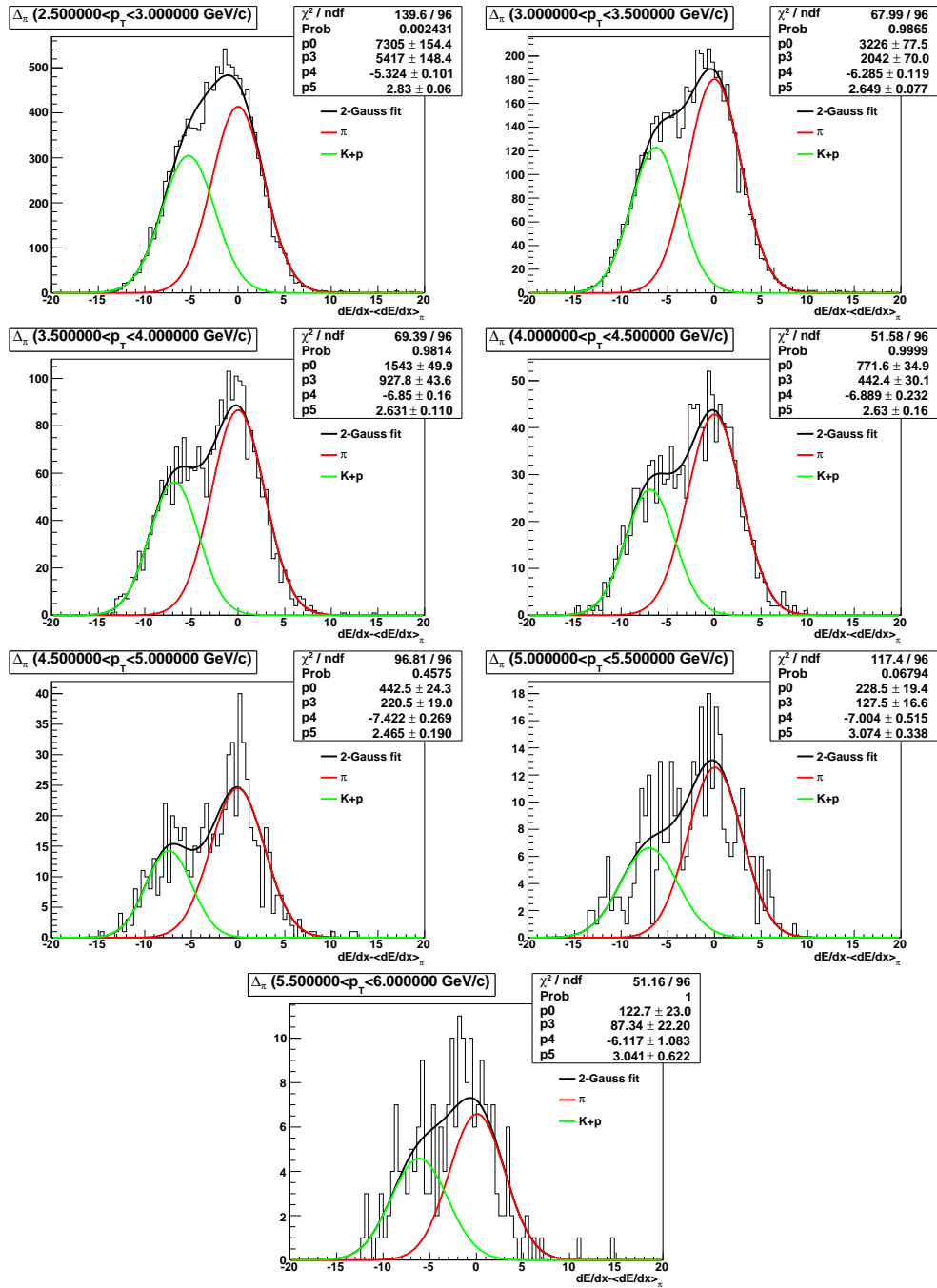Figure E.1: Double Gaussian fits for positive particles ($\sqrt{s} = 7$ TeV).
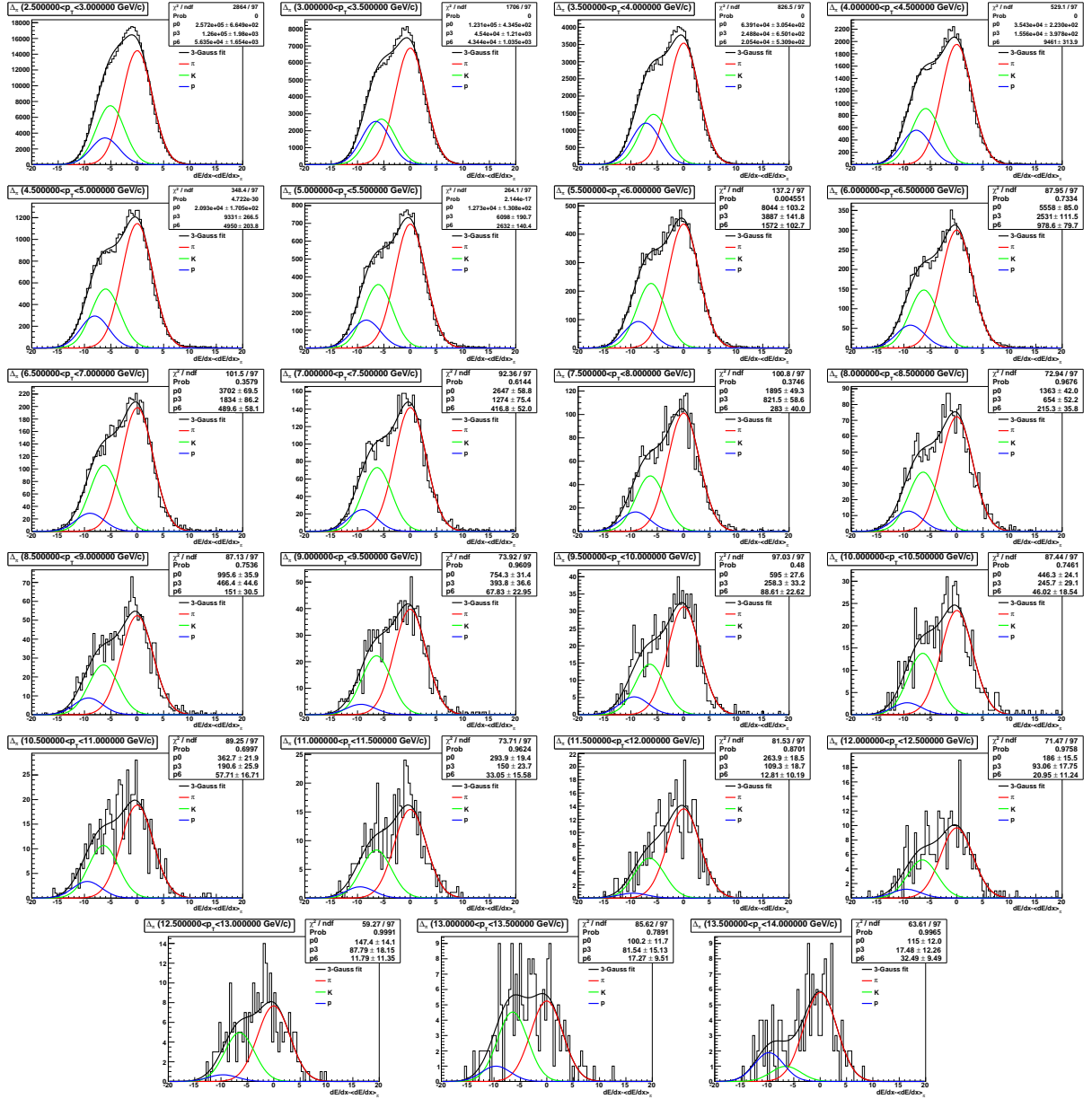
Figure E.2: Triple Gaussian fits for positive particles ($\sqrt{s} = 7$ GeV). The fits describe very well the pions, while the kaons and protons are poor estimated due to the strong correlations presented in Section 8.4. Also the method fails to describe the kaons and protons for the first bins because the separation between particles is not clean (see Fig. 9.13), while the limited statistics influences the fits in the last bins.

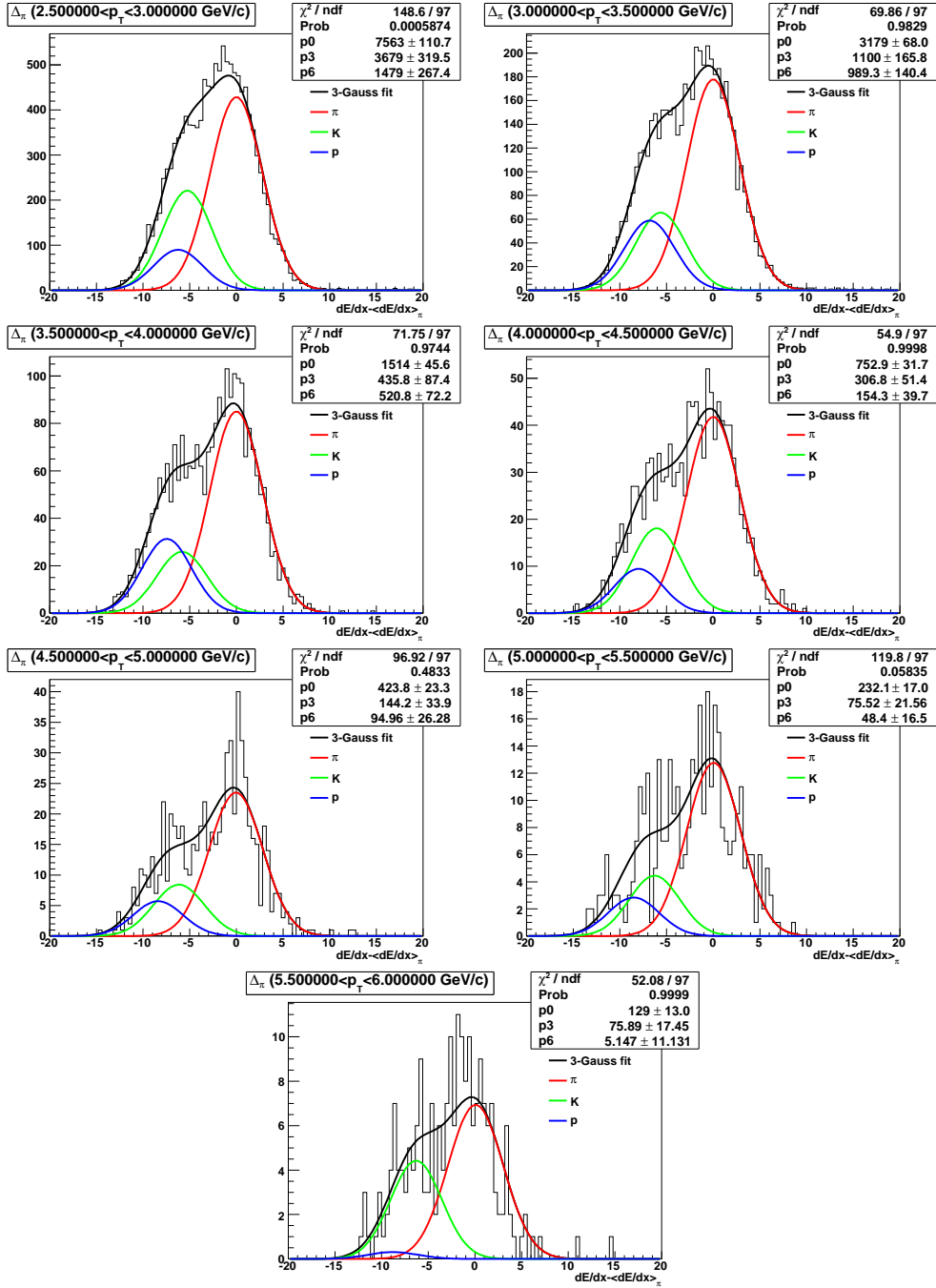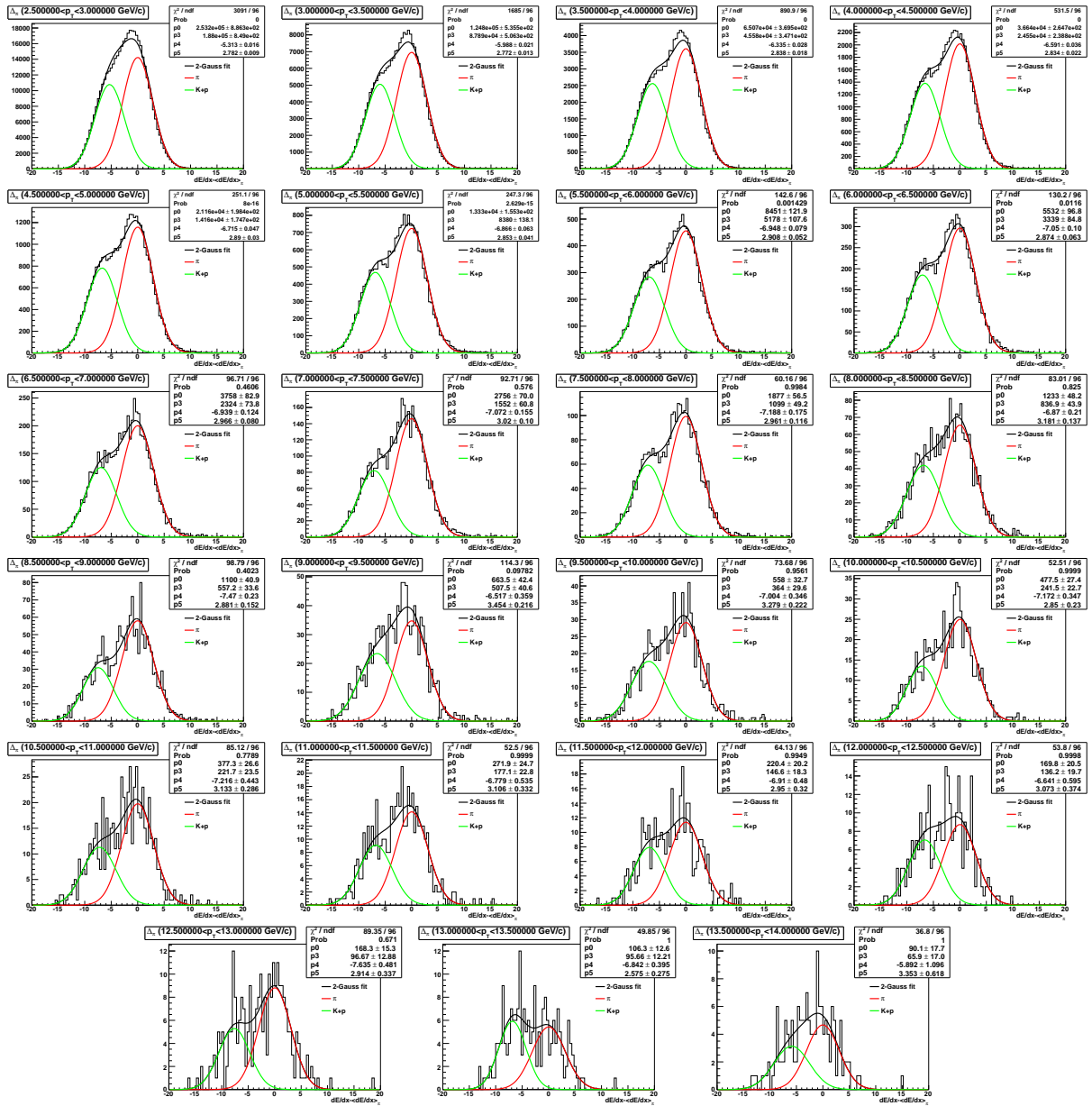Figure E.3: Double Gaussian fits for negative particles ($\sqrt{s} = 7$ TeV).
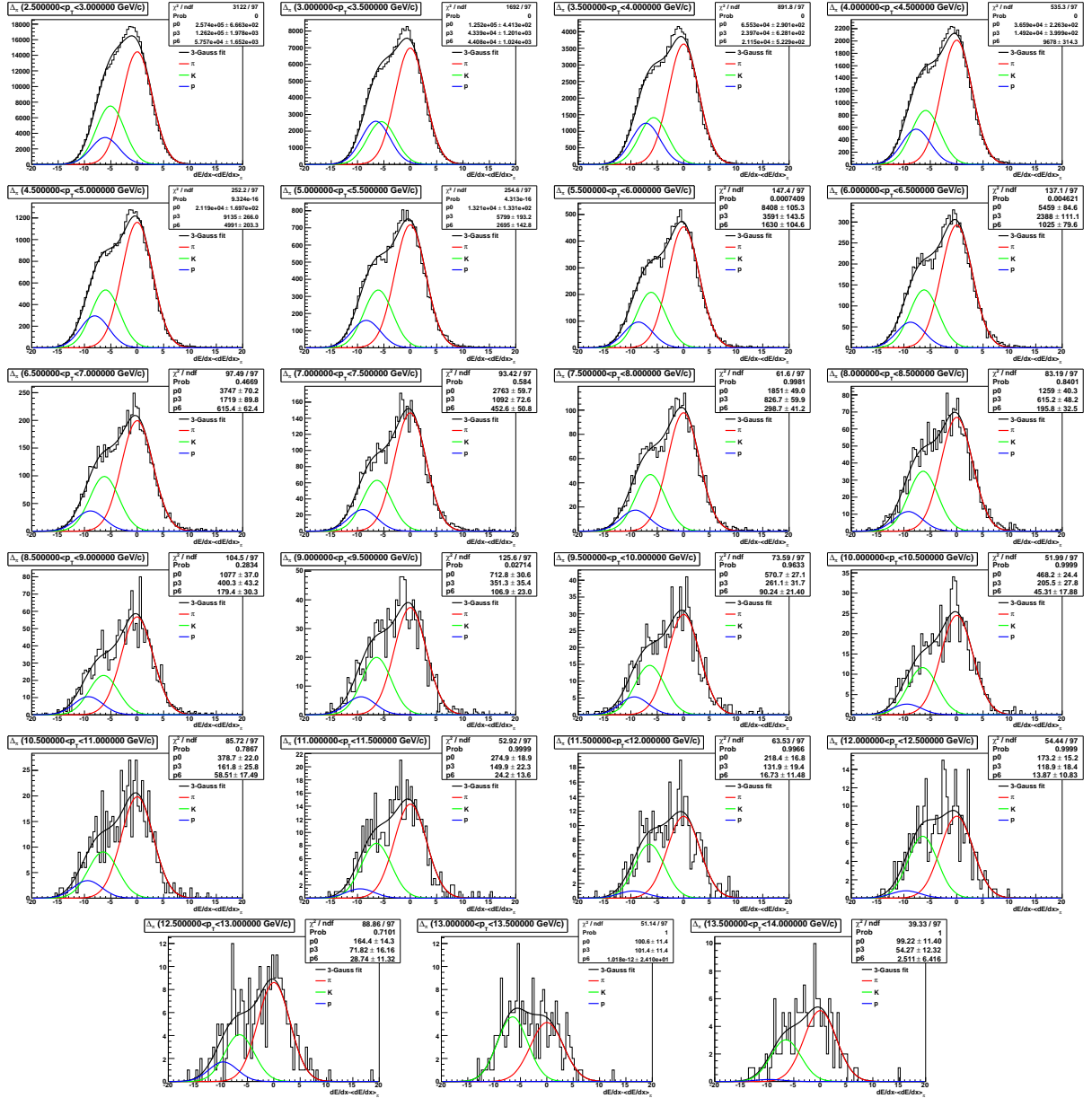
Figure E.4: Triple Gaussian fits for negative particles ($\sqrt{s} = 7$ GeV). The fits describe very well the pions, while the kaons and antiprotons are poor estimated due to the strong correlations presented in Section 8.4. Also the method fails to describe the kaons and antiprotons for the first bins because the separation between particles is not clean (see Fig. 9.13), while the limited statistics influences the fits in the last bins.

Bibliography

[1] S. L. Glashow, Nucl. Phys. **B22** (1961) 579.

[2] S. Weinberg, Phys. Rev. Lett. **19** (1967) 1264.

[3] A. Salam, in *"Elementary particle Theory"*, *The Nobel Symposium no 8*, edited by N. Svartholm, Almquist and Forlag, Stockholm (1968).

[4] P. W. Higgs, Phys. Lett. **12** (1964) 132; Phys. Rev. Lett. **13** (1964) 508; Phys. Rev. **145** (1966) 1156.

[5] F. Englert and R. Brout, Phys. Rev. Lett. **13** (1964) 321.

[6] G. Kane, *Modern Elementary Particle Physics: The Fundamental Particles and Forces*, Perseus Publishing, Cambridge (1993) 352 p.

[7] J. F. Donoghue, E. Golowich and B. R. Holstein, *Dynamics of the Standard Model*, Cambridge University Press (1992) 540 p.

[8] M. E. Peskin and D. V. Schroeder, *An Introduction to Quantum Field Theory*, Perseus Books, Cambridge(1995) 842 p.

[9] C. Amsler *et al.* (Particle Data Group), Phys. Lett. **B667**, 1 (2008) and 2009 partial update for the 2010 edition.

[10] R. K. Ellis, W. J. Stirling and B. R. Webber, *QCD and Collider Physics*, Cambridge University Press (1996) 435 p.

[11] G. Arnison *et al.* (UA1 Collaboration), Phys. Lett. **B122** (1983) 103.

[12] M. Banner *et al.* (UA2 Collaboration), Phys. Lett. **B122** (1983) 476.

[13] G. Arnison *et al.* (UA1 Collaboration), Phys. Lett. **B126** (1983) 398.

[14] P. Bagnaia *et al.* (UA2 Collaboration), Phys. Lett. **B129** (1983) 130.

[15] D. Decamp *et al.* (ALEPH Collaboration), Phys. Lett. **B235**, (1990) 399.

[16] D. N. Spergel *et al.*, Astrophys. J. Suppl. **148** (2003) 175, astro-ph/0302209.

[17] C. L. Bennett *et al.*, Astrophys. J. Suppl. **148** (2003) 1, astro-ph/0302207.

[18] W. de Boer, Prog. Part. Nucl. Phys. **33** (1994) 201, hep-ph/9402266.

[19] C. Quigg, Rept. Prog. Phys. **70** (2007) 1019, hep-ph/0704.2232.

[20] H. Nilles, Phys. Rept. **110** (1984) 1;
H. Haber and G. Kane, Phys. Rept. **117** (1985) 75;
R. Barbieri, Riv. Nuovo Cim. **11** (1988) 1.

[21] S. P. Martin, *A Supersymmetry Primer*, hep-ph/9709356.

[22] H. Nishino *et al.*(The Super-Kamiokande Collaboration), Phys. Rev. Lett. **102** (2009) 141801, hep-ex/0903.0676.

[23] G. R. Farrar and P. Fayet, Phys. Lett. **B76** (1978) 575.

[24] A. H. Chamseddine, R. Arnowitt and P. Nath, Phys. Rev. Lett. **49** (1982) 970;
J. Ellis, D. V. Nanopoulos and K. Tamvakis, Phys. Lett. **B121** (1983) 123.

[25] G. F. Giudice and R. Rattazzi, Phys. Rept. **322** (1999) 419, hep-ph/9801271.

[26] L. Randall and R. Sundrum, Nucl. Phys. **B557** (1999) 79, hep-th/9810155;
G. F. Giudice, M. A. Luty, H. Murayama and R. Rattazzi, JHEP **9812** (1998) 027, hep-ph/9810442.

[27] N. Arkani-Hamed and S. Dimopoulos, JHEP **06** (2005) 073, hep-th/0405159.

[28] G. F. Giudice and A. Romanino, Nucl. Phys. **B699** (2004) 65, hep-ph/0406088.

[29] S. Bethke, Eur. Phys. J. **C64** (2009) 689, hep-ph/0908.1135.

[30] B. Andersson *et al.*, Phys. Rept. **97** (1983) 31.

[31] T. Sjöstrand, S. Mrenna and P. Skands, JHEP **05** (2006) 026, hep-ph/0603175.

[32] J. D. Bjorken and E. A. Paschos, Phys. Rev. **185** (1969) 1975.

[33] R. P. Feynman, Phys. Rev. Lett. **23** (1969) 1415.

[34] C. Targett-Adams, hep-ex/0507024.

[35] J. C. Collins, D. Soper, and G. Sterman, Nucl. Phys. **B261** (1985) 104.

[36] R. J. Glauber, *Lectures in theoretical physics*, Inter-Science, New York (1959), Vol. 1.

[37] M. L. Miller, K. Reygers, S. J. Sanders and P. Steinberg, Ann. Rev. Nucl. Part. Sci. **57** (2007) 205, nucl-ex/0701025.

[38] F. Karsch, Nucl. Phys. **A698** (2002) 199.

[39] F. Karsch *et al.*, Phys. Rev. **D74** (2006) 054507.

[40] C. Ristea, *The Rapidity Dependence of High p_T Suppression in Au+Au Collisions at BRAHMS Experiment* (2007), available at: http://www4.rcf.bnl.gov/brahms/WWW/thesis/.

[41] D. d'Enterria, nucl-ex/0902.201.

[42] I. Arsene *et al.* (BRAHMS Collaboration) Nucl. Phys. **A757** (2005) 1.

[43] B. Abelev *et al.* (STAR Collaboration), Phys. Rev. **C76** (2007) 054903.

[44] K. Adcox *et al.* (PHENIX Collaboration), Nucl. Phys. **A757** (2005) 184.

[45] J. Adams *et al.* (STAR Collaboration), Nucl. Phys. **A757** (2005) 102.

[46] R. C. Hwa and C. B. Yang, Phys. Rev. **C70** (2004) 024905.

[47] R. C. Hwa, Phys. Rev. **D22** (1980) 1593.

[48] R. C Hwa and C. B. Yang, Phys. Rev. **C70** (2004) 024904.

[49] R. C Hwa and C. B. Yang, Phys. Rev. Lett. **97** (2006) 042301.

[50] LHC Design Report Volume I+II+III, CERN-2004-003-V-1, CERN-2004-003-V-2, CERN-2004-003-V-3 (2004), available at: http://lhc.web.cern.ch/LHC/LHC-DesignReport.html.

[51] L. Evans and P. Bryant (editors), JINST **3** (2008) S08001.

[52] ALICE Collaboration, *Technical Proposal for A Large Ion Collider Experiment at the CERN LHC*, CERN/LHCC 95-71 (1995), available at: http://cdsweb.cern.ch/record/293391/files/.

[53] K. Aamodt *et al.* (ALICE Collaboration), JINST **3** (2008) S08002.

[54] Minutes of Hundredth (second part) and Hundred-and-first Sessions of CERN Council, Geneva, 16 December 1994, CERN/2079, available at: http://cdsweb.cern.ch/record/33733/files/CM-P00079684-e.pdf.

[55] CERN Press Office, http://press.web.cern.ch/press/.

[56] G. Aad *et al.* (ATLAS Collaboration), JINST **3** (2008) S08003.

[57] S. Chatrchyan *et al.* (CMS Collaboration), JINST **3** (2008) S08004.

[58] A. Augusto Alves Jr. *et al.* (LHCb Collaboration), JINST **3** (2008) S08005.

[59] O Adriani *et al.* (LHCf Collaboration), JINST **3** (2008) S08006.

[60] G Anelli *et al.* (TOTEM Collaboration), JINST **3** (2008) S08007.

[61] P. Lebrun, *Interim Summary Report of the Analysis of the 19 September 2008 Incident at the LHC*, CERN EDMS 973073, ver. 1 (2008), available at: https://edms.cern.ch/document/973073/1.

[62] K. Aamodt *et al.* (ALICE Collaboration), Eur. Phys. J. C **65** (2010) 111, hep-ex/0911.5430.

[63] CERN Press Release, available at: http://press.web.cern.ch/press/PressReleases/Releases2010/PR07.10E.html.

[64] LHC 2010 Accelerator Draft Schedule, available at: http://lpc.web.cern.ch/lpc/.

[65] ALICE Collaboration, *Technical Design Report of the Inner Tracking System* CERN/LHCC/1999-12 (1999), available at: https://edms.cern.ch/document/398932/1.

[66] K. Aamodt *et al.* (ALICE Collaboration), JINST **5** (2010) P03003.

[67] ALICE Collaboration, *Technical Design Report of the Time Projection Chamber* CERN/LHCC/2000-01 (2000), available at: https://edms.cern.ch/document/398930/1.

[68] J. Alme *et al.* (ALICE TPC Collaboration), Nucl. Instrum. Meth. **A** (2010) 10.1016/j.nima.2010.04.042, physics.ins-det/1001.1950.

[69] ALICE Collaboration, *Technical Design Report of the Transition Radiation Detector* CERN/LHCC/2001-021 (2001), available at: https://edms.cern.ch/document/398057/1.

[70] ALICE Collaboration, *Technical Design Report of the Time of Flight System* CERN/LHCC/2000-12 (2000); Addendum CERN/LHCC/2002-16 (2002), available at: https://edms.cern.ch/document/460192/1.

[71] A. Akindinov *et al.*, Eur. Phys. J. **C32** (2004) 165.

[72] ALICE Collaboration, *Technical Design Report of the High-Momentum Particle Identification Detector* CERN/LHCC/1998-19 (1998), available at: https://edms.cern.ch/document/316545/1.

[73] ALICE Collaboration, *Technical Design Report of the Photon Spectrometer* CERN/LHCC/1999-4 (1999), available at: https://edms.cern.ch/document/398934/1.

[74] ALICE Collaboration, *Technical Design Report of the Electromagnetic Calorimeter* CERN/LHCC/2008-014 (2008), available at:
http://aliceinfo.cern.ch/Collaboration/Documents/EMCal.html.

[75] ALICE EMCal Collaboration, physics.ins-det/0912.2005.

[76] ALICE Collaboration, *Technical Design Report of the Dimuon Forward Spectrometer* CERN/LHCC/1999-22 (1999), available at:
https://edms.cern.ch/document/470838/1;
Addendum CERN/LHCC/2000-046 (2000), available at:
http://aliceinfo.cern.ch/Collaboration/Documents/TDR/index.html.

[77] ALICE Collaboration, *Technical Design Report on Forward Detectors: FMD, T0 and V0* CERN/LHCC/2004-025 (2004), available at:
https://edms.cern.ch/document/498253/1.

[78] ALICE Collaboration, *Technical Design Report of the Photon Multiplicity Detector* CERN/LHCC/1999-32 (1999), available at:
https://edms.cern.ch/document/398931/1;
Addendum CERN/LHCC/2003-038 (2003), available at:
https://edms.cern.ch/document/575585/1.

[79] ALICE Collaboration, *Technical Design Report of the Zero Degree Calorimeter* CERN/LHCC/1999-5 (1999), available at:
https://edms.cern.ch/document/398933/1.

[80] ALICE Collaboration, *Technical Design Report of the Trigger, Data Acquisition, High-Level Trigger and Control System* CERN/LHCC/2003-062 (2003), available at: https://edms.cern.ch/document/456354/2.

[81] J. F. Grosse-Oetringhaus, *Measurement of the Charged-Particle Multiplicity in Proton-Proton Collisions with the ALICE Detector* (2009), available at:
http://cdsweb.cern.ch/record/1175646/files/CERN-THESIS-2009-033.pdf.

[82] ALICE Collaboration, *Technical Design Report of the Computing* CERN/LHCC/2005-018 (2005), available at:
http://aliceinfo.cern.ch/Collaboration/Documents/TDR/Computing.html;
The ALICE experiment offline project, http://aliceinfo.cern.ch/Offline.

[83] *ROOT: A data analysis framework*, http://root.cern.ch/drupal/.

[84] R. Engel, Z. Phys. **C66** (1995) 203;
R. Engel and J. Ranft, Phys. Rev. **D54** (1996) 4244.

[85] M. Gyulassy and X. N. Wang, Comput. Phys. Commun. **83** (1994) 307.

[86] R. Brun, R. Hagelberg, M. Hansroul and J. C. Lassalle, CERN-DD-78-2-REV (1978).

[87] S. Agostinelli *et al.* (GEANT4 Collaboration), Nucl. Instrum. Meth. **A506** (2003) 250.

[88] A. Fasso *et al.*, hep-ph/0306267.

[89] I. Foster and C. Kesselmann, *The grid: blueprint for a new comuting infrastructure*, Morgan Kaufmann Publishers, U.S.A. (1999).

[90] P. Saiz *et al.*, Nucl. Instrum. Meth. **A502** (2003) 437;
AliEn home page, http://alien2.cern.ch/.

[91] B. Alessandro *et al.* (ALICE Collaboration), J. Phys. G: Nucl. Part. Phys. **32** (2006) 1295.

[92] Y. Belikov, J. Bracinik, M. Ivanov and K. Safarik, physics/0306108.

[93] R. M. Sternheimer, S. M. Seltzer, M. J. Berger, Phys. Rev. **B26** (1982) 6067; erratum in Phys. Rev. **B27** (1983), 6971.

[94] L. D. Landau, J. Exp. Phys. (USSR) **8** (1944) 201.

[95] H. Bichsel, Rev. Mod. Phys. **60** (1988) 663.

[96] H. Bichsel, Nucl. Instrum. Meth. **A562** (2006) 154.

[97] A. Kalweit, private communication.

[98] W. Blum, W. Riegler and L. Rolandi, *Particle Detection with Drift Chambers*, Second Edition, Springer-Verlag (2008), 448 p.

[99] A. Kalweit, *Energy Loss Calibration of the ALICE Time Projection Chamber* (2008), available at:
http://aliceinfo.cern.ch/TPC/Documents/Theses/index.html.

[100] W. W. M. Allison and J. H. Cobb, Ann. Rev. Nucl. Part. Sci. **30** (1980) 253.

[101] R. L. Gluckstern, Nucl. Instrum. Methods **24** (1963) 381.

[102] M. Fairbairn *et al.*, Phys. Rept. **438** (2007) 1, hep-ph/0611040.

[103] J. L. Feng and T. Moroi, Phys. Rev. **D61** (2000) 095004, hep-ph/9907319.

[104] A. J. Barr *et al.*, JHEP **03** (2003) 045, hep-ph/0208214.

[105] J. L. Feng, S. Su and F. Takayama, Phys. Rev. **D70** (2004) 075019, hep-ph/0404231.

[106] S. Raby, Phys. Lett. **B422** (1998) 158, hep-ph/9712254.

[107] C. H. Chen, M. Dress and J. F. Gunion, Phys. Rev. **D55** (1997) 330, hep-ph/9607421.

[108] P. Gambino, G. F. Giudice, P. Slavich, Nucl. Phys. **B726** (2005) 35, hep-ph/0506214.

[109] J. L. Hewett, B. Lillie, M. Masip and T. G. Rizzo, JHEP **09** (2004) 070, hep-ph/0408248.

[110] C. Balazs, M. Carena, C. E. M. Wagner, Phys. Rev. **D70** (2004) 015007, hep-ph/0403224.

[111] T. Appelquist, H. C. Cheng and B. A. Dobrescu, Phys. Rev. **D64** (2001) 035002, hep-ph/0012100.

[112] C. Friberg, E. Norrbin and T. Sjöstrand, Phys. Lett. **B403** (1997) 329, hep-ph/9704214.

[113] G. Ingelman, C. Wetterich, Phys. Lett. **B174** (1986) 109.

[114] P. H. Frampton, P. Q. Hung and M. Sher, Phys. Rep. **330** (2000) 263.

[115] W. Beenakker, R. Höpker, M. Spira, P. M. Zerwas, Nucl. Phys. **B492** (1997) 51, hep-ph/9610490.

[116] W. Beenakker, M. Klasen, M. Krämer, T. Plehn, M. Spira, P. M. Zerwas, Phys. Rev. Lett. **83** (1999) 3780, hep-ph/9906298.

[117] T. Plehn, Czech. J. Phys. **55** (2005) 213, hep-ph/0410063.

[118] A. C. Kraan, *Interactions and Detection of R-hadrons* (2004), available at: http://www.pi.infn.it/ aafke/aafke.html.

[119] A. De Rujula, H. Georgi and S. L. Glashow, Phys. Rev. **D12** (1975) 147.

[120] Y. R. De Boer, A. B. Kaidalov, D. A. Milstead, O. I. Piskounova, J. Phys. **G35** (2008) 075009, hep-ph/0710.3930.

[121] R. Mackeprang and A. Rizzi, Eur. Phys. J. **C50** (2007) 353, hep-ph/0612161.

[122] R. Mackeprang and D. Milstead, Eur. Phys. J. **C66** (2010) 493-501, hep-ph/0908.1868.

[123] G. Abbiendi *et al.* (OPAL Collaboration), Phys. Lett. **B572** (2003) 8, hep-ex/0305031.

[124] A. Heister *et al.* (ALEPH Collaboration), Eur. Phys. J. **C31** (2003) 327, hep-ex/0305071.

[125] T. Aaltonen *et al.* (CDF Collaboration), Phys. Rev. Lett. **103** (2009) 021802, hep-ex/0902.1266.

[126] V. Abazov *et al.* (D0 Collaboration), Phys. Rev. Lett. **102** (2009) 161802, hep-ex/0809.4472.

[127] A. Dobrin, P. Christiansen, H-Å. Gustafsson, P. Gros, A. Oskarsson and E. Stenlund, *Search for Heavy Stable Charged Hadrons in pp Collisions with the ALICE Experiment*, ALICE-INT-2008-017 (public).

[128] A. Dobrin (ALICE Collaboration), AIP Conf. Proc. **1200** (2010) 730, hep-ph/0910.0759.

[129] PYTHIA 6 HepForge Page, available at: http://projects.hepforge.org/pythia6/.

[130] ALICE First Physics Meeting December 14 (2007), available at: http://indico.cern.ch/conferenceDisplay.py?confId=23995.

[131] Y. Nomura and D. Tucker-Smith, Nucl. Phys. **B 698** (2004) 92, hep-ph/0403171.

[132] Y. Nomura and B. Tweedie, Phys. Rev. **D 72** (2005) 015006, hep-ph/0504246.

[133] J. Adams *et al.* (STAR Collaboration), Phys. Lett. **B637** (2006) 161, nucl-ex/0601033.

[134] B. I. Abelev *et al.* (STAR Collaboration), Phys. Rev. Lett. **97** (2006) 152301.

[135] B. I. Abelev *et al.* (STAR Collaboration), Phys. Lett. **B655** (2007) 104.

[136] P. Christiansen *et al.*, Nucl. Instrum. Meth. **A609** (2009) 149.

[137] A. Kalweit, talk given at "TPC reconstruction and online/offline software workshop", http://indico.cern.ch/conferenceDisplay.py?confId=67782.

[138] A. Matyja, talk given at "TPC reconstruction and online/offline software workshop", http://indico.cern.ch/conferenceDisplay.py?confId=67782.

[139] M. Shao *et al.*, Nucl. Instrum. Meth. **A558** (2006) 419.

[140] Y. Xu *et al.*, physics.ins-det/0807.4303.

[141] K. Aamodt *et al.* (ALICE Collaboration), Eur. Phys. J. **C68** (2010) 89, hep-ex/1004.3034.

[142] J. Otwinowski, private communication.

[143] K. Aamodt *et al.* (ALICE Collaboration), Eur. Phys. J. **C68** (2010) 345, hep-ex/1004.3514.

[144] J. F. Grosse-Oetringhaus *et al.*, ALICE Internal Note ALICE-INT-2009-022 (2009).

[145] K. Aamodt *et al.* (ALICE Collaboration), Phys. Lett. **B** (2010) doi:10.1016/j.physletb.2010.08.026, hep-ex/1007.0719.

[146] V. Khachatryan *et al.* (CMS Collaboration), Phys. Rev. Lett. **105** (2010) 022002, hep-ex/1005.3299.

[147] C. Tsallis, J. Stat. Phys. **52** (1988) 479.

[148] P. Z. Skands, hep-ph/1005.3457.

[149] J. Schukraft, talk given at ICHEP 2010.

[150] L. Betev and P. Chochula, *Definition of the ALICE Coordinate System and Basic Rules for SubDetector Components Numbering*, ALICE-INT-2003-038 (2003), available at: https://edms.cern.ch/document/406391/2.

[151] W. R. Leo, *Techniques for Nuclear and Particle Physics Experiments*, Springer-Verlag, 1994.

[152] A. Kühmichel, Nucl. Instr. Meth. **A360** (1995) 52.

[153] M. E.. Rose, S. A. Korff, Phys. Rev. **59** (1941) 850.